THESE DE DOCTORAT

Présentée à
L'UNIVERSITE DE LILLE 1
École doctorale Sciences de la matière, du rayonnement et de l'environnement

Pour obtenir le grade de
DOCTEUR EN SCIENCES
Dans la spécialité: Molécules et matière condensée (MMC)

par

Zaidao LI

Influence of the microstructure on mechanical properties and damage mechanisms in Al-Si-Cu alloys by using 2D and 3D in-situ analysis

Influence de la microstructure sur les propriétés mécaniques et les mécanismes d'endommagement d'alliages Al-Si-Cu étudiés via des analyses in-situ 2D et 3D

Soutenance prévue le 23 Novembre 2016 devant le jury composé de :

Rapporteur	*Jean-Yves Buffière, Professeur, MATEIS, INSA Lyon, Villeurbanne*
Rapporteur	*Luc Salvo, Professeur, Grenoble INP – PHELMA, Grenoble*
Président du jury	*Henri Nguyen Thi, Professeur, Université d'Aix-Marseille, Marseille*
Examinateur	*Pierre Osmond, Spécialiste comportement des matériaux métalliques, PSA Peugeot Citröen, Vélizy*
Co-encadrante	*Nathalie Limodin, Chargée de recherche CNRS, LML, École Centrale de Lille, Villeneuve d'Ascq*
Co-encadrante	*Amina Tandjaoui, Maître de Conférences, LML, École Centrale de Lille, Villeneuve d'Ascq*
Co-encadrant	*Philippe Quaegebeur, Maître de Conférences, LML, École Centrale de Lille, Villeneuve d'Ascq*
Directeur de thèse	*David Balloy, Professeur, UMET, Université Lille 1, Villeneuve d'Ascq*

Thèse préparée au Laboratoire de Mécanique de Lille (FRE CNRS 3723) et Unité Matériaux et Transformations (UMR CNRS 8207)

REMERCIEMENTS

Cette thèse a été réalisée aux Laboratoire de Mécanique de Lille (LML) ER3 et Unité Matériaux et Transformations (UMET), j'aimerais donc remercier leurs directeurs respectifs, Eric Charkaluk et Alexandre Legris, de m'avoir accueilli dans leur laboratoire. J'aimerais également remercier le financement de China Scholarship Council (CSC) et le support de projet INDiANA qui m'ont permis de bénéficier d'excellentes conditions de travail et d'une liberté très appréciable dans mes travaux.

Je voudrais remercier les membres du Jury de m'avoir accordé de leur temps à la lecture, à la critique et à l'amélioration de mon travail. Je tiens à exprimer toute ma gratitude à Henri Nguyen Thi pour l'honneur qu'il m'a fait de présider mon jury, ainsi qu'à Jean-Yves Buffière et Luc Salvo d'avoir accepté de rapporter ce travail et d'avoir eu leurs regards d'experts sur mes travaux. Je tiens aussi à remercier Pierre Osmond pour avoir examiné et suivi ce travail, le tout avec beaucoup de gentillesse.

Je tiens à remercier chaleureusement mon directeur de thèse David Balloy, Professeur à l'Université Lille 1, pour la confiance qu'il m'a accordée en acceptant d'encadrer ce travail doctoral, sa disponibilité, ses précieux conseils et son soutien. Durant ces 38 mois de thèse, son aide a été précieuse pour mes recherches, mes études et ma vie en France.

Je remercie mon encadrante Nathalie Limodin, chargée de recherche au CNRS, pour ses précieux conseils tout au long de ce projet, et tout particulièrement pour son soutien et sa disponibilité durant la rédaction de cette thèse. Mes plus sincères remerciements vont également à mes encadrants Amina Tandjaoui et Philippe Quaegebeur, Maître de Conférences à l'Ecole Centrale de Lille, pour m'avoir fait confiance en m'attribuant ce travail de recherche et pour m'avoir laissé suffisamment de liberté lors de ces travaux tout en me donnant des conseils très enrichissants.

Je tiens à remercier plus spécialement Nora Dahdah, pour son accompagnement et son aide pendant ces trois années en France. Sans sa gentillesse, ma thèse aurait été différente et ma vie en France n'aurait pas été si agréable. Je remercie vivement tous les membres du LML et UMET, plus particulièrement : Ahmed El Bartali (essai de traction), Katia Biotteau (MEB), Olivier Lagache (OM), Jean-Francois Witz (corrélations 2D et 3D), François Lesaffre (usinage des éprouvettes), Franck Béclin (MEB), Fabienne Delepaut, Brigitte Warocquier, Valerie Sulis (secrétariat), Gregory Hauss (ISIS4D), Long Wang, Jerome Hosdez, Zhifan Jiang, ainsi que tous mes collègues et amis pour les divers services qu'ils m'ont rendu dans les domaines scientifiques, techniques et administratifs. Cela m'a ainsi permis l'aboutissement de ce projet et ce dans un environnement de travail des plus agréables. J'en profite également pour remercier l'ensemble des thésards pour leur aide et leur contribution à cette bonne ambiance dans le laboratoire.

Enfin, ces dernières lignes sont destinées à mes parents, à toute ma famille et à mes amis que je voudrais remercier pour m'avoir soutenu et encouragé. Je vous suis très reconnaissant d'avoir toujours été là pour moi.

Contents

List of Figures

List of Tables

Introduction

Contents

Background

Due to economic and environmental requirements, it is becoming increasingly important to reduce vehicle weight. For such an objective, aluminium casting alloys, particularly those belonging to the aluminium-silicon (Al-Si) system, are now extensively used in various automotive components such as wheels and cylinder heads because of their light weight in addition to a range of desirable engineering properties. These properties include high strength to weight ratio, good corrosion resistance, high electrical and thermal conductivity (Cobden and Banbury 1994), good machinability and excellent surface finishing (Gruzleski and Closset 1990).

The cylinder head (Figure 0-1) which is made of an aluminium-silicon alloy (in this case an A319 alloy) locally experiences temperature cycles ranging from 20 to 300 °C (Thomas, Verger et al. 2004). In particular, the inter-valve zone in fire deck is the most critical area where temperature can reach the value of 300 °C during the engine operation. Therefore a high requirement for the mechanical properties of the material used for cylinder head had to be met in order to adapt to these working conditions.

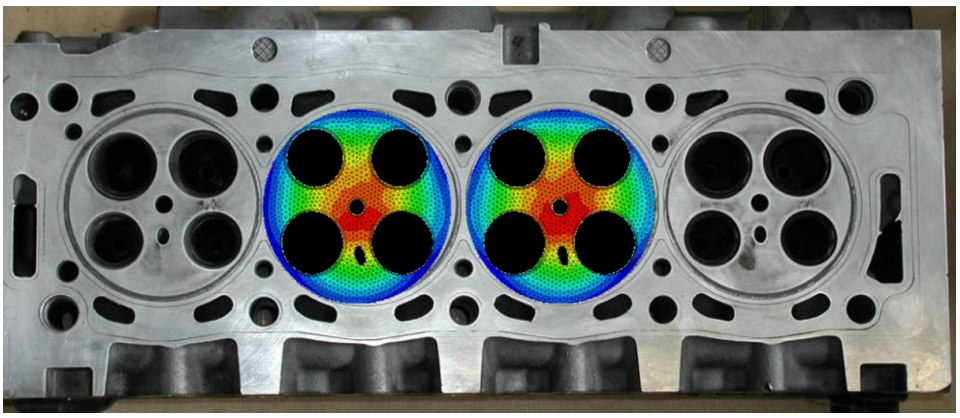

Figure 0-1: Cylinder head and temperature field in the fire deck (PSA data)

Introduction

The microstructure of Al-Si-Cu alloys can widely affect the mechanical properties, damage mechanisms and the fatigue failure. The various microstructural parameters to consider are the Secondary Dendrite Arm Spacing (SDAS), the eutectic Si particle size and morphology. Moreover, the amount and morphology of iron-intermetallics and Al_2Cu phase observed in the microstructure are also to be considered.

Microstructures of Al-Si-Cu alloys are largely influenced by the alloy composition, casting process and heat treatment condition. Some studies (Seifeddine and Svensson 2013) (Fabrizi, Ferraro et al. 2013) have already been performed in order to research the influence of alloying elements addition (i.e. Sr, Fe and Mn) on the microstructure and mechanical properties of these alloys.

Silicon improves castability and reduces hot shortness in Al-Si-Cu alloy (Kaufman and Rooy 2004), it forms eutectic silicon phase with aluminium in Al-Si alloys. Mechanical properties of Al–Si alloys are influenced by the size and morphology of eutectic silicon particles (Sui, Wang et al. 2015). Hence, modification of the normally acicular, flake-like morphology of the eutectic Si to a fibrous form is usually carried out through the addition of certain elements (Na, K, Rb, Ce, Ca, Sr, Ba, La, Yb etc.) or with a rapid cooling rate (Hegde and Prabhu 2008).

Iron is probably the most detrimental element and exists as a common impurity element in Al–Si alloys, especially in recycled aluminium alloy (Moustafa 2009). During solidification process, iron, together with other alloying elements (Cu, Mg, Zn, Mn, Ti, etc.) partly goes into solid solution in the matrix and partly forms Fe-rich intermetallic particles (Narayanan, Samuel et al. 1994). In Al-Si-Cu alloy, the most common iron-intermetallic is the platelet-like β-Al_5FeSi. Due to its brittle nature, this phase can be quite deleterious to the alloy properties. Under conditions of high stress intensity factor, the β-platelets fracture or separate from the matrix, providing preferential crack paths ahead of the advancing crack, thereby lowering the impact properties of alloys (Ma, Samuel et al. 2014). In addition, high iron content was shown to have a significant effect on the formation of porosity in Al-Si-Cu–based foundry alloys (Dinnis, Taylor et al. 2006). Mn additions are used to reduce the detrimental effects of the β phase by replacing it with the less-detrimental Chinese script α-$Al_{15}(Fe,Mn)_3Si_2$ phase (Narayanan, Samuel et al. 1994).

Copper, as the main alloying element (~3.5 wt. %) in A319 casting alloy, forms an intermetallic phase with aluminium that precipitates during solidification either as block like Al_2Cu or in eutectic form as ($Al+Al_2Cu$) (Li, Samuel et al. 2003), and can also affect the mechanical properties of A319 casting alloy (Li 2003).

The casting process also can affect the microstructure and then the properties of alloys (Okayasu, Ohkura et al. 2012). For the purpose of geometry optimization, cost reduction and consumption control of automotive cylinder head, Gravity Die Casting (DC) process, as the conventional casting process, is progressively being replaced by the Lost Foam Casting (LFC) process. However, a major disadvantage of Lost Foam Casting is that a coarser microstructure is produced comparatively to Die

Casting processes at faster cooling rates (Table 0-1) (Tabibian 2011). This coarse microstructure, which consists of hard second phase particles (eutectic Si, Al_2Cu phase, and iron-intermetallics), large pores and microshrinkage cavities, has a major influence on the fatigue properties (Tabibian, Charkaluk et al. 2010).

In addition, heat treatment is usually performed to achieve an increase in strength through precipitation hardening for Al-Si-Cu alloys, and the effect of heat treatment on the mechanical properties in terms of hardness and tensile strengths is well studied, while the influence on plastic deformation behaviour and elongation to fracture is less studied (Mohamed and Samuel 2012).

Mechanical properties and tensile behaviour are strongly influenced by microstructure. Thus the effect of various alloying elements additions, different casting methods and heat treatment conditions on microstructural changes and on the mechanical properties and damage mechanisms of Al-Si-Cu casting alloys should be further studied.

Table 0-1: LFC and DC casting process

	Die casting	Lost foam casting
Equipment	Dies, metallic and sand molds	Polystyrene assembly
Geometry	-	Complex
Weight	-	- 1Kg
Price	-	- 15%
Solidification rate (°C/s)	30	0.15-0.8
SDAS (µm)	35	85

Objectives

The aim of the present work was to study the influence of the microstructure on mechanical properties and damage mechanisms in Al-Si-Cu alloys by using 2D and 3D in-situ analysis.

Firstly, metallurgical parameters controlling the microstructure of Al-Si-Cu alloy were studied. In order to achieve this, four alloys with different Sr, Fe, and Mn content were used. A full metallographic 2D and 3D characterization of the microstructure through optical- and Scanning Electron Microscopy (SEM) and laboratory X-ray tomography was performed in order to study the influence of variation in Sr, Fe, and Mn content within the composition tolerance of the AlSi7Cu3 alloy and of the casting process (i.e. DC and LFC) on the microstructure and solidification parameters. Then, mechanical tests (tensile test and hardness test) were performed on these four alloys to study the relationship between microstructure and mechanical properties. Secondly, 2D in-situ tensile test observations with Digital Image Correlation (DIC) were performed on two DC A319 alloys with different Fe/Mn content in order to study the effect of Fe-rich intermetallic on tensile damage

mechanisms in the A319 alloy. This method allows identifying the relation between damage mechanisms and casting microstructure on surface.

Thirdly, the influence of heat treatment on the microstructure and damage mechanisms of Lost Foam Casting A319 alloy was studied. Two different heat treatments were carried out for the LFC A319 alloy which was extracted from one cylinder head. The evolution of microstructures was analysed using optical- and Scanning Electron Microscopy (SEM) and laboratory X-ray tomography. Then, 3D in-situ tensile observations with Digital Volume Correlation (DVC) were performed on the two alloys with different heat treatment. This method allows following the evolution of the cracks in volume and analysing the relation between the measured fields and damage behaviour.

In addition, post-mortem analysis using Scanning Electron Microscopy (SEM) and Energy Dispersive X-ray (EDX) analysis was performed on these failed 2D/3D tensile specimens to give more details about the damage mechanisms.

Besides, in order to study the relationship between the microstructure and damage mechanisms of as cast Al-Si-Cu alloy by in-situ fatigue test, a temperature gradient casting set-up will be implemented to realize normalized specimens with an equivalent microstructure as in fire deck area of cylinder heads while controlling the defects in the centre of specimen.

Thesis structure

This thesis contains seven chapters. Chapter 1 is literature review, and Chapter 2 is experimental part. Chapter 3 is divided into two sections. First, the influence of different Sr, Fe, and Mn content and casting process on the microstructure of Al-Si-Cu alloys is presented. The second section studies the solidification sequences of Al-Si-Cu alloys by thermal analysis, and discusses the effect of Sr, Fe and Mn on the solidification parameters.

The relationship between the different microstructures and the mechanical properties are first presented in Chapter 4. Then the effect of Fe-rich intermetallics on damage mechanisms on a micro scale level is discussed for two DC Al-Si-Cu alloys with different Fe contents.

In Chapter 5, two heat treatment conditions were performed on specimens that were extracted from an A319 LFC cylinder head. A comparative study of 2D and 3D microstructural characteristics is performed on these alloys before and after the heat treatment. Lab-CT tomography was used to monitor in situ tensile tests on specimens in order to study the damage mechanisms of alloys in 3D, while the field measurements and post-mortem analysis are performed to give more information about the damage mechanisms.

Chapter 6 introduces the experimental methods and the set-up for temperature gradient casting. Then, some results and prospects are given for future work.

Finally, the principal conclusions of this study along with some suggestions for further investigation are presented in chapter 7.

1 Chapter 1 Literature review

Contents

1.1 Aluminium-silicon alloys

Aluminium-silicon alloys containing silicon as the major alloying element are the popular choice for the majority of aluminium castings because of their excellent castability, good corrosion resistance and machinability (Hielscher, Sternau et al. 2002). They constitute 85-90% of the total aluminium cast parts produced (Wang and Lu 2012). In standardized commercial cast aluminium-silicon alloys, the silicon content is usually in the range of 5 to 23 wt. % (Warmuzek 2004). Small amounts of Cu, Mg, Mn and Ni, etc. are usually being added to achieve strengthening of Al-Si alloys (Wang and Lu 2012).

The structure of the alloys can be hypoeutectic, hypereutectic, or eutectic, as shown in Figure 1-1 (Warmuzek 2004).

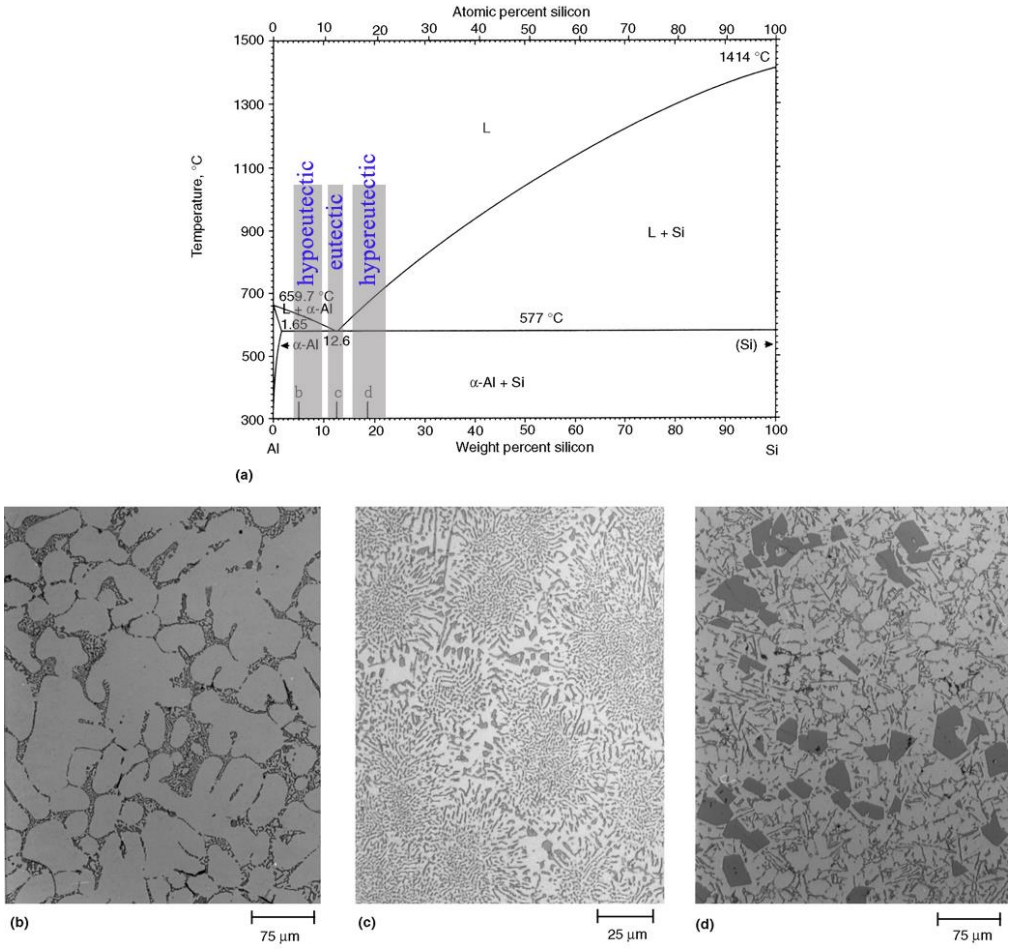

Figure 1-1: Commercial cast aluminium-silicon alloys. (a) Al-Si equilibrium diagram. (b) Microstructure of hypoeutectic alloy. (c) Microstructure of eutectic alloy. (d) Microstructure of hypereutectic alloy (Warmuzek 2004)

1.1.1 Al-Si-Cu alloy system

Among the most widely used aluminium casting alloys are those that contain silicon and copper. The addition of copper to Al–Si alloys enables the formation of Al-Al_2Cu eutectic and/or blocky Al_2Cu phases and other intermetallic compounds, which increase strength and machinability of casting parts after heat treatment through precipitation hardening, Silicon improves castability and reduces hot shortness (Kaufman and Rooy 2004). The A319 alloy is a typical hypoeutectic Al–Si alloy (Figure 1-1(b)) and contains ~7.5 wt. %Si, ~3.5 wt. % Cu, ~0.3 wt. % Mg and various other minor elements and impurities (Kaufman and Rooy 2004). The 319 type alloys have received increased interest in the recent past in the automotive industry and are being widely used in cylinder head. Due to its application and high demand in the automotive industry, the A319 alloy requires detailed information on the relationship between the microstructures and the mechanical properties.

1.1.2 Recycled aluminium alloy

In recent years, more than half of all the aluminium currently produced in the EU originates from recycled raw materials and that trend is on the increase due to its ecological and economic advantages (Bacaicoa, Dwivedi et al. 2016). The production of recycled aluminium requires 95% less energy than primary aluminium, and producing aluminium by recycling creates only about 5 % as much CO_2 as by primary production (Tillová, Chalupová et al. 2012).

Nevertheless, there is a major challenge in using recycled aluminium as many accumulated elements can only be removed with a very costly process from the melt, hence limiting its use for high-performance applications (Bacaicoa, Dwivedi et al. 2016). Among the impurity elements, iron, which is present in much higher concentrations in recycled aluminium, forms brittle intermetallic inclusions. The detrimental needle-like β-Al_5FeSi phase can generate high local stress concentrations, act as the main crack initiation sites and cause failure (Yi, Gao et al. 2004). Consequently, the damage mechanism of the high iron-content Al-Si-Cu alloy requires more study.

1.2 Solidification of Al-Si-Cu alloy

Solidification plays a vital role in influencing the microstructure and hence affecting the quality and mechanical properties of cast products. It is therefore important to develop an understanding of the mechanisms of solidification and of how the resulting microstructure is affected by parameters such as temperature, time, and cooling rate.

1.2.1 Reactions during the solidification of Al-Si alloy

The solidification process of hypoeutectic Al–Si alloy can be explained by the phases diagram (Figure 1-1(a)). Firstly, the temperature is high enough so that the alloy is at liquid phase. When the alloy is cooled, it remains in liquid state until it reaches the temperature where it crosses the liquidus line, which separates the liquid phase and α+liquid phase. Below the liquidus, alpha phase starts to solidify at favourable nucleation sites. As the alloy continues to cool, the existing nucleation sites grow as dendrites and further nucleation sites form within the liquid part of the mixture. The alpha phase forms until the remaining liquid is at the eutectic composition at the eutectic temperature. At this temperature where it crosses the eutectic line, the α-Al stops forming further and the remaining liquid solidifies into lamellar structure of a eutectic composition (Chirita 2011). The solidification reactions of two A319 alloys that correspond to the solidification diagram of hypoeutectic Al-Si alloy are presented in Table 1-1 and the corresponding chemical compositions of the two alloys is shown in Table 1-2. In fact, some parameters can affect the solidification reactions during the casting. For example, the cooling rate (Valtierra and Lacaze 2005), the presence of additional alloying elements such as Sr (Valtierra and Lacaze 2005), as well as Fe and Mn (Lu and Dahle 2005) can lead to a more complex

solidification sequence. (Alkahtani, Elgallad et al. 2016) reported that introduction of 100 ppm Sr to A356 alloy reduced the eutectic temperature by about 7 °C. (Lu and Dahle 2005) found that increasing the Fe content changes the precipitation sequence of the β phase using Interrupted Quenching Test. At low iron contents, the β phase is expected to form at a lower temperature through a ternary eutectic reaction. At higher iron contents, the majority of β phase precipitates prior to the eutectic Si, leading to the formation of coarse platelets.

Table 1-1: Reactions occurring during solidification of some 319 alloys (Valtierra and Lacaze 2005) according to Backerud et al. (Backerud, Chai et al. 1990) and to Samuel et al. (Samuel, Samuel et al. 1996)

Backerud et al.	**Temperature (°C)**	**Samuel et al.**	**Temperature (°C)**
(Al) dendritic network	609		610
Liq. → (Al) +$Al_{15}Mn_3Si_2$+ (Al_5FeSi)	590		
Liq.→(Al) + Si + Al_5FeSi	575	Precipitation of eutectic Si	562
		Precipitation of $Al_6Mg_3FeSi_6$+Mg_2Si	554
Liq. → (Al) + Al_2Cu + Si + Al_5FeSi	525	Precipitation of Al_2Cu	510
Liq. → (Al) + Al_2Cu + Si + $Al_5Mg_8Cu_2Si_6$	507	Precipitation of $Al_5Mg_8Cu_2Si_6$	490

Table 1-2: Chemical composition of the alloys mentioned in Table 2-1 (wt. %)

	Si	**Cu**	**Fe**	**Mn**	**Mg**	**Ti**	**Sr (ppm)**
Backerud et al.	5.7	3.4	0.62	0.36	0.10	0.14	_
Samuel et al.	6.23	3.8	0.46	0.14	0.06	0.14	_

1.2.2 Effect of solidification rate

The solidification rate is perhaps the most important of the various parameters influencing microstructure during casting, as it directly or indirectly affects almost all the microstructural parameters, such as Secondary Dendrite Arm Spacing (SDAS), the degree of eutectic silicon modification and grain refinement, and the amount of microporosity, the morphology and size of intermetallic compounds.

- ✓ **Secondary Dendrite Arm Spacing (SDAS)**

SDAS is used to describe dendrite refinement. The larger the SDAS, the coarser the microconstituents and the more pronounced their effects on properties. Finer SDAS is desirable for improved mechanical property (Seifeddine and Sj 2013).

Several researchers have analysed the coarsening phenomenon in dendritic growth. One of the most effective models to deal with a correlation between SDAS and solidification parameters was proposed. According to (Kirkwood 1985), the SDAS is given by the simple empirical equation:

$SDAS = 5.0 (M*t_f)^{1/3}$

Where t_f is the solidification time and M is a coefficient that slightly depends on the chemical composition.

Microstructure of AlSi7Cu2 cast alloys solidified at cooling rate of 0.16 $^oCs^{-1}$, 0.46 $^oCs^{-1}$ and 0.72 $^oCs^{-1}$ are shown on Figure 1-2(a), (b) and (c) respectively (Dobrzański, Maniara et al. 2007). It is shown that the samples solidified with high cooling rate have smaller silicon particles than sample with lower cooling rate. In terms of microstructure, the SDAS, which gives a measure of the fineness of the microstructure, can vary considerably with the cooling rate. Figure 1-3 illustrates the SDAS values obtainable in a 356 alloy over a range of cooling rates (Shabani and Mazahery 2011).

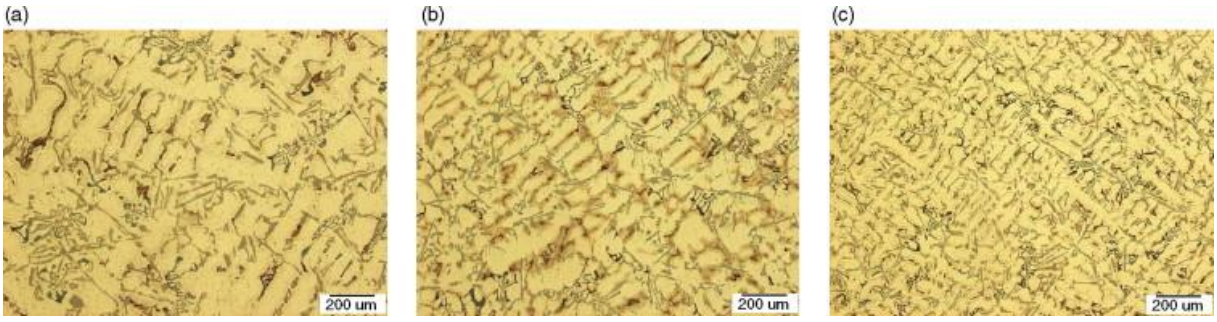

Figure 1-2: Microstructure of AlSi7Cu2 alloy solidified with rate (a) 0.16 °Cs^{-1}; (b) 0.46 °Cs^{-1}; (c) 0.72 °Cs^{-1} (Dobrzański, Maniara et al. 2007)

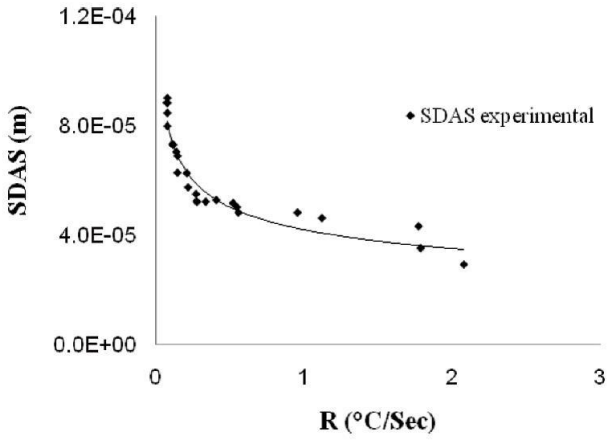

Figure 1-3: SDAS as a function of cooling rate for A356 alloy (Shabani and Mazahery 2011)

The size of the dendrites is affected not only by heat transfer rate during solidification of the casting into mould but also by the chemical composition of the alloy. The effect of minor variation in alloying elements, e.g. Si, Cu, content on SDAS has been reported by some researchers (Fabrizi, Ferraro et al. 2013, Sanna, Fabrizi et al. 2013). (Fabrizi, Ferraro et al. 2013) reported that the value of SDAS decreased when the content of alloying elements such as Sr, Cu and Mg increased in Al-Si-Cu based DC alloys for a fixed solidification time. In this thesis, the effect of Sr, Fe and Mn content on the SDAS in AlSi7Cu3 alloy has also been studied and will be discussed in detail in Chapter 3.

- ✓ **Hardness**

Cooling rate also can affect the hardness of alloys, the hardness of two Al–9%Si alloys as a function of cooling rate (i.e. SDAS) is shown in Figure 1-4. According to (Seifeddine, Johansson et al. 2008), as the material is rapidly solidified, the dendrites are likely to get enriched with Si and the materials exhibit higher hardness; as the cooling rate is gradually reduced, the Si seems to diffuse from the Al-dendrites resulting in a great loss of both strength and ductility of the material.

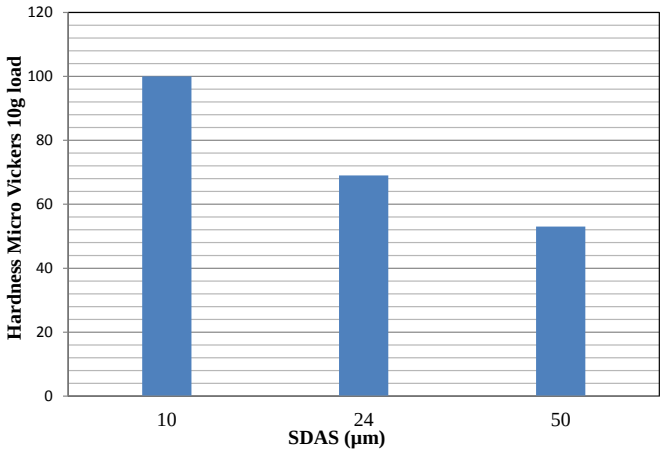

Figure 1-4: Illustration of the 10 g micro-Vickers hardness of the Al-dendrites at various cooling rates, i.e. SDAS, for Al–9%Si alloys (Seifeddine, Johansson et al. 2008)

- ✓ **Porosity**

Cooling rate is also very important in the formation of porosity. In general, with a higher cooling rate, grain density increases, dendrite arm spacing decreases, and the average pore size will decrease. With a lower cooling rate, more gas can precipitate from the melt and thus produce higher porosity.

It has been observed that a decrease in the cooling rate or increase in SDAS increases both the total amount of porosity and the average pore size in both modified and unmodified Al–Si alloy castings (Seifeddine and Sj 2013). The effect of various cooling rates on the porosity levels of the A356 alloy is shown in Figure 1-5. At increasing solidification rates, less time is available for hydrogen to diffuse into the interdendritic spaces of the partially solidified metal, resulting in smaller pores sizes.

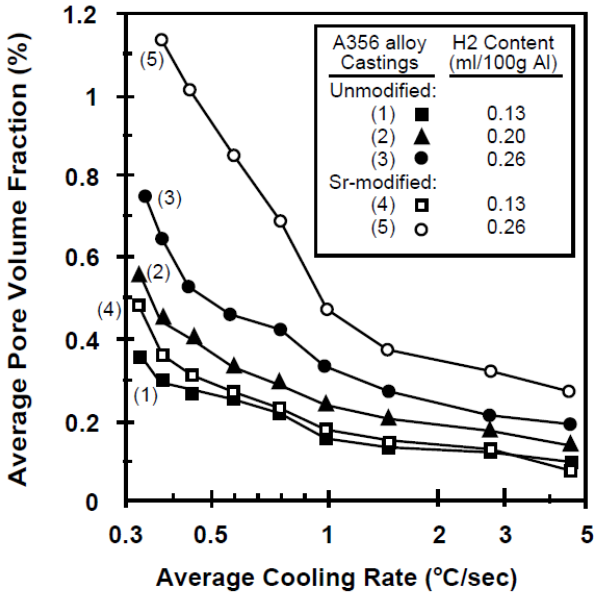

Figure 1-5: The effect of cooling rate on the porosity levels of A356 alloys (Emadi and Gruzleski 1995)

In addition, (Li, Samuel et al. 2004) have reported that the higher temperature gradients present under rapid solidification conditions can limit the length of the mushy zone, making feeding easier and retarding porosity formation, castings cooled at higher rates tend to contain less and more finely dispersed porosity.

- ✓ **Eutectic modification**

Rapid solidification can also affect the degree of eutectic silicon modification and result in a fibrous eutectic structure; this will be discussed in the following sections.

1.2.3 Die Casting and Lost-Foam Casting

Different casting parameters can change the microstructure of castings. For the production of cylinder heads, many casting technologies are applied, such as Die Casting (DC) and Lost Foam Casting (LFC).

- ✓ **Die Casting**

Gravity DC is a process where the liquid metal is poured into permanent metallic moulds without application of any external pressure (Figure 1-6) (Niane and Michalet 2011). It is widely used for the possibility of obtaining net to shape components of complex geometry at high production rates. And due to the rapid process of solidification, die castings have a dense, fine-grained structure with good strength characteristics. However, the drawback of this casting method is that sand core should be remade to produce the internal complex shape in each mould, thus causing prices to rise.

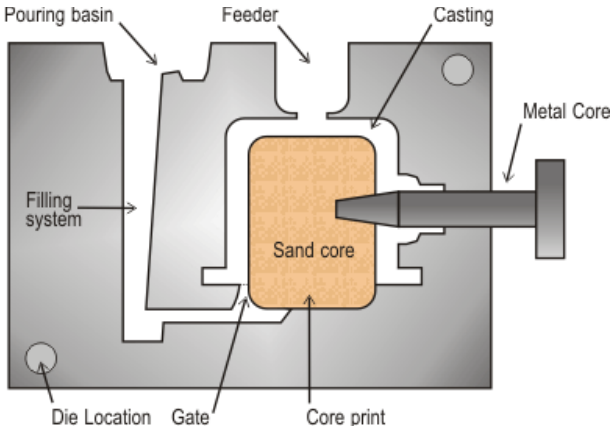

Figure 1-6: Illustration of gravity die casting (Niane and Michalet 2011)

- ✓ **Lost foam Casting**

Lost foam Casting (LFC) is a relatively new process that begins with a Styrofoam assembly that replicates the part being cast, and it allows the realization of very complex geometries together with the use of cast-in liners, additional chilling.

Due to its environmental and technical benefits such as no binder usage, minimum required machining and production of complex cast parts, LFC process is currently gaining an increased attention in automotive and aerospace industries (Jafari, Idris et al. 2013). As shown in Figure 1-7 (Niane and Michalet 2011), the lost foam casting process includes the following steps:

1. The coated replica/pattern is placed in a flask and loose sand is placed around the pattern and shaken into its voids.
2. Molten aluminium is then poured through a foam funnel, into the sand where the hot metal melts and displaces the foam of the pattern.
3. The metal cools in the shape of the part.

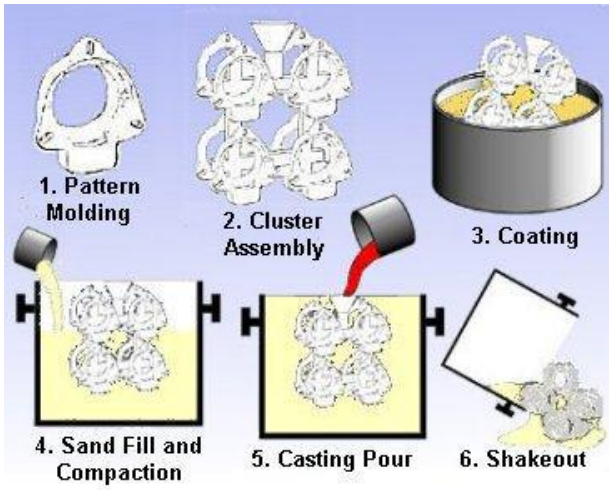

Figure 1-7: Illustration of lost foam casting (Niane and Michalet 2011)

Lost Foam process offers today some industrial advantages (Kaufman and Rooy 2004), for example, no cores are required in LFC; reduction in capital investment and operating costs; no binders or other additives are required for the sand, which is reusable; Flasks for containing the mould assembly are inexpensive, and shakeout of the castings in unbonded sand is simplified and do not require the heavy shakeout machinery that is required for other sand casting methods; casting cleaning is minimized since there are no parting lines or core fins. Therefore, the LFC process has yet to be optimized to achieve reductions in cost and time. The costs are between 15% and 30% lower compared to more conventional methods of moulding (Niane and Michalet 2011). The conventional DC process is being gradually replaced by LFC process.

A major specificity of LFC is the fact that the cooling rate of the process is relatively slow compared with DC process (LFC around 0.3-1.5 °C/s and DC around 30 °C/s) (Dezecot, Buffiere et al. 2015). The lower cooling rate will create a coarser microstructure when measured in term of DAS, as shown in Figure 1-8. Besides, the porosity and inclusions (intermetallics, oxides) are increased and clustered. All of these phenomena can significantly reduce overall mechanical properties and the component life (Tabibian, Charkaluk et al. 2010).

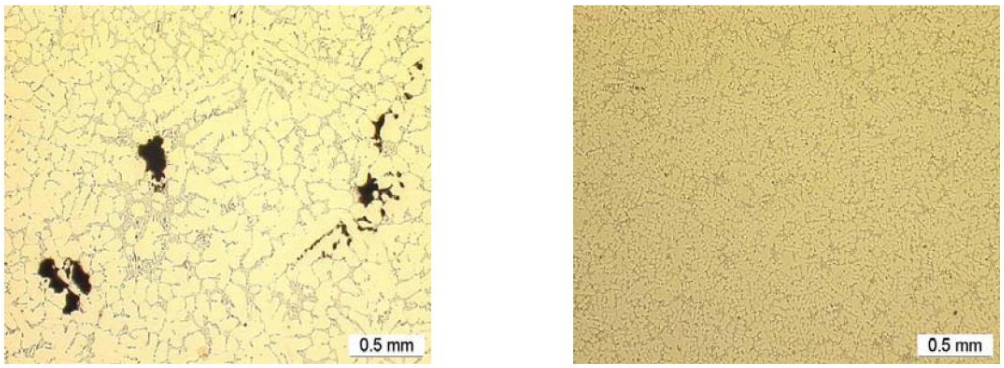

Figure 1-8: Microstructure of A356 issued with (a) LFC process, DAS: 85µm; (b) traditional DC process, DAS: 35µm (Tabibian, Charkaluk et al. 2010)

1.3 Modification of the eutectic silicon

As mentioned previously, Al-Si alloys are widely used in a variety of applications where good strength and light weight are required, or where corrosion resistance or castability are desired qualities. However, the commercial application of these alloys often depends on the successful modification of the eutectic silicon. An unmodified alloy contains an acicular eutectic silicon structure; such brittle, acicular Si particles act as internal stress raisers in the microstructure and provide easy paths for fracture. With modification, the eutectic structure becomes finer and the eutectic silicon particles become rounded, which contribute to higher values of ultimate tensile strength and of ductility (Liu 2004).

In general, a finer, more fibrous eutectic structure can be obtained by the addition of chemical modifiers. Calcium, sodium, strontium, and antimony are known to influence the degree of eutectic modification that can be achieved during solidification (Hegde and Prabhu 2008).

Apart from the use of modifiers, the eutectic silicon can also be 'modified' through solution heat treatment (Al Kahtani, Doty et al. 2014) or the use of high cooling rates (Khan and Elliott 1996). However, full modification is difficult to achieve by only increasing the cooling rate of the casting, and thus Al-Si alloys are generally modified by modifying agents (Pan, Cherng et al. 1994). These are usually added to the alloy melt in the form of master alloys in desired quantities, to achieve a well-modified eutectic structure.

1.3.1 Effect of strontium (Sr) modification

Several elements are known to cause eutectic silicon modification during the casting. It is well known that trace additions of strontium (a few hundred parts per million) to hypoeutectic aluminium–silicon alloys result in a transformation of the eutectic silicon morphology from a coarse plate-like structure to a well-refined fibrous structure (Lu and Hellawell 1987). Therefore, strontium has been widely used because of its greater stability in the melt when compared with sodium; furthermore it has a longer decay time than sodium. The addition of Sr neutralizes the effect of P and promotes the formation of a fibrous silicon structure by retarding the growth rate of silicon (Hegde and Prabhu 2008). Figure 1-9 (Dahle, Nogita et al. 2005) shows the microstructure of unmodified vs. Sr-modified hypoeutectic aluminium–silicon alloys.

Among the first to report on the modification effect of Sr were Hess and Blackmun (Hess and Blackmun 1975) who studied strontium as a modifying agent for hypoeutectic Al-Si alloys. From their work, they concluded that strontium is an effective modifying agent for hypoeutectic Al-Si alloys. As for the effect on mechanical properties, strontium modification caused significant increases in the mechanical properties of Al-Si alloy permanent mould castings. Pure strontium can readily react with air and water and be covered with SrO, SrO_2, $Sr(OH)_2$ and $(CaSr)NO_3$. This layer, which can only be removed mechanically, will completely prevent dissolution, thus, Al-Sr master alloys are always used to modify Al-Si alloys (LIU 2003).

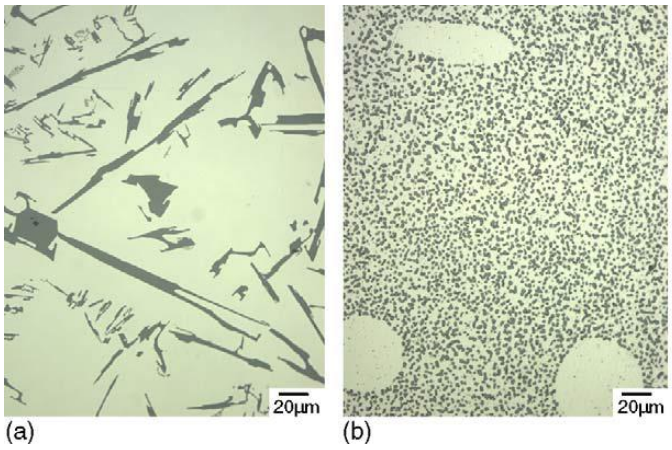

Figure 1-9: Comparison of the silicon morphology in (a) unmodified, (b) Sr-modified (300 ppm Sr), hypoeutectic aluminium–silicon alloys (Dahle, Nogita et al. 2005)

1.3.2 Effect of Cooling Rate on Modification

Cooling rate plays also an important role on the eutectic structure as well as on the silicon particles morphology. As shown in Figure 1-10, modification of silicon can also be achieved by rapid cooling or quench: a fibrous eutectic structure is obtained in the absence of chemical modifiers by rapid solidification (growth rate of 400–1000 µm/s) (Khan and Elliott 1996).

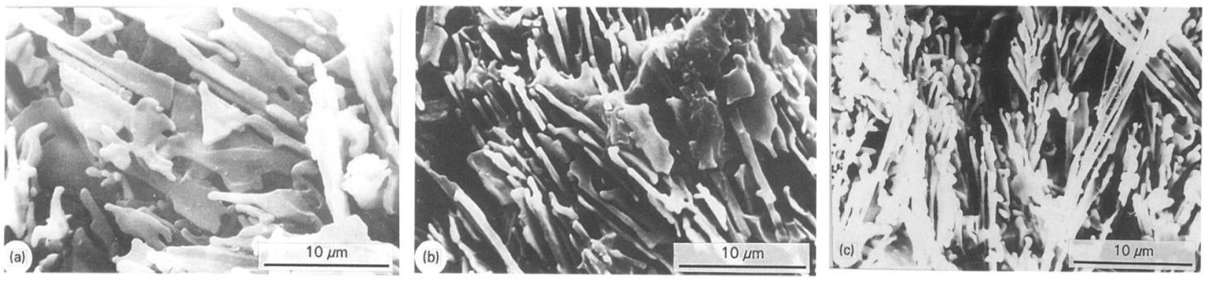

Figure 1-10: The change in the silicon phase morphology with growth velocity. (a) Completely flake structure grown at 308 µm/s, (b) mixed form of flake and fibrous structure grown at 505 µm/s, (c) completely fibrous structure grown at 807 µm/s (Khan and Elliott 1996)

(Dobrzański, Maniara et al. 2007) suggested that increasing the solidification rate can result in a significant reduction of the size of the Si particles from about 66µm^2 for the lowest solidification rate (0.15°C.s^{-1}) to about 25µm^2 for the highest solidification rate (0.7°C.s^{-1}).

1.3.3 Effect of solution heat treatment on modification

Solution heat treatment has been used together with chemical modification to change the morphology of silicon from a polyhedral to globular structure and produce the desired casting properties. Solution heat treatment is carried out by heating the alloy to a suitable temperature, which is usually close to the eutectic temperature. During this process, the change in the eutectic Si particle morphology takes

place in three stages: fragmentation, spheroidisation and coarsening. The solution treatment temperature, time and the original eutectic Si particles morphology in the as cast condition are the main factors that will control the effect of the solution heat treatment (Al Kahtani, Doty et al. 2014). Figure 1-11 (Paray and Gruzleski 1994) shows a schematic representation of the three stages of eutectic Si particles development, i.e. fragmentation, spheroidisation and coarsening, with the progress of solution treatment.

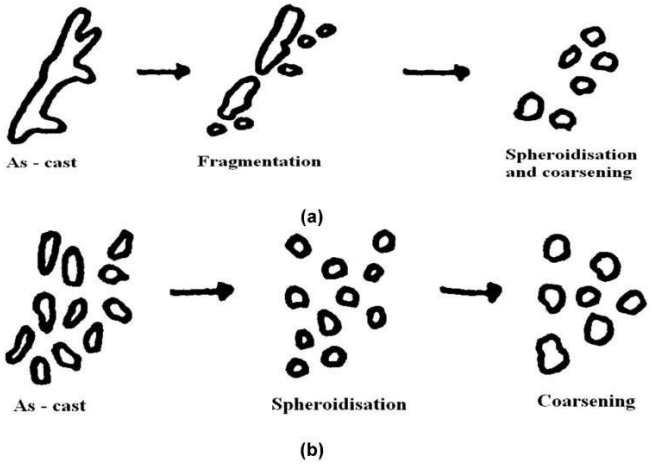

Figure 1-11: Schematic representations of three stages of eutectic Si particle development during solution heat treatment in the case of (a) unmodified and (b) modified Al-Si alloy (Paray and Gruzleski 1994)

Increasing the solution temperature can expedite the process of fragmentation, spheroidisation and coarsening, It should be noted that the temperature should not be high enough to cause any microstructural local melting of the alloy (Al Kahtani, Doty et al. 2014).

As can be seen from Figure 1-12 (Shivkumar, Ricci et al. 1990), for a given solution temperature, as the solution time increases, Si particles undergo necking and are broken down into smaller fragments. The fragmented particles are gradually spheroidised. Prolonged solution treatment leads to extensive coarsening of the particles.

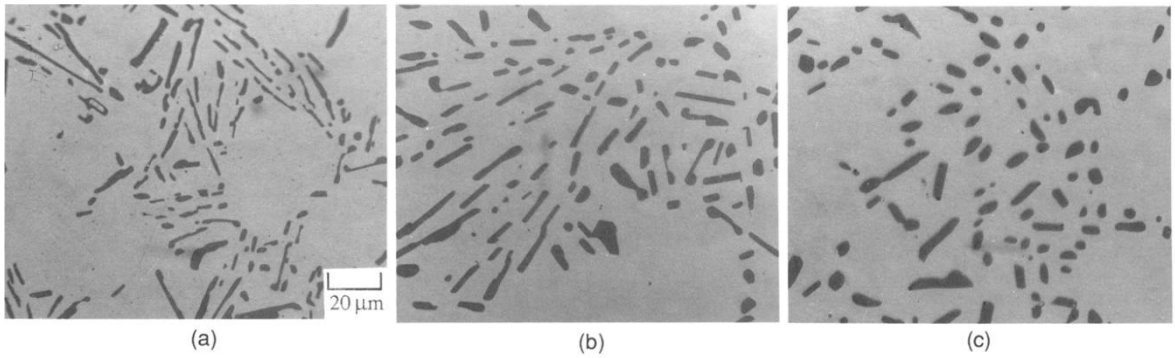

Figure 1-12: Typical microstructures of Unmodified A356.2 alloy as a function of solution time (solution temperature = 540°C) (500X). (a) 50 min (b) 400 min (c) 1600 min (Shivkumar, Ricci et al. 1990)

1.4 Intermetallics

Iron is a common impurity element in aluminium alloys. During solidification of Al–Si foundry alloys, iron, together with other alloying elements such as Cu, Mg, Zn, Mn, Ti, etc., partly goes into solid solution in the matrix and partly forms intermetallic compounds, including three different morphologies: thin platelet (β-Al_5FeSi iron intermetallic phase), Chinese script (α-$Al_{15}(Mn,Fe)_3Si_2$ iron intermetallic phase) and polyhedral crystals (sludge). Figure 1-13 shows examples of the three iron intermetallic types (Backerud, Chai et al. 1990).

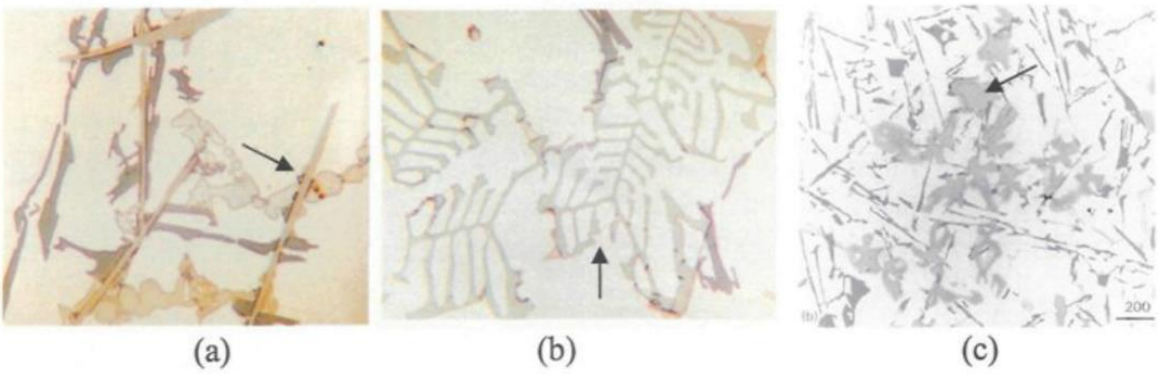

Figure 1-13: Optical micrographs showing (a) β-AI_5FeSi, (b) α-$Al_{15}(Fe,Mn)_3Si_2$, and (c) sludge iron intermetallics (arrowed) (Backerud, Chai et al. 1990)

Copper is commonly added to Al-Si alloys to improve strength and hardness in the as-cast and heat treated conditions because of the influence of Cu on the precipitation behaviour of these alloys during age-hardening treatment (Li, Brusethaug et al. 2006). Al_2Cu is usually formed as a secondary phase in the temperature interval of 520 °C to 500 °C at a critical concentration during the solidification of 319 alloys. This critical concentration depends on the efficiency of the nucleation sites. In the 319 alloys, two different morphologies of the Al_2Cu phase exist, one is the blocky Al_2Cu type, and the other is the finer eutectic (Al+ Al_2Cu) type.

1.4.1 The θ-Al_2Cu Phase

Based on the aluminium–silicon (Al–Si) system, copper (Cu) is one of the main alloying elements. Addition of copper to Al–Si alloys causes formation of Al_2Cu phases, which increase strength of casting alloys. It is well known that at ~548°C, the amount of Cu in solid solution in Al is about 5.7 wt. %. This value decreases with decreasing temperature, reaching 0.1– 0.2 wt. % at 250°C (Hansen, Anderko et al. 1958). In 319 alloys, copper forms an intermetallic phase with Al that precipitates during solidification either as block-like Al_2Cu or in eutectic form as (Al+Al_2Cu). Fig. 2-14 (Li, Samuel et al. 2003) exhibits the two distinct forms of the copper phase: (a) the eutectic-like (Al+Al_2Cu) phase, and (b) the blocky Al_2Cu phase.

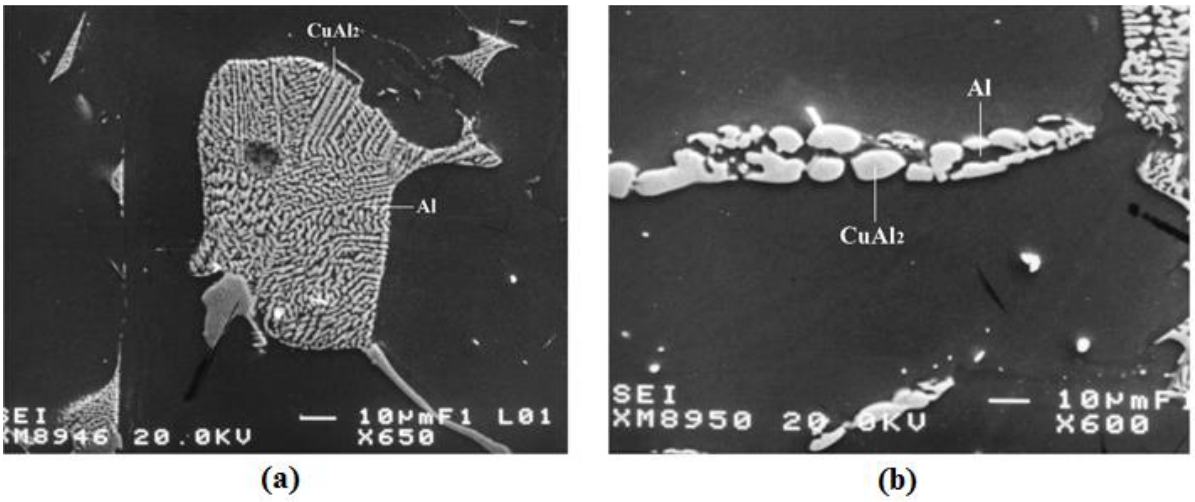

Figure 1-14: (a) Eutectic Al_2Cu and (b) blocky Al_2Cu (Li, Samuel et al. 2003)

In Al-Si-Cu alloys, solution heat treatment is routinely carried out to put the maximum amount of hardening solutes such as Cu and Mg into solid solution in the aluminium matrix (Han, Samuel et al. 2014). (Samuel 1998) reported that the tensile strength and elongation properties of Al-Si-Cu alloys show a linear increase with the amount of dissolved copper increase in the matrix. However, control of the solution-treatment temperature is also very critical because, if the melting point is exceeded, there is localized melting at the grain boundaries and micro pores are grown so that the mechanical properties will also be reduced. Most of the research works (Samuel 1998) recommended that heat treatments of Al-Si-Cu alloys are restricted to solution temperature below the final solidification point (equilibrium heat treatment), which was listed in Table 1-1, in order to avoid the melting of copper-containing phases. The Al_2Cu phase is expected to melt at 510°C. Under equilibrium heat treatment conditions, it is not possible to take the full amount of Al_2Cu phase into solid solution, and even at long solution treatment times, the majority of the copper-rich phases remain undissolved (Narayanan, Samuel et al. 1995).

Thus, non-equilibrium heat treatment was also suggested by Toda and Nishimura for Al-Si-Cu alloy (Toda, Nishimura et al. 2010). This treatment involves solution treatment at temperatures slightly higher than the final solidification temperature of (Al-Al_2Cu) eutectic. This process is expected to enhance dissolution of Al_2Cu in the aluminium matrix. Figure 1-15 (Toda, Nishimura et al. 2010) shows the solution treatment that was performed at 807 K with various time periods for an Al-Si-Cu alloy (arrows indicate red regions, which indicate Cu concentrations higher than 30 wt. %). Toda et al. (Toda, Nishimura et al. 2010) studied both the positive and negative effects exerted on the mechanical properties of an aluminium alloy by a high-temperature solution treatment and concluded that the positive effects can outweigh the negative effects even above the eutectic temperature.

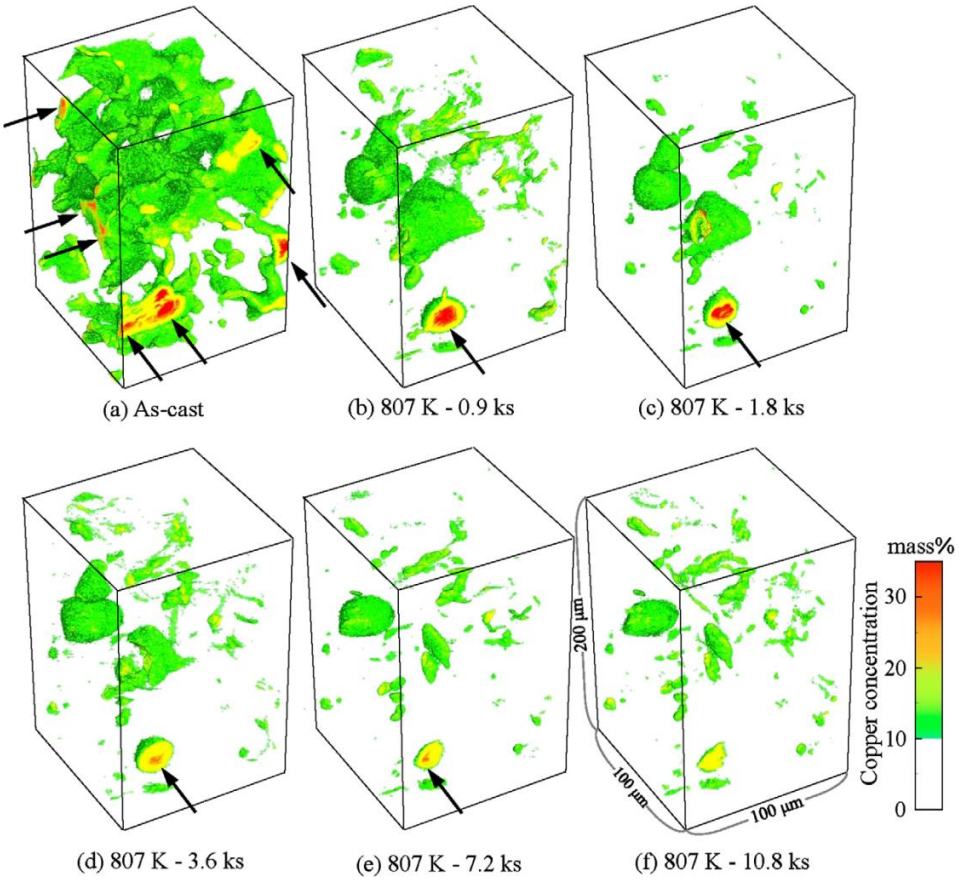

Figure 1-15: 3-D perspective views of copper-bearing phase in the material shown as the Cu concentration contour (Toda, Nishimura et al. 2010)

In addition, (Li, Samuel et al. 2003) found that Sr leads to segregation of the Al_2Cu phase away from the Al-Si eutectic regions, which slows down its dissolution during solution heat treatment. On the other hand, (Djurdjevic, Stockwell et al. 1999) reported that increasing Sr level in the A319 alloy also results in a larger area fraction of the blocky Al_2Cu structure and in a lower area fraction of the eutectic Al-Al_2Cu structure.

1.4.2 The β-Al_5FeSi Iron Intermetallics

The β-Al_5FeSi phase is considered the most commonly observed intermetallic in the Al-Si alloys, this compound tends to form thin platelets appearing as needles in cross section, which are very hard and brittle and have relatively low bond strength with the matrix (Narayanan, Samuel et al. 1994). Figure 1-16 shows the shape of the β-Al_5FeSi phase (Dinnis, Taylor et al. 2005).

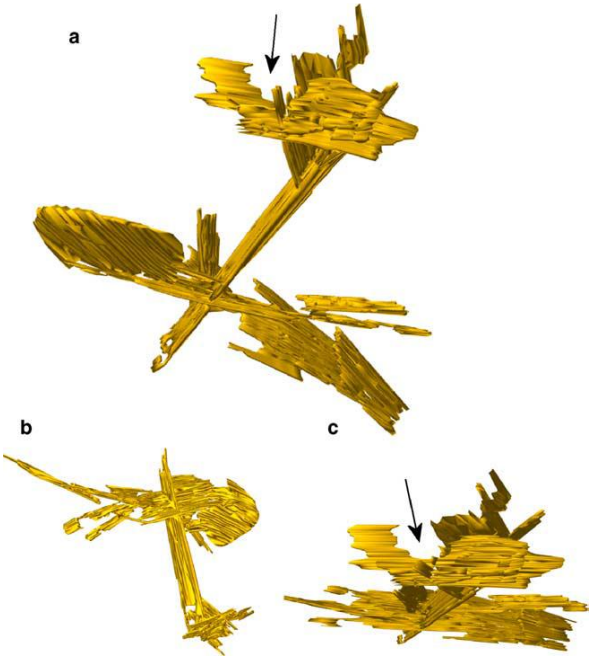

Figure 1-16: 3D networks of β-Al_5FeSi platelets obtained from reconstructed serial sections and shown in three orientations (a, b and c) (Dinnis, Taylor et al. 2005)

The size and amount of β-Al_5FeSi phase in Al-Si-Cu (Fe) alloys are strongly influenced by the Fe content, Mn content and cooling rate. The formation of β-Al_5FeSi phase can be suppressed in two ways: addition of sufficient manganese and high cooling rates (Dinnis, Taylor et al. 2005). A low cooling rate favours the precipitation of the β-phase. In the manganese-containing Al-Si-Cu alloys, the iron compound crystallizes in α phase at low cooling rates and in both α and β phases at high cooling rates.

In addition, some research works (Narayanan, Samuel et al. 1995) (Bacaicoa, Dwivedi et al. 2016) suggested to use a higher solution temperature (Non-equilibrium heat treatment) for the heat treatment of Al-Si-Cu (Fe) alloys to dissolve the β-iron phase. (Bacaicoa, Dwivedi et al. 2016) reported that solution heat treatment at 520°C-525°C for 1 hour of Al-Si Cu alloy can minimize the harmful effect of the β-iron phase. However, under normal heat treatment conditions (solution temperatures below the final solidification point) for copper containing A1-Si alloys, the iron-intermetallics do not undergo any change.

(Narayanan, Samuel et al. 1995) studied the process of dissolution of iron intermetallics in Al-Si alloy through non-equilibrium heat treatment. They proposed an explanation for the mechanism of β-Al_5FeSi phase dissolution during the heat treatment (Figure 1-17) and concluded that:

- with increasing solution temperature, the β-iron phase platelets dissolve slowly through concurrent fragmentation along plate widths and dissolution at the platelet tips;

- Solution temperature plays a much more important role in the dissolution of iron intermetallics than does solution time;

- The thinner and shorter the β-iron phase platelets, the faster the fragmentation and dissolution process.

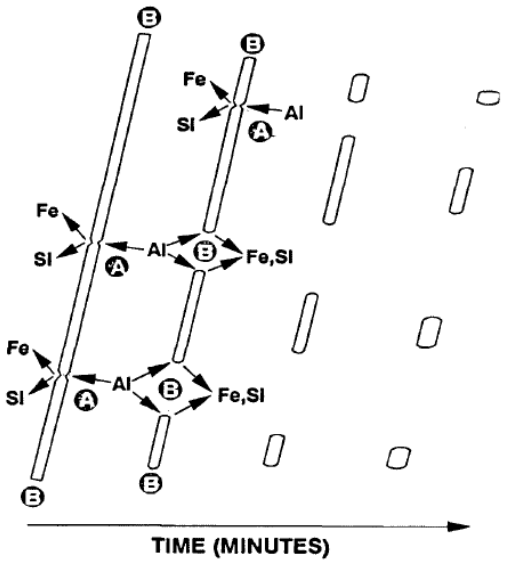

Figure 1-17: Schematic illustration of the mechanism of β-Al_5FeSi phase fragmentation and dissolution (Narayanan, Samuel et al. 1995)

However, the positive effects of a Non-equilibrium heat treatment should be balanced with its negative effects. For Al-Si alloys, the positive effects would consist in homogenization and suppression of the brittle fracture of Si and intermetallic compound particles. On the other hand, the negative effects are incipient melting and the resultant microstructural defects, such as micro pores. A successful solution treatment depends on the as-cast microstructure (volume fraction, distribution, morphology and composition of phases, degree of modification of Si particles, Al_2Cu phase, β-Al_5FeSi phase etc.), in combination with the solution treatment parameters (temperature, time) chosen.

1.4.3 The α-$Al_{15}(Fe,Mn)_3Si_2$ Iron Intermetallics

The formation of coarse β-Al_5FeSi phase can be suppressed by addition of manganese during the solidification that leads to the formation of a more compact and less harmful α-$Al_{15}(Fe,Mn)_3Si_2$ (Lu and Dahle 2005). The α-phase shows an irregular, curved crystal growth, conforming to the complicated shape of the interdendritic spaces during solidification. Figure 2-10 shows the 3D shape of the α-$Al_{15}(Fe,Mn)_3Si_2$ (Dinnis, Taylor et al. 2005).

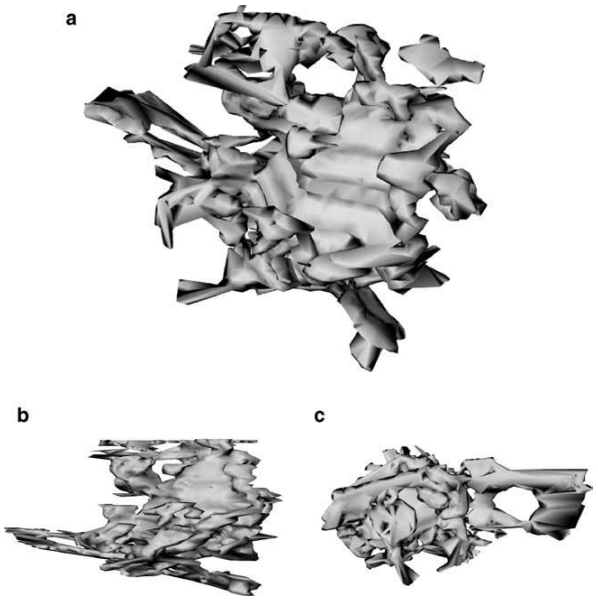

Figure 1-18: Three-dimensional reconstruction of an α-$Al_{15}(Fe,Mn)_3Si_2$ particle, shown in three orientations (a, b and c) (Dinnis, Taylor et al. 2005)

However, addition of Mn increases the total amount of iron-rich intermetallic phases, despite its benefit in modifying the Fe-rich intermetallics. In addition, cooling rate also affect the degree of transformation (Narayanan, Samuel et al. 1994). (Seifeddine, Johansson et al. 2008) showed that Mn additions are not able to totally nullify the formation of β-Al_5FeSi-needles onto α-$Al_{15}(Fe,Mn)_3Si_2$-Chinese scripts at high cooling rates for a 2:1 Mn:Fe ratio in an Al-9w.%Si alloy.

1.5 Porosity

Porosity in aluminium results from the precipitation of hydrogen from liquid solution or by shrinkage during solidification, and more usually by a combination of these effects (Kaufman and Rooy 2004). The presence of porosity has a detrimental effect for most casting product, in terms of the surface finish, corrosion resistance and mechanical properties. Compared to other defects in cast aluminium products, the porosity has been held responsible for the majority of failures (Mayer, Papakyriacou et al. 2003).

According to cause, porosity in aluminium alloys is classified into two kinds:

1) Gas porosity
2) Shrinkage porosity

The gas porosity, in contrast to shrinkage porosity, is generally round, isolated and well distributed. It is formed during solidification, because of rejection of hydrogen from the melt. On the other hand shrinkage porosity is interconnected or clustered and of an irregular shape, corresponding to the shape of the interdendritic regions and it is mainly caused by the inability of the liquid metal to compensate

the solidification contraction. Figure 1-19 (Roy, Samuel et al. 1996) shows an example of a pore composed of a shrinkage pore and a gas pore.

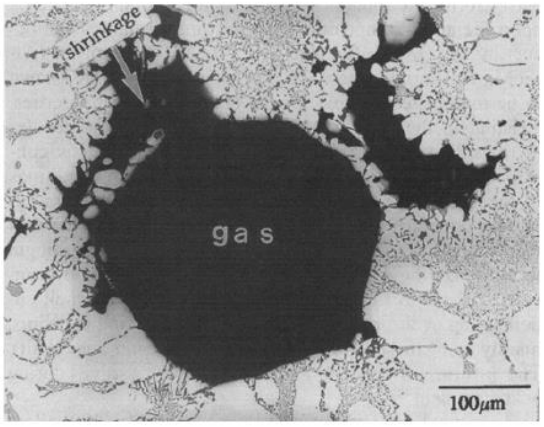

Figure 1-19: A shrinkage pore and a gas pore merged together to form a single pore in an AI-9 wt. % Si-3 wt. % Cu alloy (Roy, Samuel et al. 1996)

There are many factors that can affect the amount and size of porosity in aluminium alloys, such as the hydrogen concentration in the melt, cooling rate (Kaufman and Rooy 2004), Sr modification (Dinnis, Dahle et al. 2004), as well as other minor element additions made to the melt (Taylor, Schaffer et al. 1999).

- **Effect of degassing**

Hydrogen is the only gas capable of dissolving to a significant extent in molten aluminium. The dramatic decrease in its solubility at the solidification point of aluminium results in outgassing, and leads to the formation of hydrogen porosity. Thus, several methods are currently in use to degas aluminium. These methods include rotary degassing using nitrogen or argon or mixture of either of these with chlorine as a purge gas, tablet degassing using hexachloroethane (Samuel and Samuel 1992), vacuum degassing (Popescu, Gheorghe et al. 1996), and ultrasonic degassing (Xu, Han et al. 2008).

Figure 1-20 (Puga, Barbosa et al.) compares the hydrogen content with different degassing time and techniques for an AlSi9Cu3 alloy. Compared to the nitrogen or argon degassing, ultrasonic degassing seems to decrease hydrogen content quickly.

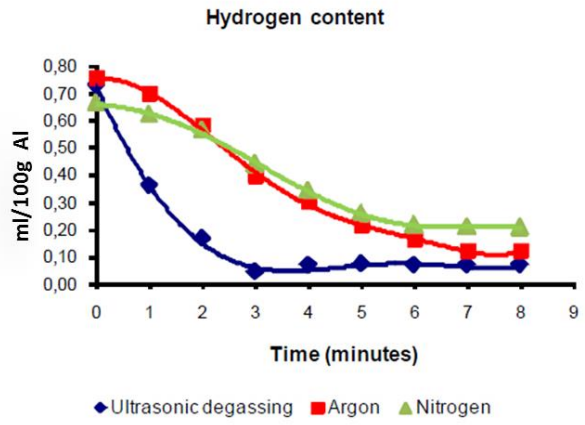

Figure 1-20: Evolution of the hydrogen content with different degassing time and techniques for an AlSi9Cu3 alloy (Puga, Barbosa et al.)

- **Effect of Strontium addition**

As mentioned before, Sr is added to Al-Si alloys in order to modify the eutectic Si from acicular flakes to a fibrous like form, thereby improving mechanical properties, however, some studies (Dinnis, Dahle et al. 2004) (Campbell and Tiryakioğlu 2010) reported that the addition of Sr changes the amount of porosity.

(Argo and Gruzleski 1988) reported that large pores may be observed in modified alloys because of problems associated with interdendritic feeding. The reduction of eutectic temperature increases the length of the mushy zone in modified alloys, and therefore large pockets of interdendritic liquid may become isolated. In addition, pore nucleation may also be facilitated by the presence of oxide films. Pores observed in Sr-modified alloys are frequently associated with strontium oxides (films or particles) in (Liu, Samuel et al. 2003). These particles/films are formed during melting, due to the high oxygen affinity of strontium, and are extremely difficult to remove during degassing.

- **Effect of Fe and Mn**

Iron content can also affect the porosity formation. (Moustafa 2009) claims that iron-intermetallics help nucleating pores and that the porosity level increases with the Fe content in the Al-Si alloys. However, according to (Taylor 2004), there is a critical Fe content for a minimum porosity formation and different solidification paths resulting from different Fe levels lead to variations in microstructural permeability, i.e. interdendritic feedability, and hence in porosity formation. At Fe levels above a critical point, the β-phase is already well developed when ternary eutectic solidification commences, whereas at lower Fe levels, the β-phase forms as a component of the ternary eutectic only after the binary Al-Si eutectic is formed. In both cases, large binary β-phase blocks the interdendritic regions, leading to a high porosity level in castings. However, at the critical Fe content, the ternary eutectic consists of small ternary β-platelets that nucleate many fine Al–Si eutectic, this results in improved feeding through the most open and permeable dendritic structure, thereby minimising porosity. In

contrast, the study of (Puncreobutr, Lee et al. 2012) reported that larger pores were observed to nucleate before the intermetallics during in-situ solidification of an A319 alloy at 0.36°C/s. Moreover, the addition of Mn was observed to reduce the amount of porosity in (Dinnis, Taylor et al. 2004); the addition of 0.5%Mn to a 1%Fe-containing Al-9%Si alloy can reduce porosity levels to those obtained in the same alloy with 0.6%Fe. However, (Lu and Dahle 2005) reported that addition of Mn caused no discernible change in casting porosity level.

It should be noted that most of these results about the characteristics of pores are based on 2D examination (Puncreobutr, Lee et al. 2014). Thus, maybe it would be more interesting to study the influence of Fe/Mn content on the porosity formation through in-situ solidification experiment, and then reveal the characteristics of pores in 3D.

1.6 Mechanical properties and damage mechanisms of Al-Si alloy

1.6.1 Mechanical properties

The mechanical properties, such as hardness, ultimate tensile strength (UTS), yield strength (YS) and elongation (%El) values in the Al-Si alloy, are strongly influenced by the microstructure involved, viz. SDAS, amount, size of eutectic Si, intermetallic compounds, and porosity. Their relationships are presented separately in the following sections.

- **Secondary dendrite arm spacing (SDAS)**

SDAS has a great effect on the mechanical properties (Li, Samuel et al. 2004, Seifeddine and Svensson 2013). In general, Al-Si alloys having a low SDAS value, induced by high solidification rate, show better mechanical properties, the tensile strength, ductility and elongation increase as DAS refines. An example of this is shown in Figure 1-21, where the variation of tensile properties in six T5 heat-treated Al-Si-Cu alloys having different Fe and Sr content has been plotted as a function of DAS (Li, Samuel et al. 2004).

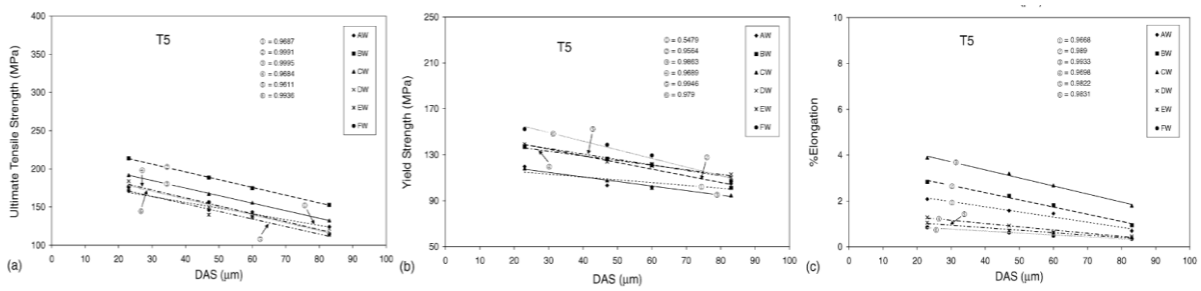

Figure 1-21: Tensile properties of six Al-Si-Cu alloys (T5 condition) as a function of DAS: (a) UTS, (b) YS, (c) %El (Li, Samuel et al. 2004)

As mentioned in §1.2.2, the hardness of Al-Si alloys decreases with an increase in the size of SDAS. Besides, the cooling rate also can affect the size and the distribution of porosity and intermetallic

particles in the casting. As SDAS becomes smaller at a higher cooling rate, porosity and second phase constituents (eutectic Si and intermetallic compounds) are dispersed more finely and evenly. This refinement of the microstructure leads to substantial improvement in mechanical properties (Shabestari and Moemeni 2004).

- **Eutectic silicon**

As described in §1.3, eutectic modification (such as Sr modification, heat treatment and higher cooling rate) can affect the morphology of eutectic silicon in Al-Si alloys, and these microstructural changes will directly influence the mechanical properties.

Mechanical properties of modified and non-modified eutectic Al-Si alloys were investigated by (Hafiz and Kobayashi 1994).Their results showed that the impact toughness is highly sensitive to the Si morphology in the eutectic matrix, where a fibrous Si morphology enhances toughness. Tensile properties, in particular elongation, are greatly improved as a result of the Sr modification. The higher toughness and ductility of the modified alloy were attributed to the fine fibrous morphology of the Si particles achieved by modification.

According to (Ibrahim, Elgallad et al. 2016), the presence of long, acicular Si particles in the Al-Si alloys accelerates crack propagation, leading to poor ductility. However, over-modification leads to the precipitation of Sr in the form of primary Al4SrSi2 particles which have a negative influence on the alloy tensile properties.

- **Iron-intermetallic**

In addition to eutectic silicon, iron-intermetallic phases in Al-Si alloys also affect mechanical properties, the mechanical properties are dependent on the amount, type and morphology of the formed intermetallic compounds (Seifeddine 2007). (Sanna, Fabrizi et al. 2013) reported that brittle plate-like Fe-rich compound (β-Al_5FeSi) has an impact on the ultimate tensile strength and a deleterious effect especially on the elongation to fracture. By contrast, the α-$Al_{15}(Fe,Mn)_3Si_2$ phase appears as Chinese script, which is thought to be less detrimental to the alloy's mechanical properties because of its compact and globular morphology (Liu, Mohamed et al. 2009).

In addition, the formation of Fe-rich intermetallic is in relation with the iron content and cooling rate. Figure 1-22 (Seifeddine and Svensson 2013) illustrates the relationship between the iron content and tensile properties (elongation to fracture) for an Al-Si-Cu alloy under different cooling conditions. (Seifeddine and Svensson 2013) concluded that the ultimate tensile strength appears to be slightly decreased whereas yield strength appears to be increased by the increase in iron content. In contrast, the increased iron content seems to severely damage the ductility of the alloys, and the lowering of ductility might be due to the presence of brittle and complex iron-rich compounds. Besides, (Tash, Samuel et al. 2007) and (Moustafa 2009) reported that the increase of Fe content increases the

hardness of Al-Si alloys as the Fe- intermetallic surface fractions increase. This can be attributed to the higher hardness of intermetallic compounds than that of Al matrix.

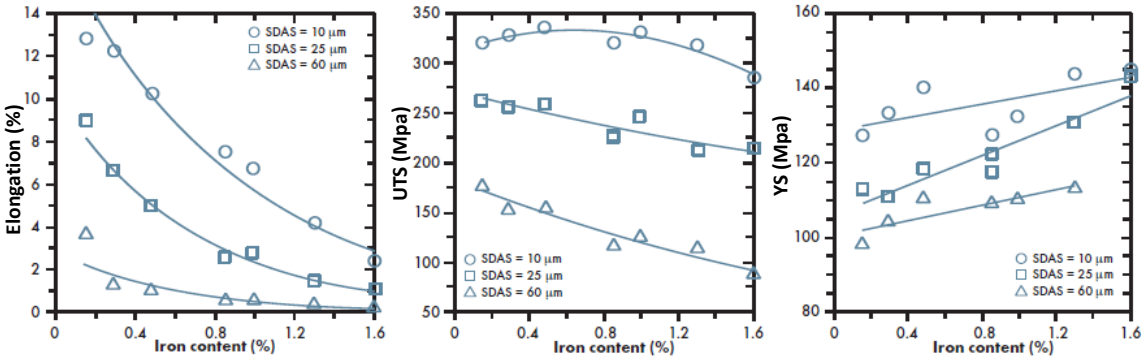

Figure 1-22: Tensile properties (UTS, YS and EI %) of an Al-Si alloy as function of iron content under different cooling conditions (Seifeddine and Svensson 2013)

- **Al_2Cu phase**

The effect of Al_2Cu on the mechanical properties mainly depends on the precipitation behaviour of the alloys during the age-hardening treatment.

A study by (Samuel 1998) shows the relationship between mechanical properties of an Al-Si-Cu alloy and the dissolved copper concentration in the aluminium matrix (Figure 1-23). It is evident that the ultimate tensile strength (UTS), yield strength (YS) and elongation (EI %) are increased by increasing the dissolved Cu content.

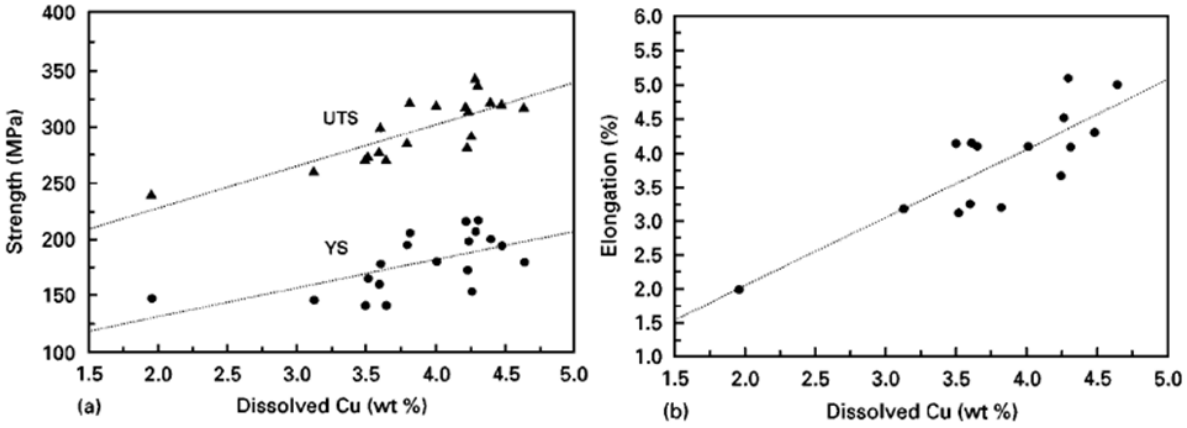

Figure 1-23: (a) Variation in YS and UTS, (b) variation in El%, as a function of copper concentration in the aluminium matrix (Samuel 1998)

However, it should be noted that complete dissolution of the Al_2Cu phase is not usually possible. The solution temperature and time must be chosen carefully to avoid the coarsening of the microstructural constituents and the possible formation of secondary porosity, which can deleteriously affect the mechanical properties (Prasad and Dan 1991).

- **Porosity**

The effect of various porosity parameters on the mechanical properties has been reported in some studies (Mugica, Tovio et al. 2004, Ma, Samuel et al. 2008). The influence of volumetric porosity on the tensile properties of Al-Si alloy obtained by (Mugica, Tovio et al. 2004) is shown in Figure 1-24. As can be seen, an increase in the volume of the porosity is deleterious to alloy ductility and UTS. The effect of porosity on yield strength may be attributed basically to the loss of effective stress-bearing area resulting from the presence of pores.

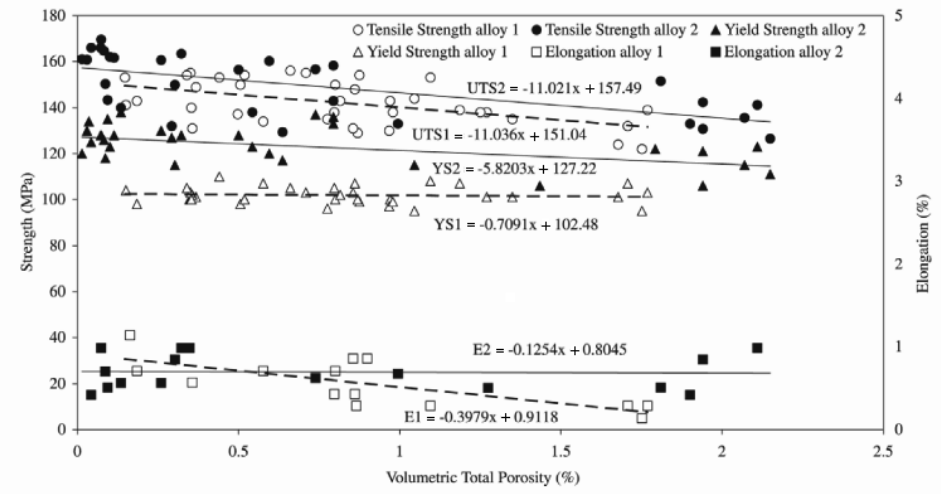

Figure 1-24: Tensile strength, yield strength and elongation rate as a function of volumetric porosity for two 380 aluminium alloys (Mugica, Tovio et al. 2004)

According to (Ma, Samuel et al. 2008), the pore area and pore length parameters can provide a better correlation with the tensile properties. They indicated that porosity is always harmful to alloy ductility and tensile strength. As shown in Figure 1-25, with any increase in maximum pore area, an overall decrease in all the properties is observed.

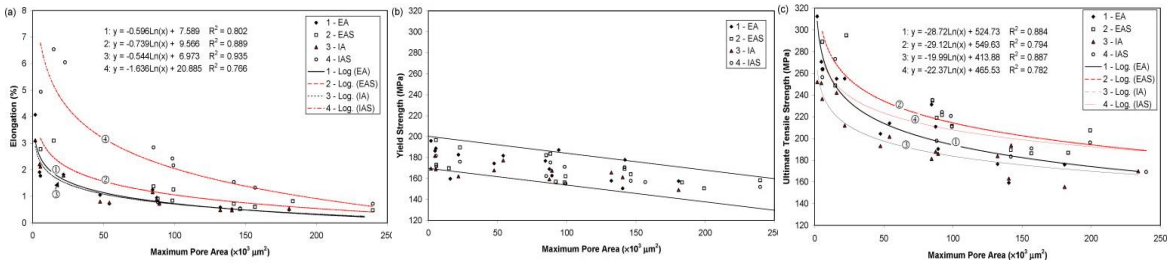

Figure 1-25: The correlations between the tensile properties and maximum pore area for samples obtained from 319.2 alloys (Ma, Samuel et al. 2008)

1.6.2 Damage mechanisms of Al-Si alloy

In Al-Si alloys, cracks often occur at various microstructural inhomogeneities, such as inclusions and pores. Their influences are discussed in the following.

1.6.2.1 Influence of porosity

It is well known that pores act as preferential crack nucleation sites and therefore are the main cause of the poor fatigue properties exhibited by Al-Si components (Serrano Munoz 2014) (Boromei, Ceschini et al. 2010). Especially for large surface pores, they play a decisive role by providing preferential crack initiation sites by creating a high stress concentration in the material adjacent to the pores (Wang, Limodin et al. 2016). In addition, they accelerate fatigue crack propagation as they increase the stress level. According to (Wang, Apelian et al. 2001), castings with defects, i.e. pores, show at least an order of magnitude lower fatigue life compared to defect-free materials. Pores can be considered to affect failure using four parameters:

- **Pore size**

Some studies (Zhang, Chen et al. 2000, Buffière, Savelli et al. 2001, Mu, Nadot et al. 2014) found that there exists a critical size below which pores no longer influence the fatigue life and crack nucleation is transferred to other microstructural features (eutectic Si or intermetallics particles). However the critical size values reported in the literature vary depending on the study and tested material.

In cast aluminium alloy AS7G06-T6, (Mu, Nadot et al. 2014) found that a defect decreases the fatigue strength only when its size exceeds a critical size of 400 µm and 200 µm for R = -1 and 0.1, respectively. This value has the same order of magnitude as the grain size (259-573 µm), but is really bigger than the SDAS (38 µm). (Zhang, Chen et al. 2000) identified that fatigue cracks initiate from surface and subsurface pores when pore size is greater than a critical value of $L_{max} \approx 80$ µm (maximum length of pores).

(Buffière, Savelli et al. 2001) found that pores with an equivalent diameter lower than 50µm did not initiate any crack, when pores larger than the critical size exist.

- **Pore position**

As described in (Serrano Munoz 2014)'s study, pores can be classified as: internal pore, sub-surface pore or surface pore depending on their distance with respect to the free surface. It is well known that tensile/fatigue behaviour of cast components is influenced when casting defects (such as pores) are present at the free surface or subsurface. They are more likely to act as a crack initiation site and to decrease the fatigue life as they create regions of high stress concentrations. (Serrano-Munoz, Buffiere et al. 2016) reported that artificial defects, which are placed at the specimen free surface, can produce a reduction of the fatigue life; however, no reduction is observed when test is performed in vacuum. In addition, (Roy, Nadot et al. 2012) suggest that surface shrinkage pore is more detrimental to the fatigue life than subsurface pore of the same size in A356-T6 alloy.

- **Pore quantity**

A large number of pores reduces the effective load bearing cross-sectional area of material under monotonic tensile loading (Sinha and Farhat 2015), and acts as a stress concentration site for strain

localization and damage, then decreasing both strength and ductility. (Buffière, Savelli et al. 2001) found that the number of pores per unit volume in Al-Si alloy is one of the major factors which control the fatigue life and its scatter, especially at high stress level.

- **Pore morphology**

The morphology of porosity could also influence the tensile/fatigue behaviour as a sharp shape is more prone to stress concentration. Shrinkage cavities appear more critical than gas pores due to their more complex shapes (Buffière, Savelli et al. 2001). (Wicke, Luetje et al. 2016) studied the role of pore morphology on tensile behaviour based on the stress concentration factor computed by FE analysis of a 3D volumetric pore model. As shown in Figure 1-26, the peak stress concentration is located at a hole in the defect, which can thus be identified as hot spot. (Fan, McDowell et al. 2003) suggest that the local curvature of the pore has an influence on fatigue crack initiation.

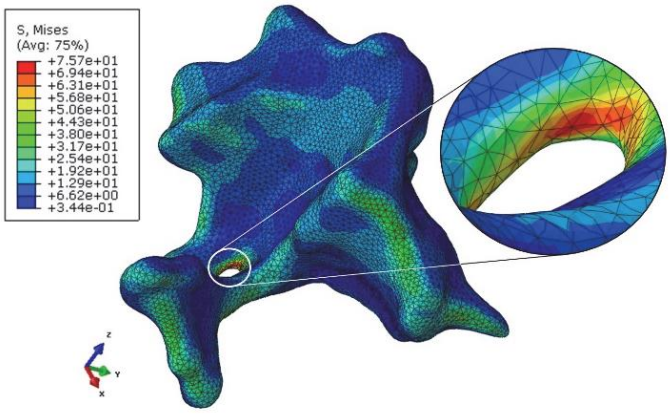

Figure 1-26: Stress distribution on surface of a pore (z-axis parallel to loading direction) (Wicke, Luetje et al. 2016)

1.6.2.2 Influence of hard inclusions

Besides the porosity defects, the hard inclusions of alloys, such as eutectic Si, iron-intermetallics and Al_2Cu phase, also play an important role on the tensile/fatigue behaviour.

- **Eutectic Si particles**

The fatigue characteristics of Al–Si alloys are strongly influenced by the eutectic Si particles. Silicon particles within eutectic regions can act as crack initiation sites when there is high local stress concentration; this stress concentration may be induced by large pores or by specimen geometry such as the edge of the specimen (Wang 2015). (Zeng, Sakamoto et al. 2014) also reported that the initiation of fatigue crack in Al-Si alloys is generally a result of a crack in the large eutectic Si particles, which is mostly attributed to the high local stress-concentration around the particles.

(Lee, Major et al. 1995) explain their observation of Si particle-induced fatigue crack formation through the higher silicon content of 12% in the studied alloy as compared to 7% Si for A356-T6. They reported that during cyclic plastic deformation, formation of cracks occurred by particle–matrix

interface separation and/or by particle cracking. The interfacial strength between particle and matrix is a primary factor controlling crack formation, silicon particles are much stiffer than the surrounding aluminium rich matrix and deform elastically (Seifeddine, Johansson et al. 2008).

(Samuel and Samuel 1995) found that microcracks are initiated in the Si phase and then grow and coalesce until complete fracture occurs for A356 alloy, and the initiation of these microcracks in the Si phase is attributed to the fact that the cohesive force between the Si particles and the aluminium matrix is stronger than the bonding force among the Si atoms within the Si phase.

(Lee, Major et al. 1995) also reported that the size, volume fraction, shape, strength, location, and orientation of particles all may contribute to the void/microcrack initiation process, they found that the presence of large and irregularly shaped Si particles with large aspect ratios facilitates and accelerates crack formation due to the additional stress concentration effect of particles.

In addition, failure mode of eutectic Si was studied in some researches (Gall, Yang et al. 1999) (Lee, Major et al. 1995): silicon particles in cast Al-Si alloys have a tendency to debond or fracture, depending on the crack tip driving force (Gall, Yang et al. 1999) and the eutectic Si characteristic (Lee, Major et al. 1995).

Debonding of Si particles appears to dominate the fatigue crack growth process at a maximum stress intensity factor, K_{max}, of less than 6 MPa$\sqrt{m}$, but fracture of Si particles dominates at K_{max} > 6 MPa$\sqrt{m}$ (Gall, Yang et al. 1999). (Plumtree and Schafer 2013) observed that fatigue cracks initiate at Si particles by debonding at the interface with the aluminium matrix or by cracking of the Si particles, the former is associated with low cyclic strain ranges and long lives.

Besides, fracture of Si particles is reported to be the dominant mechanism in an unmodified Al-Si-Mg alloy with large (~3-9 μm) Si particles (Lee, Major et al. 1995) while decohesion of Si particles from the Al-matrix always occurs in the smaller Si particles. Similarly in (Gall, Yang et al. 1999), debonding was only observed at small rounded silicon particles while the fatigue crack propagated at high crack growth rates.

Once cracks initiated, they are prone to propagate through the 3D network of cracked hard inclusions (such as eutectic Si, iron-intermetallics and Al_2Cu phases) (Dezecot, Buffiere et al. 2016). Plumtree and Schafer (Plumtree and Schafer 2013) reported that fatigue cracks initiated at the silicon particles in the eutectic region, and then propagated through the eutectic regions that include eutectic Si particles rather than through the dendrites.

- **Iron-intermetallics**

(Yi, Gao et al. 2004) found that in the absence of other defects such as porosity, the large plate-like β-Al_5FeSi in high Fe-content castings of A356 alloy promote crack initiation by raising the stress-strain concentration in the eutectic region.

Compared to the α-$Al_{15}(Fe,Mn)_3Si_2$, the β-Al_5FeSi phase is the more detrimental Fe-rich compound especially for Very-High-Cycle-Fatigue. This is due to its long needle-like shape that generates high local stress concentrations, from which cracks initiate and cause premature failure (Bacaicoa, Dwivedi et al. 2016). Figure 1-27 shows a SEM fractograph taken from the fracture surface of an as-cast Al-Si-Cu tensile specimen; failure occurs by cleavage of a massive brittle β-Al_5FeSi platelet (Bacaicoa, Dwivedi et al. 2016).

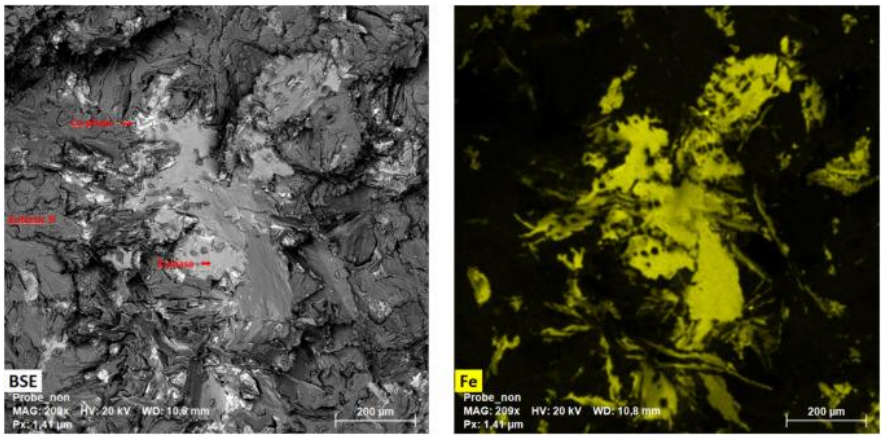

Figure 1-27: SEM fractograph of an as-cast Al-Si-Cu alloy fractured tensile specimen (Bacaicoa, Dwivedi et al. 2016)

(Ma, Samuel et al. 2014) reported that cracks initiate through the fragmentation of Si particles, β-iron intermetallics, and Al_2Cu particles in unmodified 319 alloys with low iron levels and high cooling rates (0.4% Fe, 23µm DAS) while they propagate through the linking of the fragmented particles. At high iron levels and low cooling rates (0.8% Fe, 83µm DAS), in the unmodified condition, crack initiation and propagation occur through cleavage of β-Al_5FeSi platelets rather than by decohesion of the β-platelets from the matrix.

After the cracks initiated at hard inclusions, they mainly propagate through the coalescence of fractured Si particles in the unmodified condition, except where β-iron intermetallics are present, in which case the latter takes priority in fracture propagation.

- **Al_2Cu phase**

Compared to the hardness of Al matrix (i.e. 3.1 GPa), the Al_2Cu phase (i.e. 6.54 GPa) is harder (Tabibian, Charkaluk et al. 2015). As mentioned before, the interfacial strength between particle and matrix can affect crack formation. (Ma, Samuel et al. 2014) reported that cracks also initiate and propagate through the fracture of Al_2Cu, as well as through Si particles and iron-intermetallics.

A crack was observed to initiate in the vicinity of the shrinkage pore on a neighbouring large Al_2Cu phase after a few cycles during high temperature fatigue test in (Dezecot, Buffiere et al. 2016) (see Figure 1-28). In (Dahdah, Limodin et al. 2016), micro-cracks are observed in the Al_2Cu phase due to the stress concentration during the fatigue test of LFC A319 alloy. According to (Ma, Samuel et al.

2014), cracks also propagate through the fracture of undissolved Al_2Cu, as well as through fragmented Si particles.

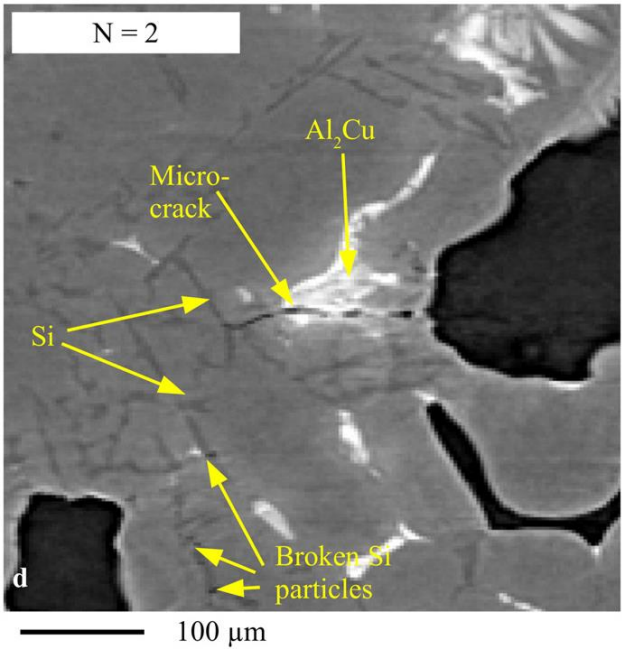

Figure 1-28: Reconstructed 2D X-ray tomography slice showing the initiation area under the surface at the corner of a pore after 2 cycles (Dezecot, Buffiere et al. 2016)

Briefly, in addition to porosity defects, the hard inclusions, such as Si-particles, iron-intermetallic and Al_2Cu phases, also emerge as important determinants of fatigue/tensile performance for Al-Si alloy. It is therefore important to investigate the interaction between these microstructural features and the damage evolution in the castings.

1.7 Summary of literature review

Microstructure in cast Al-Si alloys will change due to different chemical compositions and casting conditions. These relationships are summarized in Table 1-3. In addition, the properties of the alloy are greatly dependent on the microstructure (such as SDAS, eutectic Si, Al_2Cu phase and iron-intermetallics) in the alloy (see Table 1-4).

In order to improve the mechanical properties of Al-Si alloy, the morphology of the eutectic silicon change from acicular to fibrous through Sr additions, and the modification degree depends on the Sr content and cooling rate. However, some researchers found that the addition of Sr affects the amount of porosity, which is detrimental to the fatigue behaviour of Al–Si alloys. Therefore, it is better to expand understanding of the effect Sr addition on the microstructures and mechanical properties of Al-Si cast alloys.

Besides, as presented in Table 1-3, cooling rate is one of the most important variables that affect microstructure and mechanical properties of Al-Si cast alloys. As mentioned before, the Lost Foam Casting (LFC) process with lower cooling rate progressively replaces the traditional Die Casting (DC) process to save the cost in manufacturing of cylinder heads. Therefore, it is necessary to compare the differences of microstructure and mechanical properties between the two casting processes.

Recycled aluminium is widely used as replacing primary alloys due to significant cost savings. Therefore, effect of iron on the microstructure and damage mechanisms of Al-Si-Cu alloy is of particular interest because it is present in much higher concentrations in recycled aluminium.

The size and amount of α-$Al_{15}(Fe,Mn)_3Si_2$ phase and β-Al_5FeSi phase in Al-Si-Cu (Fe) alloys are strongly influenced by the Fe content, Mn content and cooling rate. As can be seen in Table 1-4, the β-Al_5FeSi phase is harmful to the properties of the alloy and Mn additions are used to reduce the detrimental effects of the β-Fe phase by replacing it with the supposedly less-detrimental Chinese script α-$Al_{15}(Fe,Mn)_3Si_2$ phase. In addition, some researchers reported that the Fe content can promote the formation of pores, which is in contradiction with the work by others, who claimed the existence of a critical Fe content for a minimum porosity formation in Al-Si-Cu alloy. Thus, the effect of Fe/Mn content on the microstructures and damage mechanism of Al-Si-Cu alloy needs to be further studied.

As listed in Table 1-3, the effect of heat treatment on the microstructures has been studied by some researchers. However, most of these studies have been based on two-dimensional (2D) analysis of the microstructure due to the complexity in characterizing their three-dimensional (3D) microstructure. In fact, the over-idealized 2D microstructure does not effectively allow understanding the spatial morphologies of various constituents. Thus, a full 3D characterization of the microstructure to study how these constituents are affected by heat treatment would appear to be particularly important.

Although the damage mechanisms of as-cast LFC A319 alloy studied in a previous Ph. D. thesis (Wang, 2015) revealed the important role of pores and hard inclusions, the influence of different amount, size and morphology of hard inclusions, especially for the Al_2Cu phase, which result from different heat treatment conditions, on the damage mechanisms of LFC A319 alloy are still not clear and need to be further studied. Besides, quantitative assessment of local strain at cracked particles could help understanding differences in the damage mechanisms of the various hard inclusions.

Thus, in this thesis, the effect of different Sr, Fe, and Mn content and casting process on the microstructures of Al-Si-Cu alloys will be discussed in Chapter 3, and the evolution of microstructure in Al-Si-Cu alloy with different alloying element addition will be studied by thermal analysis.

The relationship between the different microstructures and the mechanical properties are investigated in Chapter 4. In particular, the damage mechanisms of two DC Al-Si-Cu alloys with different Fe contents (0.1 wt.% and 0.8 wt. %) will be studied by 2D in-situ tensile test.

In Chapter 5, the evolution of the microstructure of LFC A319 alloy from as-cast condition to subsequent solution treatments for 2h30 and 50h at 495°C is investigated by optical microscopy and X-Ray tomography. The damage mechanisms of the two LFC A319 alloys with different hard inclusions characteristics inherited from heat treatment will be investigated by 3D in-situ tensile tests.

Table 1-3: Some parameters affecting the microstructures of Al-Si alloy

Microstructures and properties		**Parameters**				
		Cooling rate	**Sr addition**	**Fe**	**Mn**	**Heat treatment**
Microstructure constituents	**α-Al**	High cooling rate could refine all microstructure constituents, and vice versa.	Increasing the Si, Fe, Cu level has been reported to have a restricting effect on SDAS in Al-Si alloys			Precipitation hardening
	Si phase		Sr additions to Al-Si alloys result in a finer lamellar or fibrous eutectic network	-	-	Modification eutectic Si phase
	Iron-intermetallics (α and β phase)		-	1) Increasing the Fe content could increase the amount and size of β-phase; 2) Change precipitation sequence of α and β phases	Transform β-phase into α-phase, but increase the total amount of Fe-rich intermetallics	Dissolve the iron-intermetallics at a higher solution temperature (Non-equilibrium heat treatment)
	Cu-containing phase (Al_2Cu + $Al_5Mg_8Cu_2Si_6$)		Sr promotes the Al_2Cu phase precipitation in the blocky form rather than in the fine eutectic form	β-platelets can act as nucleation sites for the copper phase particles	-	Dissolution of Cu-containing phase
Casting defects (porosity)		Lower cooling rate could promote the formation of porosity	Sr addition introduce more dispersed and round pores	1)High Fe content can promote the formation of pores; 2)Existence of a critical Fe content for a minimum porosity formation	Addition of Mn could reduce the amount of porosity	Incipient melting could generate pores (>495°C)

Table 1-4: Effect of microstructures on the mechanical properties and damage mechanisms of Al-Si alloy

Microstructural features/constituents	**Mechanical properties**	**Damage mechanisms**	
		Crack initiation	**Crack propagation**
SDAS	Lower SDAS result in better mechanical properties.	-	-
Pores	Increasing volume of the porosity is deleterious to alloy ductility and UTS.	Large pores act as preferential crack nucleation sites by creating a high stress concentration	Pores can reduce effective stress-bearing area and accelerate crack propagation
Eutectic Si	Noticeable improvement in strength and elongation in Sr modified alloy	1) Cracks nucleate at eutectic Si, iron-intermetallics and Al_2Cu phases in areas where there are enough stress concentrations; 2) Higher elastic modulus of hard inclusions make them more fragile than Al matrix thus act as crack initiation sites; 3) Sharp morphology (acicular Si particles and needle-like β-Al_5FeSi phase) of hard inclusions generates high local stress concentrations and leads to cracks initiation and failure.	1) Cracks are prone to propagate through the fracture of Al_2Cu, Si particles and iron-intermetallics rather than Al matrix. 2) the failure mode of hard inclusions may be (i) fracture or (ii) debonding depending on the crack tip driving force and hard inclusions morphology
Iron-intermetallics	1) UTS appears to be slightly decreased whereas YS appears to be increased by the increase in iron-intermetallics content. 2) Brittle needle-like β-Al_5FeSi has a deleterious effect on the elongation		
Al_2Cu phase	Precipitation strengthening (UTS, YS and EI % are increased by increasing the dissolved Cu content.)		

2 Chapter 2 experimental part

Contents

Chapter 2

2.1 Introduction

This chapter introduces the experimental techniques and protocol that have been used to understand the development of the microstructure in multicomponent Al-Si alloys and the influence of different microstructures upon the mechanical properties and damage mechanisms.

As shown in the flow chart in Figure 2-1, a full metallographic 2D and 3D characterization of the microstructure through optical- and Scanning Electron Microscopy (SEM) and laboratory X-ray tomography was performed in order to study the influence of variation in Sr, Fe, and Mn content within the composition tolerance of the AlSi7Cu3 alloy and of the casting process, i.e. Die Casting (DC) and Lost Foam Casting (LFC), on the microstructure. Mechanical properties have been also determined using conventional tensile test and Vickers hardness test.

In order to achieve this, two primary DC AlSi7Cu3 alloys (alloy A and B), with low Fe levels and with different Sr content were used to study Sr effect on the microstructure and mechanical properties. At the same time, two secondary DC AlSi7Cu3 alloys (alloy C and D), with high Fe levels and with different Mn:Fe ratios were used to clarify the role of Fe and Mn. Besides, the secondary alloy with a lower ratio of Mn to Fe, which is usually used to manufacture commercial cylinder heads, was produced by two different casting methods, DC and LFC, in order to study the effect of these processes.

In addition, thermal analysis was performed on the four alloys in order to study the effect of Sr, Fe and Mn upon the solidification reactions of AlSi7Cu3 alloy (see §2.3).

In order to study the influence of iron-intermetallics resulting from different Fe content on the damage mechanisms of AlSi7Cu3 alloy, 2D in-situ tensile tests observations were performed on two specimens which were extracted from the DC cylindrical parts, Digital Image Correlation (DIC) technique were used for field measurements.

In this work, the effect of heat treatment on microstructures and damage mechanisms of as cast LFC A319 alloy were also studied. Firstly, heat treatments tests were performed to achieve two levels of Al_2Cu dissolution, namely partial dissolution and almost complete dissolution, while maintaining the same matrix hardness as in the untreated alloy.

Then, two selected heat treatment conditions (see Figure 2-1) were performed on the suitable specimens which were selected through a series of methods (see §2.4.2.2). 2D/3D microstructures analysis through Optical Microscopy (OM) and laboratory X-ray tomography were performed on these specimens before and after heat treatment in order to study the morphological evolution of microstructures during different heat treatments (see §2.5). Additionally, the in-situ 3D tensile tests observations were performed on the selected specimens which were subjected to two different heat treatment conditions (see §2.6.2.3). Digital Volume Correlation (DVC) technique was used for field measurements (see §2.6.3).

Finally, fractographic examinations were performed with OM, SEM and EDS on the failure specimens (see §2.6.4).

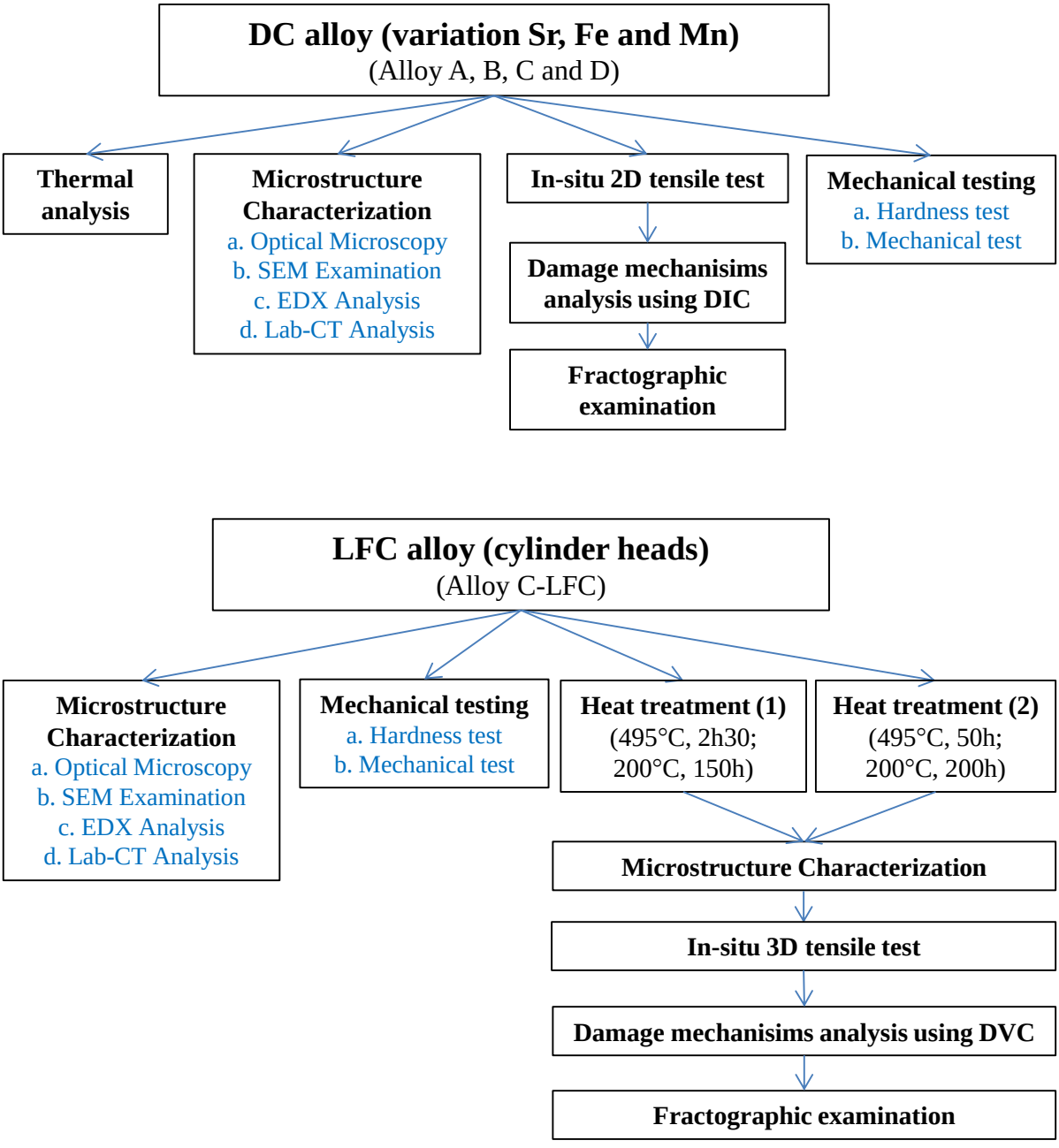

Figure 2-1: Flow chart summarizing the experiments performed on the studied alloys

2.2 Alloy preparation and heat treatment test

2.2.1 DC alloy

The four Die Casting (DC) AlSi7Cu3 alloy used in this work were supplied by PSA in the form of rods with a diameter of 20 mm and a length of 200 mm. The processing route is detailed below.

For the two primary DC AlSi7Cu3 alloys with different Sr content (alloy A and B respectively low and high Sr), the base alloys were supplied as commercial ingots of primary alloy. Sr addition was achieved by introducing different amounts of an Al–10 wt. % Sr master alloy to the molten base alloy. For the two DC AlSi7Cu3 alloys with different Mn:Fe ratios (alloy C and D respectively high and low Mn:Fe ratio), the base alloy was received as ingots of secondary alloy. Different amounts of Sr, Fe and Mn in the form of Al–10 wt. % Sr, Al–25%Fe and Al–25%Mn master alloys were added into the melt.

The ingots were cut into smaller pieces, dried, and melted in a silicon carbide crucible, using an electric resistance furnace (temperature deviation of ±5 °C). The melting temperature was held at 735 ± 5 °C. High purity dry argon was used as degasser; the degassing period was 12 min with a flow of 2 l/min. The melt was then poured into the mold at about 720℃.

The mold produced at the end of casting process with the distribution of micro-porosity simulated by Flow 3D is shown schematically in Figure 2-2. Metallographic examination reveal that the obtained alloys have a similar SDAS (20.7 μm) as the one in commercial cylinder heads produced by LFC process (Zhang, Garro et al. 2013). Thus, these samples are representative of the DC process for cylinder heads. The cylinder part, which is marked by a circle in the Figure 2-2, was studied in this work.

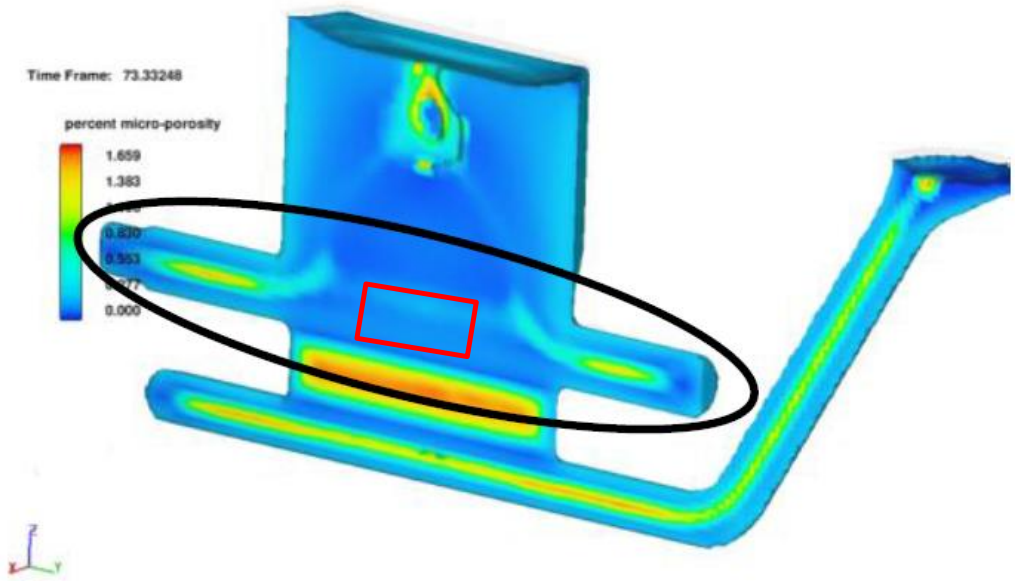

Figure 2-2: Schematic view showing the casting mold and the distribution of micro-porosity (PSA)

After the casting, 30 cylindrical cast specimens with a 20 mm diameter and 200 mm length were obtained for each alloy; all the specimens were examined with X-ray radiography in order to assess the specimen porosity level. Each specimen was classified with a range between 1 to 8 according to the ASTM E155 standard (Standard 2010). The compositions of the experimental alloys were measured using a mass spectrometer and the results are given in Table 2-1.

Table 2-1: Chemical compositions of the experimental alloys (wt. %)

Alloy	Casting method	Al	Si	Fe	Mn	Mn/Fe	Sr	Cu	Mg	Ti	Pb	Zn
A	DC	bal.	6.91	0.10	0.007	-	**0.0047**	2.89	0.29	0.11	0.003	0.022
B	DC	bal.	7.01	0.14	0.010	**0.07**	**0.0133**	3.36	0.30	0.11	0.004	0.033
C	DC	bal.	7.66	**0.49**	**0.130**	**0.26**	0.0120	3.67	0.31	0.11	0.054	0.33
	LFC	bal.	7.85	**0.30**	**0.190**	-	0.0120	3.05	0.28	0.098	0.015	0.16
D	DC	bal.	7.00	**0.80**	**0.510**	**0.64**	0.0100	3.45	0.28	0.12	0.05	0.24

2.2.2 LFC alloy

- **As cast samples**

In order to clarify the role of different casting processes (LFC and DC) on the microstructure and mechanical properties of Al-Si-Cu alloy. Some samples, which have a chemical composition similar to DC alloy C as shown in Table 2-1, were directly extracted from industrially manufactured cylinder heads produced by the LFC process.

- **Heat treatment test**

In this part, some samples, which were cut from industrially manufactured cylinder heads obtained by LFC process, were used to test the heat treatment parameters, which will be applied to specimens for 3D in-situ tests.

The aims of these tests are to design heat treatments that can give two levels of Al_2Cu dissolution, namely partial dissolution and almost complete dissolution, while maintaining the same matrix hardness as in the untreated alloy:

a. The test samples are thus divided into two groups. The first group will achieve partial dissolution of the Al_2Cu phase after solution heat treatment as compared to the as-cast LFC alloy. The second group of samples will be heat treated long enough to allow for a near total dissolution the Al_2Cu phase after solution heat treatment.
b. The hardness of the matrix needs to remain the same as the as-cast LFC alloy. This was achieved through ageing after heat treatment.

Note that after the solution heat treatment carried out to dissolve Al_2Cu, due to the small size of the specimen, the quench in air from solution temperature will be more rapid than LFC cooling rate in cylinder heads. This leads to form Al_2Cu less interconnected.

The design of the solution and ageing heat treatment was carried out at PSA. Quantitative microscopic metallographic analysis and hardness test were performed to test the amount of Al_2Cu phase and hardness of the matrix after heat treatment. The two different heat treatment conditions that allow achieving the aims previously defined are listed in Table 2-2.

Table 2-2: The heat treatment conditions used for the suitable specimens (wt. %)

	Heat treatment (1)	**Heat treatment (2)**
Number of specimen	6	5
Solution heat treatment	495°C for 2h30	495°C for 50h
Quenching	Air cooling to room temperature	
Ageing	200°C for 150h	200°C for 200h

2.3 Thermal analysis

Thermal Analysis (TA) method is a useful tool to determine a wide range of solidification features for aluminium alloys (Farahany, Ourdjini et al. 2013). This approach can provide the fundamental relationship between characteristic temperature and time, alloy composition, addition elements (Alkahtani, Elgallad et al. 2016), and cooling condition (Farahany, Ourdjini et al. 2013). This method is based on the recording of the temperature changes in the sample from a fully liquid to a fully solidified phase during cooling, and on the subsequent analysis of the cooling curve, i.e. the plot of temperature as a function of time.

The cooling curve can reflect the release of latent heat of solidification. This release of latent heat in multi-component alloys changes the slope of the cooling curve which can be used to detect the characteristics of transformations and phase reactions during solidification. However, due to the small amounts of heat generated in some phase transformations, the characteristic features of these phase transformations may not be obvious from the cooling curve. Normally, in order to reveal the characteristic temperature of certain reactions, the first derivative cooling curve (dT/dt) is employed (Farahany, Ourdjini et al. 2013).

The four AlSi7Cu3 alloys with chemical composition shown in Table 2-1 were studied with thermal analysis. The alloys were melted in a ceramic crucible of 30 mm in diameter by 50 mm in height (see Figure 2-3). A high sensitivity thermocouple of K type was used to record the temperature at the center of the mould; a support was used to fix the top of the thermocouple to assure that it remained in place during cooling. Data were acquired by a high speed data acquisition system linked to a PC computer. Before all temperature measurements, the thermocouples were calibrated at the solidification point of pure aluminium (660°C) to ensure accurate and precise reading.

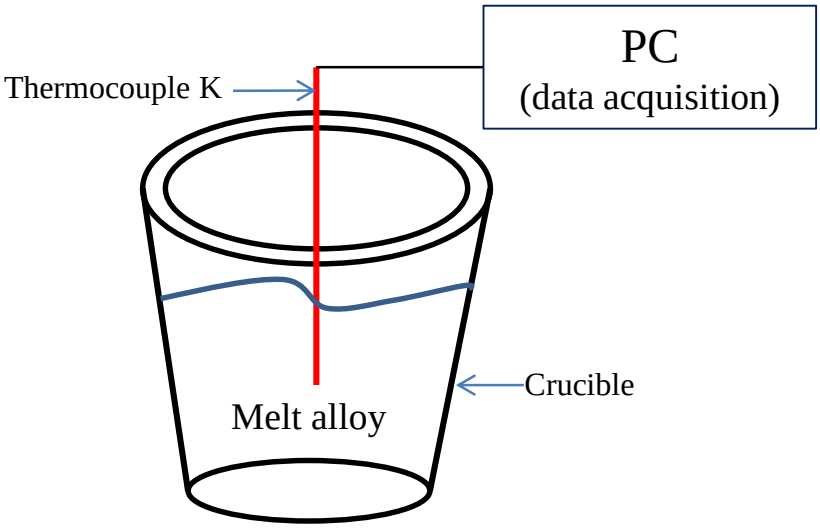

Figure 2-3: A schematic view of the thermal analysis setup

Metallographic analysis of the TA test samples was performed with OM/SEM to verify the nature of the phases formed. Thus, after thermal analysis, each sample was sectioned horizontally where the tip of the thermocouple was located and it was prepared by standard grinding and polishing procedures.

In order to reveal and clarify the solidification sequence of the alloys, the interrupted quenching method (i.e. interrupting the solidification process and quenching the solidifying sample into water) was carried out. This method has been previously proven to work by (Lu and Dahle 2005). Samples were quenched at different temperatures and the "water-quenched" structure was then compared with the "normally solidified" structure. The solidification process of the alloy could be revealed and the solidification sequence and microstructure could be determined.

2.4 Specimens preparation and selection

In this section, the protocol of specimen preparation and selection for 2D/3D characterization and in-situ tensile test is described. The specimens include DC and LFC alloy.

2.4.1 DC alloy

2.4.1.1 Preparation of specimens for 2D/3D characterization

For microstructural examination purposes, 2D metallographic DC samples were used for the characterization of microstructural constituents, such as SDAS, eutectic silicon and intermetallic compounds. Samples were prepared using standard procedure that includes cutting, mounting, grinding and polishing. Firstly, samples were taken from the center of cylinder bar (see the red box in Figure 2-2) for the four alloys. Then, all the samples were polished using abrasive papers of grades up to 4000 grits in succession and then using polishing cloths and suspensions up to 1/4 μm. Finally,

polishing was performed with a commercial 0.04 µm silica oxide colloidal suspension (OPS), until the sample surface becomes mirror like.

The samples for 3D porosity characterization were extracted from the same area as 2D metallographic samples; all the samples were small cylinder samples (Ø 4 mm×10 mm). Due to the working principle of the X-ray microtomography, polishing is not necessary before scanning.

2.4.1.2 Preparation of specimens for 2D in-situ tensile test

In this work, in order to study the role of Fe-rich intermetallics on the damage mechanisms of Al–Si-Cu alloy, two DC alloys (A and D) which contain different Fe/Mn content were selected and prepared for the in-situ 2D tensile test. Figure 2-4 summarizes the process of specimen preparation.

Figure 2-4: Scheme of specimen preparation for DC alloy

2.4.1.2.1 Extraction of specimens

As can be seen in Figure 2-5(a), all the specimens were extracted from the center of cylindrical parts with the 20 mm diameter and 200 mm length. Each round bar can produce two tensile specimens. 4 specimens were prepared for each alloy with the geometry shown in Figure 2-5(b). Note that a shallow hole in the center of specimen was introduced to have a stress concentration in the chosen ROI (Region Of Interest) that could force the final fracture to occur here.

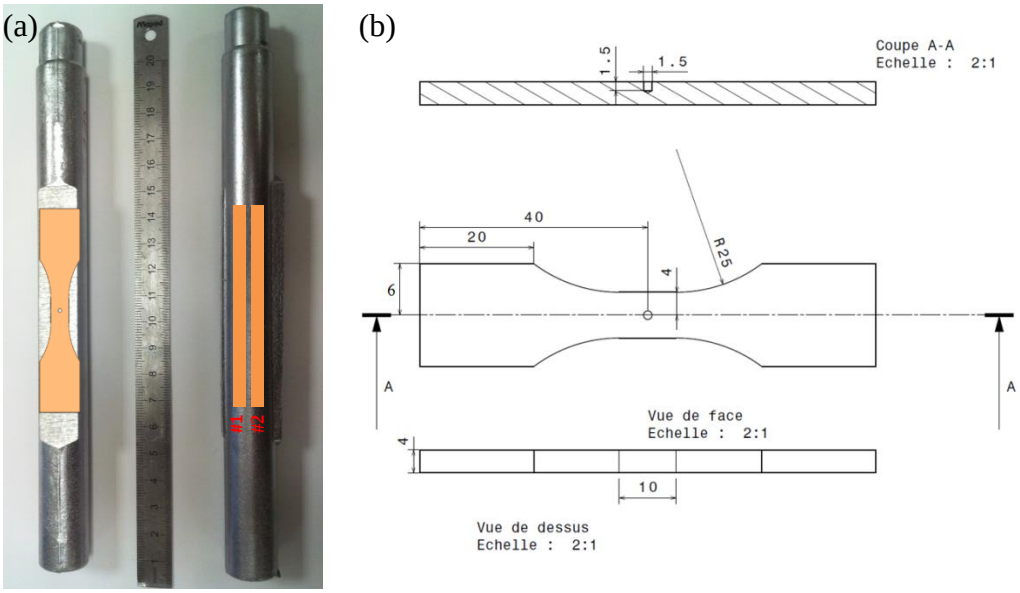

Figure 2-5: (a) Extraction of specimens from the middle of the round bars, (b) Geometry of extracted specimens (in mm) for tensile tests with 2D in-situ observation

2.4.1.2.2 Polishing and OM observation

Grinding was performed on four sides and each corner of specimens. Fine polishing was only performed on the observed surface (i.e. the surface that contains the artificial hole) in order to obtain a flat surface where in situ optical observations could be performed. Each of the specimens was examined using a microscope before etching; several OM images, at a high spatial resolution as compared to the observations performed in-situ during the tensile, were taken in the area close to the hole in order to compare to the strain localizations calculated by DIC analysis after. An appropriate overlap between adjacent images is necessary for the further stitching of the images to a larger image.

2.4.1.2.3 Etching (Pattern making)

For DIC analysis to succeed, the specimen surface must have a random speckle pattern that can deform with the surface as carrier of deformation information. Natural pattern of the specimen and artificial white-light speckle patterns, which are obtained by black/white spray paint (Armanjo 2015), are commonly used as speckle patterns.

Speckles size plays a critical role to ensure a suitable balance between measurement accuracy (bias error) and precision (standard deviation error) (Pan, Lu et al. 2010). In the case of Al-Si alloy, due to the featureless areas of α-Al dendrites, the spatial resolution of the DIC measurement will be decreased. However, the drawback of paint speckle pattern is that the speckle also masks the microstructure underneath and thus prevents the study of the relationship between microstructural features and strain heterogeneities. Thus, at micro-scale level, small size speckles are required. In the present work, an etching method was used to produce a suitable speckle pattern on the microstructure of specimens for OM imaging and DIC analysis. The present speckle preparation method is as follow:

The reagent used in here is:

- 100 mL water,
- 4g $KMnO_4$ and once dissolved 1g NaOH,

Etching procedure:

- Fine polishing of sample surface,
- Etching (speckle generating) by 20 seconds immersion in reagent.

Figure 2-6 shows the metallographic image of studied alloy before and after color etching, and the corresponding gray-level distributions in the same area of the specimen surface. Before etching, the histogram shows one tall peak for the Aluminium matrix and other very small peaks (see arrows in Figure 2-6(a)) for pores, eutectic Si particles and intermetallics. After etching, the image dynamic shows a wider range of gray-levels within the Aluminium matrix where etching has revealed segregation and precipitates (Petzow 1999). Compared to the image before etching, the large standard

deviation of the gray-level distribution of the specimen surface shows a richer speckle pattern which is expected to be sufficient to use DIC technique on the microstructural scale.

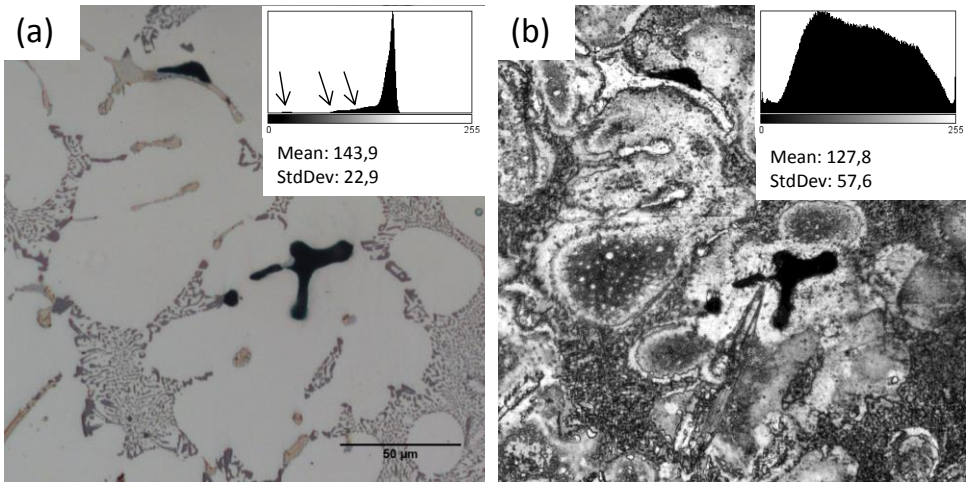

Figure 2-6: OM images of the specimen surface (a) before and (b) after etching

2.4.2 LFC alloy

2.4.2.1 Preparation of specimens for 2D/3D characterization

The samples of LFC alloys which are used for 2D/3D characterization can be divided into two parts; the first part is used for comparison with the DC alloy in order to study the effect of casting process (i.e. DC and LFC) on the microstructures of A319 alloy, and the other part is used for study the effect of different heat treatment on the microstructure of LFC A319 alloy. We named them LFC^1 and LFC^2, respectively.

Thus, the first part of LFC samples (LFC^1), which have the same chemical composition as alloy C, were extracted from the automotive cylinder heads in the inter-valve area. The procedure of preparation of these specimens for 2D/3D characterization is the same as DC alloys, which isd described in §2.4.1.1.

For the second part of LFC samples (LFC^2), quantitative 2D and 3D microstructure characterization analysis were carried out on the tensile specimens machined as described in the following part before and after the different heat treatment. Fine polishing of the flat surface of specimens is necessary for the 2D observations. The details of extraction of the tensile specimen will be introduced in the following part.

2.4.2.2 Preparation of specimens for 3D in-situ tensile test

The process of specimen preparation and selection for in-situ 3D tensile test are summarized in Figure 2-7. The specimens were extracted from prototype cylinder heads, and then several steps were

performed to select the specimens for the in-situ 3D tensile test, to define the test configuration, i.e. to choose the best Region of Observation for the tomography, and to perform the heat treatments that will allow obtaining different amount of Al_2Cu dissolution. These steps are described in details hereafter.

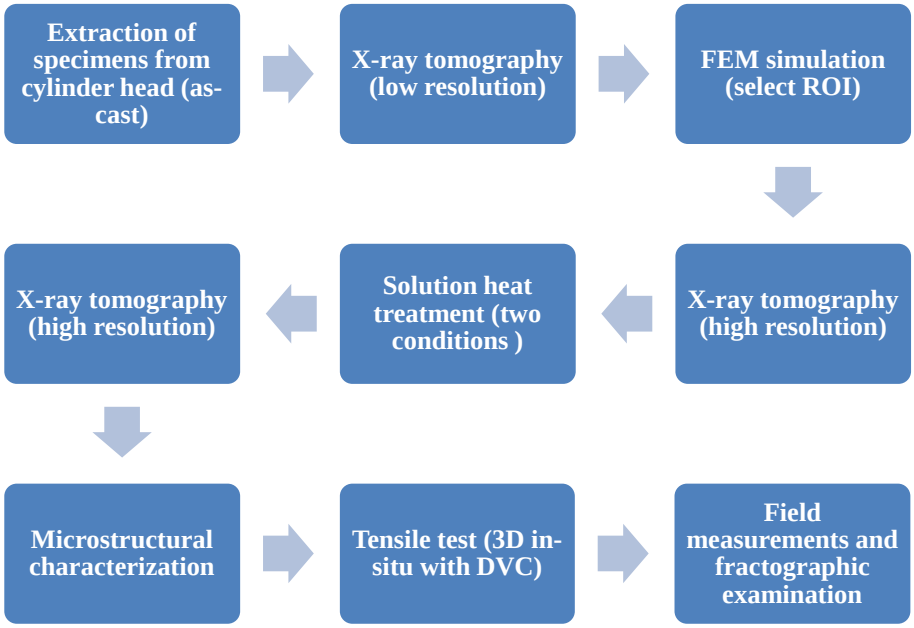

Figure 2-7: Workflow of 3D in-situ tensile test for LFC alloy

2.4.2.2.1 Extraction of specimens

All the specimens were extracted from A319 prototype cylinder heads manufactured using LFC process, and 30 specimens in total with the same geometry were extracted from the fire deck area that is the most critical area in cylinder head (Figure 2-8). Figure 2-8(a) shows the extraction area of specimens from prototype cylinder heads.

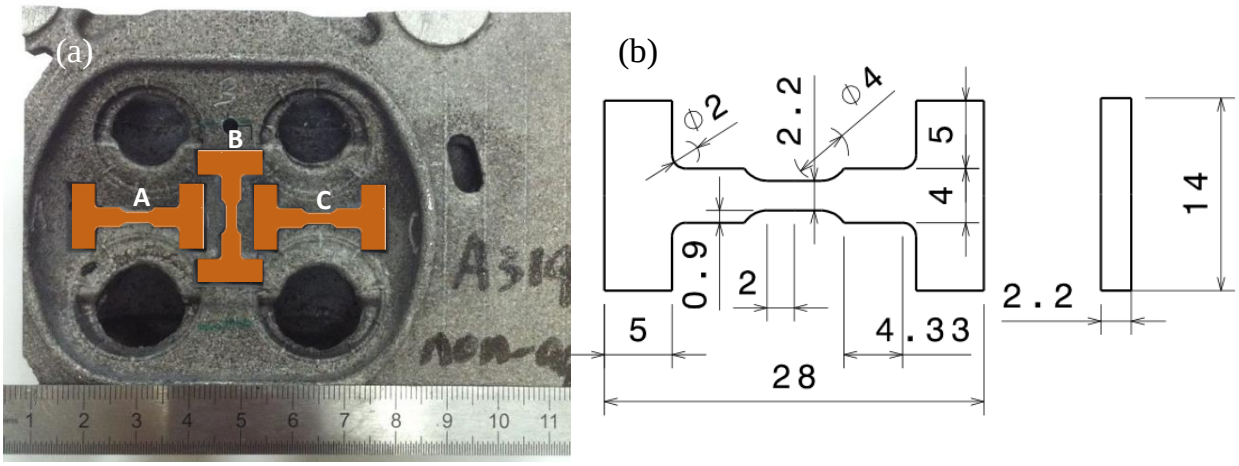

Figure 2-8: (a) Extraction of specimens from prototype cylinder heads (b) Geometry of extracted specimens (in mm) for tensile tests with 3D in-situ observation

2.4.2.2.2 X-ray tomography observation (low resolution)

The primary selections were performed using lab-CT (ISIS4D) in the fast scan mode, i.e. the scan lasts about 15 minutes, at a 4.5 μm voxel size. These medium resolution images allow revealing the location, size and shape of the large pores rapidly. The scan was carried out in the center of specimen, the height of the tomographic image is 13.7 mm, and thus the whole gauge length between the specimen's shoulders could be characterized. The suitable specimens were selected by using the 3D rendering of pores. In order to select the most suitable specimens, the requirements are as follows:

a. The chosen specimens have no large defects near the shoulders;
b. The specimens have defects with a size compatible with the specimen cross-section in the gauge length.

This preliminary selection is to ensure that the final failure occurs in the center of specimens where 3D in-situ observations are done. Using this methodology, only 11 specimens can be kept as suitable for the in-situ 3D tensile test.

2.4.2.2.3 FEM simulation for selection ROI

Thanks to FEM simulation, the most strained area where crack initiation is expected can be predicted in the specimen before the in-situ 3D tensile test. Thus, we can focus on this interesting area and reduce the scan duration by limiting scan height.

Porosity has an important influence on strain localization during tensile test, 3D images with a voxel size of 4.5 μm (used for suitable specimen selection) obtained by laboratory tomography were used to generate FE model representing solid matrix and pores. The FEM models include the entire gauge length of the specimen. FEM simulations were performed on 11 suitable specimens which were selected by the method mentioned before.

The basic process of the FE mesh can be summarized as in following:

a. The solid matrix of these specimens was segmented from the X-ray tomography 3D image by Avizo software.
b. A triangular surface was reconstructed by using "Generate Surface" module; the number of triangles of the reconstructed surface was reduced for the subsequent operations by using the "Surface Simplification" Editor in Avizo. The minimum and maximum sizes of the triangle element were set as 0.2 and 10 pixels respectively. The mesh is built in such a way that elements of the mesh generated around the pores have a smaller size than in other areas in order to decrease the number of elements.
c. A cumbersome and complex surface edition by manual and automatic tools was carried out before the tetrahedral grid generation.

d. A volumetric tetrahedral grid was then built by "TetraGen" module. Herein, FEM model was constructed and meshed.

For more details please refer to (Wang 2015). Then, the model was imported in Abaqus for FE computation. The material property is set as elastoplastic using a stress-strain curve from a conventional test on A319 LFC alloy. After the FEM simulation, the cumulated plastic strain distribution is computed and plotted in order to localize potential critical area, the areas, where the high strain localizations in the FEM strain field will be selected as ROI for in-situ 3D tensile test.

2.4.2.2.4 Polishing

Before the in-situ tensile test, grinding was performed on four sides and each corner of specimens to ensure that all the surfaces are smooth, and thus prevent the generation of stress concentration, and minimize the possibility of initiation from machining marks on the corners of the samples. Fine polishing was performed on both flat surfaces for the postmortem analysis using SEM.

2.5 Microstructure Characterization

For microstructural examination purposes, samples were prepared from the different alloys (alloys A, B, C, and D), casting processes (DC and LFC) and heat treatment condition as described before, then they will be examined using various characterization techniques. This part presents details of specimen microstructure analysis process. The microstructural constituents which were characterized for these alloys are listed in Table 2-3.

Table 2-3: Microstructural constituents characterizations

Alloy	**Microstructures**	
	2D (OM/SEM/EDS)	**3D (Lab-CT)**
DC	Eutectic silicon, intermetallic compounds, SDAS	Pore
LFC[1]		
LFC[2]	Eutectic silicon	Intermetallic compounds, Pore

Notes: 1. The specimens are used to study the effect of casting process.
2. The specimens are used to study the effect of heat treatment.

2.5.1 Characterization technologies

This part presents details on the microstructure characterization methods used, namely conventional 2D image analysis using OM and SEM-EDX and advanced 3D imaging using X-ray tomography (Lab-CT).

2.5.1.1 Optical microscope observation

The main aim of using Optical Microscopy (OM) is to obtain highly contrasted micrographs for observing the morphology and distribution of all phases. OM gives enough contrast between the

intermetallic phases and eutectic silicon in the alloys, thus quantitative measurements of the eutectic Si particles characteristics, the iron-intermetallic compounds characteristics and the dendrite arm spacing were performed with a Nikon YM-EPI light microscope equipped with a Sony color video camera. This microscope was fitted with 2.5, 10, 20 and 50 objective lenses and the corresponding magnifications were 25, 100, 200 and 500.

A certain number of fields in high magnification was selected and examined for each sample so as to represent the features of the whole sample. For the eutectic Si particles and iron-intermetallic compounds measurements, over fifty fields were examined at a magnification of 500. The parameters of the analyzed images are listed in Table 2-4.

Optical micrographs at 5x and 10x magnifications were used to measure SDAS of LFC and DC specimens, respectively.

Table 2-4: Parameters used for image analysis by OM

Alloy code	Casting process	Magnification(X)	Resolution (μm/pixel)	Analyzed area(mm^2)
A	DC	500	0.07	1.17
B	DC			1.36
C	DC			1.27
	LFC[1]			0.87
	LFC[2]			4.40
D	DC			1.02

Notes: 1. The specimens are used to study the effect of casting process.
2. The specimens are used to study the effect of heat treatment.

2.5.1.2 Scanning electron microscopy – Energy Dispersive X-ray analysis

Scanning Electron Microscopy (SEM) is one of the most versatile instruments available for the examination and analysis of the microstructural characteristics of solid objects (Goldstein, Newbury et al. 2012). It uses a focused beam of high-energy electrons to generate a variety of signals at the surface of solid specimens. The signals that derive from electron-sample interactions reveal information about the sample including external morphology (texture), chemical composition, and crystalline structure and orientation of materials making up the sample (Hashmi 2014). Secondary Electrons (SE), having very low energy and the smallest interaction volume are therefore capable of giving a better spatial resolution than the other signals. SE is very sensitive to the surface topography. Back Scattered Electrons (BSE) possess a much higher energy and their signal strongly depends on the atomic number. The higher the atomic number, the brighter the appearance of the respective microstructural feature. Therefore, the BSE imaging mode allows detecting variations in composition (Chen 2006). Thus, the BSE mode was mostly used in this work. Energy dispersive X-ray spectroscopy (EDX) analysis is a chemical microanalysis technique performed in conjunction with SEM. It has been used to investigate and identify phases by determining their chemical composition. X-ray mapping in SEM with EDX

builds on the basics of qualitative X-ray microanalysis by providing a visual representation of the elements present (Nylese and Anderhalt 2014). X-ray mapping provides images of elemental distributions in the analyzed area.

In this work, the microstructure and micro-cracks observations were done using a JEOL 7800 F LV SEM. The EDX analyses were performed using the equipped OXFORD System Aztec and an X-Max 80 mm^2 premium spectrometer Microanalysis System to identify the morphology and stoichiometry of the intermetallic phases. X-ray mapping was primarily performed to characterize the elements distribution in the fracture surface.

2.5.1.3 X-ray tomography observation

2.5.1.3.1 X-ray tomography principle

X-ray Computed Tomography (CT) is a non-destructive technique used in visualizing the interior of an opaque solid object with the aim of obtaining digital information of the internal structure of the objects at a microscopic level (Onifade 2013). The basis of CT is similar to conventional radiography except that it involves acquisition of a large number of radiographs while rotating the sample typically between 0° to either 180° or 360°. A filtered back-projection algorithm is often used to reconstruct the volume of the sample from the radiographs (Salvo, Cloetens et al. 2003). Figure 2-9 illustrates the principle of X-ray Computed Tomography (Limodin, Buffière et al. 2013).

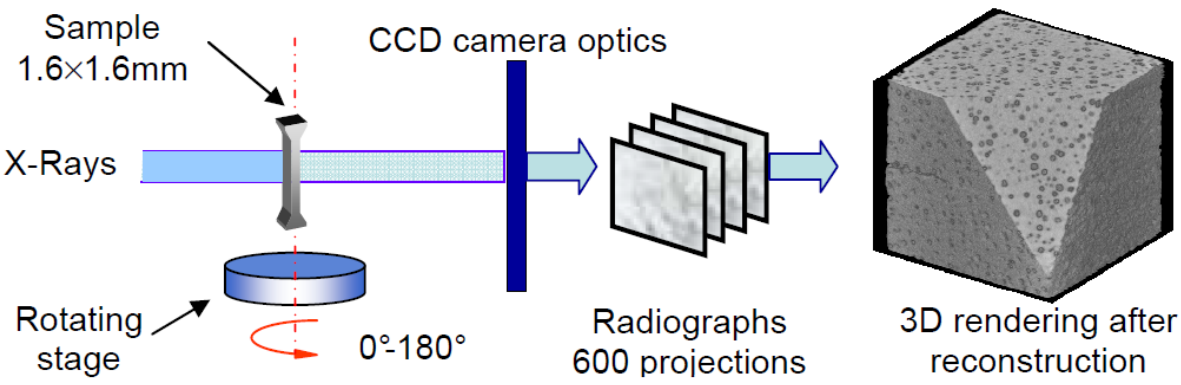

Figure 2-9: Principle of tomography (Limodin, Buffière et al. 2013)

The different microstructure features may present different grey levels in the reconstructed 3D image. The contrast in the image is due mainly to the difference of the X-ray absorption coefficients. This absorption coefficient depends on the density of the material, the atomic number and the energy of the X-rays (Salvo, Suéry et al. 2010).

2.5.1.3.2 X-ray tomography experiments

In the present work, X-ray microtomography was realized on ISIS 4D platform (Lille, France) within an Ultratom Lab-CT system from RX Solution (Figure 2-10). The X-ray source is an open

transmission Nanofocus tube that delivers an X-ray cone beam, whose acceleration voltage can be adjusted from 20 to 160 kV. The voxel size can be adapted by modifying the position of the rotating object placed between the X-ray source and the detector. Since the X-ray cone beam diverges, a complete rotation of 360° is required to fully capture the sample microstructure. The closest as possible sample distance to the source sets the minimum voxel size that can be reached. If small voxel sizes are required, the sample dimensions must be consequently reduced.

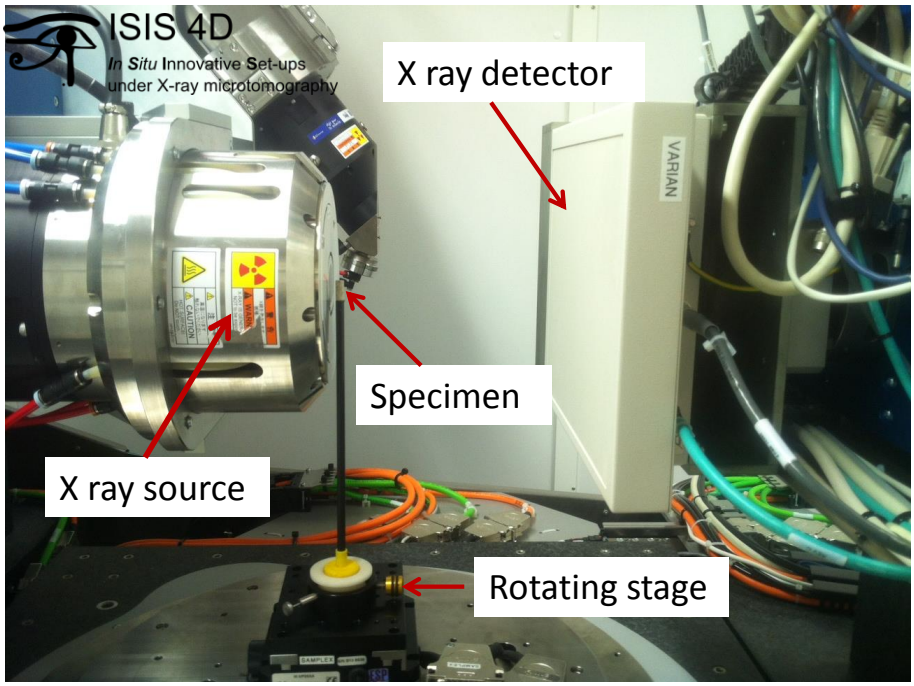

Figure 2-10: View of ISIS4D tomograph showing the X-ray source, the rotating stage and the detector

The measurement of pores characteristics was performed on DC and LFC alloys with X-ray Laboratory Computed Tomography (Lab-CT). Thanks to the absorption contrast provided by Lab-CT, pores can be easily distinguished from the matrix.

3D characterization for the Si phase could not be achieved with Lab-CT as Al and Si have close atomic numbers hence similar X-ray attenuation. Thus, as mentioned before (§2.5.1.1), 2D metallographic analysis was used to characterize the Si phase in both DC and LFC alloys.

As for intermetallic compounds, their size in DC alloys is too small compared to the tomography resolution. However, the coarser intermetallic compounds in LFC alloys can be revealed and distinguished with X-ray microtomography. Therefore, 3D characterizations for intermetallic compounds were performed on the LFC alloys.

The parameter settings used for the DC and LFC specimens in this study are listed in Table 2-5. 3D porosity characterization analysis was carried out on the as-cast DC and LFC specimens; this allows showing the pore distribution and characteristics in 3D.

Besides, in order to characterize the microstructure evolution in 3D for LFC specimens during heat treatment, high resolution (voxel size of 2 µm) Lab-CT was performed on the ROI of 11 suitable specimens before and after heat treatment (see Figure 2-7).

Table 2-5: Parameter settings of Lab-CT

Parameters	DC LFC[1]	LFC[2]
Microstructural analysis	Pore	Pore, Al_2Cu phase, iron-intermetallics
Voxel size (µm)	2.45	2
Focal spot size (µm)	2	2
Acceleration voltage (kV)	70	80
Filament type	W	W
Filament current (µA)	150	109
Target material	Mo	W
Acquisition time per image (ms)	330	1100
Number of projections per scan	4320	2000
Number of averaged frames	3	5
Image size (voxels)	1520×1520×1700 ($3.7\times3.7\times4.1mm^3$)	1200×1200×1300 ($2.4\times2.4\times2.6mm^3$)

Notes: 1. The specimens are used to study the effect of casting process.
2. The specimens are used to study the effect of heat treatment.

2.5.2 Image processing and analysis

2D and 3D images were processed and analyzed using ImageJ/Fiji and Avizo Fire softwares using the following procedure:

1) median filtering was applied prior to segmentation in order to reduce the noise in the image;
2) a simple grayscale thresholding technique was used to segment the different phases: hard inclusions and pores in the 2D/3D images.

Quantitative analysis could then be realized to label the objects: to attribute each individual object a given label or color, and to measure several characteristics of the labelled objects. Objects that are small as compared to the resolution of the images, with a volume less than 9 voxels in 3D or with an area less than 9 pixels in 2D, were neglected and discarded from the analysis.

The main parameters used to characterize the morphology of intermetallics, Si particles and pores are Feret diameter, sphericity and granulometry (Boulos, Fristot et al. 2012).

Feret diameter is defined as the longest distance measured between two parallel tangents on each side of the 2D or 3D object of interest. Feret diameter was used to assess the size of either pores or hard inclusions as it could better reflect not only the size but also the shape of objects.

Sphericity corresponds to the ratio between the particle area and the area of the circle with the same perimeter as the object in 2D (Ruxanda and Stefanescu 2002) or to the ratio between the object volume and the volume of a sphere with the same surface as the object in 3D.

Granulometry estimates 3D objects sizes using morphological opening operations: openings are performed step by step with an increasing structuring element size until all objects in the volume have disappeared in the input binary image. The number of non-zero pixels still present in the image is collected after each step (Wang 2015). Thus Granulometry reflects the local thickness statistically of a given phase in 3D.

In order to determine the average value of the Secondary Dendrite Arm Spacing (SDAS) in one sample, the size of SDAS was obtained as an average value of at least 10 measurements.

2.6 Mechanical testing

2.6.1 Vickers hardness Test

The Vickers diamond pyramid indentation technique was used to determine the hardness of the alloys. A Vickers pyramid hardness testing machine was used. Each polished sample was placed on the platform of the test machine and a load was applied on the sample surface with the diamond pyramid to make an indentation point on the sample. The Vickers hardness (HV) is given by the following equation:

$$HV = \frac{F}{A} = 1.8544\frac{P}{d^2}$$

Where F is the force applied to the diamond in daN, A is the surface of the pyramid in mm²; P is the load in kilograms and d is the average diagonal of the pyramid base in mm. As seen in Figure 2-11, the indentation diagonals, d1 and d2 are measured and the Vickers hardness is calculated using the average diagonal length (d = (d1 +d2)/2); an average over 10 indentations was measured for each sample.

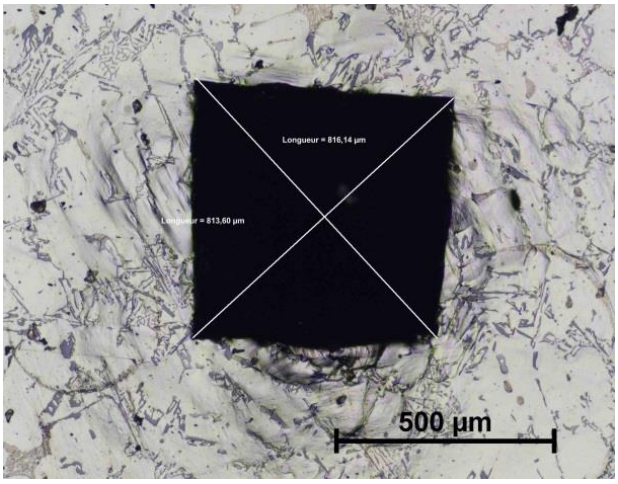

Figure 2-11: Typical indentation in the surface of LFC A319 alloy

2.6.2 Tensile test

2.6.2.1 Conventional tensile test

Tensile test specimens were machined according to ISO 6892-1 (ISO 2009). For each alloy, three tensile tests were carried out on a computer controlled testing machine (Instron) at a constant cross head speed of 1 mm/min. All the tests were performed at room temperature (~25°C). A strain gauge extensometer (gauge length of 25 mm) was used to measure the 0.2% proof stress, ultimate tensile strength and the elongation up to fracture.

2.6.2.2 2D in-situ tensile tests for DC alloy

In-situ 2D tensile tests were performed at a displacement rate of 16 µm/s using an Instron 8501 servo-hydraulic testing machine. During the tensile test, the applied load was recorded by an extensometer, which was installed across the center area of the specimen (see Figure 2-12), to measure the macroscopic deformation. The experimental set-up is illustrated in Figure 2-13.

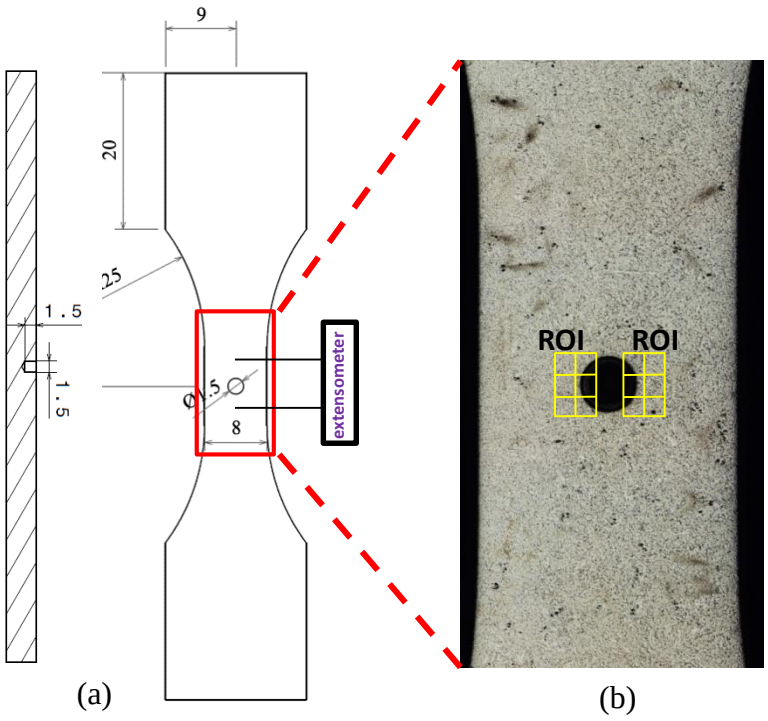

Figure 2-12: (a) Schematic drawing of a tensile specimen including dimensions, and (b) photograph of sample showing the hole in the center of specimen and the Region Of Interest (ROI) for the DIC analysis. All dimensions are in mm.

In order to record the deformation images during the tensile tests, the test was interrupted at different load step with the specimen held under load and images were taken using a JAI 500 CCD camera with a resolution of 2048×2048 pixels and fitted with a Questar long distance microscope. The camera was mounted on a translation stage perpendicular to the tensile test set-up. Digital pictures were taken in

several adjacent zones of the ROI with a pixel size of about 0.23/0.27 μm in order to cover the area of interest (see Figure 2-12). Stitching of the images acquired at each load step was performed using the plugin MosaicJ in Image J software (Thévenaz and Unser 2007) which allows rigid registration of images. An appropriate overlap between adjacent images is necessary for the further stitching of the images to a larger image which covers the ROI.

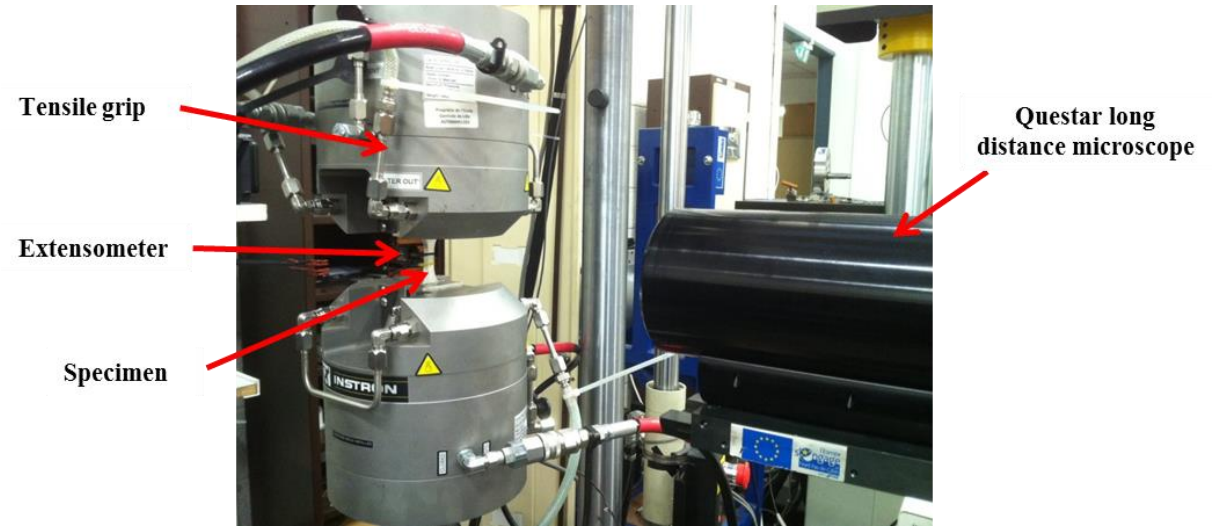

Figure 2-13: Experimental set-up with Questar microscope

2.6.2.3 3D in-situ tensile tests for LFC alloy

In-situ 3D tensile tests were performed on the heat treated specimens using an in-situ test rig. The main features of the in situ tensile test setup are given in Figure 2-14.

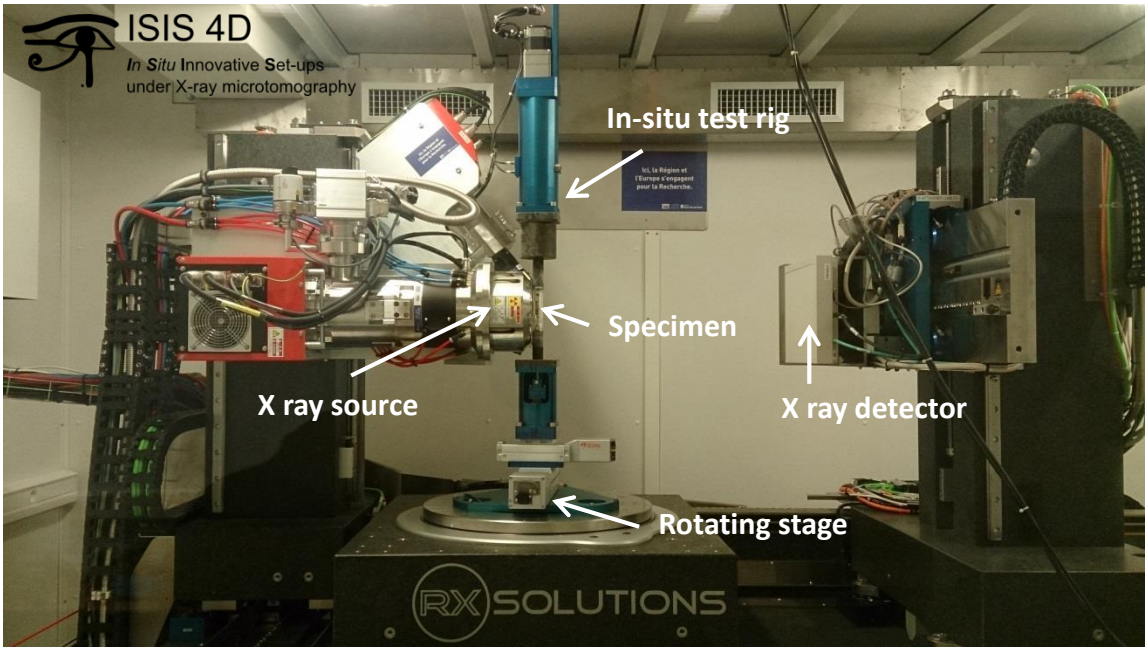

Figure 2-14: In-situ 3D tensile test set-up at LML

A preliminary tensile test without interruption was realized on unsuitable specimens before real tests to define the load steps for the following tensile tests. The aim is firstly to obtain several images at different loads between the elastic limit and the ultimate tensile stress to study damage evolution.

The in-situ tensile machine is directly mounted on the rotating stage of the tomograph. A Quartz tube (see Figure 2-15) was used as part of the load rig, this thin tube allows a 360° rotation without hiding the specimen from the beam, and it gives a constant but negligible attenuation of the X-ray photons. A force sensor allows recording the applied load in real time during the tests that were performed in displacement control mode at a speed of 1 μm/s. The specimen was loaded step by step until fracture. 3D tomography images were taken in the selected ROI before loading and at each load step when the test was interrupted.

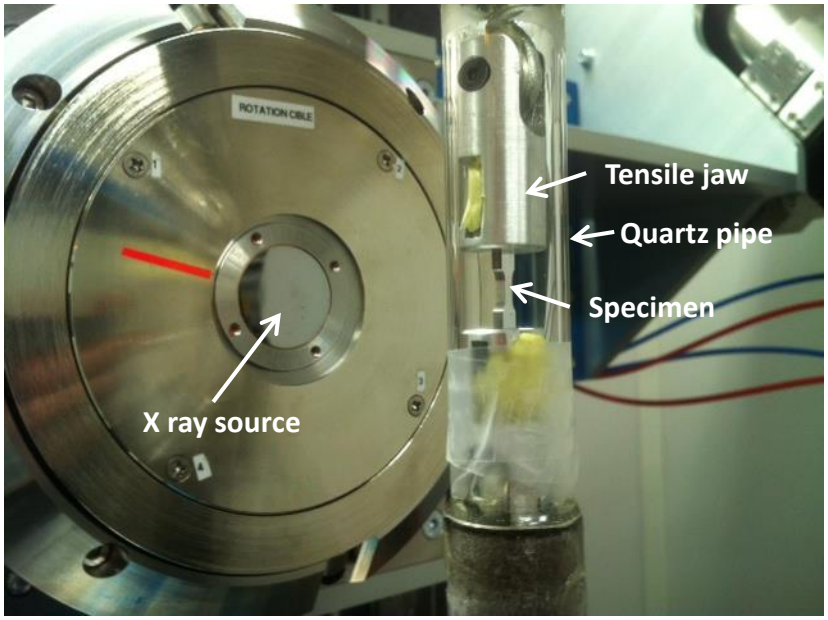

Figure 2-15: Zoom of the Quartz pipe

In order to distinguish the different phases and obtain high quality tomography images, a high resolution is necessary, thus a voxel size of about 3 μm was chosen. The height of the scanned volume is 750×760×1300 voxels. For each step, 1024 projections were taken while the sample was rotating over 360° along its vertical axis; the total scan time was equal to 33 min for each step. Acquisition parameters are listed in Table 2-6.

After the specimen failure, a scan was also performed on one of the two parts of the broken specimen for each tensile test to identify the 3D fracture surface.

Table 2-6: Parameter settings for 3D in-situ tensile test

Specimen	HT1a	HT1b	HT2
Heat treatment condition	495°C, 2h30+200°C, 150h		495°C, 50h+200°C, 200h
Acceleration voltage	90kV		
Number of projections per scan	1024		
Exposure time	330ms		
Number of averaged frames	6		
Pixel size	3µm		
Scan time	33min		
Scan step	7	14	21
Reconstructed image size	750×750×1300 voxels		

2.6.3 Field measurements

Digital Image Correlation (DIC) was first developed by a group of researchers at the University of South Carolina in the 1980s (Sutton, Mingqi et al. 1986). It is an optical-numerical measurement technique for determining complex displacement and strain fields on the materials surface for static as well as dynamic application (Sutton, Orteu et al. 2009). The Digital Volume Correlation (DVC) technique is a 3D extension of the well-developed DIC method and they have similar principles. DVC was developed from the end of 1990s (Bay, Smith et al. 1999), and is now widely used due to the development of 3D advanced imaging devices (Limodin, Réthoré et al. 2009).

The image analysis method is based on grey value digital images. DIC and DVC correlate the grey values of a reference undeformed image with a deformed image to determine displacement and strain of the deformed image. If g denotes the deformed and f the reference images, these functions are related by:

$$f(\mathbf{x}) = g(\mathbf{x} + \mathbf{u}(\mathbf{x})) \text{ (Eq.1)}$$

Where **x** is the vector denoting the position of any pixel/voxel, **u** is the displacement vector for each position **x.**

2.6.3.1 YaDICs software

In this study, Displacement and strain field measurements were performed with a DIC/DVC technique using YaDICs software developed at LML laboratory (Lille, France) (Seghir, Witz et al.). This platform is based on C++ and it has been proven efficient for the correlation of large 3D volumes (Dahdah, Limodin et al. 2016).

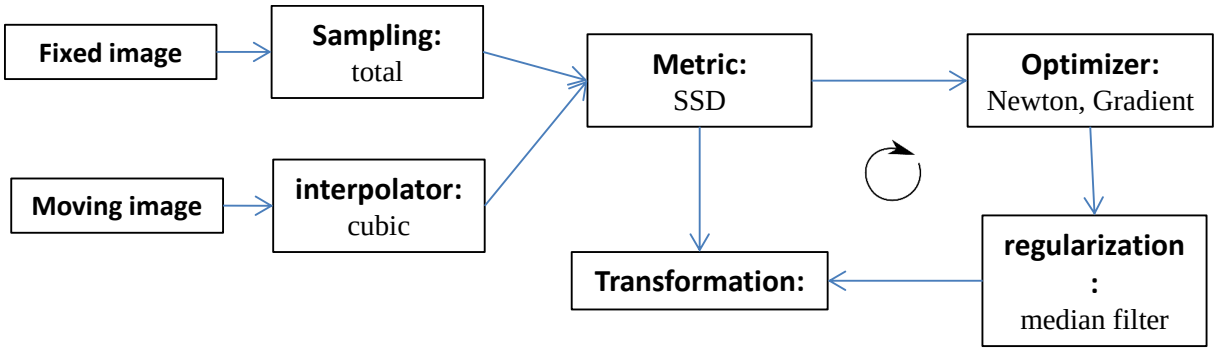

Figure 2-16: The basic registration components of YaDICs (Seghir, Witz et al.) image correlation platform at LML

As shown in Figure 2-16, in order to identify the transformation, several steps are necessary: define a metric, choose a sampling and an interpolator, then an optimizer and finally a regularization method.

In the present case, global (rigid and homogeneous) and elastic transformation were chosen in order to compute the Sum of Squared Difference (SSD) metric chosen. The metric is evaluated on the whole image (i.e. total image). The gradient descent is retained as optimizer method; the gradient of the metric is computed regarding the transformation parameters (Eq.2):

$$\frac{\partial SSD}{\partial \boldsymbol{u}} = \frac{2}{\Omega}\sum_{\boldsymbol{x}\in\Omega}\left(f(x) - g(\boldsymbol{x}+\boldsymbol{u}(\boldsymbol{x}))\right)\frac{\partial g\left(\boldsymbol{x}+\boldsymbol{u}(\boldsymbol{x})\right)}{\partial \boldsymbol{u}} \quad (Eq.2)$$

Finally, a bi-cubic interpolator is employed to apply the transformation to the moving image at each iteration. The correlation is based on a multiscale resolution strategy like a pyramid scheme. At each scale the transformation searched for may be different: homogeneous deformation are looked for at the coarsest scales while at more finer scales, local deformations are searched for at the nodes of a FE-like grid whose spacing gets finer and finer until the last scale, i.e. the full resolution image, is reached. In this work, six scales were used, the coarsest one is “scale 5” where one “macro” voxel is averaged over $2^5\times2^5\times2^5$ voxels, while the full resolution image corresponds to “scale 0” (Dahdah, Limodin et al. 2016).

For the 2D DIC analysis, analysis sequence “OFI_H, OFI_H, OFI_H, OFFEM, OFFEM, OFFEM” was used:

- OFI_H is defined by the OFI method, and assumes a homogeneous deformation such as rigid body motions, i.e. translations and rotations, and global strains. It measures the similarity by using Sum of Squared Differences (SSD).
- OFFEM is the Optical Flow elastic transformation based on Finite Element Methods; it is used for the elastic deformation, as it has a good spatial coherence.

For the 3D DVC analysis, the following analysis sequence was used "OFI_RB, OFI_H, IC, OFFEM, OFFEM, OFFEM":

- OFI_RB is defined by Optical Flow Integrated (OFI) method definition for rigid body motion.
- IC corresponds to the Intercorrelation method which is based on Normalized Cross Correlation (NCC).

The detailed parameters used in this work are presented in Table 2-7.

Table 2-7: The parameters for DIC/DVC analysis using YaDICs

	2D tensile test with Questar		**3D tensile test with Lab-CT**		
	DIC/2D		**DVC/3D**		
Specimen name	A	D	HT1a	HT1b	HT2
Pixel/voxel size(μm)	0.27	0.23	3		
Element size(μm)	16*16		8*8*8		
Measured field(μm)	500*500	500*300	1980*1980*2500	2250*2250*2250	2190*2190*2190
Analysis sequence	Scale: 5, 4, 3, 2, 1, 0 OFI_H, OFI_H, OFI_H, OFFEM16, OFFEM16, OFFEM16		Scale: 5, 4, 3, 2, 1, 0 OFI_H, OFI_H, IC, OFFEM8, OFFEM8, OFFEM8		

Note: OFFEM8 means the element size is 8×8pixels or 8×8×8 voxels for DIC or DVC, respectively.

2.6.3.2 Measurement uncertainty

Uncertainty analysis was used to quantify the performances of DIC and DVC (Zappa, Mazzoleni et al. 2014). It is estimated from the standard deviation of the displacement field measured between two images, one at a reference position and another one after a small translation (Limodin, El Bartali et al. 2014).

In the present work, the uncertainty of the measured displacement field was calculated to assess the feasibility of DIC and DVC, and the methods are presented below:

- DIC measurement uncertainty method

The specimen was placed on a translation stage, and after acquisition of a reference image, the specimen was shifted by approximately 10 μm in a direction perpendicular to the optical axis of the Questar microscope, then the standard deviation of the displacement field was calculated between the two images and different element size were tested as uncertainty strongly depends on the size of element.

- DVC measurement uncertainty method

The X-ray tomography scan was performed on the specimen at a reference position, and then another scan was taken after a translation along the beam direction. As the lab-CT X-ray beam is conical, the voxel size will change from 3.05 µm to 3 µm in the present case after a translation along the beam direction, and then a known displacement field in all directions, i.e. a dilatation, which correspond to a maximum displacement of 15 voxel, was applied. Then, the standard deviation of the displacement is calculated for the three different directions, and used to verify if there is one favored direction in the noise.

The change in the uncertainty versus element size is shown in Figure 2-17. The increase in accuracy with the element size decrease is easily seen.

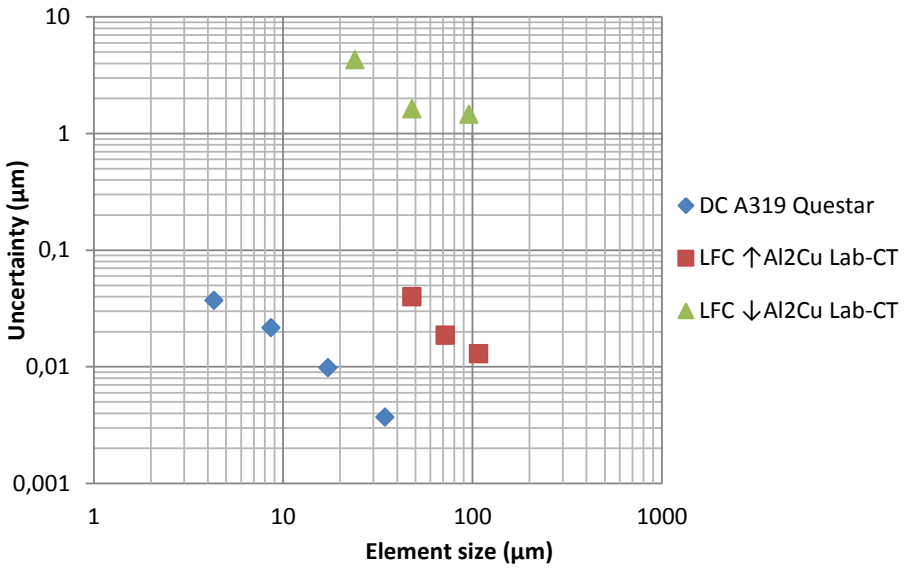

Figure 2-17: Measurements uncertainties (Uz)

In 2D, the microstructural features, such as iron intermetallics, copper containing phases, eutectic Si and Al matrix, revealed by Questar long distance microscope can be used as natural markers for DIC. In addition, etching method applied on the surface of specimen reveals segregation of Si that gives contrast to Al matrix. However, as eutectic Si cannot be revealed by lab-CT, 2D measurements on the etched surface have higher accuracy than the 3D measurements using lab-CT images.

Resolution of DVC technique depends on the presence of numerous and finely dispersed microstructural features like matrix and hard inclusions. As characterized in Chapter 1, the Al_2Cu phase will be dissolved after solution heat treatment, however, because the amount of dissolution of Al_2Cu phase varies with the solution heat treatment time, less Al_2Cu phases will be present in the A319 alloy with long-time (50 h) solution heat treatment as compared to the alloy with short-time (2h30) solution heat treatment. Thus DVC measurements using lab-CT images may have higher

accuracy for short-time solution heat treatment A319 than for long-time solution heat treatment alloy for a given spatial resolution.

2.6.4 Fractographic examination/ Postmortem analyses

Postmortem analyses were performed on the fracture specimens using HITACHI 3600N SEM in order to identify the microcracks on surface, the microstructure along final fracture on flat surface, and to analyze the microstructural constituents in the fractures surfaces. . X ray energy dispersive spectroscopy (EDS) was performed using the equipped NORAN System SIX X-ray Microanalysis System. X-ray tomography scan was also performed on one of the two parts of the broken specimen for each tensile test with 3D in-situ observations to allow identifying the fracture locations in 3D.

In order to identify the damage mechanisms of hard inclusions, X-ray mappings were performed on all the fracture surfaces of tensile specimens by using EDS. For 2D in-situ tensile specimen, due to the large size of fracture surface, X-ray mappings were only performed on the areas below surface that corresponds to ROI and that are close to the artificial hole instead of on the whole fracture surfaces; for the 3D in-situ tensile specimen, the X-ray mappings were carried out on the whole fracture surfaces.

For more details about the X-ray mapping parameters performed in this case, please refer to (Wang 2015). Each obtained elemental map is registered on the same area BSE image in order to observe the relations between the fracture surface features and the distribution of the constituents. If the same constituents are identified in the same location on both fracture surfaces for one specimen, the failure mechanism of the corresponding hard particles is fracture. Otherwise, the failure mechanism is decohesion/debonding.

3 Chapter 3 The influence of Sr, Fe and Mn content and casting process on the microstructure and solidification parameters of Al–Si based alloys

Contents

3.1 Introduction

This chapter is focused on the study of the effect of Sr, Fe and Mn content and casting process on the microstructure and the thermodynamics of solidification of AlSi7Cu3 alloy. As introduced in Chapter 2, four different DC alloys, namely alloys A, B, C and D, and one LFC alloy, which has a chemical composition similar to DC alloy C, were studied.

A full metallographic 2D and 3D characterization of the microstructure through OM (optical microscopy), SEM and laboratory X-ray tomography was performed in order to study the influence of variation in Sr, Fe, and Mn content within the composition tolerance of the AlSi7Cu3 alloy and of the casting process, i.e. Die Casting (DC) and Lost Foam Casting (LFC), on the microstructure. The

sampling procedure and characterization methods have been already described in chapter 2. In addition, thermal analysis was performed on the four alloys to investigate the effect of the alloying elements (i.e. Sr, Fe and Mn) upon the solidification reactions.

3.2 Results

3.2.1 Microstructure examination

As described in Chapter 1, the microstructure of AlSi7Cu3 alloy consists of the α-aluminium primary phase in the dendritic form, eutectic Al-Si and various intermetallic phases such as α-$Al_{15}(Fe,Mn)_3Si_2$, β-Al_5FeSi, Al_2Cu, and $Al_5Cu_2Mg_8Si_6$ phase.

In the present investigation, microstructural properties such as SDAS, size and morphology of eutectic Si, volume fraction of pores, size and volume fraction of intermetallic compounds (i.e. iron-intermetallics and Al_2Cu) were examined as a function of the contents of alloying elements and casting process.

3.2.1.1 Secondary Dendrite Arm Spacing (SDAS) analysis

Typical microstructures obtained from alloy C, i.e. with standard composition, are shown in Figure 3-1; micrographs (a) and (b) refer to the DC and LFC, respectively. Compared with the DC alloy, the LFC alloy shows a coarser microstructure, i.e. larger SDAS, plate-like eutectic Si particles, needle-like iron-intermetallics; SDAS values are given in Table 3-1. The average size of SDAS increased from 18.4μm to 76.4μm when the cooling rate decreased from 30°C/s (DC) to 0.8°C/s (LFC).

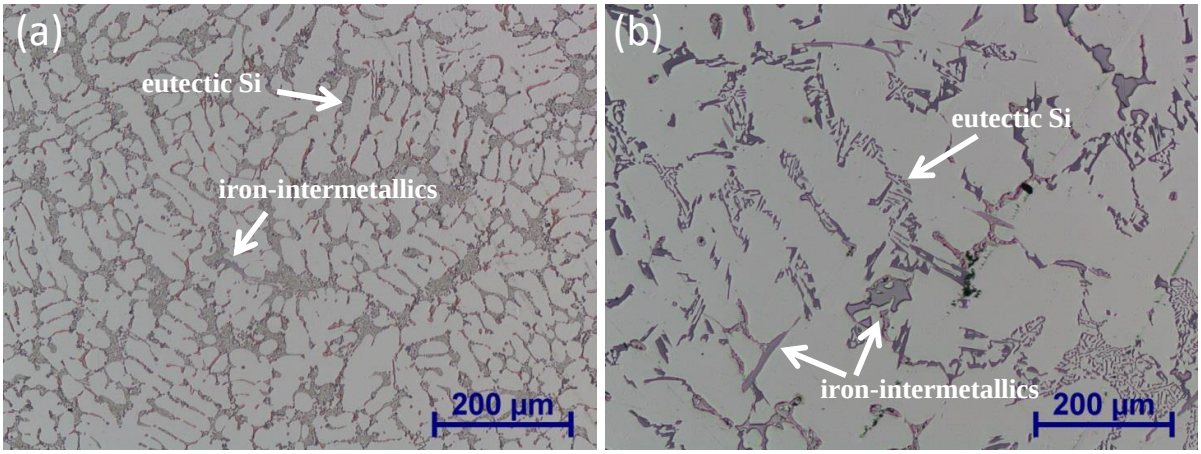

Figure 3-1: Optical microstructures of Alloy C in (a) DC and (b) LFC

Although the size of the dendrites appears strongly affected by the cooling rate, the chemical composition of the alloy has also some effect on this structural characteristic. In order to study the effect of Sr, Fe and Mn content on the size of the microstructure, SDAS measurements were performed on the four alloys introduced in Chapter 2 (see Table 2-1). The optical micrographs shown

in Figure 3-2 already reveal differences of SDAS that are confirmed with the average SDAS values listed in Table 3-1. Comparing alloy A and alloy B, the addition of Sr from 47ppm to 133ppm leads to a SDAS reduction of about 6.25%. Besides, the SDAS slightly decreased from 19.5 μm to 17.0 μm when the content of Fe and Mn increased from 0.14 wt. % and 0.01 wt. % to 0.80 wt. % and 0.51 wt. %, respectively. Thus, the factors affecting the SDAS include the cooling conditions and the alloy composition. Higher concentration of alloying element will cause the formation of finer SDAS.

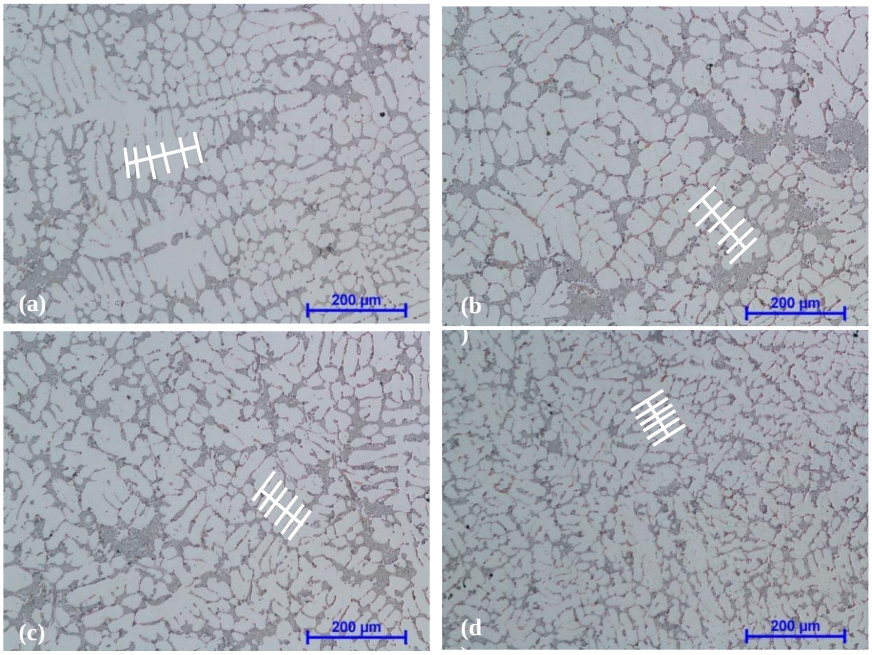

Figure 3-2: Optical micrographs of Alloy (a) A, (b) B, (c) C, (d) D showing the different SDAS in Die Casting.

Table 3-1: SDAS values measured in the four alloys

Alloy code	Casting method	SDAS (μm)	
		Mean	Standard deviation
A	DC	20.8	2.4
B	DC	19.5	2.4
C	DC	18.4	2.1
	LFC	76.4	6.9
D	DC	17.0	2.3

3.2.1.2 Porosity characterization

After casting, the presence of porosity was studied by X-ray radiography for studied DC alloys A, B, C and D. For each alloy, 30 cylindrical cast specimens with the 20 mm diameter and 200 mm length were analyzed, ASTM E155 standard (Standard 2010) gives the criteria to define the 'qualitative'

amount of porosity allowable and each specimen was classified with a range between 1 to 8 (pore density from minimum to maximum) which is representative of different porosity level.

Figure 3-3 shows the frequency distribution of shrinkage cavity level according to the standard ASTM E155. Compared to alloy B, the alloy A which contains lower Sr content shows lower pore density. The maximum pore density is observed at alloy B which has the lowest Fe and Mn content among alloys B, C and D. The 2D X-ray radiography characterization shows that the porosity level seems to decrease with an increase in the Fe and Mn content.

In order to better understand the effect of chemical composition on the pore formation in Al-Si alloy, 3D characterization of pores was performed on these four studied alloys using Lab-CT.

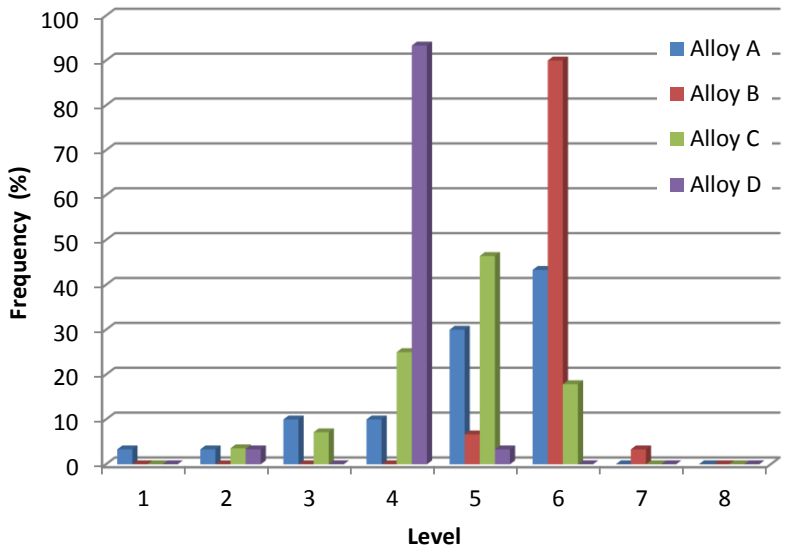

Figure 3-3 Frequency distribution of shrinkage cavity level according to the ASTM E155 standard in 30 specimens for alloys B, C and D

Some researchers (Dinnis, Dahle et al. 2004) (Dinnis, Taylor et al. 2006) have studied the influence of different elements on pores formation in Al-Si alloys. However, their measurements are based on 2D analysis which cannot accurately characterize the features of pores. In the present work, in order to quantitatively characterize the distribution and size of pores in 3D, cylindrical specimens with 3 mm length and 4 mm diameter were extracted from the center of the cast cylindrical bars and scanned with X-ray tomography. This allowed determining the volume fraction and characteristics of pores. Figure 3-4 shows the 3D rendering of the pores in different alloys and for different casting process at a voxel size of 2.45 µm. The pores are visible in the different cylinder specimens and different colors indicate unconnected particles within the studied volume. Then quantitative analysis was performed, and the measured pores characteristics for the four AlSi7Cu3 alloys are provided in Table 3-2.

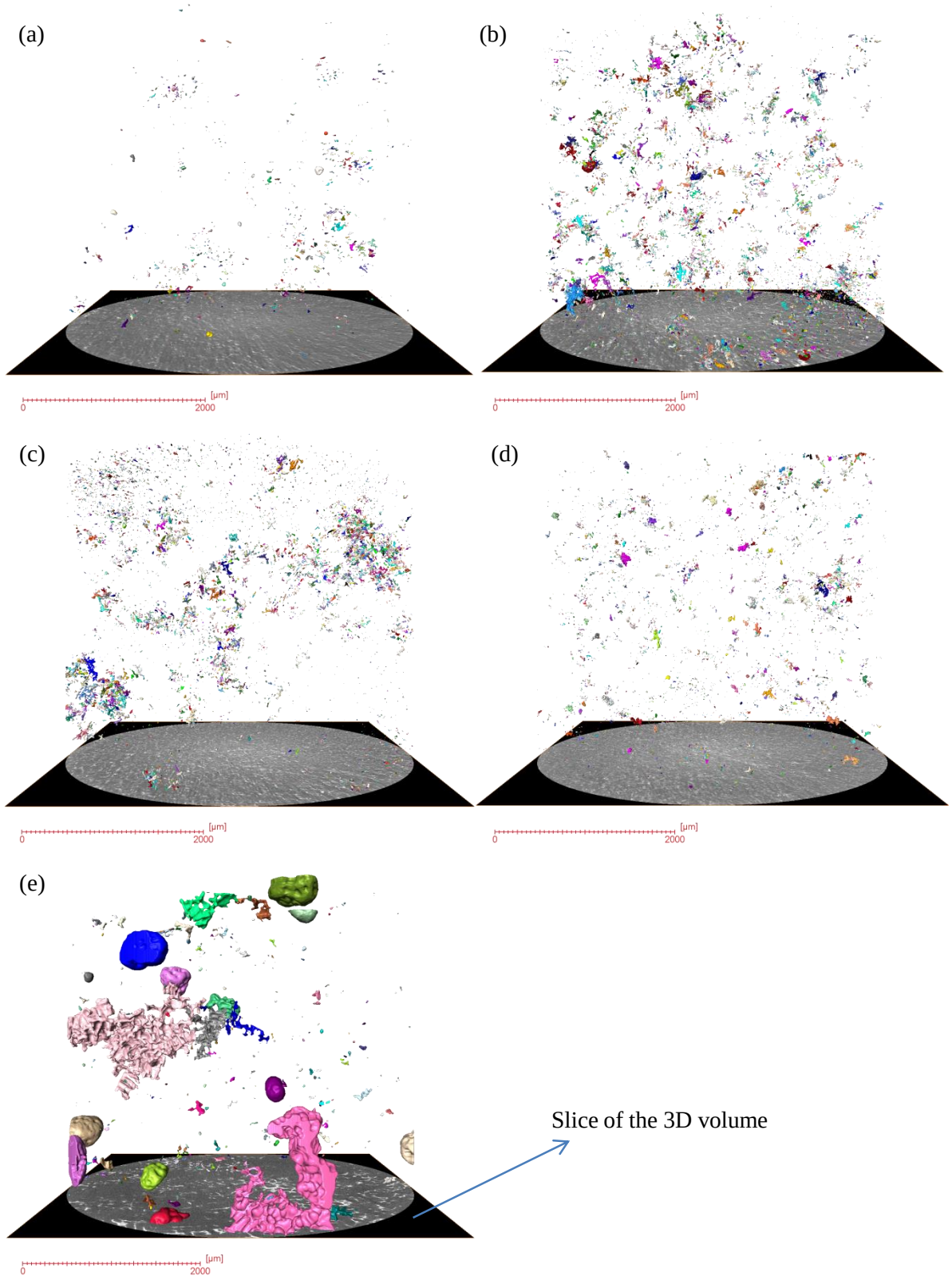

Figure 3-4 3D rendering of pores for alloys (a) A, (b) B, (c) C and (d) D in DC, and (e) alloy C in LFC. (Dimension: Ø3.7mm×Height 3mm)

Table 3-2: Porosity characteristics as a function of alloy composition and casting method

Alloy	Casting method	Volume fraction %	Feret diameter (µm)		Analysed volume (mm^3)	Number of objects/mm^3
			Av.	Max.		
A	DC	0.034	30.3	275.7	30.8	93
B	DC	0.065	28.4	294.4	31.2	200
C	DC	0.045	27.1	278.7	31.2	174
	LFC	0.940	64.1	1535.9	33.0	17
D	DC	0.032	23.8	299.3	31.6	99

Comparing alloys A and B, the number and the volume fraction of pores increased by more than twice (Table 3-2) with the Sr content increase from 47 ppm to 133 ppm. The distributions of pores as a function of Feret diameter in alloy A and B in Figure 3-5 show that increasing Sr content introduces more fine pores in the range of 10 to 50 µm but also more large microshrinkage cavities in the range of 50 to 300 µm. As a result, the higher pore volume fraction corresponds mainly to larger pores in alloy B (high Sr level).

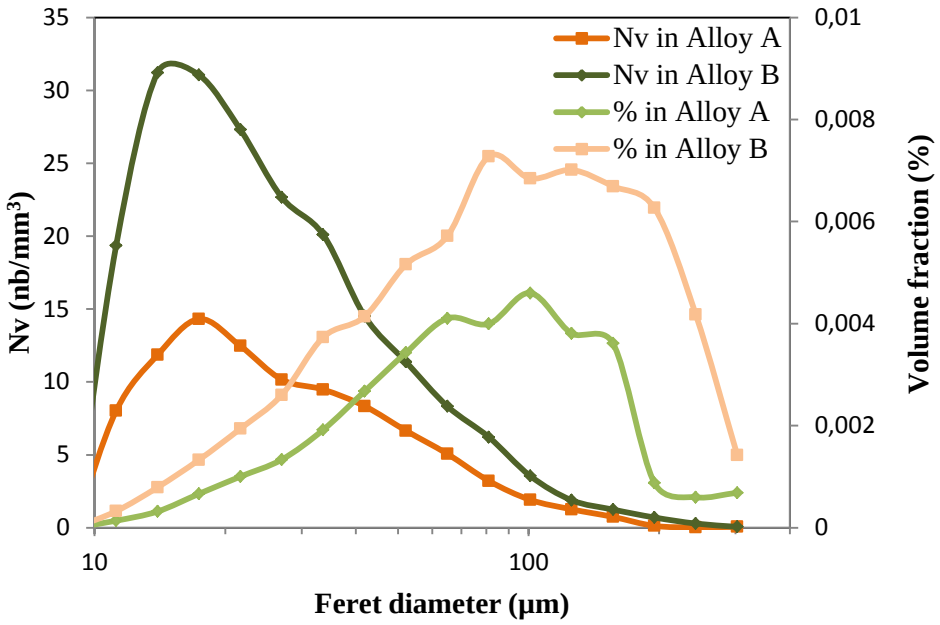

Figure 3-5: Size distribution of pores in number for alloy A and B in Die casting

From the 3D characterization results (Table 3-2), the volume fraction of pores decreased from 0.065% to 0.032% when the Fe content increased from 0.14% to 0.80% for the DC alloys B, C and D. This confirms the previous qualitative results of 2D characterization, and it also proves that a decreased porosity level results from an increase of Fe content in some extent.

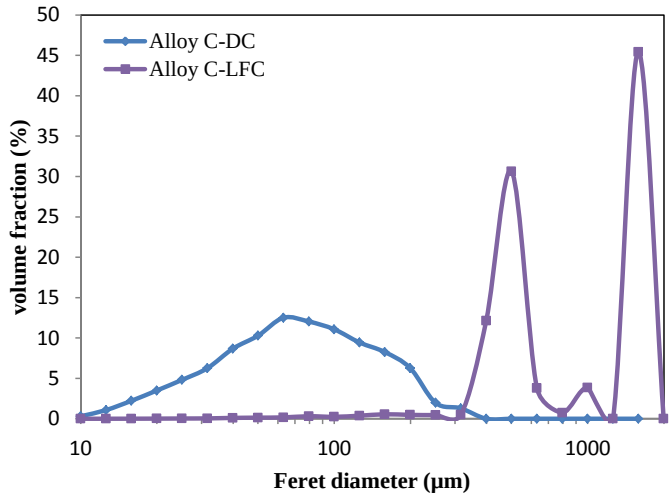

Figure 3-6: The distribution of pores as function of Feret diameter for DC and LFC alloys

The effect of casting process (DC vs. LFC) on porosity was also investigated. As shown in Figure 3-6, a decrease in cooling rate from 30°C/s (DC) to 0.8°C/s (LFC) increases both the total volume of porosity and the average pore size measured in alloy C (Table 3-2). The distribution of pores as function of Feret diameter for DC and LFC is shown in Figure 3-6. DC alloy has more micropores within the range of 10 to 200 µm than LFC alloy. However LFC alloy has larger pores with a maximum Feret diameter up to 1535µm, and the largest pore represents approximately 45% of the total volume fraction of the pores population (see Figure 3-6).

3.2.1.3 Eutectic Si characterization

Mechanical properties of Al–Si alloys are known to be influenced by the size, shape and distribution of eutectic silicon (Sui, Wang et al. 2015). As their microstructures depend strongly both on composition and casting process, Al-Si alloys are generally subjected to Si modification in order to improve mechanical properties. Si modification, which transforms the acicular silicon morphology to fibrous one resulting in a noticeable improvement in elongation and strength (Hegde and Prabhu 2008), can be achieved in three different ways: modification by addition of some elements (chemical modification) or with a rapid cooling rate (quench modification) and spheroidization by high temperature annealing.

3.2.1.3.1 The effect of Sr content

The effect of Sr content on the modification of the eutectic Si particles was studied in alloys A and B. The micrographs of alloy A and alloy B at different magnification are compared in Figure 3-7. Eutectic Si appears as the darkest phase. In both cases the effect of modification of eutectic Si is visible. However, significant differences in the extent of the modification between alloy A and B cannot be observed by naked eye from Figure 3-7. Thus, quantitative metallographic characterization

of eutectic Si particles was performed with image analysis in terms of Feret diameter and sphericity. The distribution of eutectic Si particles as a function of Feret diameter in Figure 3-8(a) show that the average size of eutectic Si particle slightly decreases with the Sr content increases from alloy A to B. Figure 3-8(b) show that more eutectic Si particles with sphericity above 0.4 were present in alloy B compared to alloy A; this means that the amount of plate-like morphology eutectic Si decreases with an increase in the content of Sr. As a result, the higher the Sr content, the more eutectic Si shows a fibrous and globular morphology in Sr-modified alloy.

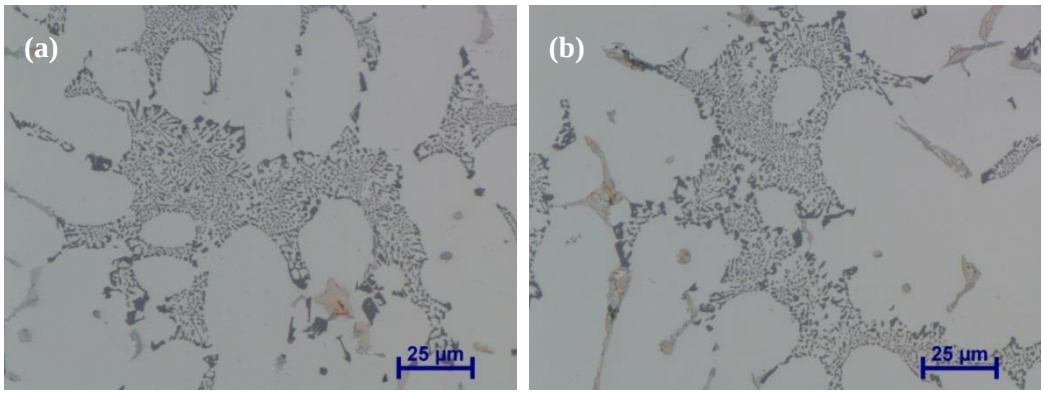

Figure 3-7: Optical micrographs of alloy A (a) and alloy B (b) in Die Casting; eutectic Si is the dark phase

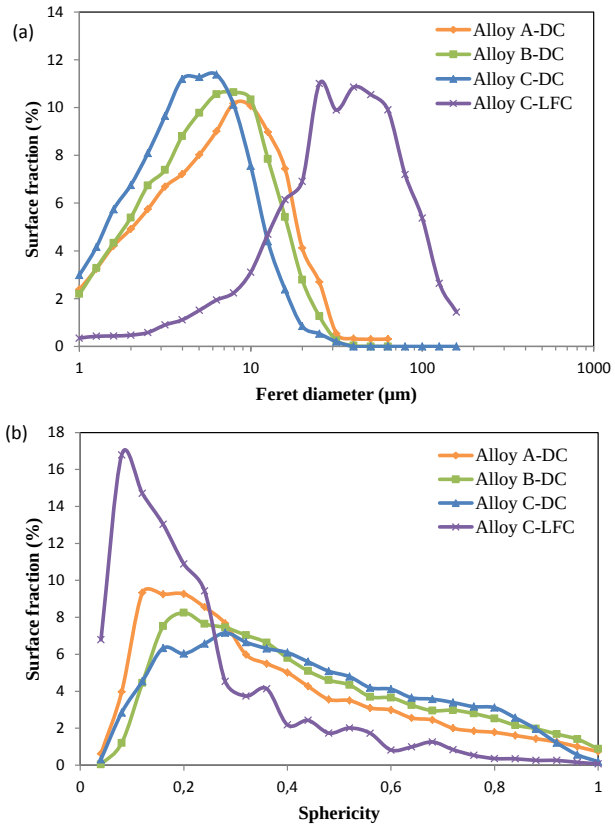

Figure 3-8: Distributions of Feret diameter (a) and sphericity (b) of eutectic Si particles in alloys A, B, C and D

3.2.1.3.2 The effect of cooling rate

A typical eutectic microstructure of both DC and LFC AlSi7Cu3 alloy is shown in Figure 3-9 in the same magnification. From this figure, casting process appears to have a significant impact on eutectic modification for AlSi7Cu3 alloy at the same Sr content. The DC alloy in Figure 3-9(a) clearly shows the fine fibrous morphology of the eutectic Si phase. In contrast, the LFC alloy in Figure 3-9(b) reveals a eutectic Si phase that appears as platelets.

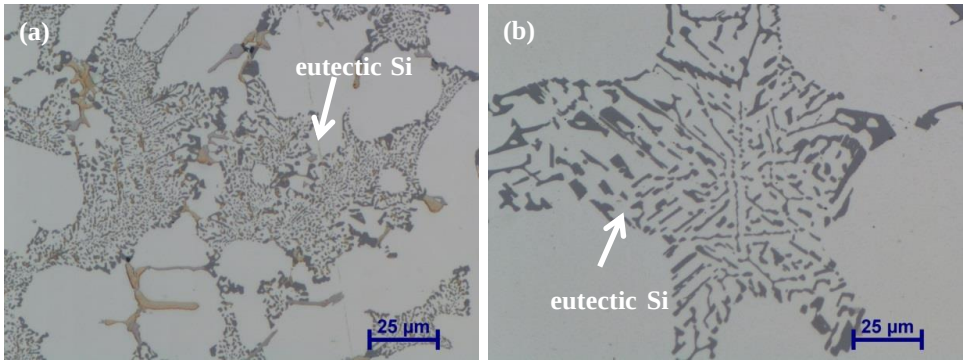

Figure 3-9: Optical micrographs showing eutectic Si microstructure in (a) Die casting, (b) Lost foam casting for alloy C

The distributions of eutectic Si phase as function of Feret diameter in DC and LFC alloy C are shown in Figure 3-8(a). Due to the differences in cooling rate between LFC and DC, the distributions of eutectic Si phase as function of Feret diameter are quite different from each other. On the one hand, more small eutectic Si particles, i.e. with a size between 1 and 13 µm, are distributed in DC alloy compared to LFC alloy. On the other hand, more large eutectic Si particles, which correspond to most of the surface fraction, were revealed in LFC alloy; the largest Feret diameter of eutectic Si can reach up to 141 µm in LFC compared to 32 µm in DC. In addition, the distributions of sphericity in Figure 3-8(b) show that at low cooling rate (i.e. LFC alloy), alloy C shows more Si particles with sphericity less than 0.3 than at high cooling rate (i.e. DC alloy). As shown in Figure 3-9, most of the eutectic Si present in DC appears with a fibrous morphology when the Sr content is 120 ppm in alloy C. However, the addition of the same Sr level to LFC AlSi7Cu3 alloy was less effective in modifying the morphology of eutectic Si from plate-like shapes to fibrous one at low cooling rate.

Eutectic Si particles modification was shown to depend not only on the cooling rate, but also on the Sr content. Besides the effect due to cooling rate is stronger than that due to Sr addition at higher cooling rate (i.e. SDAS=20µm).

3.2.1.4 Intermetallic compounds

The effect of Fe, Mn content and casting process on the formation of the Fe-rich intermetallic compounds was studied in alloys B, C, and D.

The size and morphology, i.e. maximum length and surface area fraction, of iron-intermetallics are listed in Table 3-3. Small size α-phase is extremely difficult to distinguish from β-phase as their shapes and gray levels are similar in 2D optical images as well as in BSE images. Thus the iron-intermetallics mentioned in this part include both α- and β-phases. The distributions of iron-intermetallics as functions of Feret diameter and sphericity for alloy B, C and D are presented in Figure 3-10(a) and (b). As can be seen from Figure 3-10(a), when the Fe and Mn content increases from 0.14% and 0.01% to 0.80% and 0.51%, the average size of iron-intermetallics increases from 5.6 μm to 15.8 μm. Figure 3-10(b) shows that surface fraction of iron-intermetallics with sphericity less than 0.3 increases with increasing content of Fe and Mn. It can be concluded that the amount of β-Al_5FeSi phase in needle-like shape increases with the Fe content increase in the alloys.

Table 3-3: Maximum length and surface area fraction of iron-intermetallics for alloys B to D

Alloy	**Fe (wt. %)**	**Mn (wt. %)**	**Mn/Fe**	**Casting process**	**Dimension and quantity of iron-intermetallics**	
					maximum length (μm)	Surface area fraction(%)
B	0.14	0.01	0.07	DC	23.2	0.22
C	0.49	0.13	0.26	DC	56.3	1.81
	0.30	0.19	0.63	LFC	245.5	2.32
D	0.80	0.51	0.64	DC	63.0	2.48

Table 3-4: EDX analysis of the intermetallic compounds in Figure 3-11

Alloy	**Number**	**Element content (at. %)**				**Identified phase**	**Measured stoechiometry**
		Al	Si	Mn	Fe		
B	1	62.97	24.76	0.34	11.93	Al_5FeSi	$Al_{5.2}FeMn_{0.03}$ Si_2
C	2	71.12	12.40	3.51	12.97	Al_{15} $(Fe,Mn)_3Si_2$	$Al_{11.5}Fe_2Mn_{0.5}Si_2$
	3	52.59	32.49	2.56	12.36	Al_5FeSi	$Al_{4.3}FeMn_{0.21}$ Si_2
D	4	60.90	26.03	4.06	9.02	Al_5FeSi	$Al_{6.7}FeMn_{0.45}$ Si_2
	5	71.52	11.86	6.93	9.69	Al_{15} $(Fe,Mn)_3Si_2$	$Al_{12}Fe_{1.6}Mn_{1.2}Si_2$

As shown in Table 3-3, the maximum length and the surface fraction of the iron-intermetallics increase as the iron and manganese content increases. All alloys exhibit almost linear relationships: the higher the iron and manganese content, the higher the surface fraction of the iron-intermetallics.

Figure 3-11(a)-(h) shows SEM micrographs of AlSi7Cu3 alloys with different Fe and Mn content, i.e. alloy B, C and D; the corresponding EDX microanalyses are shown in Table 3-4. Based on the EDX results and on the morphology of the phase, the observed phase can be specified as either α-Al_{15} $(Fe,Mn)_3Si_2$ or β- Al_5FeSi phase. As shown in Figure 3-11(a)-(h), α-phase (green arrow) can be identified from its script morphology (point 2 and 5) and β-phase (yellow arrow) from its acicular or plate-like morphology (point 1, 3 and 4). As seen from Figure 3-11(c), (g) and (h), alloy D, with the highest content of Fe and Mn, shows the largest surface fraction of iron-intermetallic compounds,

which mainly consists in the β-phase with the needle-like morphology (Figure 3-11(g)), and in some α-phase (Figure 3-11(h)). Figure 3-11(a) and (d) show that in alloy B, with the lowest content of Fe and Mn, only a few amount of small size β-Al_5FeSi phase with its typical needle-like morphology is observed. A higher fraction of iron-intermetallic compounds is detected in alloy C, with intermediate Fe content and a Mn to Fe ratio of 0.26, as compared to alloy B. Besides the addition of Mn promotes the formation of script α-phase $Al_{15}(Fe,Mn)_3Si_2$ (Lu and Dahle 2005). Figure 3-11(a), (b) and (c) show that the ratio of α to β phases increases as the Mn/Fe ratio increases from alloy B to alloy D.

The influence of the cooling rate on distributions of iron-intermetallics as functions of Feret diameter and sphericity can be observed in Figure 3-10(a) and (b). Optical micrographs show the β platelets (arrowed) in the microstructure of alloy C in both DC (Figure 3-12(a)) and LFC (Figure 3-12(b)). For the LFC alloy C, large size intermetallics (i.e. Feret diameter larger than 50μm) with small sphericity represent most of the total volume fraction of the intermetallics phase. The maximum length of iron-intermetallic compounds increases from 56.3 μm to 245.5 μm when the cooling rate decreases from 30°C/s (DC) to 0.8°C/s (LFC), respectively (Table 3-3). Moreover, the surface area fraction of the iron-intermetallics also increases from 1.81% in DC alloy to 2.32% in LFC alloy (Table 3-3**)**.

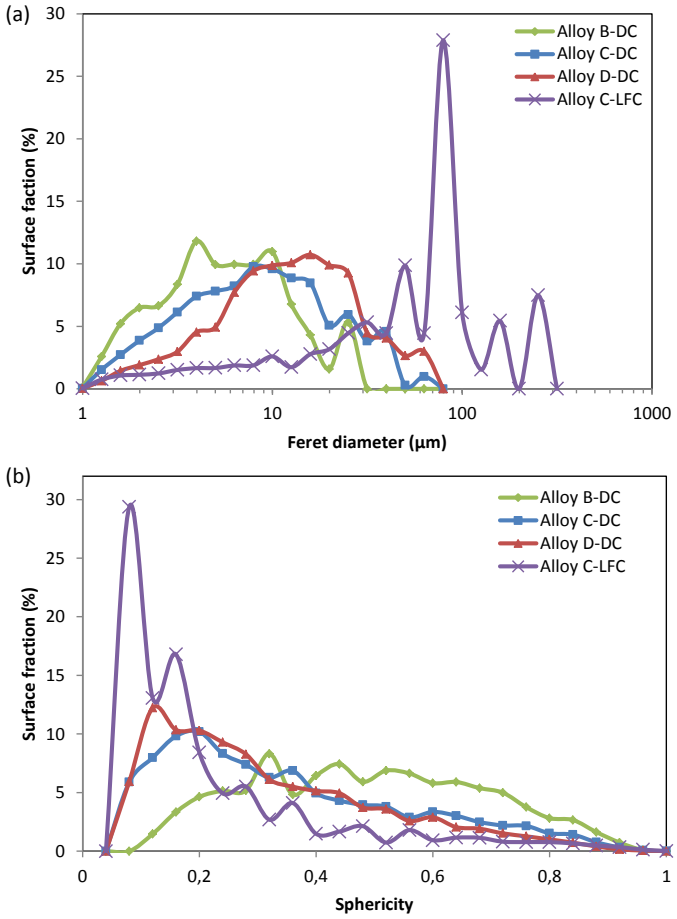

Figure 3-10: Distributions of iron-intermetallics as functions of Feret diameter (a) and sphericity (b) in alloy B, C and D

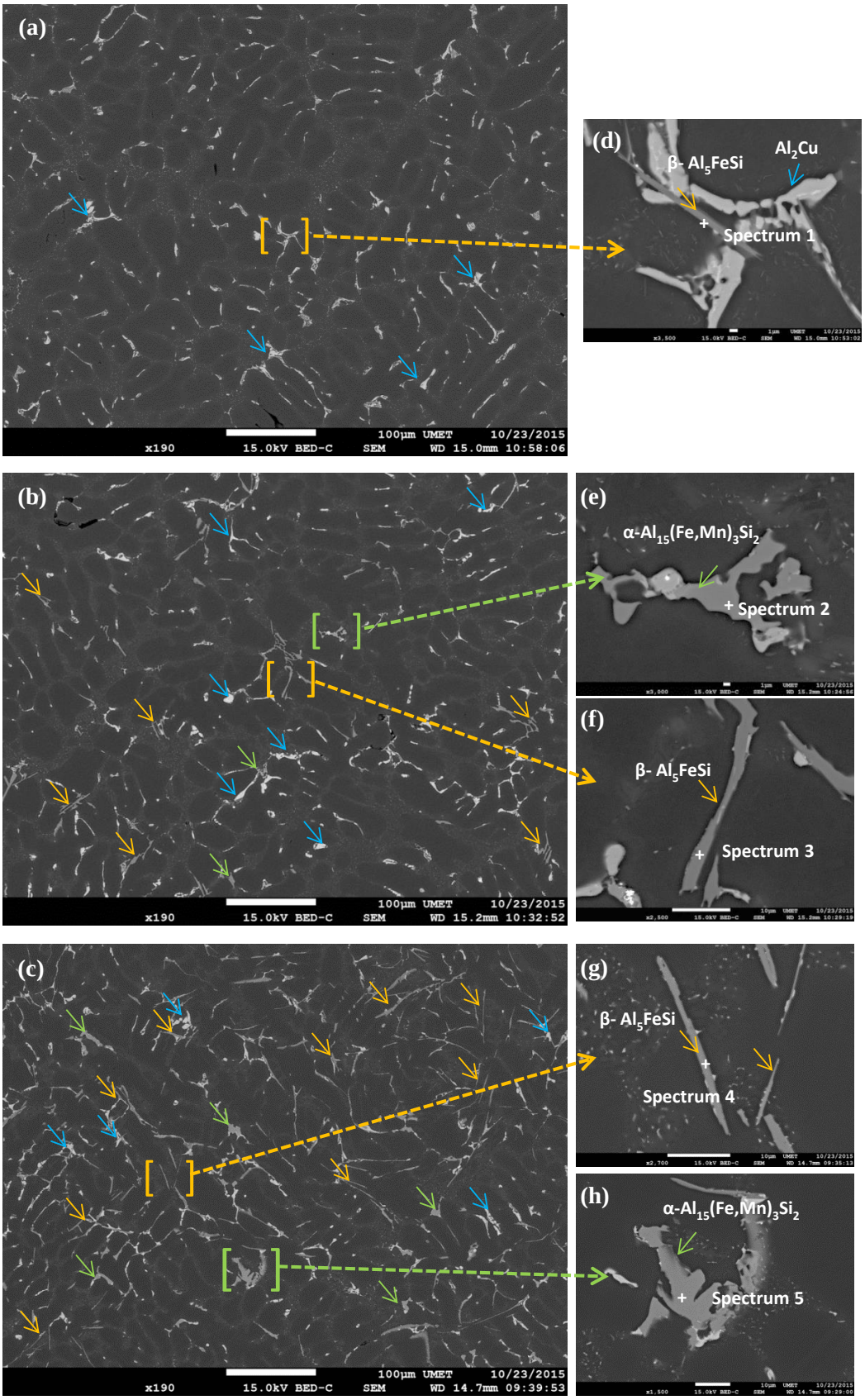

Figure 3-11: BSE SEM micrographs showing the distribution of α-phase Al_{15} $(Fe,Mn)_3Si_2$ (green arrow), β-phase Al_5FeSi (yellow arrow) and Al_2Cu phase (blue arrow) in the (a) alloy B, (b) C and (c) D. Points of EDX microanalysis are labeled, and the results are available in Table 3-4

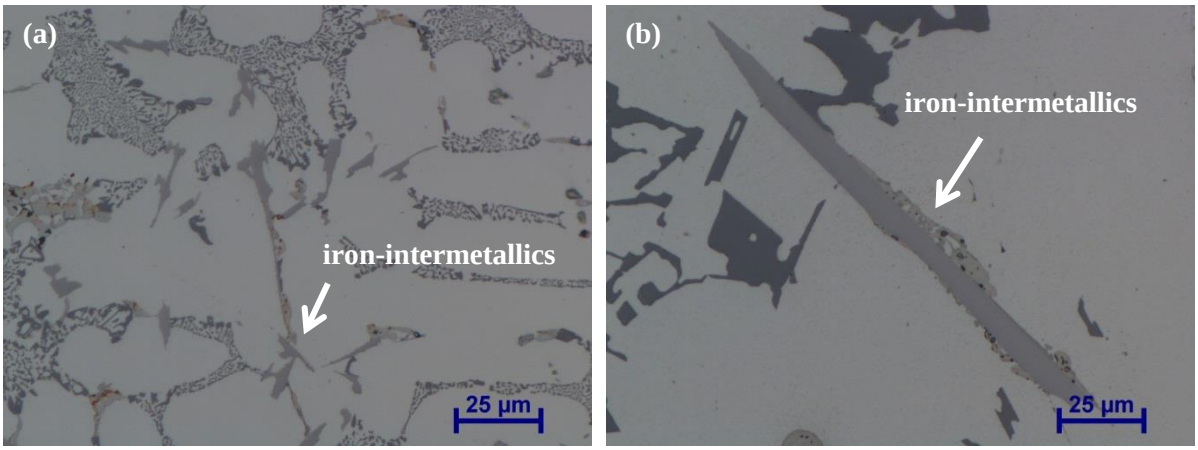

Figure 3-12: Optical micrographs showing iron-intermetallics in (a) DC, (b) LFC for alloy C

3.2.1.5 Copper based phase

Cu-bearing particles were also detected in the studied alloys. As shown in Figure 3-11(d), the Al_2Cu phase connects with the iron intermetallics so that it can be reasonably assumed that the β-platelets act as nucleation sites for the copper phase particles (Li, Samuel et al. 2003).

In this work, the quantitative metallography analysis shows that alloying elements (such as Sr, Fe and Mn) and casting process have no obvious effect on the amount of Al_2Cu phase. However, it was found that higher amount of iron-intermetallics reduces the max size of Al_2Cu phase, and that the density of the Al_2Cu particles increases with an increase of iron-intermetallics resulting from higher Fe content (Table 3-5). This result indicates that the increase of iron should favor multiple nucleation of Al_2Cu phase hence inducing smaller Al_2Cu particles.

Table 3-5: Parameters of Al_2Cu phase in four alloys

Alloy	Casting process	Max. Feret diameter (µm)	Surface fraction (%)	Density (particles/mm²)
A	DC	39	1.20	2212
B	DC	45	1.27	2116
C	DC	31	1.30	2946
	LFC	69	1.27	1196
D	DC	27	1.33	3136

In addition, some researchers (Djurdjevic, Stockwell et al. 1999) (Samuel, Samuel et al. 1996) reported that the presence of Sr leads to an increase in the amount of the Al_2Cu phase that precipitates in the blocky form rather than in the fine eutectic form. However, in the present work, we found that it is difficult to distinguish and quantitatively analyze the blocky Al_2Cu phase and eutectic Al_2Cu phase using image processing of optical micrographs. The reason may be the high cooling rate that induces fine microstructural features including Al_2Cu phase in the studied alloys.

The cooling rate resulting from different casting process can significantly affect the formation of Al_2Cu phase. The distributions of Al_2Cu as functions of Feret diameter and sphericity in DC and LFC for alloy C are reported in Figure 3-13(a) and (b). The LFC alloy with the lower cooling rate presents larger Al_2Cu particles, which correspond to most of the surface fraction (Figure 3-13(a)). Figure 3-13(b) shows that more Al_2Cu phase with sphericity above 0.3 is present in DC alloy compared to LFC alloy. Thus, the morphology of Al_2Cu phase becomes rounder with an increase in the cooling rate.

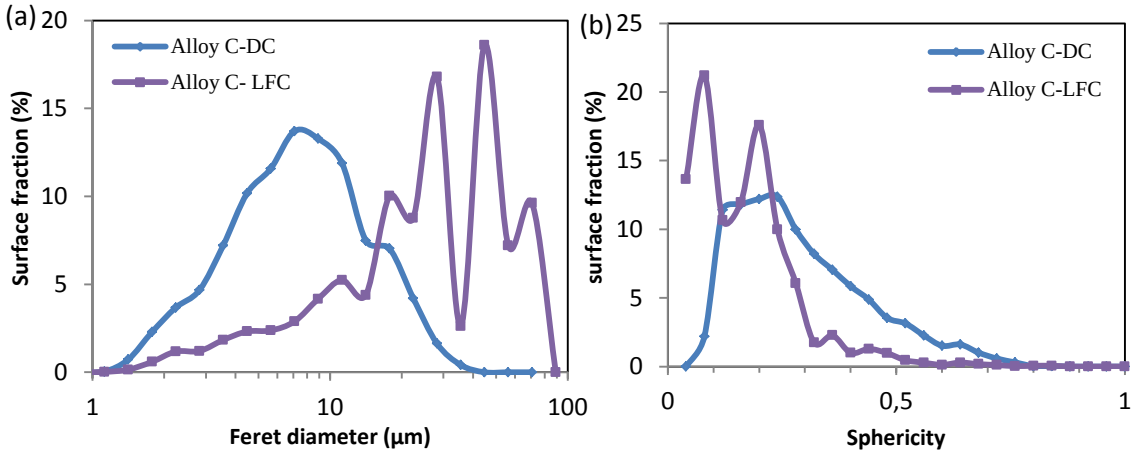

Figure 3-13: Distributions of Al_2Cu as functions of Feret diameter (a) and sphericity (b) in DC and LFC for alloy C

3.2.2 Thermal analysis

In order to better understand the microstructure developed with different alloying elements content during solidification, thermal analyses coupled with microstructure observation were performed on the four alloys (see §2.2.1, Table 2-1). In this part, the evolution of microstructures during solidification of the standard Al-Si-Cu alloy (i.e. alloy C), and the effect of Sr, Fe and Mn content on the solidification reaction of Al-Si-Cu alloy were studied.

3.2.2.1 Solidification Reaction and Sequence of the Al-Si-Cu alloy

Figure 3-14 shows the cooling curve and its first derivative, with an average cooling rate of approximately 0.13 °C/s, obtained during the solidification of the sample alloy C (i.e. A319 alloy), which is the standard chemical composition used for the cylinder heads at PSA. Five peaks were observed in the first derivative curve, marked 1 to 5, which correspond to thermal events that occurred during solidification of the alloy.

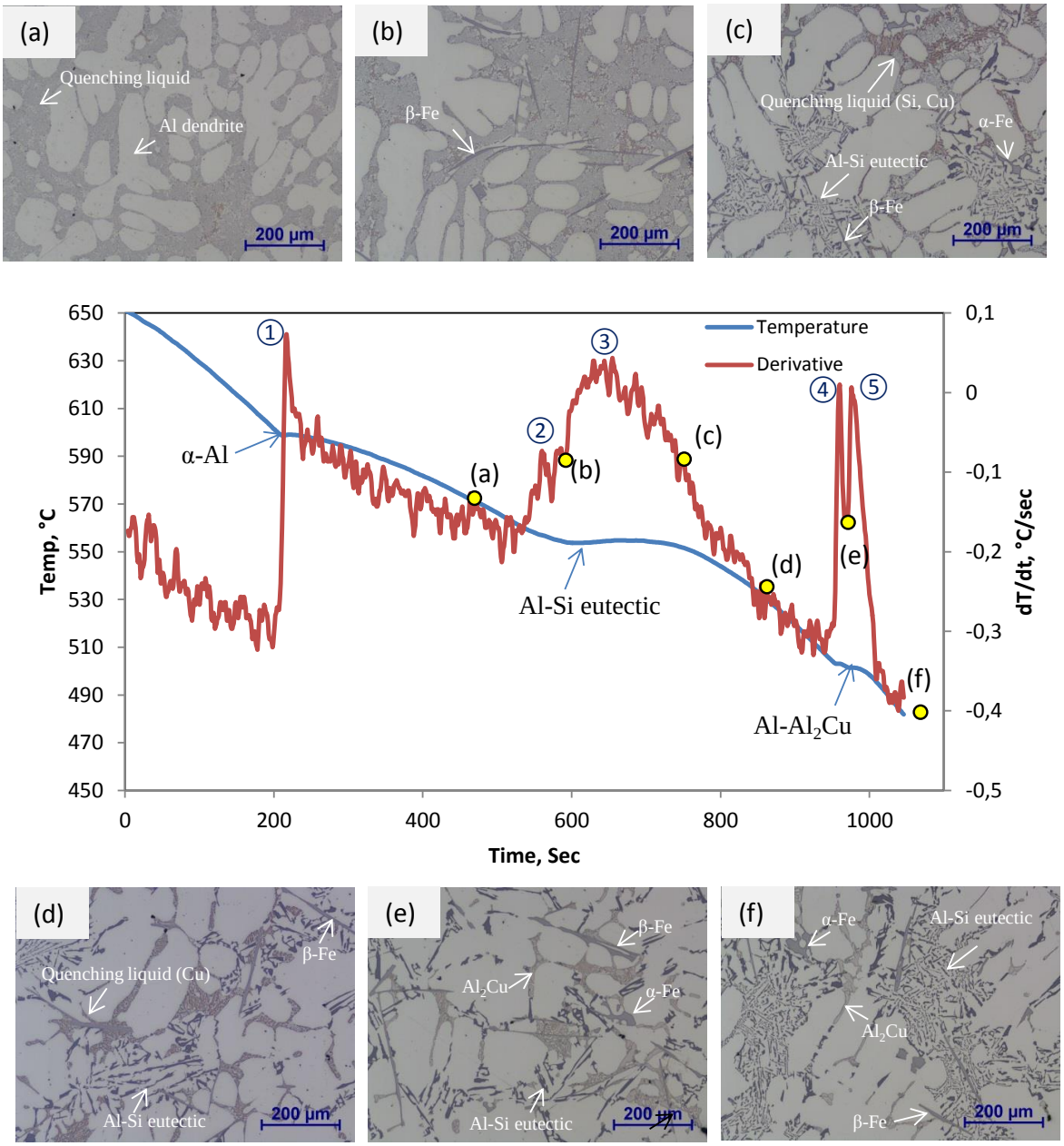

Figure 3-14: Solidification curve and its first derivative of A319 alloy C and optical micrograph after interrupted quenching at different temperatures: (a) 560°C, (b) 554°C, (c) 547°C, (d) 520°C, (e) 502°C and (f) full solidification

In order to determine whether these peak-like fluctuations are associated with precipitation of any phase and to link the peaks to reactions that happened during solidification, a series of interrupted water-quenching test were performed at different stages of the solidification of the alloy C. Subsequent observation by OM and SEM of the quenched microstructures is performed to study the solidification reactions and sequence.

The yellow points, i.e. from (a) to (f), in the first derivative curve represent the quench tests performed on the sample, and the corresponding metallographic microstructures are shown in Figure 3-14(a)-(f).

In the sample quenched at 560°C, only Al dendrites were observed in Figure 3-14(a), thus the first solid phase formed is the primary aluminium dendrites at peak 1. Nucleation temperature of α-Al is about 603°C. Figure 3-14(b) shows that the iron-intermetallic phase, β-Al_5FeSi, was found in the sample quenched at 555°C, therefore, Peak 2 in first derivative curve indicates the nucleation temperature of β-Fe phase at 560°C. In the sample quenched at 547°C (Figure 3-14(c)), eutectic Si and α-Fe phases were observed. As some water-quenched structures which contain Si and Cu elements could still be found, the formation of eutectic Si phase was not completely finished, and the Al_2Cu phase has not yet been precipitated. Therefore, Peak 3 indicates the main Al–Si eutectic reaction. The microstructure of a sample quenched at 520°C in Figure 3-14(d) reveals that almost all the eutectic silicon phase was formed. Two reaction peaks were observed on the first derivative at 505°C and 502°C. Peak 4 is related to the nucleation temperature of Al_2Cu phase as confirmed by microstructural study of quenched sample. As seen from the Figure 3-14(e), Al_2Cu phase was found in the sample quenched at 502°C but some quenching liquid structure could still be observed.

In order to determine the reaction that occurs in Peak 5, the microstructures in the samples quenched at temperatures immediately before and after peak 4, after peak 5, respectively, have been compared and identified using SEM-EDS in Figure 3-15. The different points marked as 1, 2, 3, 4 and 5 have been identified and their chemical compositions are given in Table 3-6. The EDS analysis was acquired in the spot mode in a small area around the point.

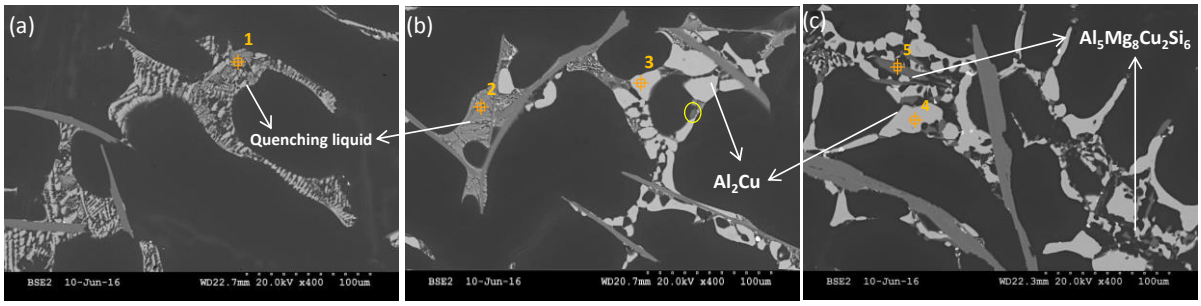

Figure 3-15: BSE micrograph of the sample quenched at temperature (a) before peak 4 and immediately after (b) peak 4 and (c) peak 5

Table 3-6: EDX analysis of the phases in Figure 3-15

Sample	Number	Element content (at %)				Identified phase	Measured stoechiometry
		Mg	Al	Si	Cu		
Quenched before peak 4	1	3.10	77.89	6.46	11.68	--	--
Quenched after peak 4	2	3.60	76.50	8.02	11.88	--	--
	3	-	71.29	1.09	27.62	Al_2Cu	$Al_{2,5}Cu$
Quenched after peak 5	4	-	70.98	1.35	27.67	Al_2Cu	$Al_{2,5}Cu$
	5	36.38	20.73	34.31	8.59	$Al_5Mg_8Cu_2Si_6$	$Al_{4,8}Mg_{8,4}Cu_2Si_8$

In the sample quenched before Peak 4, the quenching liquid structure was detected (as shown in Figure 3-15(a)), the EDX analysis revealed that this structure in point 1 contains some Mg, Al, Si and Cu with concentration of Mg and Cu between 3 to 4 at.% and 11 to 12 at.%, respectively. Figure 3-15(b) and (c) show the microstructures of sample quenched after peak 4 and 5, respectively, a white phase identified by EDX at points 3 and 4. According to the chemical composition given by the spectrum analysis (Table 3-6), this phase corresponds to the Al_2Cu phase. Thus, Peak 4 in Figure 3-14 indicates the formation of Al_2Cu phase at 505 °C. In the sample quenched after Peak 5, EDX analysis revealed that the structure in point 5 (see Figure 3-15(c)) consists of Mg, Al, Si and Cu, and that its stoichiometry corresponds to the $Al_5Mg_8Cu_2Si_6$ phase (Shabestari and Ghodrat 2007).

However, in the sample quenched after Peak 4, some liquid structures (point 2 in Figure 3-15(b)) still exist and also contain some Mg, Al, Si and Cu with similar chemical composition as point 1 in Figure 3-15(a). Thus, the comparison of the microstructures of samples quenched after peak 4 and peak 5 (Figure 3-15(b) and(c)), and the presence of significant Mg and Cu in the remaining liquid of sample quenched after Peak 4 allow to conclude that Peak 5 is associated with the formation of $Al_5Mg_8Cu_2Si_6$ phase. It should be mentioned that a very small amount of $Al_5Mg_8Cu_2Si_6$ phase was also observed in the sample quenched after Peak 4 (see the yellow circle in Figure 3-15(b)). The proximity between the two reaction Peaks for the formation of Al_2Cu and $Al_5Mg_8Cu_2Si_6$ phases and the uncertainty in the interrupted quenching temperature may be an explanation.

A fully solidified structure was observed in the sample quenched after peak 5 (i.e. at 480°C), see Figure 3-14(f), consequently, the solidification process can be assumed to terminate between 502°C and 480°C.

3.2.2.2 Effect of strontium on Al–Si eutectic reaction

Figure 3-16(a) depicts three thermal analysis cooling curves, with a cooling rate of approximately 0.13°C/s, obtained from melts with 47 and 130 ppm strontium (i.e. alloy A, B and C).

The cooling curves corresponding to the eutectic region for alloys containing different Sr levels are shown in Figure 3-16(b). Al–Si eutectic growth temperature T_G, which is the maximum temperature of the eutectic Peak as shown in Figure 3-16(b), is an important characteristic temperature in solidification of Al–Si alloys. It has been reported that the depression of the eutectic growth temperature is an acceptable criterion for the evaluation of eutectic modification level (Djurdjevic, Jiang et al. 2001) (Chen, Geng et al. 2006). The larger magnitude of depression is associated with a higher level of modification.

As shown on the cooling curve in Figure 3-16(b), the Sr addition increase leads to the depression of the growth temperature of eutectic reaction from 558.2°C (for 47 ppm Sr) to 556.0°C (for 120 ppm Sr).

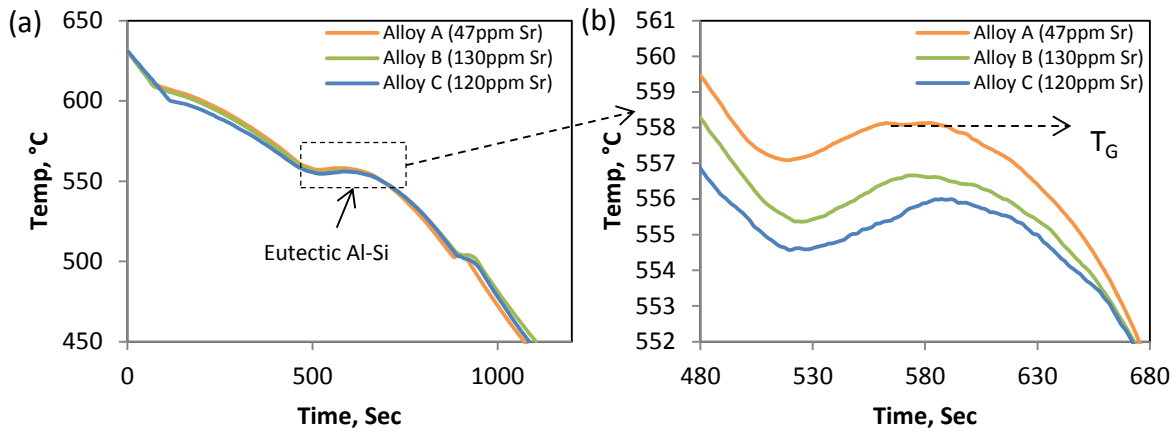

Figure 3-16: (a) Cooling curves of alloys with different Sr content (i.e. alloy A, B and C) with (b) the magnification of area related to Al–Si eutectic formation

3.2.2.3 Effect of iron and manganese on the formation of intermetallic compounds

Figure 3-17(a) shows the temperature derivatives measured during solidification for alloy C and alloy D, which contain different Fe and Mn content. Figure 3-17(b) and (c) show the microstructures of the quenched samples at 560°C (i.e. the temperature immediately after the arrowed Peak) for the two alloys. Only Al dendrites and quenching liquid structures were observed in alloy C. However, in alloy D, which has 0.8 wt. % Fe and 0.51wt. % Mn, both α and β phases were observed prior to the eutectic Si as shown in Figure 3-17(c).

Comparing the microstructures of the alloy C quenched at the temperatures immediately before and after Peak 2 in Figure 3-17(b) and Figure 3-17(c), it can be concluded that the increase of Fe and Mn content shifts the precipitation sequence of α and β phases toward a higher temperature. The Peak (dotted arrow in Figure 3-17(a)), which represents the formation of iron-intermetallic in alloy C is less significant and occurs at a lower temperature than in the alloy D with high Fe and Mn addition.

In addition, the temperature of nucleation of α-Al dendrite is observed to increase from 600°C to 605°C from alloy C to alloy D, and the reason will be discussed in the following section.

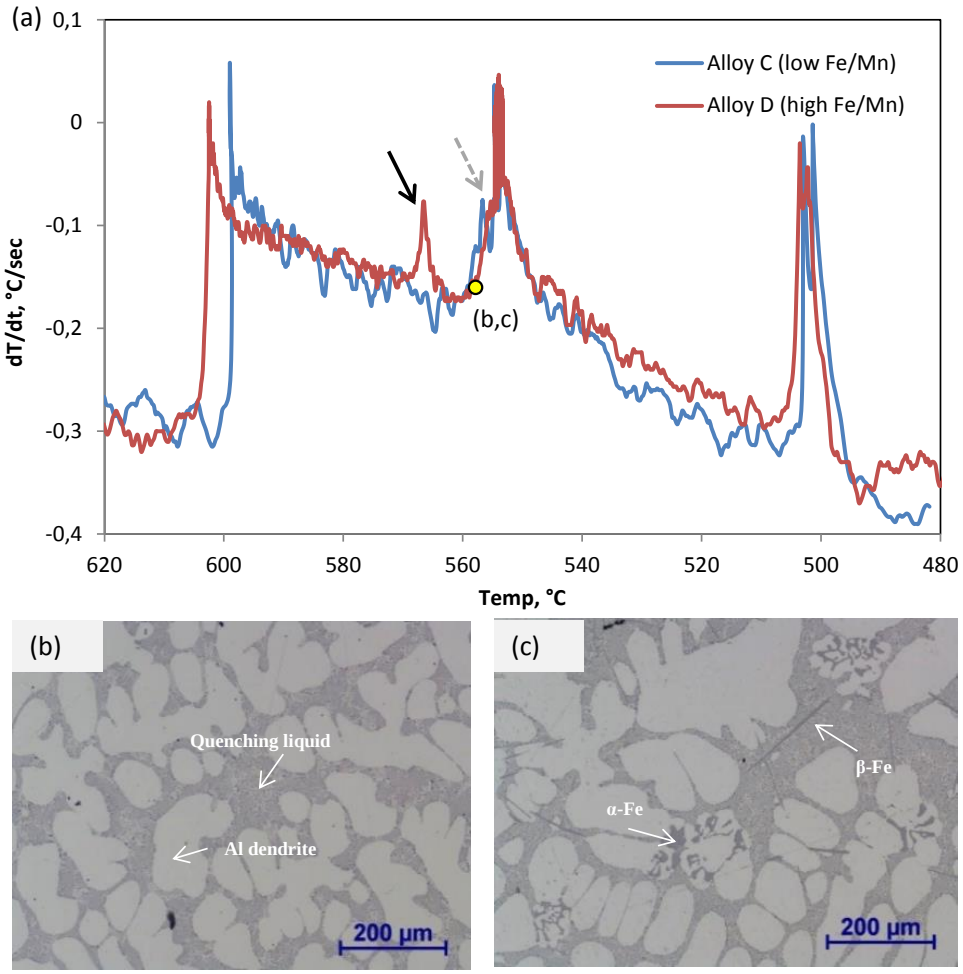

Figure 3-17: Temperature derivatives measured from the melts with different Fe/Mn addition. Microstructures of samples quenched at 560°C for (b) alloy C and (c) alloy D

3.3 Discussion

3.3.1 Phase formation in Al–Si–Cu alloy

The first derivative of the cooling curve clearly reveals peaks which correspond to the phase reactions during the solidification. Based on the microstructural observation of the quenched and fully solidified samples, the possible reactions corresponding to each individual peak were identified and all possible solidification reactions and sequences were summarized in Table 3-7.

Table 3-7: Reactions occurring during solidification of studied Al-Si-Cu alloys

Peak	Solidification reactions	Approximate temperature, °C
1	(Al) dendritic network	600-611
2	Precipitation of α/β-Fe phases	560-568
3	Precipitation of eutectic Si	556
4	Precipitation of Al_2Cu	505
5	Precipitation of $Al_5Mg_8Cu_2Si_6$	502

The solidification of the studied Al-Si-Cu alloy can be described as follows:

1) A primary α-aluminium dendritic network forms between 600-611°C. The exact temperature depends mainly on the amount of Si and Cu in the alloys. As shown in Figure 3-16, the temperature of nucleation of α-Al dendrite increases from 600°C to 604°C when the Si and Cu content decreases from 7.66 wt. % and 3.67 wt. % (alloy C) to 7 wt. % and 3.45 wt. % (alloy D), respectively. This is in good agreement with the results reported by (Canales, Talamantes-Silva et al. 2010) and (Đurđević and Manasijević 2014). When the Si and Cu content increases in Al-Si-Cu alloys, the nucleation temperature of α-aluminium decreases.
2) At approximately 568°C, the iron-intermetallics, including α-Fe and β-Fe phases, begin to precipitate in the high Fe/Mn level alloys. Experimental studies have demonstrated that the formation of the intermetallic compounds is influenced by the Fe and Mn content. At low Fe/Mn level (alloy C), the temperature for precipitation of iron-intermetallics is reduced to 560°C.
3) At approximately 556°C, the Al-Si eutectic phase begins to precipitate.
4) At approximately 505°C, the Al_2Cu phase forms.
5) At approximately 502°C, a fine $Al_5Mg_8Cu_2Si_6$ phase forms. This phase grows close to the eutectic Al_2Cu phase.

It should be noted that the cooling rate can influence the temperatures at which reactions occur (Shabestari and Malekan 2005). The cooling rate for the thermal analysis used in the present work (0.13°C/s) is slower than for LFC (0.15-0.8°C/s), thus maybe it is more interesting to perform thermal analysis at the cooling rates of LFC and DC in the future work, although it is more difficult to obtain.

3.3.2 The effect of Sr addition

- **Eutectic Si**

The data obtained from the thermal analysis (Figure 3-16), as well as microstructural analysis for DC alloy A and B (Figure 3-8), show that the addition of strontium decreases the aluminium-silicon eutectic growth temperature (T_G) and changes the degree of silicon modification.

Such results are in good agreement with several published papers (Shabestari and Ghodrat 2007) (Zamani and Seifeddine 2016). The effect of strontium as a modifying agent on the microstructure of gravity die cast Al–Si alloys is widely reported in literature (Hegde and Prabhu 2008) (Dahle, Nogita et al. 2005). The addition of Sr promotes the formation of a fibrous silicon structure by retarding the growth rate of silicon. It has been suggested that Sr restricts the growth of Si, acting as an impurity atom which poisons the growing layers (Makhlouf and Guthy 2001).

- **Porosity**

Sr addition can also introduce more pores in the DC alloy as confirmed in this work. The addition of Sr changes the amount of porosity as already reported by several studies (Dinnis, Dahle et al. 2004) (Emadi, Gruzleski et al. 1993) (Liu, Samuel et al. 2003) due to a complex interaction of different parameters. (Liu, Samuel et al. 2003) explain the increased porosity level with the content of Sr by the formation of strontium oxides due to the high affinity of strontium for oxygen; these strontium oxides are frequently observed associated with microporosity in Sr-modified alloys. (Emadi, Gruzleski et al. 1993) reported that the addition of Sr can reduce the surface tension, an effect that can facilitate porosity formation and result in increased porosity. (Argo and Gruzleski 1988) indicate that interdendritic feeding becomes more difficult in modified alloys as they have a longer mushy zone due to the depression of the eutectic temperature. Consequently, more pores may form over a longer period, which explains the larger microshrinkage cavities observed in alloy B.

3.3.3 The effect of Fe and Mn content

- **Intermetallic compounds**

From the results shown in § III.3.2.1.4, it is clear that, with the increase of Fe and Mn content, the total amount and size of the iron-intermetallics is increased, and the ratio of α to β phases also increases as the Mn/Fe increases because part of the Fe and Mn in the melt precipitates as a new Chinese script–like phase (i.e. α-Al_{15} $(Fe,Mn)_3Si_2$), prior to the eutectic Si. This is clearly observed in the quenched sample in Figure 3-17(c). Therefore, Mn is expected to suppress the formation of the plate-like β phase and promote the more compact, less harmful α phase (Lu and Dahle 2005).

Comparing the microstructures of quenched samples for alloy C and D in Figure 3-17(b) and (c), both α and β phases were observed in the fully solidified samples of the two alloys. However, α and β phases observed in the sample with higher Fe and Mn (i.e. alloy D) form earlier at a higher temperature; increasing the Fe and Mn content shifts the precipitation sequence of the α and β phases toward a higher temperature. Similar results were reported by (Lu and Dahle 2005). Thus, the longer time available for growth of iron-intermetallic at high Fe alloy may also explain the larger size of intermetallics present.

In addition, it was found that the increase of iron-intermetallics resulting from higher Fe content can induce more and smaller Al_2Cu particles. The β-platelets may act as nucleation sites for the copper phase particles (Li, Samuel et al. 2003)as confirmed by the observation in Figure 3-11(d).

- **Porosity**

Fe and Mn content can also affect the porosity in the DC alloy. In this work, both the 3D characterization and 2D X-ray radiography characterization for pores in the alloys with different Sr content showed that an increase of Fe and Mn content results in a decrease of porosity level in some extent. However, this result is in contradiction with some reports (Moustafa 2009) (Dash and Makhlouf 2001) that claim iron-intermetallics help nucleate pores. Studies made by (Taylor, Schaffer et al. 1999) and (Dinnis, Taylor et al. 2006) indicate the existence of a critical Fe content for a minimum porosity formation in unmodified Al-Si-Cu alloy, and report that different solidification paths resulting from different Fe levels lead to variations in microstructural permeability, i.e. interdendritic feedability, and hence in porosity formation. At Fe levels above a critical point, the β-phase is already well developed when ternary eutectic solidification commences, whereas at lower Fe levels, the β-phase forms as a component of the ternary AlSiFe eutectic only after the binary Al-Si eutectic is formed. In both cases, binary β-phase blocks the interdendritic regions, leading to a higher porosity level in castings. However, at the critical Fe content, the ternary eutectic consists of small ternary β-platelets that nucleate many fine Al–Si eutectic, this results in improved feeding through the most open and permeable dendritic structure, thereby minimizing porosity. However, the nucleation of eutectic Si on β-phase is not generally admitted and no evidence of such a role of β-phase was observed in (Lu and Dahle 2005). Besides, (Puncreobutr, Lee et al. 2012) found that larger pores were observed to nucleate before the intermetallics during in-situ solidification of an A319 alloy at 0.36°C/s. Thus, maybe it would be more interesting to study the influence of Fe content on the porosity formation through in-situ solidification experiments.

Although (Lu and Dahle 2005) reported that addition of Mn causes no significant change in casting porosity level, the present work may agree with the study of (Dinnis, Taylor et al. 2004) and suggests that the addition of Mn can also reduce the amount of porosity. Ideed, Mn additions reduce the poisoning of Al-Si eutectic nucleation sites by Fe and this leads to the formation of a greater number of smaller Al-Si grains during solidification and in turn results in improved permeability and feeding, hence a reduction in porosity. According to (Dinnis, Taylor et al. 2004), the addition of 0.5%Mn to a 1%Fe-containing Al-9%Si alloy can reduce porosity levels to those obtained in the same alloy with 0.6%Fe (i.e. the critical iron content for that composition).

Moreover, as mentioned before, the decrease of Sr content from 130 ppm to 100 ppm also can contribute to the slight decrease of porosity fraction for alloy B, C and D.

3.3.4 The effect of casting process

The cooling rate resulting from different casting process has a marked effect on the size, morphology, and distribution of all the microstructural constituents.

- **SDAS**

As shown in Figure 3-1, the size of the dendrites appears strongly affected by the casting process (i.e. cooling rate): the DC alloy with a high cooling rate shows a smaller size of dendrite than LFC alloy with low cooling rate. This result is in agreement with previous work on the relationship of cooling rate with the dendrite arm spacing (Dobrzański, Maniara et al. 2007) (Pavlović-Krstić, Bähr et al. 2009) (Rui, SHI et al. 2014). SDAS is determined by solidification time through the mushy zone, with longer solidification time resulting in larger values of SDAS (Pavlović-Krstić, Bähr et al. 2009).

- **Eutectic Si**

Figure 3-8 and Figure 3-9 clearly demonstrated that the higher cooling rate in DC results in smaller eutectic Si particles than in LFC alloy. In accordance with previous findings (Dobrzanski, Maniara et al. 2007), casting process appears to have a significant impact on eutectic modification for AlSi7Cu3 alloy. The reason for the cooling rate refinement of eutectic Si-particles can be explained based on the surface energy of the Al-Si solid interface (Makhlouf and Guthy 2001). This theory suggests that the rate of advance of the interface depends on a balance between the rate of heat flow from the liquid to the solid through the interface and the latent heat of fusion released during solidification. The difference between the magnitude of the thermal conductivity of pure Al and pure Si and the difference between the magnitude of the latent heat of fusion of pure Al and pure Si are large; Al will solidify much faster than Si. Thus, Al gains a lead during solidification of the eutectic as shown in Figure 3-18(a). The higher cooling rate intensify the lead of Al over Si, thus lead to complete encasement of the lagging Si crystal by the advancing Al as depicted in Figure 3-18(b) and(c). This theory can account for the formation of the modified eutectic structure at high cooling rates.

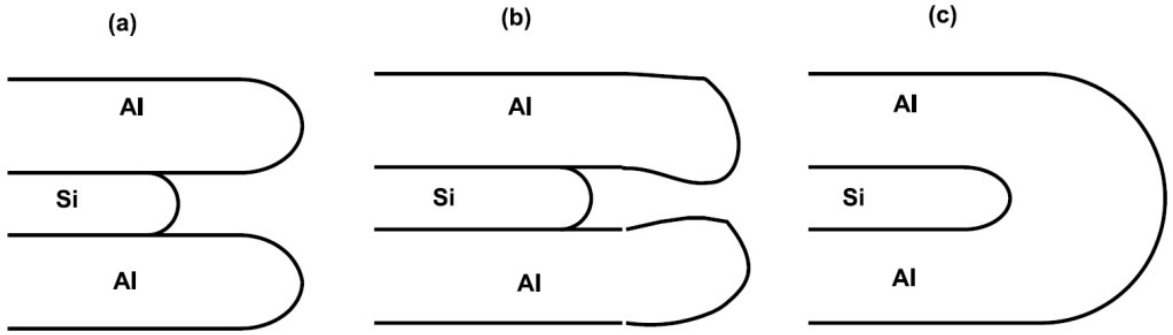

Figure 3-18 Eutectic solidification in unmodified chill cast Al–Si alloys (Makhlouf and Guthy 2001).

- **Intermetallic compounds**

As presented in §3.2.1.4, the size of intermetallic compounds (i.e. iron- intermetallic and Al_2Cu phase) is strongly affected by the cooling rate. Larger sizes of iron-intermetallics were observed in LFC alloy at lower cooling rate as compared to the DC alloy as shown in Figure 3-12; this observation is supported by quantitative measurements of iron-intermetallics (see Figure 3-10).

The longer time available for growth of iron-intermetallic at lower cooling rate may explain the larger size of intermetallics in LFC alloy. As reported by (Ceschini, Boromei et al. 2009), the size of intermetallic compounds mainly depends on the solidification time (i.e., cooling rate).

In this work, the quantitative metallography analysis shows that alloying elements (such as Sr, Fe and Mn) have no effect of the amount and morphology of Al_2Cu phase.

However, the cooling rate resulting from different casting process can significantly affect the formation of Al_2Cu phase (see Figure 3-13). The Al_2Cu phase in LFC alloy at low cooling rate is larger and coarser as compared to the DC alloy at high cooling rate. Indeed, at increasing cooling rate, an increased nuclei number could affect the number, and thus, the size and morphology of the Al_2Cu phase precipitates (Labisz, Krupiński et al. 2009).

The longer time available for growth of iron-intermetallic at lower cooling rate may explain the larger size of intermetallics.

- **Porosity**

The effect of casting process (DC vs. LFC) on the porosity in Al-Si alloy was also investigated in this work. As shown in the results presented in §3.2.1.2, the amount and size of pores in LFC alloy become larger compared to the DC alloy. The significant difference in porosity content and size between DC and LFC alloys can be explained by the different cooling rate during solidification. With increasing solidification rates, hydrogen has less time to diffuse into the interdendritic spaces of the partially solidified metal (Seifeddine and Svensson 2013), resulting in more finely dispersed porosity. Furthermore, the higher temperature gradients present at higher solidification rates tend to limit the length of the mushy zone, making feeding easier and retarding porosity formation (Emadi and Gruzleski 1995).

3.4 Conclusions

In this chapter, five batches of AlSi7Cu3 alloy with different alloying elements (Sr, Fe and Mn) contents and two different casting processes (DC and LFC) were used. Microstructural characterizations were performed to study the effect of Sr, Fe and Mn content and casting process on the microstructure of DC Al-Si-Cu alloy; the evolution of microstructures during solidification of the Al-Si-Cu alloy was investigated by thermal analysis and interrupted quenching test. The effect of Sr, Fe and Mn content on the solidification reaction and sequence of the Al-Si-Cu alloy were studied. The following conclusions are highlighted from the work:

- **Sr addition**

Increase of strontium addition slightly depresses the growth temperature of eutectic Si phase, a finer and more fibrous eutectic Si structure can be obtained with an increased Sr content. However, the modification effect of Sr is not significant at high cooling rate (such as DC alloy), and the Sr addition can also introduce more pores in the DC alloy.

- **Fe and Mn content**

Increasing the Fe/Mn level shifts the precipitation sequence of the α+β phase toward a higher temperature. At higher Fe/Mn level, the majority of α+β phase precipitates prior to the eutectic Si. However, at low Fe/Mn level, the majority of α+β phase is expected to form at a lower temperature which is close to the eutectic Si precipitation.

The size, morphology and surface fraction of iron-intermetallics are influenced by the Fe and Mn content, i.e. the size and amount of Fe-intermetallics (α-$Al_{15}(Fe,Mn)_3Si_2$ and β-Al_5FeSi phase) increase with an increase in the Fe-Mn level. Mn additions result in an increased amount of the α-Fe phase and the ratio of α and β phase increases with the increase of Mn/Fe in the alloys. Besides, the higher Fe content can introduce more and smaller Al_2Cu particles. However, the amount of Al_2Cu phases also depends on the Cu content, which is not exactly the same in the four alloys.

In addition, a slight decrease of pores volume fraction is observed with the Fe and Mn content increase in some extent for the DC Al-Si-Cu alloys.

- **Casting process**

The different cooling rates that result from the different casting processes (i.e. DC and LFC) play an important role on all microstructural features in size and morphology.

The cooling rate has a dominant impact on SDAS: increasing the cooling rate decreases significantly the SDAS. The cooling rate is also of great importance to the modification of eutectic Si: finer eutectic Si particles can be achieved at high cooling rate. The amount, size and morphology of intermetallic compounds are affected by the cooling rate. Compared to the DC alloy, the LFC AlSi7Cu3 alloy shows more casting defects (i.e. larger pores and microshrinkage cavities) and a coarser microstructure (i.e. larger SDAS, plate-like eutectic Si particles, needle-like iron-intermetallics).

Besides, the thermal analyses also show that the temperature for the nucleation of aluminium dendrites depends on the amount of Si and Cu. It was also found that the chemical composition of the alloys has also some effect on the SDAS, which slightly decreases with the incremental addition of Sr, Fe and Mn.

4 Chapter 4 The influence of Sr, Fe and Mn content and casting process on the mechanical properties and damage mechanisms of Al–Si based alloys

Contents

4.1 Introduction

The microstructures resulting from different Sr, Fe and Mn content and casting process play an import role on the mechanical properties and damage mechanisms of Al–Si based alloys.

In this part, firstly, conventional tensile tests performed on the studied alloys are analyzed to investigate the influence of different features such as intermetallic particles, Si particles and pores on the mechanical properties of Al–Si-Cu alloys.

In addition, in order to study the role of Fe-rich intermetallics on the damage mechanisms of Al–Si-Cu alloy on a microstructural level, a DIC method, which is described in Chapter 2, was performed on two Al–Si-Cu alloys: a high-Fe alloy and a low-Fe alloy. DIC allows measuring strain at the microstructure scale using image acquisition during the tensile test. Finally, the fracture surfaces of the tensile specimens were analyzed using SEM-EDX to identify the damage mechanisms.

4.2 Mechanical properties

The mechanical properties, such as hardness, UTS, YS and %El, were analyzed with respect to the different microstructure involved, viz. SDAS, amount, size of eutectic Si, iron-intermetallics, and porosity. The relationship between the microstructure and mechanical properties of the studied alloys will be discussed in the following sections.

4.2.1 Hardness test

The hardness trend observed in the different alloys shows an opposite behavior to SDAS value (Table 4-1) when comparing DC to LFC alloy C at an almost constant area fraction of iron intermetallics. The Vickers hardness of alloy C decreases from 80.8HV to 63.5HV when the SDAS increases from 18.4 µm (DC) to 76.4 µm (LFC); this result proves that the evolution of hardness also depends on the SDAS of alloys. In agreement with the results from Sanna et al. (Sanna, Fabrizi et al. 2013) and Sofyan et al. (Sofyan, Kharistal et al. 2010), the hardness decreases with an increase in the size of SDAS. According to Seifeddine et al. (Seifeddine, Johansson et al. 2008), as the material is rapidly solidified, the dendrites are likely to get enriched with Si and the materials exhibit higher hardness. To investigate the influence of Sr, Fe and Mn content on the variation in hardness, Vickers hardness measurements for each alloy are reported in Table 4-1. Sr addition from 47ppm (alloy A) to 130ppm (alloy B) has no obvious effect on the hardness. However, the hardness increases from 73.7HV (alloy A) to 80.8HV (alloy C) when the iron content increases from 0.10 wt. % to 0.49 wt. %. Besides the alloy D, where the Fe level was highest (0.8%), shows the highest hardness value. This hardness increase is in agreement with Ref. (Tash, Samuel et al. 2007, Moustafa 2009), where it is reported that the increase of Fe content increases the hardness of Al-Si alloys as the Fe-intermetallic surface fraction increases. The hardness strongly depends on the composition and fraction of phases in the material. According to Seifeddine et al. (Seifeddine, Johansson et al. 2008), the hardness of intermetallic compounds obtained from nanoindentation measurements, i.e. β-Al_5FeSi-needle (11.5 GPa) and α-$Al_{15}(Fe, Mn)_3Si_2$-script phase (14.8 GPa), is larger than that of Al matrix (2.1 GPa). Thus the almost linear hardness increase with the amount of hard phase reported in Table 4-1 can be expected for a given SDAS value.

Table 4-1: Vickers hardness, area fraction of iron-intermetallic and DAS measured from investigated alloys

Alloy	Casting process	Average Vickers hardness (HV30)	Area fraction of iron-intermetallic (%)	Mean SDAS (µm)
A	DC	73.7	0.16	20.8±2.4
B	DC	74.9	0.22	19.5±2.4
C	DC	80.8	1.81	18.4±2.1
	LFC	63.5	2.32	76.4±6.9
D	DC	83.8	2.48	17.0±2.3

4.2.2 Conventional Tensile test

The tensile properties (i.e., ultimate tensile strength, Young modulus, yield strength and elongation) at room temperature are shown in Table 4-2.

Table 4-2: Tensile properties of studied alloys

Alloy	Casting process	Young modulus [GPa]	Yield Strength [MPa]	Ultimate Tensile Strength [MPa]	Plastic Elongation [%]
A	DC	75±4.5	81	256±3	3.8±0.3
B	DC	71±3.8	83	258±4	3.2±0.5
C	DC	77±6.0	88	254±10	2.1±0.2
	LFC	67±1.2	78	180±3	0.29±0.02
D	DC	80±5.1	93	239±3	1.3±0.1

4.1.1.1 The effect of Sr

By comparing alloy A with B, the Sr content increase from 47 ppm to 130 ppm has no obvious influence on the UTS and YS. Thus slightly different morphology of eutectic Si resulting from a different Sr content has a negligible effect on the mechanical properties. The slight decrease of plastic elongation may be due to the increased pores volume fraction (Ma, Samuel et al. 2008). In addition, the Young's modulus depends on the volume fraction of the alloy components (such as Al matrix and hard inclusions) (Lasagni and Degischer 2010) and has no obvious reason to vary with Sr. Besides, as shown in Table 4-2, the variation of Young's modulus with Sr is within the standard deviation.

4.1.1.2 The effect of Fe and Mn

The effect of Fe content on the mechanical properties of the DC AlSi7Cu3 alloys is shown in Figure 4-1. A slight increase in the yield strength, a slight decrease in the UTS and a significant decrease in the elongation are observed when increasing the Fe-Mn content. The elongation to failure decreases due to the increased volume fraction of iron-intermetallics especially the needle-like β-phase (Seifeddine and Svensson 2013). As mentioned previously, the Fe-containing intermetallics particles are more easily fractured under tensile load than the aluminium matrix or the fine silicon particles (Taylor 2004). As reported by Wang et al. (Wang, Apelian et al. 1997), the cracking of Fe-rich compounds tends to account for most of the damage when the Si particles are small. On the other hand, due to the very low pores volume fraction (0.03% to 0.06%) in the DC alloys, the effect of pores on elongation is negligible compared to the effect of Fe-containing intermetallics. In addition, Fe can slightly increase the yield strength of Al–Si alloys as reported by Ji et al. (Ji, Yang et al. 2013), and this is usually accompanied by an increase in hardness. The experimental results have confirmed that

the amount of Fe-rich intermetallics significantly affects the mechanical properties of the Al–Si–Cu alloys.

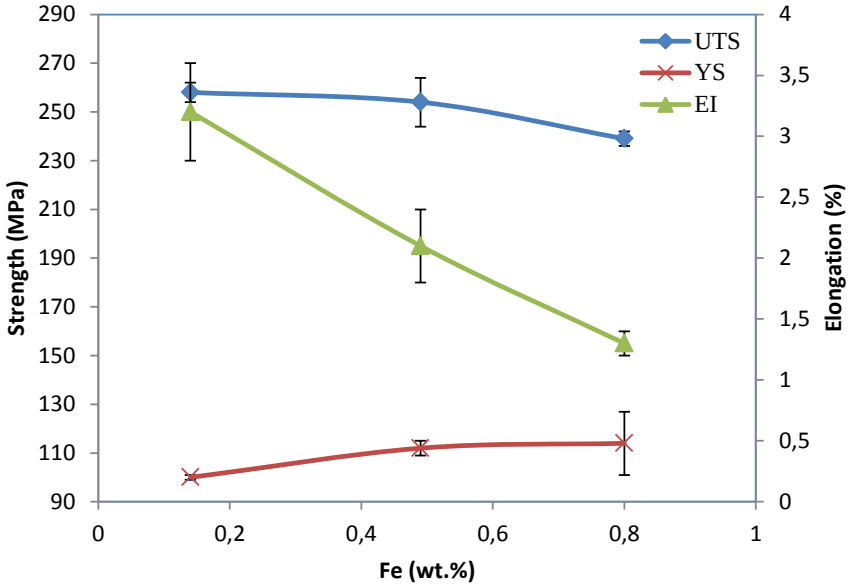

Figure 4-1: Effect of Fe content on the mechanical properties of the DC AlSi7Cu3 alloys (YS: yield strength; UTS: ultimate tensile strength; El: elongation)

Table 4-1 and Table 4-2 show that the Young's modulus increases from 71.2 GPa to 80.4 GPa when the surface fraction of iron-intermetallics increases from 0.22% to 2.48%, i.e. for the alloys B and D. This increase of Young modulus with Fe content is mainly due to the hardness and rigidity of iron-intermetallics, which is higher than that of Al matrix (Seifeddine, Johansson et al. 2008).

4.1.1.3 The effect of casting process

The mechanical properties also depend on the casting process. As shown in Table 4-2 the lower Young's modulus and yield strength of LFC alloy as compared to DC alloy can be explained by a higher pores volume fraction in LFC than in DC alloy (Mugica, Tovio et al. 2004).

The average ultimate tensile strength (UTS) significantly decreases from 254 MPa for DC alloy to 180MPa for LFC alloy. This might be due to the lower SDAS in DC alloy (Ceschini, Morri et al. 2009). Besides, the plastic elongation of LFC alloy is severely reduced compared with DC alloy with a plastic elongation that decreases from 2.1% for the DC alloy to 0.15% for the LFC. The decreased ductility can be attributed to the more numerous and larger pores and coarser microstructures in terms of larger SDAS (Li, Samuel et al. 2004), plate-like eutectic Si particles, iron-intermetallics in LFC alloy than in DC alloy. These coarser flakes of eutectic Si particles (Figure 3-9(b)) in LFC alloy promote brittleness. (Hafiz and Kobayashi 1994) reported that nucleated cracks seem to propagate in a brittle manner in the large plate-like eutectic Si particles while Si particles having a fine fibrous morphology fracture in a ductile fashion. Besides, as reported by Ma et al. [10], the β-Al_5FeSi platelet

size is also essential to Al-Si alloy ductility and increasing β platelet size from 25 μm to 200 μm causes a significant decrease in elongation (from 14% to 1%). As shown in Table 4-1, the maximum length and surface area fraction of iron-intermetallics for the alloys B to D increases from 56.3 μm in DC alloy to 245.5 μm in LFC alloy. In addition, the presence of pores facilitates fracture. Large pores, especially shrinkage pores, have an irregular 3D shape, which induces stress concentration, and they are usually responsible for crack initiation during loading (Savelli, Buffière et al. 2000). The large shrinkage porosity found in LFC alloy (Figure 3-3(e)) may impose this detrimental effect on mechanical properties. Therefore, DC alloys with refined microstructures in terms of eutectic Si and iron-intermetallics and fewer defects tend to show higher tensile properties.

4.3 Tensile damage mechanisms

Preliminary tensile tests with 2D in-situ observations were realized on two DC A319 specimens at different Fe levels, i.e. alloy A and alloy D. As shown in the results of microstructure characterization presented in chapter 3, the main difference between these two alloys is the amount of Fe-intermetallics. In addition, as previously mentioned, a different Sr content between two DC alloys (such as alloys A and B) has negligible effect on the mechanical properties. Therefore, the study of the effect of Fe-rich intermetallics resulting from different Fe/Mn content on the damage mechanisms of Al–Si-Cu can be achieved by comparison between alloys A and D.

The two tensile specimens were named ‘specimen A’ and ‘specimen D’ for alloys A and D, respectively. During in-situ tensile test, reference and deformation images were recorded by Questar long distance microscope. Strain and displacement fields at the microstructure scale were measured at different load levels (before the final fracture) using DIC.

In both cases, the specimen failed from a crack inside the ROI. Specimen A failed at a nominal gross stress of 202MPa and overall average strain of 1.29%, which is measured by extensometer, whose location can be seen in Figure 2-12, while specimen D failed at a nominal gross stress of 159MPa and an overall average strain of 0.61%.

Compared to the results of conventional tensile test, which were presented before (see Table 4-2), the elongations of the two specimens for in-situ tensile test are lower, and this can be attributed to the artificial hole in the center of specimen. Based on the hole radius used in this study, the stress concentration factor K_{tg} at the edge of a hole is 3.15, which can be found in common stress concentration factor handbook (Peterson and Plunkett 1975). This explains why the crack forms near the edge of hole due to the stress near the hole boundary, in which is higher than the nominal stress remote from the hole.

After the specimens’ failure, the fracture surfaces of the specimens were examined with SEM/EDX.

4.3.1 DIC measurements

In this part, strain and displacement fields for the two alloys (i.e. alloy A and D) are shown and compared at different load levels (before the final fracture) in the area where a crack was observed during the test, i.e. at the notch root; this area is called analysis area hereafter.

- **Low Fe alloy (Alloy A)**

For specimen A with a low Fe content, strain and displacement fields obtained by DIC at different loading step are illustrated in Figure 4-2. The OM image of analysis area has been registered to the reference Questar image and superposed to the strain and displacement fields to allow for comparison of the strain localization and microstructure.

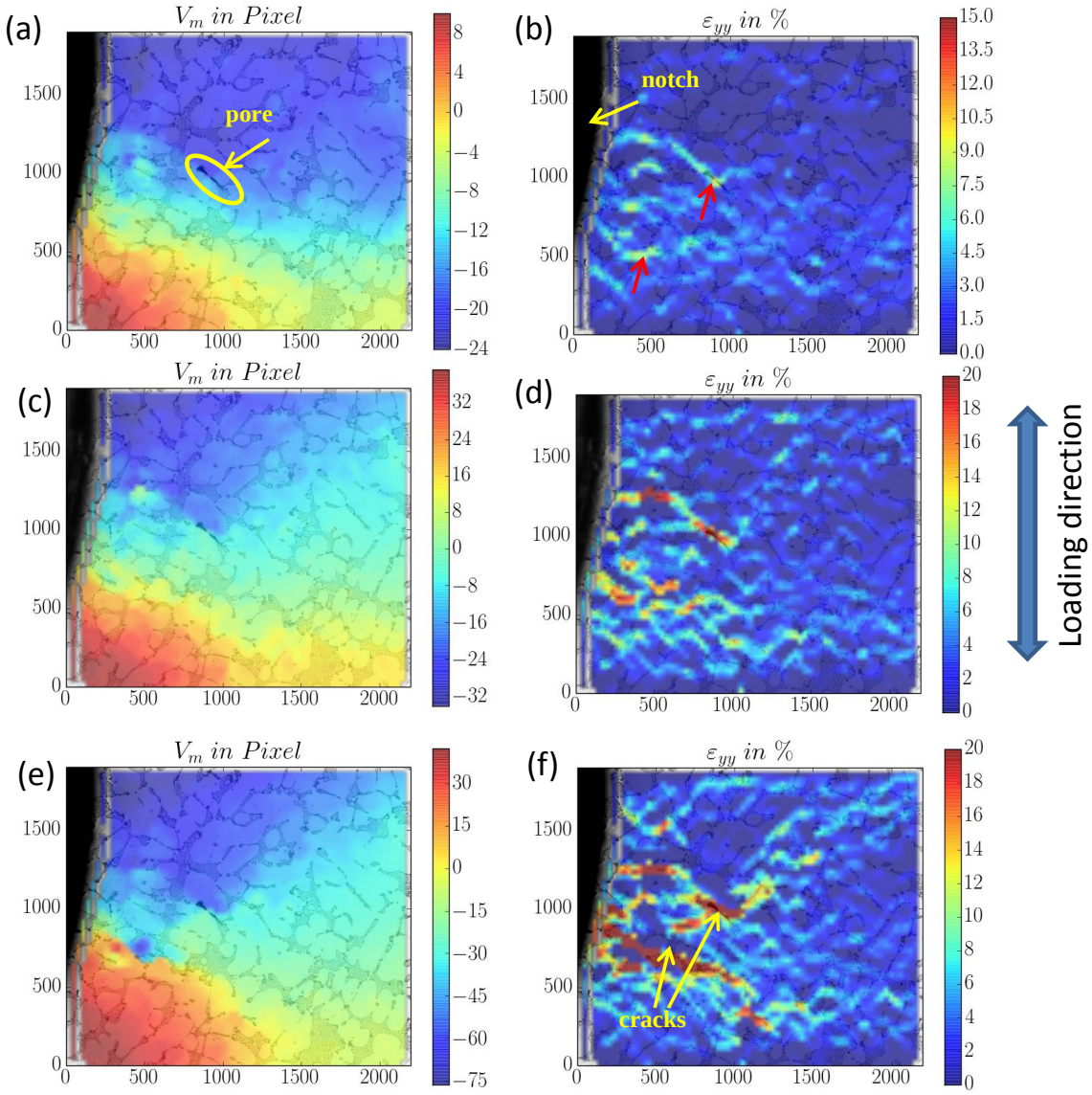

Figure 4-2: (a, c, e) Displacement and (b, d, f) strain fields (in pixels, 1pixel=0.22µm) in the Region Of Interest along the loading direction at global strain (a, b) Ɛ=0.56%, (c, d) Ɛ=0.88% and (e, f) Ɛ=1.06% for specimen A. Loading was along the vertical direction and OM images of the microstructure in the unloaded state are superimposed

Indeed, although the crack is not visible at the low strain level, i.e. at 0.56%, a slightly strain localization is already observed (see red arrows in Figure 4-2(b)), and it increases as the load is increased. The strain field within the analysis area shows some strain localization at hard inclusions and pore when the global strain is 0.88% (Figure 4-2(d)), which corresponds to the displacement discontinuities in Figure 4-2(c). The presence of a displacement discontinuity means that there is a crack already nucleated at a strain of 0.88%. This also indicates that good correlation between crack location and strain localization at the beginning of the test.

The Questar images at different loading steps for specimen A are shown in Figure 4-3. Due to the low quality of image, no obvious crack can be observed in the Questar image at the strain of 0.88% (see Figure 4-3(a)). When the load increases, the main crack becomes visible at the strain of 1.06% (as shown in Figure 4-3(b)), and corresponds to a large local strain deformation (Figure 4-2(f)), i.e. crack opening. Then it is observed to grow quickly with a further increase of loading.

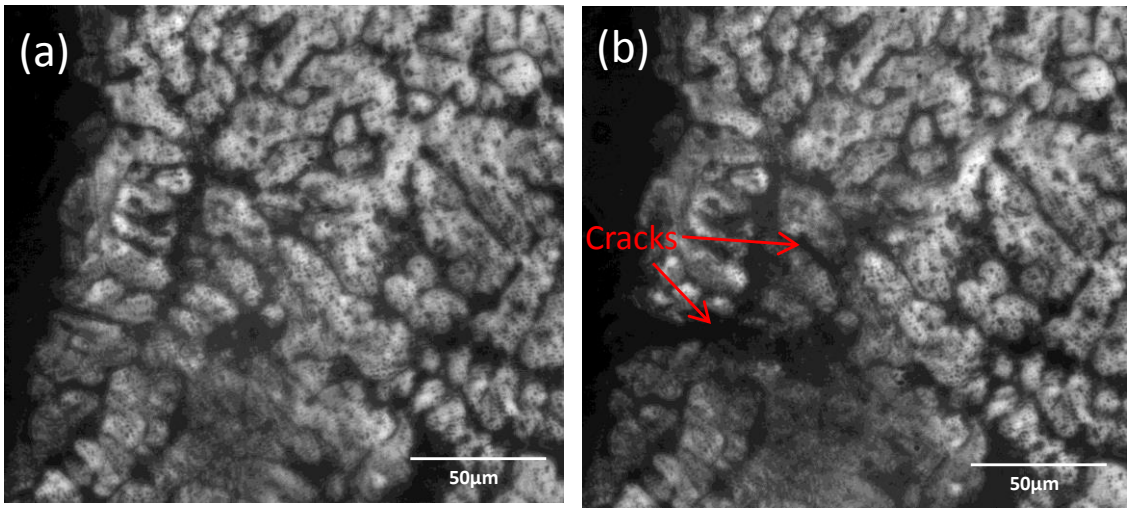

Figure 4-3: Questar image of analysis area at the strain (a) Ɛ=0.88% and (b) Ɛ=1.06% for specimen A

Due to the low quality of Questar images, cracks detected from the Questar image are faint, and it is difficult to distinguish to which microstructural constituent the cracks do correspond, therefore, the fracture surface of specimen was observed by SEM, and the details will be discussed in the following part.

- **High Fe alloy (Alloy D)**

Figure 4-4 shows the displacement and strain fields measured from analysis area for the tensile test at different loading steps for the specimen D (high Fe alloy). Figure 4-5 shows the corresponding Questar image at strain of 0.33% and 0.51%. Note that in order to show the experimental fields in high magnification, a small region which contains the crack initiation and propagation was chosen and extracted from the large examined ROI.

Chapter 4

No obvious cracks are observed in the Questar images when the global strain is 0.21% and 0.33% (see Figure 4-5). However, as can be seen in Figure 4-4(b) and (d), strain localizations are observed to increase at increasing load in these two steps in the neighbourhood of the hole which introduces high stress concentration. Visible crack (Figure 4-5(b)) is observed from the Questar image at a global strain of 0.51%, which corresponds to an obvious displacement discontinuity (see red arrows in Figure 4-4(e)), then the cracks propagates until final fracture with further load increase.

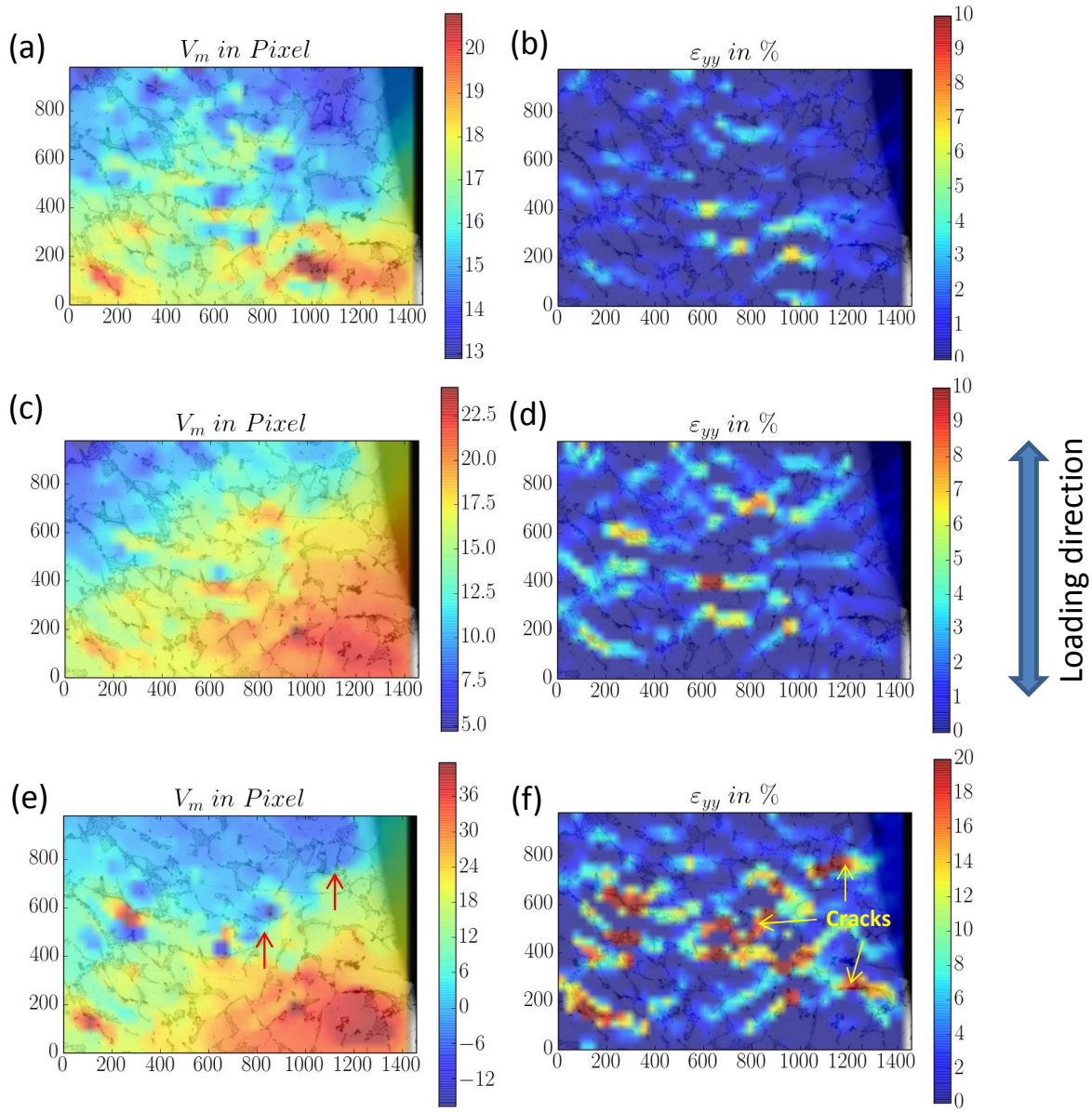

Figure 4-4: (a, c, e) Displacement field and (b, d, f) strain field displacement field (in pixels, 1pixel=0.22µm) in the Region Of Interest along the loading direction at global strain (a, b) Ɛ=0.21%, (c, d) Ɛ=0.33% and (e, f) Ɛ=0.51% for specimen D. Loading was along the vertical direction and OM images of the microstructure in the unloaded state are superimposed

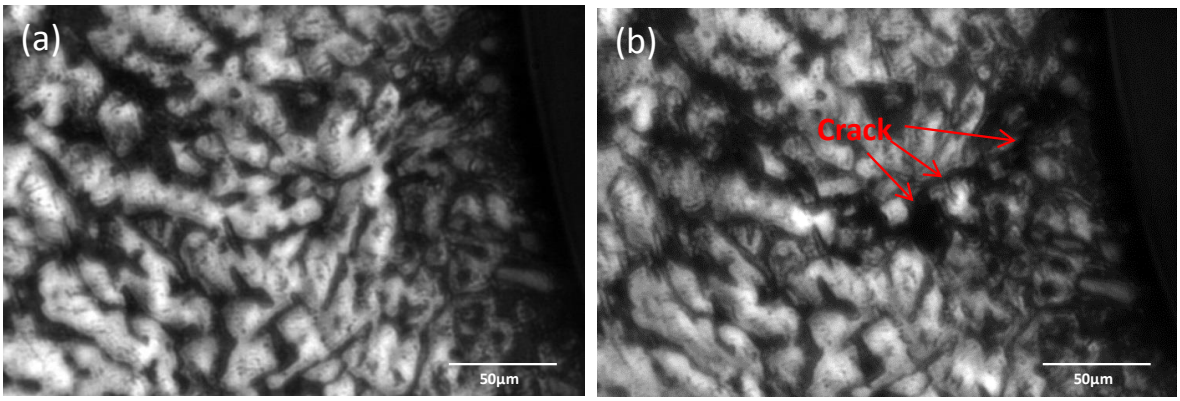

Figure 4-5: Questar image of ROI at the strain (a) Ɛ=0.33% and (b) Ɛ=0.51% for specimen D

4.3.2 Fracture surface analysis

The OM images of the microstructure in the unloaded state were systematically superimposed to the DIC fields to check the correspondence between strain localization and microstructure. However, cracks are not clearly visible in the Questar image, especially for the microcracks. Thus, in order to better understand the influence of microstructural constituents on strain heterogeneities, after failure, the specimen's surface was observed with Scanning Electron Microscope (SEM) to allow for a direct comparison of the microcracks observed at a higher resolution after the test with strain localization deduced from DIC during the tensile test. In addition, 2D observations cannot follow cracks in final fast fracture areas, thus in order to get more details about the crack propagation and final fracture in the alloys, Backscattered Secondary Electron (BSE) microscopy was used to examine the final fracture surfaces of the failed specimens.

- **Specimen A**

As seen in Figure 4-6(a), cracks paths are observed clearly in the BSE images of Specimen A, and micro-cracking occurred mainly in the Al_2Cu phase (pointed out by yellow arrows) which is distributed along the crack path. This result proves the role of Al_2Cu phase on the crack propagation during loading and that the final fracture is prone to occur along the Al_2Cu phase.

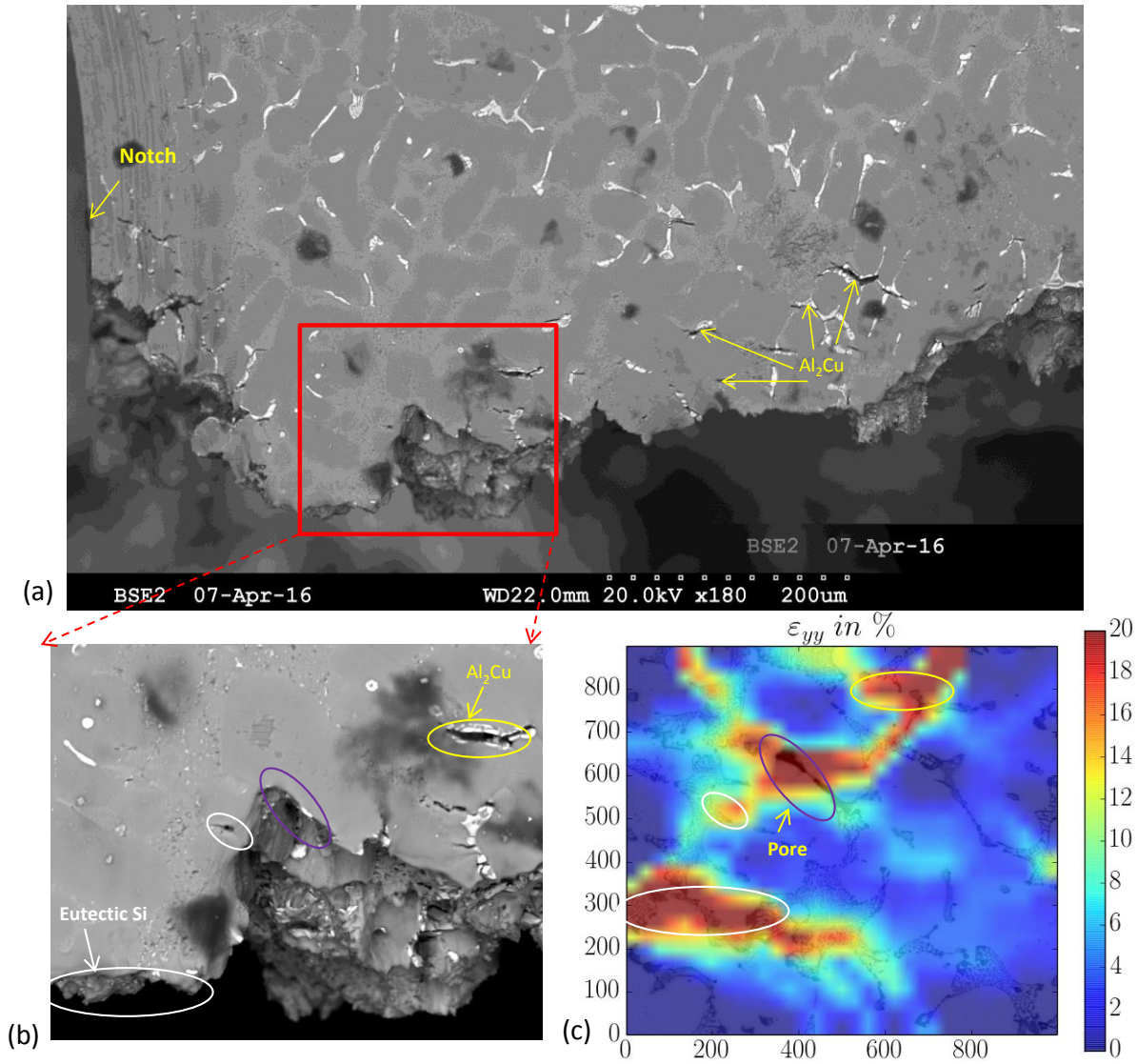

Figure 4-6: SEM image of polished flat surfaces of the specimen after tension test (a) overall view, (b) magnified view as enclosed by red box in (a), and (c) the corresponding strain field (Ɛ=0.88%) computed from DIC

In Figure 4-6(c), strain heterogeneity is observed in the selected area of the specimen (highlighted with a red frame in Figure 4-6(a)) at the step before the crack is visible in the Questar image (see Figure 4-3(b)); strain localization appears in the hard inclusions (eutectic Al-Si, Al_2Cu) and pore at a stress level of 184 MPa (average strain of about 0.88 %). Comparing Figure 4-6(b) and (c), the correlation between strain localizations and the final fracture and microcracks at Al_2Cu phase revealed by SEM is also well observed. It proves that the zones with large deformation are correlated to final fracture or microcracks.

In addition, as shown in Figure 4-7, fracture analysis using SEM-EDS was performed on the fracture surface. Figure 4-7(e) shows a general view of the fracture surface; the analysis area (marked by red box) is located below the hole where cracks initiate and propagate. BSE images of the two sides of the

fracture surface for specimen A are placed side by side (Figure 4-7(a) and (b)). The corresponding X-ray elemental mappings of the fracture surface for the specimen are shown in Figure 4-7(c) and (d).

The progress of the crack through the matrix of the low Fe alloy (alloy A) sample is shown in Figure 4-7(a) and (b): eutectic Si particles, Al_2Cu particles and iron-intermetallic are observed in the fracture surface. Figure 4-7(c) and (d) reveals that hard inclusions, i.e. Al_2Cu phase and Si particles, occupy a large area fraction of the fracture surface for specimen A. This result together with the analysis of the crack path in Figure 4-6 show that crack growth in the low Fe alloy occurs preferentially through Al_2Cu phase and Si particles.

In addition, as seen in Figure 4-7(c) and (d), both fracture (white solid arrows) and debonding (white dotted arrows) of these hard inclusions are found in the fracture surface, and the observations revealed that more fracture than decohesion is found in all fracture surfaces.

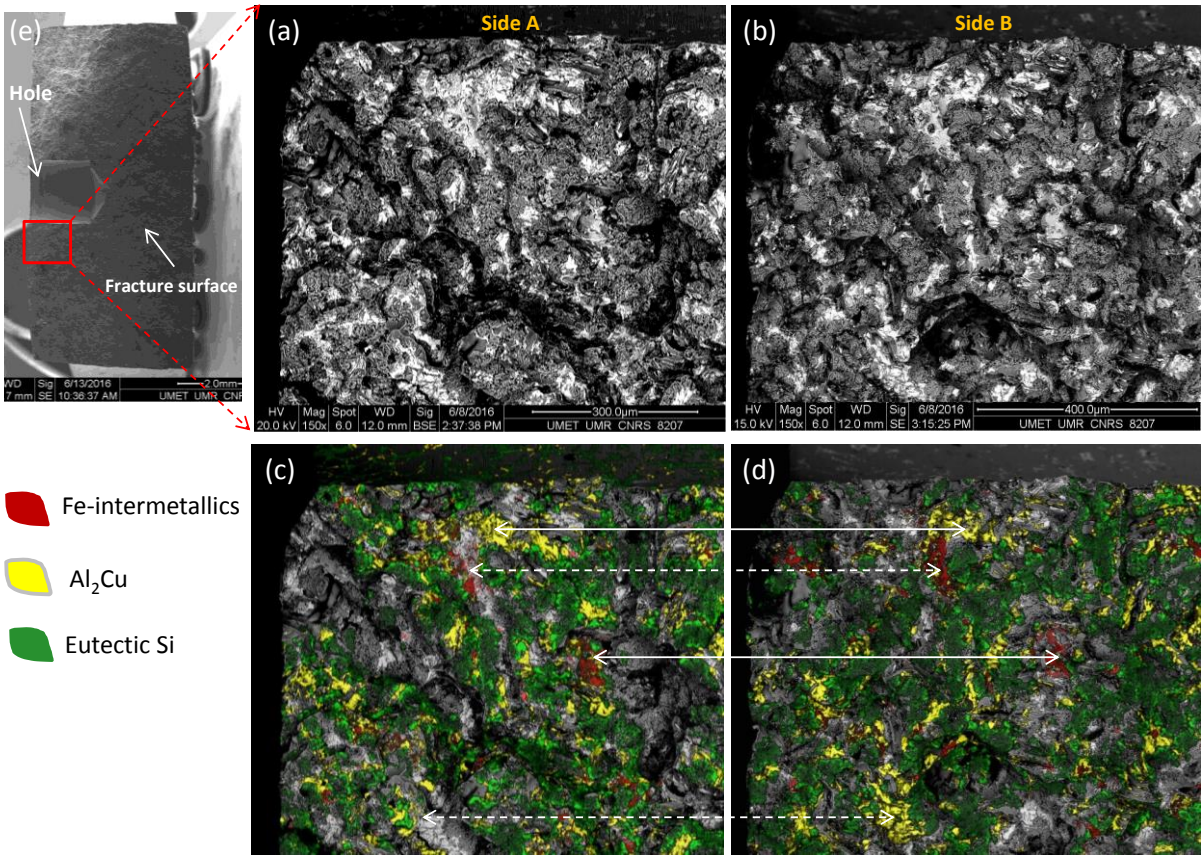

Figure 4-7: (a), (b) BSE images of the fracture surface of specimen A and (c), (d) corresponding X-ray mapping images showing the distribution of hard inclusions (eutectic Si, iron-intermetallics, Al_2Cu phases), (e) SE image of the fracture surface of specimen A showing the analysis area

- **Specimen D**

SEM observations were also performed on the fracture surface of specimen D (Figure 4-8), and were compared with OM image in the same area and with the corresponding strain field. SEM postmortem

analysis in the selected analysis area (Figure 4-8(c)) with a higher resolution than Questar images shows cracks clearly.

In order to distinguish the phases along the crack path precisely, the OM image (Figure 4-8(a)) in the analysis area is compared with the same area of BSE image (Figure 4-8(c)). In both images, the crack path is marked by a red dotted line. Figure 4-8 shows that crack goes through hard inclusions and that this crack is prone to go through iron-intermetallics (marked by yellow arrows in Figure 4-8(c)). This result highlights the role of iron-intermetallics on the crack propagation during tensile loading.

The correlations between strain localizations and the final fracture and microcracks are observed between Figure 4-8(b) and (c): most of the strain localization can be ascribed to hard inclusions, especially iron-intermetallics.

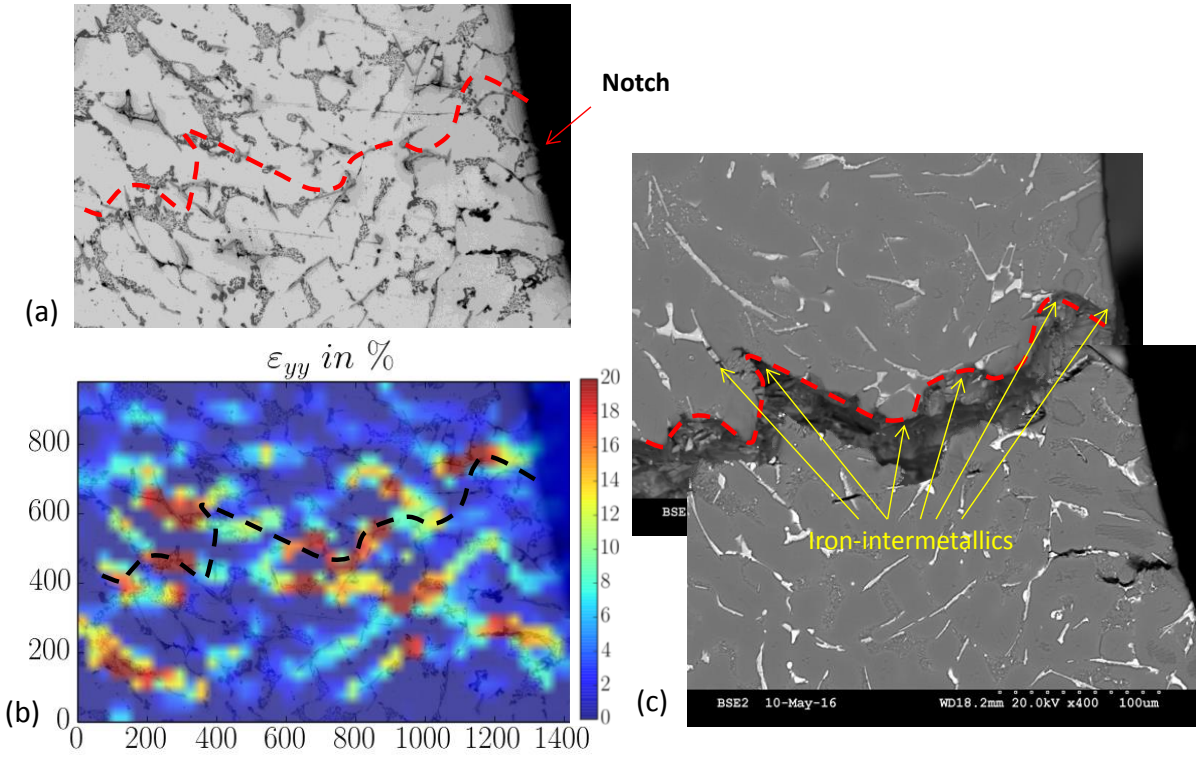

Figure 4-8: (a) OM image in ROI of specimen D, and (b) the corresponding strain field (Ɛ=0.51%) computed from DIC, (c) BSE image of the fracture surface of specimen D

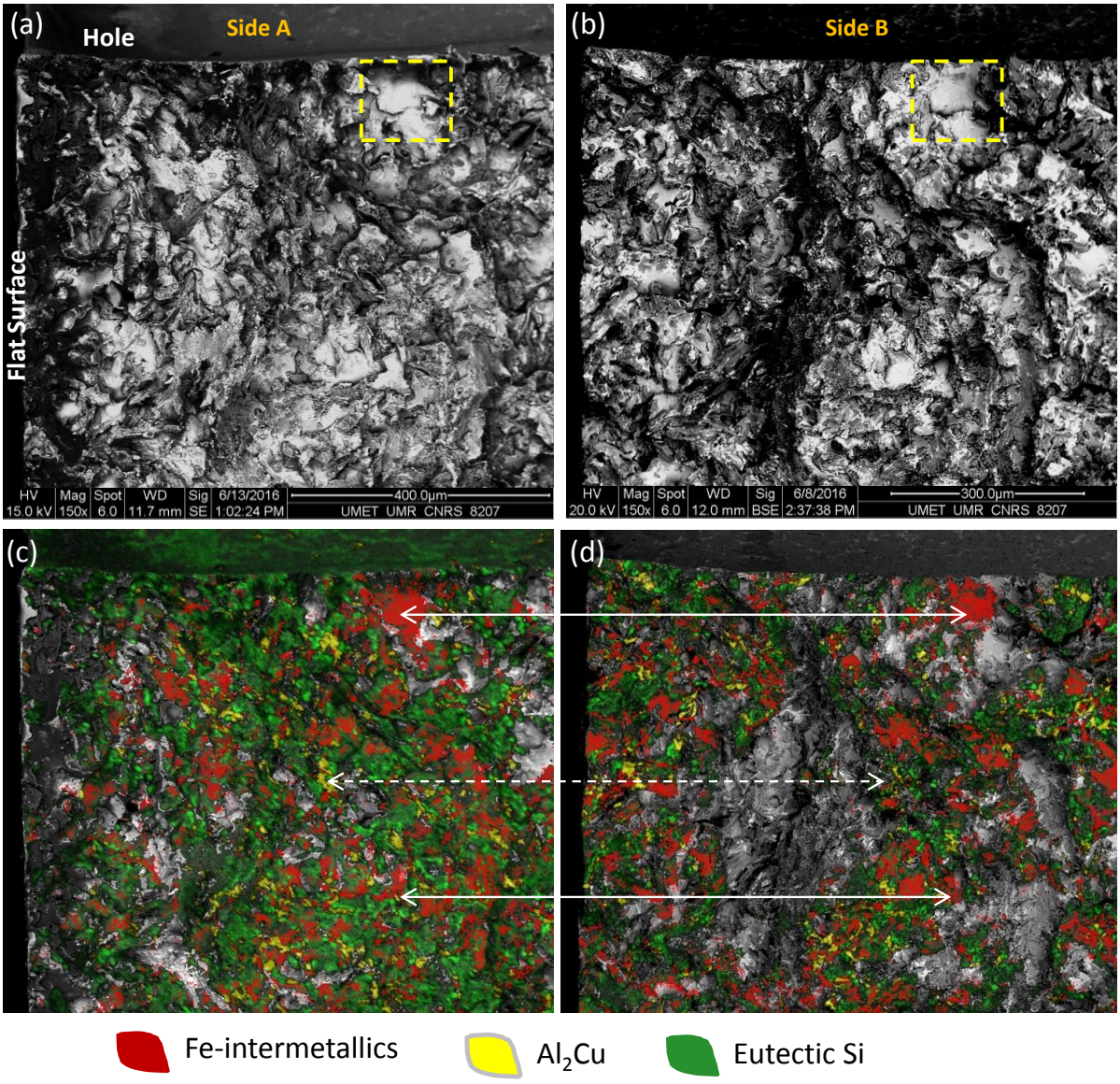

Figure 4-9: (a), (b) BSE images of the fracture surface of specimen D and (c), (d) corresponding X-ray mapping images showing the distribution of hard inclusions (eutectic Si, iron-intermetallics, Al2Cu phases)

Figure 4-9(a) and (b) show the BSE images of two fracture surfaces close to the hole in specimen D. The corresponding X-ray elemental mappings of the fracture surface for the specimen are shown in Figure 4-9(c) and (d). The analysis of fracture surfaces reveals considerably different characteristics for specimen D. A larger area of iron-intermetallics (red area) is observed, which proves the role of iron-intermetallics on the crack propagation and final fracture.

Figure 4-9 shows how the crack propagates through the fracture of hard inclusions in specimen D at high Fe level, which demonstrates that fracture (white solid arrows) and debonding (white dotted arrows) of these hard inclusions occur on the fracture surface. It is interesting to see that the fracture surface of the specimen D shows comparatively more iron-intermetallics. Fracture occurs mainly by

fracture of the iron-intermetallics (white solid arrows in Figure 4-9(c) and (d)) so that the crack propagation of the high Fe alloy was effectively controlled by the iron-intermetallics. Besides, the iron-intermetallics (β-phase) that appear as long needle-like inclusions in 2D micrographs are seen in 3D as massive platelets (marked by yellow dotted box in Figure 4-9(a) and (b)) as confirmed by the X-ray elemental mapping in Figure 4-9(c) and (d). It indicates that the fracture of the iron-intermetallics accelerates the crack formation.

- **Quantitative analysis**

A quantitative chemical composition analysis was performed on the fracture surface for the two specimens using SEM-EDX. It should be noted that there exist some areas that cannot be detected by EDX because of shadowing effects in the rough fracture surface.

The comparison of hard inclusions surface fraction between fracture surfaces and flat surfaces for the two alloys is shown in Figure 4-10; the result shows that the fraction of hard inclusions is higher in the fracture surface than flat surface of specimen for both cases. It implies that cracks and final fracture are more prone to occur at Si phase, iron-intermetallics and Al_2Cu phases than in Al dendrites.

Although the fraction of Al_2Cu phase (1.2-1.5%) and eutectic Si (7-8%) are similar in the flat surface of specimen A and D, more Al_2Cu phase (8% - 10%) and eutectic Si (12% - 16%) can be detected in the fracture surfaces of low Fe alloy than in that of high Fe alloy. The large fraction (i.e. 14% - 16%) of iron-intermetallics measured in the fracture surface of high Fe alloy as compared to the 2D examination result of the flat surface (2-2.5%) indicates that iron-intermetallics play a very important role whether in cracks initiation, cracks propagation and final fast fracture.

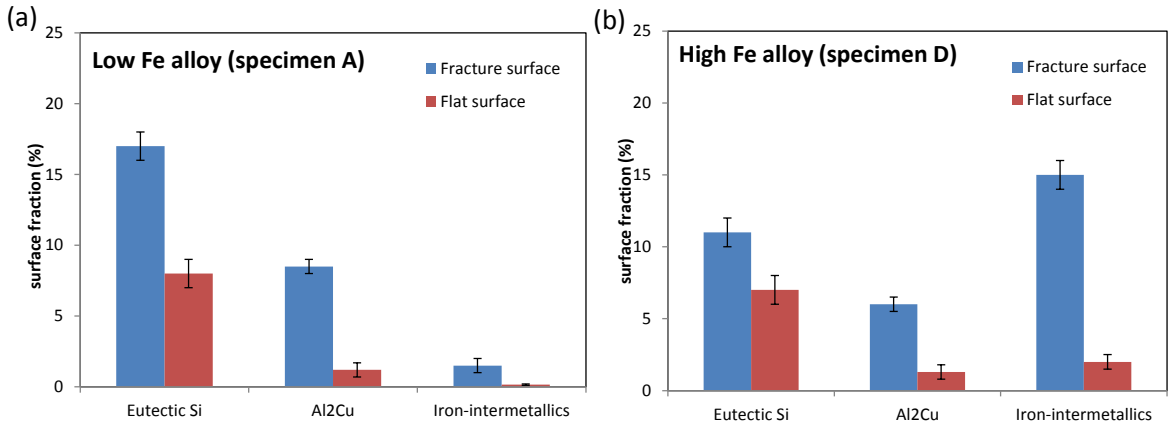

Figure 4-10: Comparison of hard inclusions surface fraction between fracture and flat surfaces for specimens (a) A and (b) D

4.3.3 Discussion

In the present test, the tensile damage mechanisms of two DC Al-Si-Cu alloys with different Fe level were studied by field measurement and fracture analysis. The results show the iron-intermetallics

inherited from Fe content play an important role on the tensile damage. As shown previously the increase of Fe content in the Al-Si-Cu alloy led to harmful tensile properties, especially a decreased ductility. This ductility reduction was primarily due to the iron-intermetallics increase with the Fe addition.

- **Cracks initiation**

During the tensile tests, the large stress concentration around hole (Pilkey and Pilkey 2008) resulted in crack initiation at a gross stress between 184 and 195 MPa for specimen A and between 133 and 150MPa for specimen D.

In specimen A, cracks initiated from hard inclusions (Si particles and Al_2Cu phase) near the artificial hole or pore where strain localizations were measured by DIC analysis. Numerous studies have shown that pores have an important influence on strain localization because they can generate enough strain localization for crack initiation (Wang, Limodin et al. 2016) (Dezecot, Buffiere et al. 2016). In this work, the artificial hole can also introduce stress concentration as well as pores, resulting in crack initiation at hard inclusions around them.

The eutectic Si and Al_2Cu phases acting as the crack initiation sites have already been reported by (Dezecot, Buffiere et al. 2016) (Horstemeyer 2012). This can be explained by the strain incompatibility between the aluminium matrix, which has an elasto-viscoplastic behavior, and the hard intermetallic particles (particularly Si particles). According to (Seifeddine, Johansson et al. 2008) and (Tabibian, Charkaluk et al. 2015), the hardness of hard inclusions obtained from nanoindentation measurements, i.e. iron-intermetallics (11.5-14.8 GPa), Si particle (13.3 GPa) and Al_2Cu phase (6.54GPa), is larger than that of Al matrix (2.1 GPa). Thus the difference in hardness may therefore explain the crack initiation on these hard particles.

In specimen D with the high Fe content, cracks initiated at iron-intermetallics rather than at eutectic Si and Al_2Cu phases, the reason for this is mainly due to stress concentration enhancement and crack formation as a result of the presence of needle-like intermetallic compounds (Ceschini, Morri et al. 2009). As reported by (Yi, Gao et al. 2004), the most detrimental Fe-rich inclusions are the brittle needle-like β-Al_5FeSi, which act as the main crack initiation sites in high Fe-content Al-Si-Cu alloys. In addition, as discussed above, crack initiation takes place at favorably stiff particles; the high hardness value of iron-intermetallics (11.5-14.8 GPa) can cause crack initiation. Moreover, sharp edges of the β-Al_5FeSi introduce severe stress concentrations in the matrix, which contribute to the crack initiation sites.

- **Cracks growth and final fracture**

Once cracks have initiated, they are prone to grow along hard inclusions including Si phase, Al_2Cu phases and iron-intermetallics. Cracks growth along hard inclusions can be ascribed to strain localizations at hard inclusions (e.g. in Figure 4-2(d)). Strain localizations were indeed observed in

areas where cracks propagations were observed in following loading (e.g. in Figure 4-2(f)). In addition, fracture surfaces were also examined with SEM in order to find the features responsible for crack growth and final fracture.

In specimen A with low Fe content, as shown in Figure 4-6 and Figure 4-7, it seems most likely that the fracture is triggered in a relatively stiff region with a high fraction of eutectic Si and Al_2Cu phases located at the fracture surface of specimen. It indicates that cracks growth is prone to occur along eutectic Si particles and Al_2Cu phases. This may be due to the elastic modulus of eutectic Si particles (185 GPa) and Al_2Cu phases (126 GPa) which are higher than that of the aluminium matrix (92 GPa), thus they are reported to play a role in crack propagation either as a barrier (Zeng, Sakamoto et al. 2014) or as a preferential path (Chan, Jones et al. 2003).

In specimen D with high Fe content, cracks growth is observed to occur along hard inclusions, essentially iron-intermetallics. As shown in Figure 4-9, more iron intermetallics than eutectic Si or copper containing phases were observed in crack growth path. Iron-intermetallics, when present, seem to have a more important role than silicon particles and Al_2Cu phases for the growth of cracks.

From the results, several reasons may be proposed:

1) The iron-intermetallics exhibit a high elastic modulus (166-180 GPa) in comparison with other eutectic/intermetallic phases (Tabibian, Charkaluk et al. 2015), which may introduce incompatibility of deformation between the iron-intermetallics particles and the aluminium matrix and leads to damage by fracture or by debonding of iron-intermetallics particles (Buffière, Savelli et al. 2001, Dezecot and Brochu 2015).
2) The two studied alloys are modified by Sr. The microstructure characterization shows that eutectic Si particles in modified Al–Si-Cu alloys appear with fibrous morphology. Consequently, compared with these fibrous Si particles, the β-Al_5SiFe platelets is more likely to generate stress concentration.

Besides, fracture and debonding of hard inclusions are observed in both specimens. However, the failure mechanism of the hard inclusions seems to be more fracture than decohesion during tensile test. The failure mode of hard inclusions within the aluminum matrix depends on the loading conditions and phase morphology (Gall, Yang et al. 1999) (Horstemeyer 2012). Fracture is likely to occur at large and irregularly shaped hard inclusions under a high crack tip driving force. In the present case, due to the high tensile stress, the hard inclusions, especially needle-like β-Al_5FeSi phases are prone to cracking rather than debonding at particle/matrix interface during the tensile loading. This result is agreement with the observations by (Ma, Samuel et al. 2014), who reported that crack initiation and propagation occur through cleavage of β-Al_5FeSi platelets rather than by decohesion of the β-platelets from the matrix.

4.4 Conclusions

In this chapter, mechanical properties of four Al–Si-Cu alloys with different Sr, Fe and Mn content and casting process (Die casting and Lost foam casting) were studied, and then the effect of Fe content on the tensile damage evolution in DC Al–Si-Cu alloy was investigated and revealed using a coupling of experimental methods. Based on the results obtained from the present study, the following conclusions may be drawn.

4.4.1 Conventional mechanical properties

Mechanical properties of Al-Si-Cu alloy are strongly affected by the microstructure. In the present study, mechanical characterizations were performed to relate microstructural features resulting from different metallurgical parameters to mechanical properties.

The major conclusions of this work can be listed as follows:

1. A finer and more fibrous eutectic Si structure can be obtained with an increased Sr content with the drawback that Sr addition can introduce more pores in the DC alloy. However, no change of the tensile properties with the Sr content increase from 47ppm to 130ppm was noticed.
2. Iron has a detrimental effect on the UTS and above all on ductility in terms of the amount of β-Al_5FeSi phase. However, Fe addition increases YS in the alloys studied, i.e. the presence of iron can harden the alloy to some extent.
3. Mechanical properties of AlSi7Cu3 alloy are highly influenced by casting process via the microstructure. The LFC AlSi7Cu3 alloy shows more casting defects (i.e. larger pores and microshrinkage cavities), a coarser microstructure (i.e. larger SDAS, plate-like eutectic Si particles, needle-like iron-intermetallics) than DC AlSi7Cu3 alloy. DC alloys showed higher UTS, YS and elongation than LFC alloy.

4.4.2 Experimental protocol of 2D in-situ tensile test with DIC

An experimental protocol to evaluate the damage mechanisms of Al-Si-Cu alloy was developed and verified. An etching procedure was successfully developed and applied to generate speckle patterns suitable for DIC and enable measurement of local strain at the microstructure of Al-Si-Cu alloys. A machined hole (Dimension: Ø1.5mm × depth 1.5 mm) is used to force crack initiation in the selected ROI.

The efficiency of the experimental protocol using in-situ tensile test with DIC to study the influence of the microstructure upon the mechanical properties of an Al-Si alloy has been proved. The field measurements allowed identifying and tracking the development and localization of deformation. In addition, microcracks, which could not be observed in the images taken with Questar long distance microscope during in-situ tensile test, could be followed by the displacement discontinuities or the

strain localizations in the measured fields. Thus, this method allowed identifying the initiation sites of microcracks during the tensile test in relation with the observed microstructure.

4.4.3 Damage mechanisms

In order to understand the damage mechanisms associated to the different fraction of iron-intermetallics. Tensile tests with in-situ observation on surface were performed on two alloys with different Fe content using Questar microscope. Damage mechanisms were revealed by the field measurements and fractographic observations.

- Low Fe alloy

In the low-Fe alloy (0.1 wt% Fe), crack initiation occurs through the fracture of Si particles and Al_2Cu particles in the high stress concentration region around the artificial hole. The existence of pores also facilitates crack initiation. Cracks growth is prone to occur along the eutectic Si and Al_2Cu phases. Micro-cracks are detected in the Al_2Cu phase which is close to the crack path in the SEM images. In addition, the fractography analysis highlighted the role of hard inclusions on crack propagation, and revealed that crack propagation under monotonic load occurs through the eutectic Si, Al_2Cu phases and primary phases, exhibiting some fracture of the Al_2Cu phases and eutectic Si particles.

- High Fe alloy

In the high-Fe alloy (0.8 wt% Fe), cracks initiate at hard inclusions in areas with sufficient stress concentrations. Cracks appear more likely to occur through the fracture of iron-intermetallics. Thereafter, crack growth occurs through the cleavage of iron-intermetallics. Cracks also propagate through the fracture of Al_2Cu, as well as through brittle Si particles.

5 Chapter 5 Effect of heat treatment on the microstructure and damage mechanisms in LFC Al-Si-Cu alloy

Contents

Chapter 5

5.1 Introduction

The aim of this chapter is to investigate the effect of heat treatment on the microstructures and damage mechanisms of LFC Al-Si-Cu alloy. For this purpose, two different heat treatment conditions were performed on LFC A319 alloy, and the developed experimental protocol, which is described in chapter 2, was applied on these specimens.

The alloy of this study in the as cast condition is the same as the one used in (Wang, Limodin et al. 2016), the results of this study will be compared with them, then try to indicate the effect of heat treatment on the damage mechanisms of LFC A319 alloy.

As described in Chapter 2, heat treatment on specimens took place at PSA. Solution heat treatment at 495°C (i.e. below the incipient melting) at two different times (i.e. 2h30 and 50h) were selected and mainly used to dissolve the Al_2Cu phase in different degrees. Then aging at different time were performed to keep the same hardness of matrix in the two heat treatment conditions.

In addition, before the 3D in-situ tensile test, FE simulations were used to predict the higher strained area where crack initiation is likely to occur in order to select the ROI. Then, a full of 2D and 3D microstructural characterization was performed on the studied specimens using optical microscopy and X-ray Laboratory computed tomography (Lab-CT); microstructural characteristics (i.e. porosity, eutectic Si, iron-intermetallics and Al_2Cu phases) changes were compared before and after two different heat treatment conditions.

Section 5.4 presents and analyzes the results of tensile tests with 3D in-situ observations and digital volume correlation (DVC). Crack initiation mechanisms and the evolution of damage during crack growth together with the localized strains at the onset of cracks were studied.

5.2 Selection of ROI

As mentioned in chapter 2, in order to reduce the scanning area during the in-situ test, and to increase the probability of having the cracks occuring in the field of view, Region Of Interest (ROI) was selected in high resolution tomography images.

In this study, FE simulations, which were described in detail in chapter 2, were performed using laboratory tomography images on the 11 suitable specimens. Only three specimens (named HT1a, HT1b and HT2) were selected and used for the in-situ tensile test. Among them the samples HT1a and HT1b were heat treated in condition (1): Solution Heat Treatment (SHT) at 495°C for 2h30 + Quenching + Artificial aging at 200°C for 150h; the sample HT2 was prepared in condition (2): SHT at 495°C for 50h + Quenching + Artificial aging at 200°C for 200h.

The selection processes are illustrated in the following Figure 5-1~Figure 5-3.

Some studies (Wang, Limodin et al. 2016) (Dezecot, Buffiere et al. 2016) show that pores have an important influence on strain localization as large pores generate enough strain localization zones for crack initiation during tensile loading. Thus, as shown in Figure 5-1(a)~Figure 5-3(a), the microstructurally realistic meshes of the microstructure within the pristine samples (pores + matrix) was generated based on 3D images obtained by laboratory tomography, numerous large pores were found in the central part of the specimen, some of them are expected to produce large stress concentrations.

Figure 5-1(b)~Figure 5-3(b) show the volumetric tetrahedral grids for the three specimens. Then, the cumulated plastic strain distribution was computed and plotted by Abaqus software to help localize potential critical area (Figure 5-1(c)~Figure 5-3(c).

The blue dotted box defines the ROI in the specimens, and the selected ROI was used for 3D microstructural characterization in high resolution tomography and in-situ tensile test observation. The following in-situ tensile test show that all the cracks of three specimens occur in the chosen ROI, this confirmed that FE simulation can be of a great help to define a consistent zone of interest for the tests.

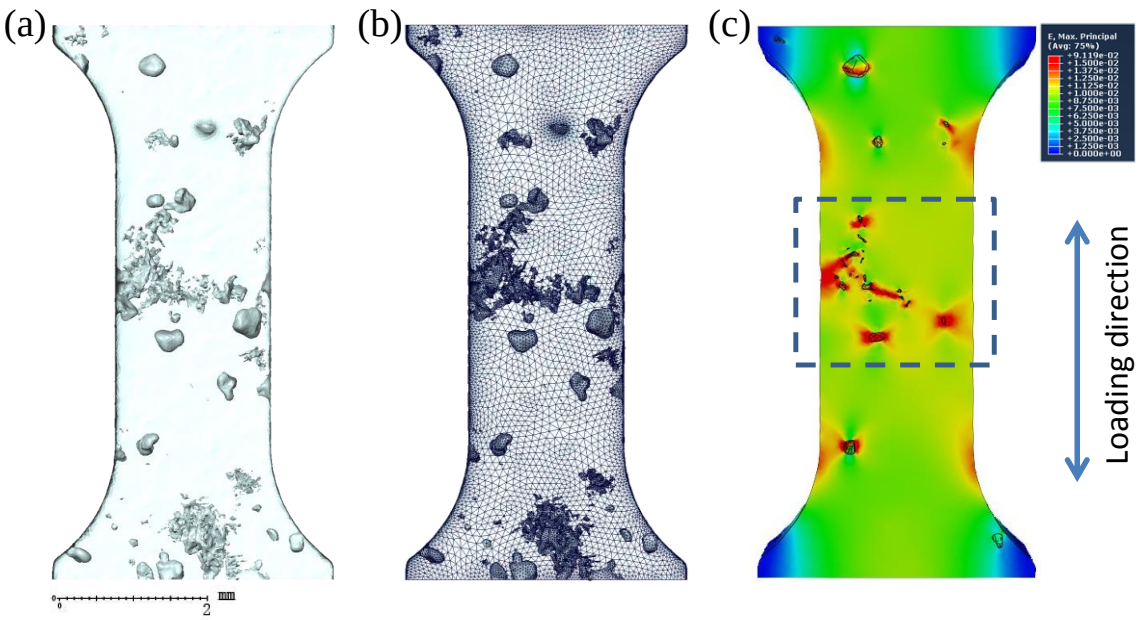

Figure 5-1: (a) 3D rendering of pores with Avizo software for Specimen HT1a, (b) 3D volume mesh, (c) FE calculation with Abaqus software showing Ɛzz

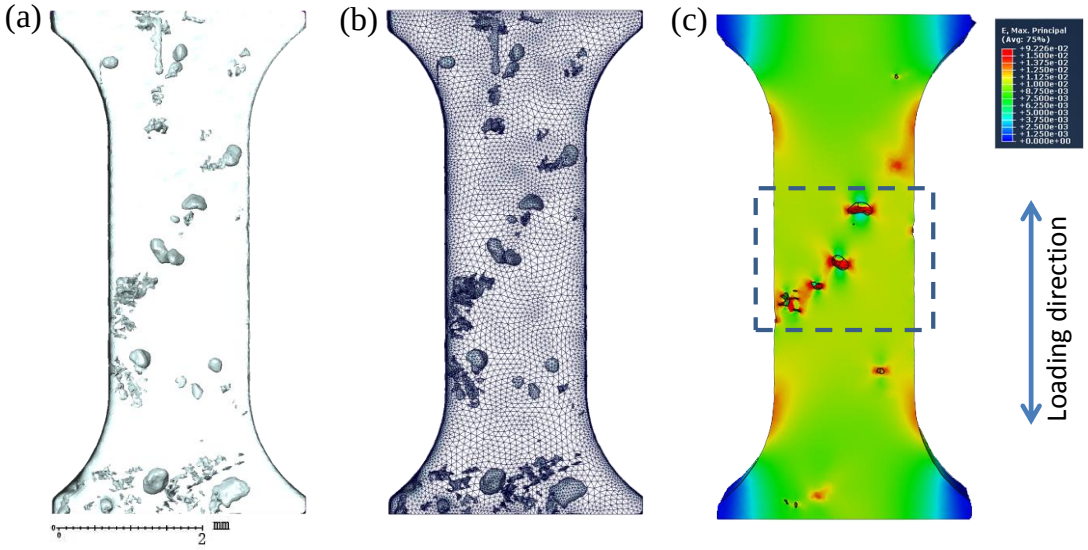

Figure 5-2: (a) 3D rendering of pores with Avizo software for Specimen HT1b, (b) 3D volume mesh, (c) FE calculation with Abaqus software showing Ɛzz

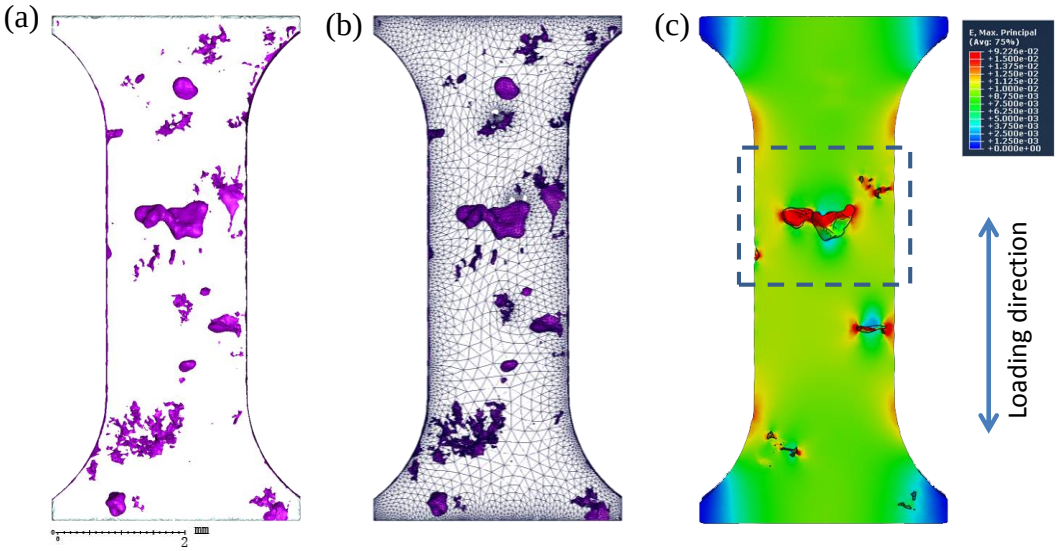

Figure 5-3: (a) 3D rendering of pores with Avizo software for Specimen HT2, (b) 3D volume mesh, (c) FE calculation with Abaqus software showing Ɛzz

5.3 Microstructure characterization

This part aims to investigate the effect of various heat treatments on the microstructures of LFC Al–Si–Cu alloys; the analyzed microstructure contains pores and hard inclusions, i.e. eutectic Si, iron-intermetallics, and Al_2Cu phases. 2D surface examination was performed on the sample to reveal the characteristics of eutectic Si phase, 3D characterization for the pores, iron-intermetallics, and Al_2Cu phases were performed on the studied specimens by Lab-CT, and the images obtained in the as cast and heat treated condition were registered using Avizo before image analysis.

5.3.1 Eutectic Si characterization

The morphology of eutectic Si as function of heat treatment time is demonstrated in Figure 5-4. Eutectic Si without heat treatment (as-cast) occurs in platelets form (Figure 5-4(a)). With a short solution time, some platelets Si particles were fragmentized into smaller platelets with spherical edges (Figure 5-4(b)). With a longer solution treatment at 495°C for 50h, the fragmented particles are partly spheroidized while some smaller Si particles were spheroidized to rounded shape (Figure 5-4(c)).

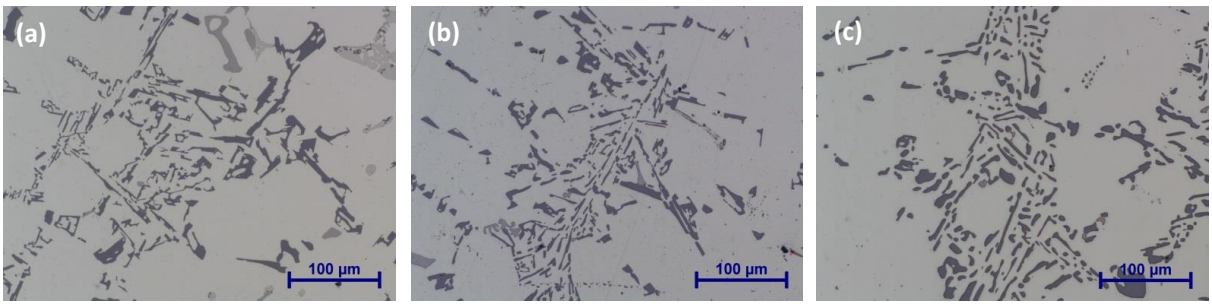

Figure 5-4: Microstructure of Al-Si-Cu alloy showing the morphology of Al-Si eutectic; (a) as-cast condition, (b) after solution treatment at 495°C for 2h30 and (c) after solution treatment at 495°C for 50 h

Quantitative metallographic characterization of eutectic Si particles was performed on the samples with different heat treatment conditions using image analysis in terms of average Si particle area (µm²), average Si particle length (µm) and sphericity. Figure 5-5(a) shows that the surface fraction of large particles (Feret diameter > 50µm) decreased with increasing solution time.

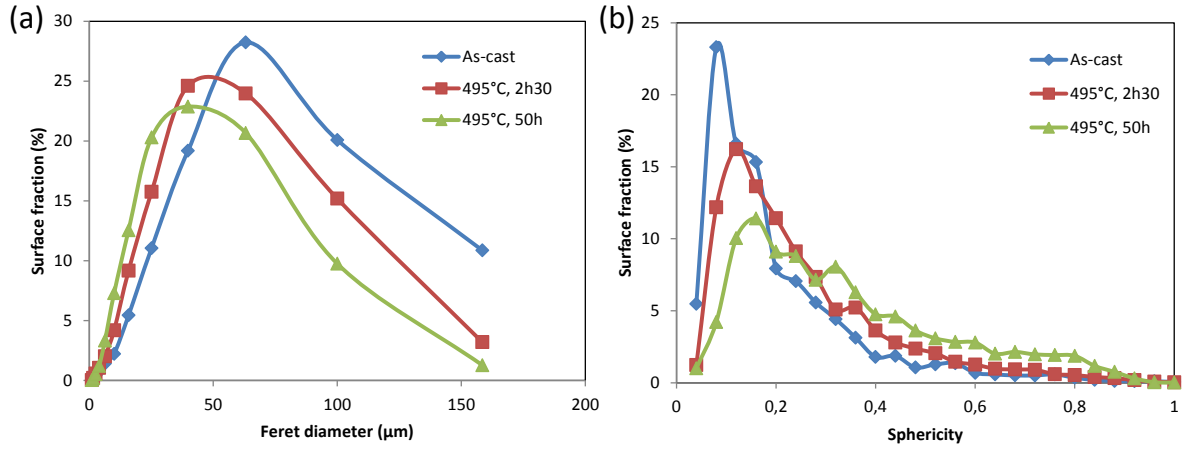

Figure 5-5: Distributions of (a) Feret diameter and (b) sphericity of eutectic Si particles in studied Al-Si-Cu alloy in as-cast condition and for different solution treatment durations

As Table 5-1 shows, in the as-cast condition, the Si particles were platelets with an average length of 10.52 µm. After the heat treatment for 2h30 at 495°C, the average Si particle area and length decreased (taking into account the standard deviation), whereas the Si particle density increased somewhat from 1416 to 2560 particles/mm², i.e., by about 80%. These results show that the Si

platelets underwent partial fragmentation. When the solution time increased to 50 h, the average Si particle area, length and the particle density decreased slightly. Besides, the decrease in the Si particle density from 2560 Nb/mm²to 2050 Nb/mm² with heat treatment increase from 2h30 to 50h (Table 5-1) may be attributed to the corsening of Si particles (El Sebaie, Samuel et al. 2008).

Table 5-1: Silicon particle characteristics following different solution treatment conditions

Heat treatment condition	Particle area (μm²)		Particle length (μm)		Density (particles/mm²)
	Av.	SD	Av.	SD	
As-cast	46.04	137.47	10.52	17.02	1416
495°C, 2h30 + 200°C,150h	35.03	95.66	10.00	13.92	2560
495°C, 50h + 200°C, 200h	34.78	82.19	9.26	11.80	2050

In addition, the heat treatment also can affect the morphology of the eutectic Si particles. The distribution of sphericity of eutectic Si particles is plotted as a function of solution time in Figure 5-5(b). More eutectic Si particles with sphericity between 0.05 and 0.2 were present in as-cast sample as compared to samples heat treated at 495°C. Increasing the solution time from 2h30 to 50h, increases the amount of particles with sphericity above 0.3. This means that the amount of eutectic Si with plate-like morphology decreased with an increase of solution treatment time: the longer the solution treatment, the more eutectic Si shows a globular morphology. Therefore, the experimental evidence indicates that increasing the solution treatment time causes the plate-like eutectic silicon phase to become fragmented and spheroidal in shape.

5.3.2 Al_2Cu phase

As mentioned in Chapter 1, copper forms an intermetallic phase with aluminum that precipitates during solidification either as block-like Al_2Cu or in eutectic form as ($Al+Al_2Cu$). These copper containing phases are easily distinguishable under X-ray tomography (voxel size = 2μm).

In order to study the effect of solution heat treatment on the dissolution of the Al_2Cu phase, the characteristics of the Al_2Cu phase were quantitatively examined through Lab-CT in the as-cast studied Al-Si-Cu alloy and after different solution treatment conditions.

The 3D analysis provides detailed information regarding the spatial distribution of the Al_2Cu phase. 3D renderings of Al_2Cu phase in specimen HT1a, HT1b and HT2 before and after the heat treatment are shown in Figure 5-6, Figure 5-7 and Figure 5-8 respectively. The distribution of Al_2Cu phase was observed in all the specimens. The dissolution is seen to increase with increasing solution time (2h30 to 50h) at 495°C.

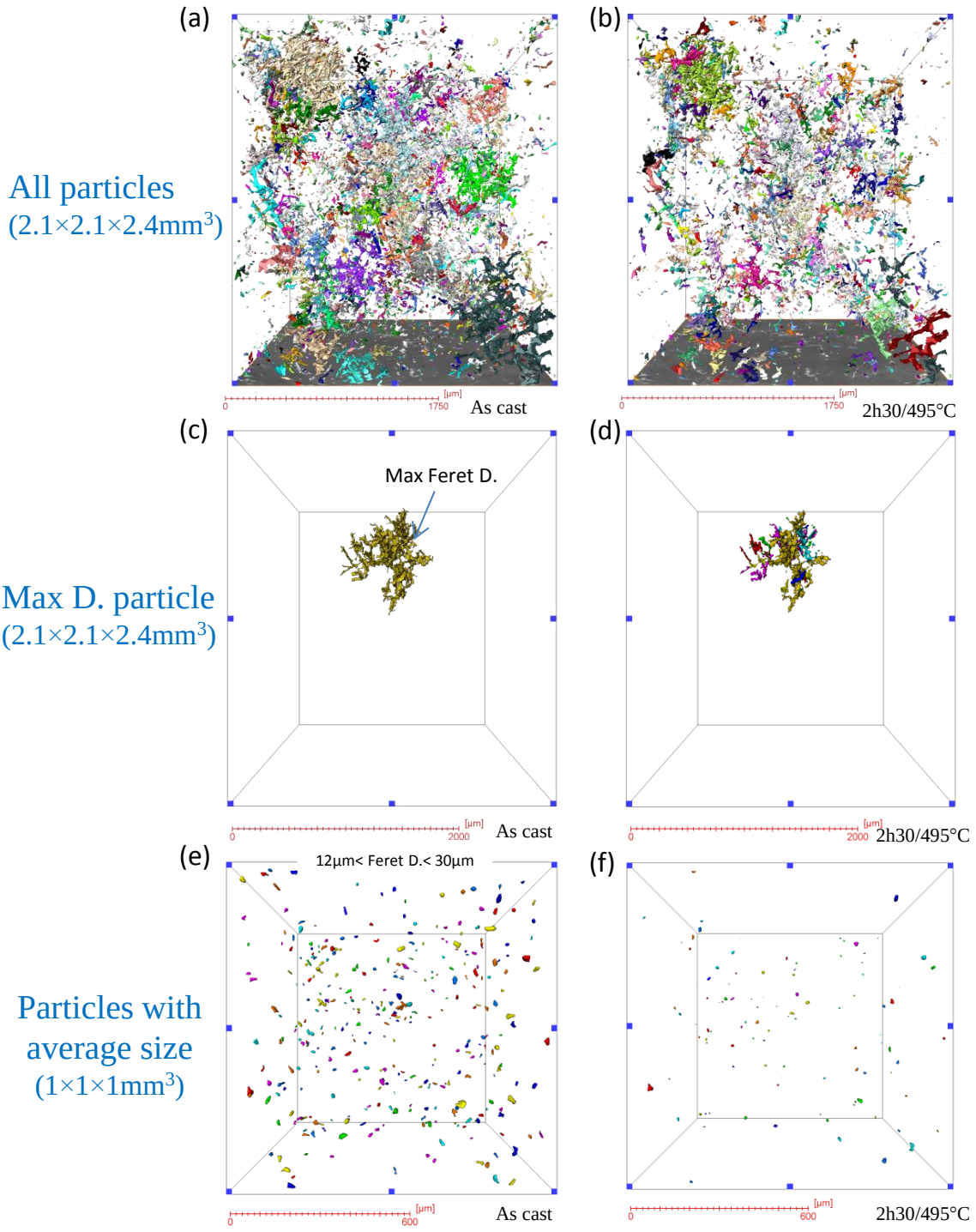

Figure 5-6: 3D rendering of the Al_2Cu phase, from top to bottom: all the particles and the largest particle in the same 2.1×2.1×2.4 mm^3 region, particles having a Feret diameter between 12 to 30µm in a sub-volume (1×1×1 mm^3) at: (a, c and e) as-cast condition and (b, d and f) after 2h30 at 495 °C for specimen HT1a

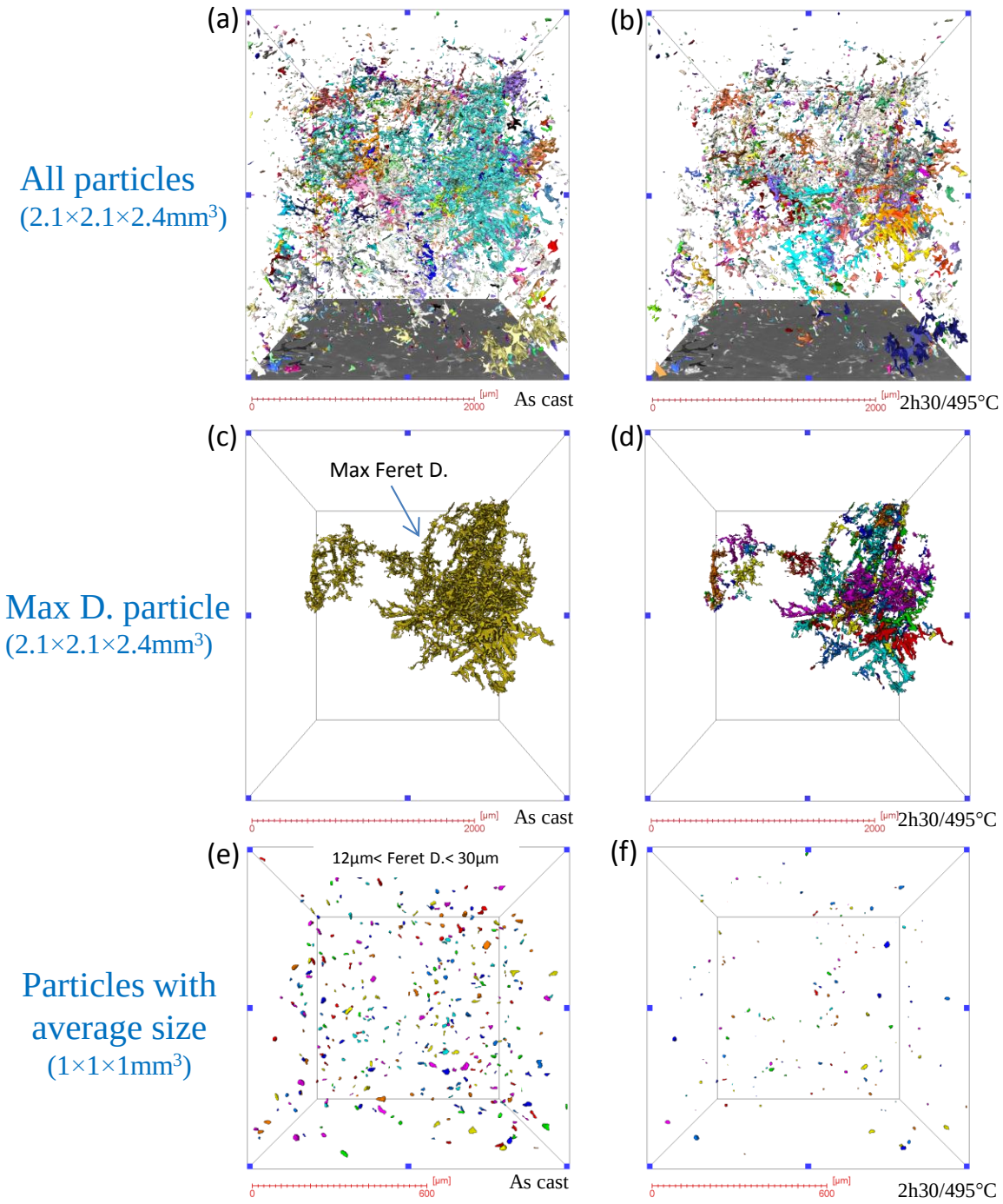

Figure 5-7: 3D rendering of the Al_2Cu phase, from top to bottom: all the particles and the largest particle in the same 2.1×2.1×2.4 mm^3 region, particles having a Feret diameter between 12 to 30µm in a sub-volume (1×1×1 mm^3) at: (a, c and e) as-cast condition and (b, d and f) after 2h30 at 495 °C for specimen HT1b

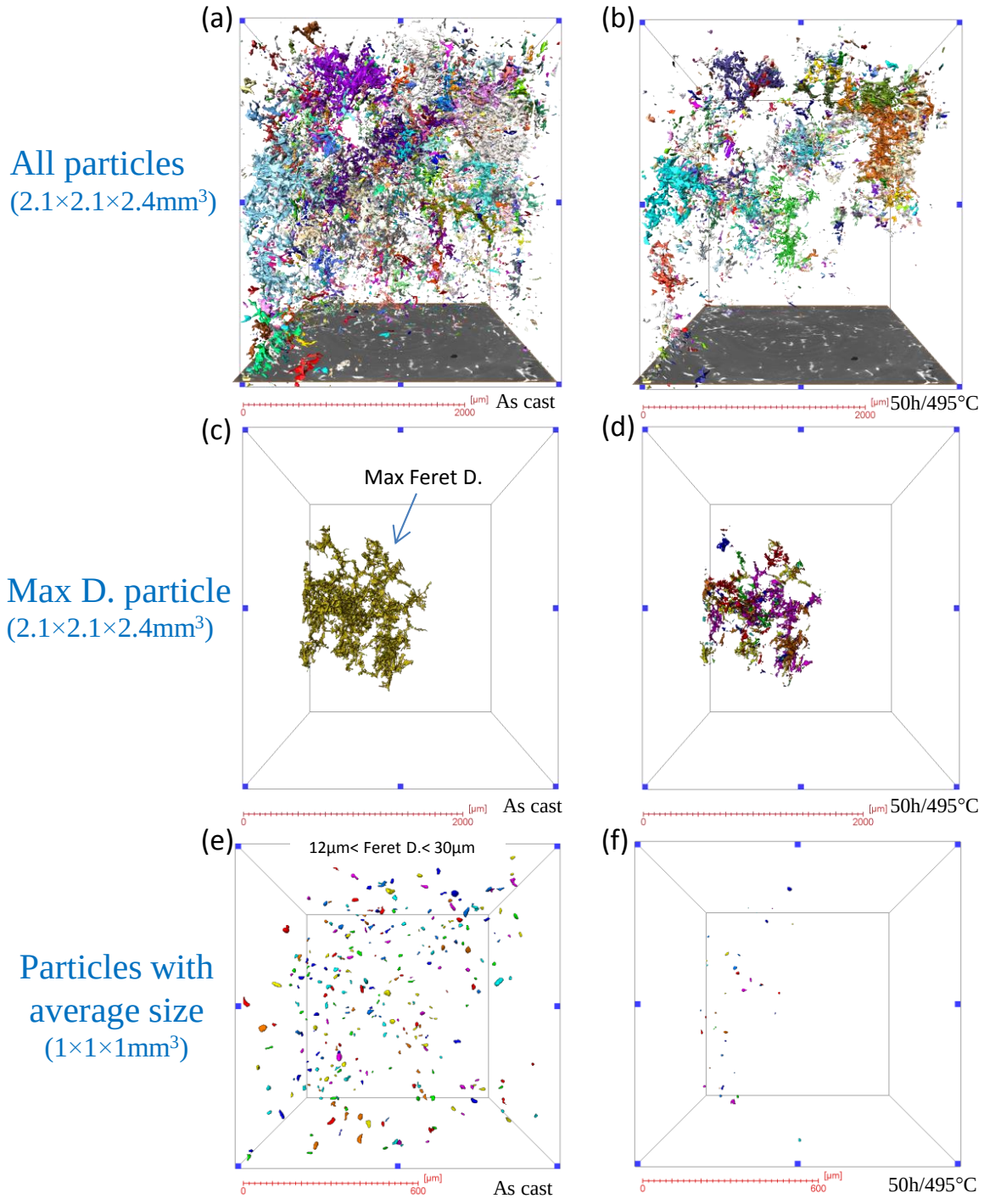

Figure 5-8: 3D rendering of the Al_2Cu phase, from top to bottom: all the particles and the largest particle in the same 2.1×2.1×2.4 mm^3 region, particles having a Feret diameter between 12 to 30µm in a sub-volume (1×1×1 mm^3) at: (a, c and e) as-cast condition and (b, d and f) after 50h at 495 °C for specimen HT2

Firstly, the heat treatment reduces the number of objects, i.e. unconnected Al_2Cu particles. The number of Al_2Cu particles in the ROI (10.58 mm^3) of tensile test specimens decreases from 13996 ± 804 to 7980 ± 71 after the 2h30 of solution treatment.

The volume fraction of undissolved Al_2Cu phase was measured as a function of solution heat treatment time. Figure 5-9 reveals the progress of Al_2Cu phase dissolution in the specimens. After 2h30 of solution treatment at 495°C, the volume fraction of Al_2Cu phase decreases significantly from about 1.4 % to 0.86%, i.e., about 33% of the total Al_2Cu phase has been dissolved in the matrix. With an increase in the solution treatment time to 50 h, the Al_2Cu phase dissolution becomes slowlier, reaching a volume fraction of 0.66%, i.e. about 58% of Al_2Cu phase was dissolved.

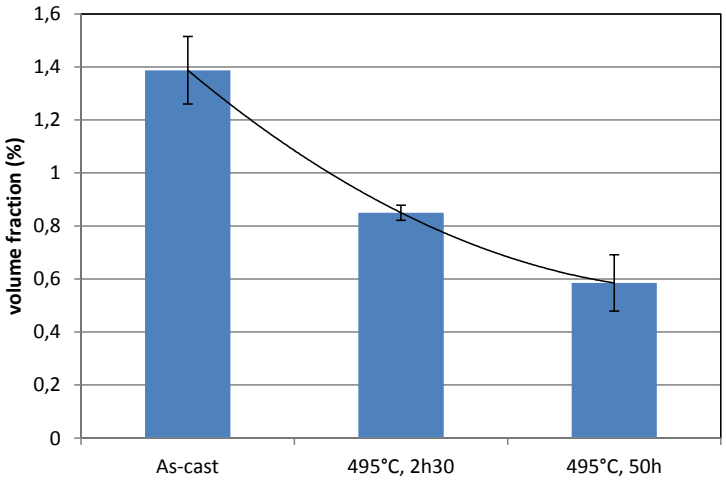

Figure 5-9: Al_2Cu phase dissolution in the studied specimens during solution heat treatment at 495°C as a function of solution treatment time

In addition, the largest Al_2Cu particles in each sample at different conditions are shown in Figure 5-6, Figure 5-7 and Figure 5-8(c) and (d) separately. The loss of interconnectivity is clearly revealed by the increase in the number of particles (different colours represent unconnected particles). As shown in Figure 5-10(a), (c) and (e), the size of the largest Al_2Cu particle decreased after the heat treatment.

As described in chapter 2, Feret diameter, which is defined as the maximum distance between two parallel planes restricting the object perpendicular to that direction, reflects the size of the object, Figure 5-10(a), (c) and (e) show that the number of particles with average size significantly decreased after the heat treatment. This result can be illustrated through the 3D rendering of Al_2Cu particles having a size that ranges from 12 µm to 30 µm in the sub-volume shown in Figure 5-6~8(e) and (f). After 50h at 495°C, most of the particles with average size have disappeared.

A granulometry analysis reflects the thickness of Al_2Cu phase. The granulometry distributions of Al_2Cu phase in Figure 5-10(b), (d) and (f) show that the thickness of all Al_2Cu particles decreases after the heat treatment, especially for the particles with average thickness (~12 µm). The maximum thickness of Al_2Cu phase was found to decrease from 44 µm to 40 µm in specimen B and C after

different heat treatment durations, which indicates that the large Al_2Cu particles are dissolved into smaller ones through heat treatment.

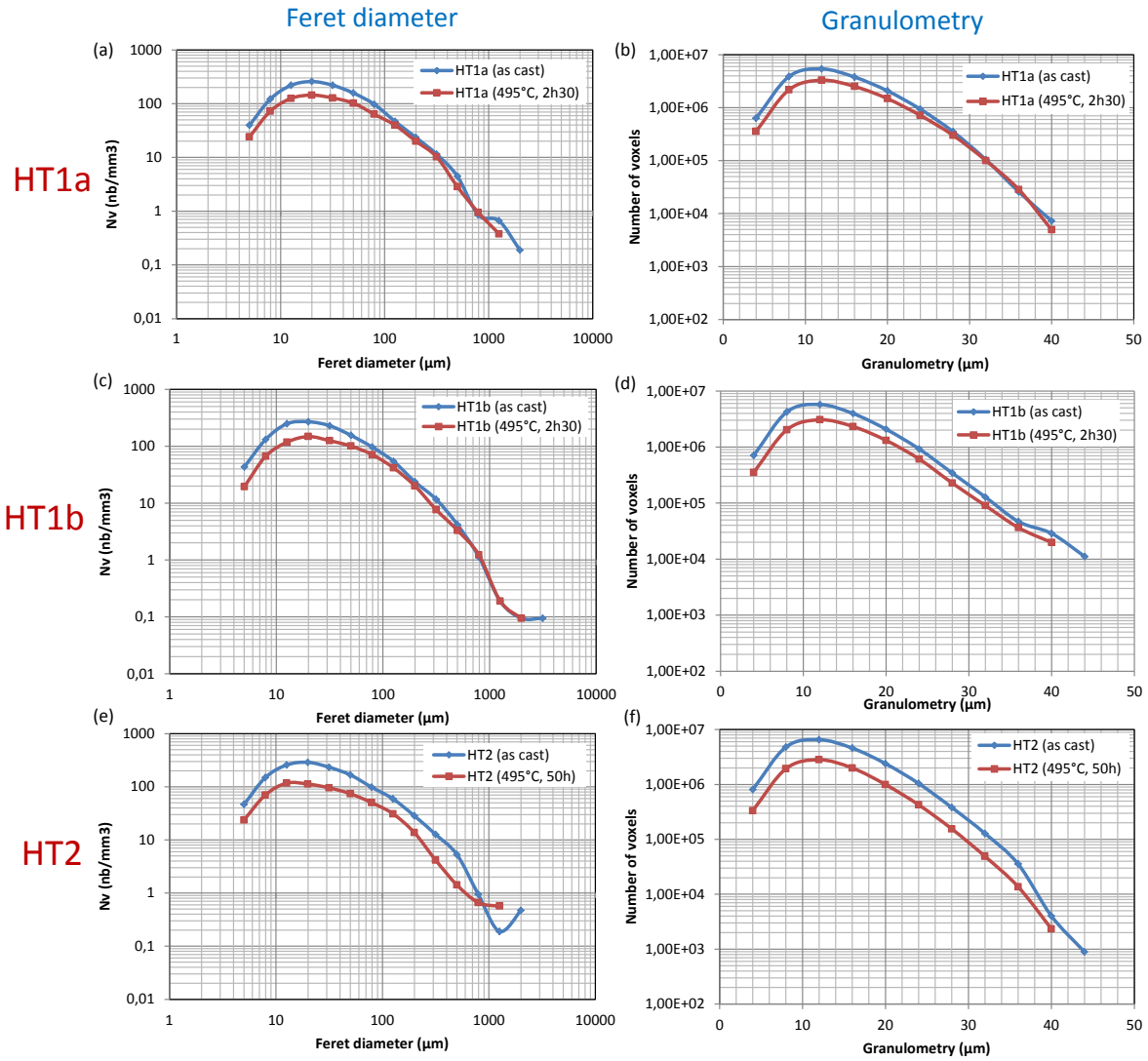

Figure 5-10: Distributions of Al_2Cu phase as functions of Feret diameter and granulometry in as-cast and solution heat treated conditions for specimen HT1a, HT1b (solution heat treatment of 2h30) and HT2 (solution heat treatment of 50h)

5.3.3 Iron-intermetallic

In this work, iron-intermetallic characteristics were also studied in the as-cast condition and after the different heat treatment conditions, the results of quantitative 3D analysis by Lab-CT are summarized in Table 5-2. The heat treatment of 2h30 at 495°C has no obvious effect on the volume fraction of iron-intermetallic in the specimen HT1a and HT1b. However, for specimen HT2, a slight decrease in volume fraction of iron-intermetallic phase was observed after the heat treatment at 495°C for 50h. These results suggest that the heat treatment time might affect the fragmentation and dissolution of iron-intermetallics.

Table 5-2: Volume fraction of Iron-intermetallic as a function of heat treatment time

Specimen	Heat treatment condition	Volume fraction (%)			Max Feret diameter (µm)	
		Before Heat treatment	After Heat treatment	Difference	Before Heat treatment	After Heat treatment
HT1a	495°C, 2h30 + 200°C, 150h	3.29	3.24	0.05	3486	3469
HT1b		4.52	4.48	0.04	3636	3613
HT2	495°C, 50h + 200°C, 200h	4.49	4.00	0.49	3753	3740

5.3.4 Porosity characterization in ROI

In order to avoid incipient melting of the copper-rich phase that would introduce micro pores, the temperature of conventional solution treatment for Al-Si-Cu alloys is restricted to 495°C (Mohamed and Samuel 2012). In the present work, the solution temperature of all the specimens is 495°C, and the comparison of 3D characterization for pores was performed on the specimens before and after the heat treatment using Lab-CT. The results confirmed that the porosity remains unchanged during solution treatment at 495°C, i.e. no incipient melting has occurred. Figure 5-11 shows the 3D rendering of the pores in different specimens (e.g. Specimen A, B and C) after heat treatment at a voxel size of 2 µm.

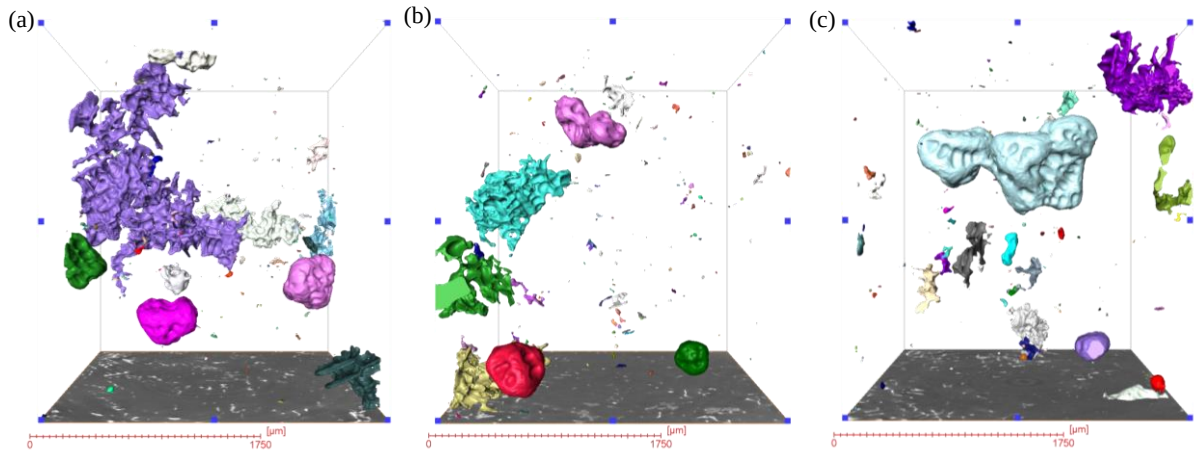

Figure 5-11: 3D rendering of pores in the ROI for specimen (a) HT1a, (b) HT1b and (c) HT2. (Dimension: 2.1× 2.1×2.4 mm^3)

The pores characteristics for the three specimens are summarized in Table 5-3 while the distributions of pores are shown in Figure 5-12.

Table 5-3: Porosity characteristics as a function of heat treatment conditions.

Specimen	Heat treatment condition	Volume fraction %	Feret diameter (µm)		Analysed volume (mm^3)
			Av.	Max.	
HT1a	495°C, 2h30 + 200°C,150h	2.04	46	1913	10.58
HT1b		1.09	42	1094	
HT2	495°C, 50h + 200°C,200h	1.33	41	1175	

In Figure 5-12, the first peak in the number distribution corresponds to small pores with a size about 20~30µm. The average size of the pores in these three specimens did not appear to be much different from each other.

For specimen HT1a, the volume fraction of pores in the ROI reaches up to 2.04%. The largest surface shrinkage pore has a 1923 µm Feret diameter (Figure 5-12) and represents most of the pores volume fraction (~45%). The volume fraction of porosity in specimen HT1b and HT2 are 1.09% and 1.33%, respectively, which is close to that measured in the large volume of studied material without any heat treatment in chapter 3 (~1%). The largest pore in specimen HT1b has a Feret diameter of 1.09 mm, which is the typical size for large defects in this material. The maximum size of pores in specimen HT2 is about 1.18 mm. This subsurface pore occupies about 68% of the total pores volume in the ROI. Taking into account the pores characteristics in the studied specimens and the results of FE simulations on realistic 3D meshes of the porous matrix, large pores may have a significant influence on tensile behavior.

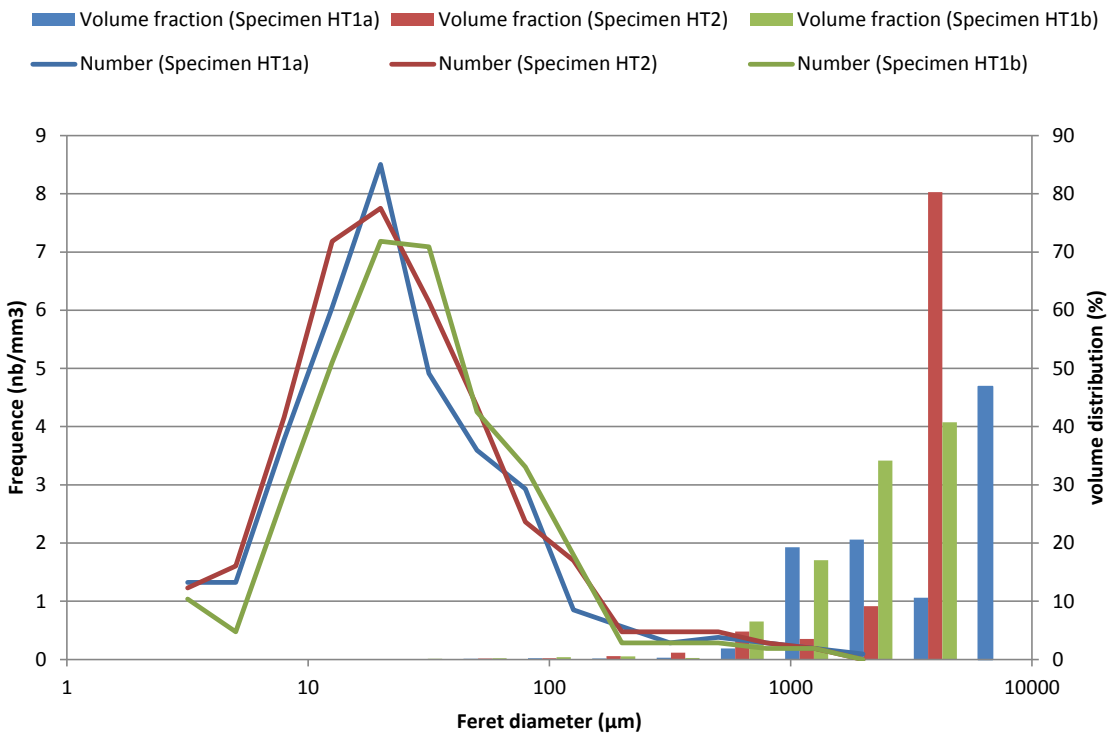

Figure 5-12: Size distributions of pores in the ROI of specimen HT1a, HT1b and HT2

5.4 Tensile tests with 3D in-situ observation

Tensile tests were performed step by step until final failure under Lab-CT on these three samples (i.e. Specimen HT1a, HT1b and HT2). Some parameters of the in-situ tensile test are summarized in Table 5-4.

Table 5-4: Results of in-situ tensile test

Specimen		**HT1a**	**HT2**	**HT1b**
Heat treatment conditions		495°C, 2h30 + 200°C,150h	495°C, 50h + 200°C,200h	495°C, 2h30 + 200°C,150h
Number of scan steps		6	14	21
Final failure	**Normal stress**	165MPa	187MPa	186MPa
	Location	Inside ROI		
Analysis zone for DVC		660×660×500 pixels	730×730×730 pixels	750×750×750 pixels

Specimen HT1a broke at a lower applied load compared to Specimen HT2 due to the largest pore volume fraction (2.04 %) in the ROI of specimen HT1a. Thus, in order to study the real damage mechanisms of the sample, a supplementary test was performed on specimen HT1b, which has the same heat treatment condition as specimen HT1a but less pores. In addition, due to the brittle fracture mechanism of studied material, the specimen will break as soon as the force is larger than the ultimate tensile strength. Thus, in order to better observe the crack growth, numerous scan steps were performed above the yield strength and slightly below the UTS, such as in specimen HT1b and HT2.

In order to reduce the duration of the calculation time, the displacement and strain fields were computed by DVC on a subvolume of the scan containing all the observed cracks during the tensile test and the final fracture path.

The average strains in the analysis zone for each step were calculated from DVC. Then, these data were used to draw the stress-strain curves of in-situ tests on Specimens HT1a/b and HT2 that were compared to a standard tensile stress-strain curve. As shown in Figure 5-13, the stress-strain curves of these three specimens are a little below the standard test. The reason can be that the small DVC analysis volume which contains almost all the large pores and main cracks shows higher mean strain value compared with value from the standard test, i.e. with appropriate extensometer measurement on larger specimens. Besides, large pores proportion in specimen HT1a (2.04%) reduces the effective bearing area seriously thus leading to a low tensile strength.

Therefore, the results confirmed that DVC measurements could be considered reliable.

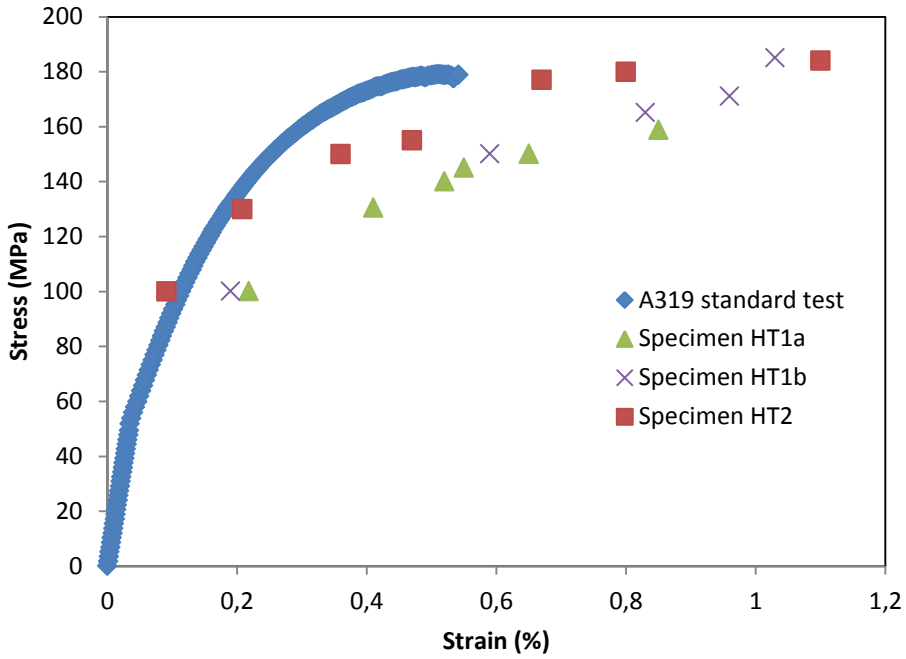

Figure 5-13: Stress-strain curves deduced from DVC measurements for Specimens A and B and from a standard test performed on LFC A319 alloy

5.4.1 Specimen HT1a

The final failure of Specimen HT1a occured trough a cluster of pores. As shown in Figure 5-14, four large pores, i.e. pore A, B, C and D, were observed on the fracture surface. Strain fields along the loading direction, which were measured from DVC at different loading steps before failure, were superimposed on one part of the fracture surface to allow comparison of the crack path with local deformation.

The tomographic images of Specimen HT1a at different cycles were analyzed slice by slice, no obvious cracks were observed at the first step (145 MPa) in the tomography images. However, slight strain localization was observed around the pores A and B (as shown in Figure 5-14(a)). The two main cracks, which nucleated around the pores A and B, were first detected in the tomographic image at an applied stress of 158 MPa, and then they were observed to grow with a further increase in the applied stress. As shown in Figure 5-14, the localizations of strain field, at the crack nucleation site and path, were observed to increase with the load increase. No obvious cracks were observed around the pores C and D before the final fracture.

In order to analyze the evolution of cracks during the tensile test, the fracture surface of Specimen HT1a was divided into cracks initiation and growth area and final fracture area, i.e. the fracture that occurred between the last scan and failure of the specimen; the pores C and D are located on the region of final fracture area.

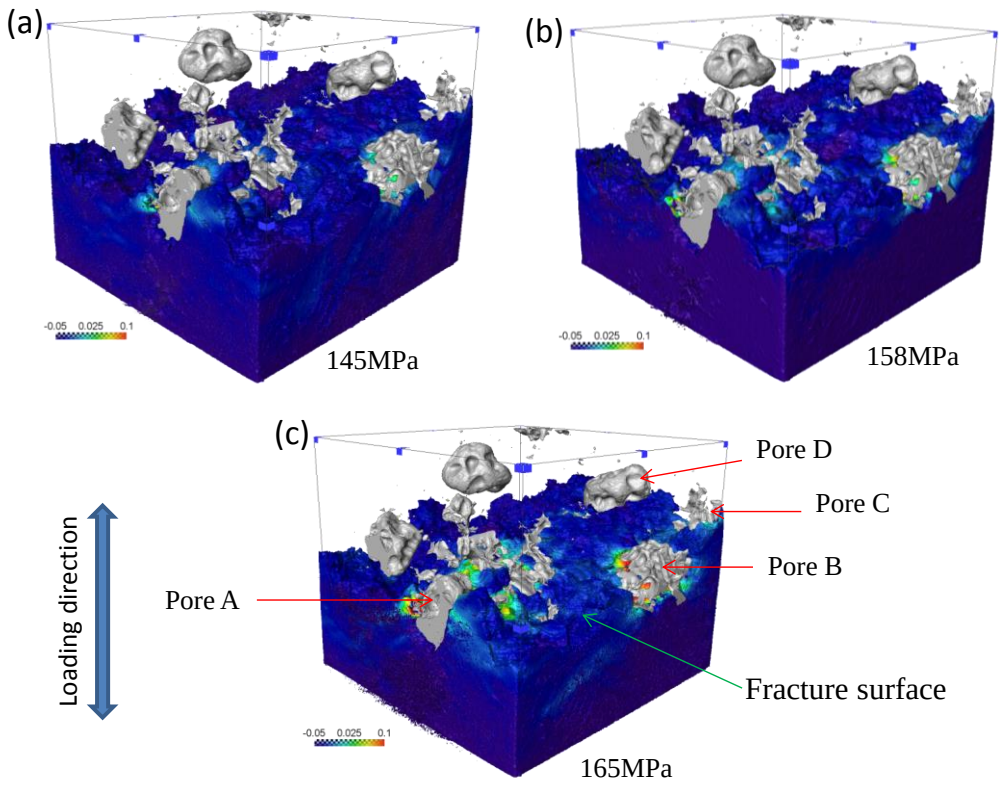

Figure 5-14: 3D rendering of pores and fracture surface of specimen HT1a: the ε_{zz} strain calculated by DVC for different loading steps are superimposed on the fracture surface at: (a) 145MPa, (b) 158MPa and (c) 165MPa

The results highlight the role of pores on crack initiation and final fracture of LFC A319 alloy during monotonic loading. In addition, some studies show (Wang, Limodin et al. 2016) (Dezecot, Buffiere et al. 2016) that the size and location of pores are important factors that control the tensile behavior of Al-Si alloy.

In the present work, Lab-CT techniques were used to determine the pore morphology (pores size and shape distribution), as well as pore location. The main parameters of the four pores which are located on the fracture surface are given in Table 5-5.

These four pores occupy 73% of all the pores volume in the ROI of specimen HT1a. The surface pore A, at the crack initiation site, is the largest pore in Specimen HT1a and large strain localization was observed in FE simulation results at this pore (Figure 5-1(c)); its Feret diameter is about 1913 µm, and its volume fraction is close to 47% of all pores in specimen HT1a. Moreover, this pore has a very irregular shape (F=0.0386) that is likely to introduce a greater amount of local stress concentration during the tensile loading so that cracks initiation was first observed at Pore A.

Surface pores B and C own the second and third largest Feret diameter after Pore A. Although the size of Pore B is only a little larger than that of Pore C, its volume is three times larger. This may be one of

the reasons why cracks initiated at Pore B rather than at C and it emphasizes the importance of the size of pores on cracks initiation.

Subsurface pore D has a relatively round shape (F=0.640). However, as it is the second largest pore in volume (Volume=0.0339mm^3) and as it is located in the same plane as Pore A, B and C perpendicularly to the loading direction, it might increase the stress concentration around Pores A and B, and decrease the effective bearing area during the tensile loading, thus leading to a quick final fracture when the cracks around Pores A and B are large enough.

Table 5-5: Parameters of the pores on the fracture surface of specimen HT1a

Pore	Feret diameter (μm)	Volume (mm^3)	Sphericity (F)	Type	Region
A	1913	0.1015	0.039	Surface pore	Crack initiation and growth zone
B	950	0.0175	0.139	Surface pore	
C	914	0.0054	0.108	Surface pore	Final failure zone
D	553	0.0339	0.640	Subsurface pore	

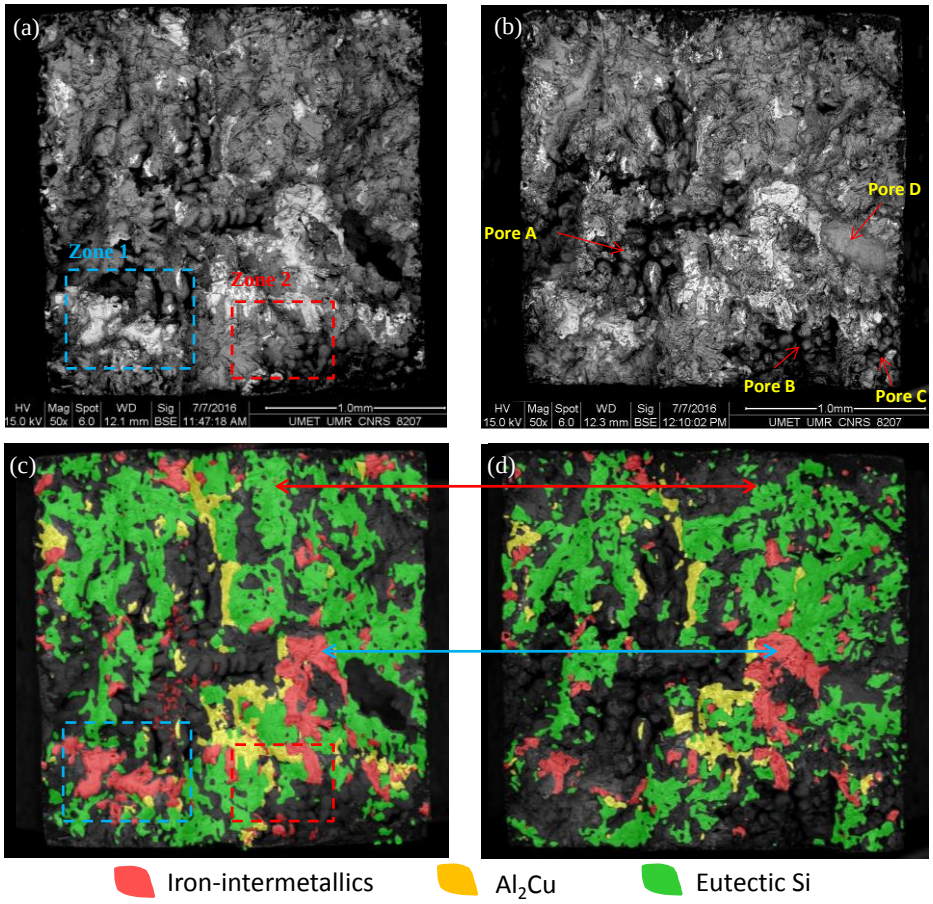

Figure 5-15: (a), (b) BSE images of the fracture surface of specimen HT1a and (c), (d) corresponding X-ray mapping images showing the distribution of hard inclusions (eutectic Si, iron-intermetallics, Al_2Cu phases); zone 1 and 2 are representative of the two main cracks initiation and growth zone

After final fracture, fracture analysis using SEM-EDS was performed on the fracture surface, BSE images of the two sides of the fracture surface are placed side by side (Figure 5-15 (a) and (b)). The corresponding X-ray elemental mapping of the fracture surface are shown in Figure 5-15 (c) and (d). The detected elements are Si, Fe and Cu that correspond to eutectic Si, iron-intermetallics, and Al_2Cu phases sequentially.

As shown in Figure 5-15, the progress of the crack through the matrix and iron intermetallics, Al_2Cu phase and Si particles can be observed. The four pores (i.e. Pore A, B, C and D) were marked with red arrows in Figure 5-15(b), and quantitative analyses show that these pores occupy about 30% of the cross-sectional area of the fracture surfaces of specimen HT1a. Meanwhile the hard inclusions (i.e. iron-intermetallics, Al_2Cu phase and Si particles) also occupy a large area proportion of the fracture surface: almost 9.5% iron-intermetallics, 23% eutectic Si and 5.6% Al_2Cu phase are detected in one part of fracture surface (Figure 5-15(c)). The surface fractions of hard inclusions in the fracture surface are higher than in the 2/3D examination results in the specimen HT1a (i.e. 3.2% for iron-intermetallics, 9.0% for eutectic Si and 1.3% for Al_2Cu phase). It indicates that the crack growth is prone to occur along eutectic Si, iron-intermetallics and copper containing phases.

As described in chapter 2, if the same constituents are identified in the same location on both fracture surfaces, the failure mechanism of hard particles is fracture. Otherwise, the failure mechanism is decohesion/debonding. As shown in Figure 5-15 (c) and (d), fracture of iron-intermetallics (see the blue arrows in Figure 5-15 (c) and (d)) and decohesion of eutectic Si (see the red arrows in Figure 5-15 (c) and (d)) were detected in final fracture regions. However, the failure mechanism of specimen HT1a seems to be more fracture in the hard inclusions than decohesion.

The two main cracks initiation and growth zone (zone 1 and 2) were marked with blue and red dotted box in Figure 5-15 (a) and (c), respectively. In zone1, the failure occurs by fracture of a massive brittle iron-intermetallic platelet. However, in zone 2, eutectic Si, iron-intermetallics and copper containing phases are all observed close to Pore B; this indicates that the initiation and growth of crack 2 mainly occur along the hard inclusions.

In order to study in more details the initiation of damage and its evolution during tensile loading, the 3D cracks were extracted using residual errors result from DVC measurements at each step of the tests; for more details, please refer to (Wang, Limodin et al. 2016) (Limodin, El Bartali et al. 2014). As shown in Figure 5-16, two main cracks in black (i.e. crack 1 and 2) were visible around the Pores A and B; the ε_{zz} strain calculated by DVC at an applied stress of 165 MPa (last step before final fracture) is superimposed on the pores. A good correlation can be observed between strain localization in the measured fields and the crack location at pores. Two small volumes in which the two main cracks were observed were extracted for the following analysis to illustrate the mechanisms of crack initiation and propagation in specimen HT1a.

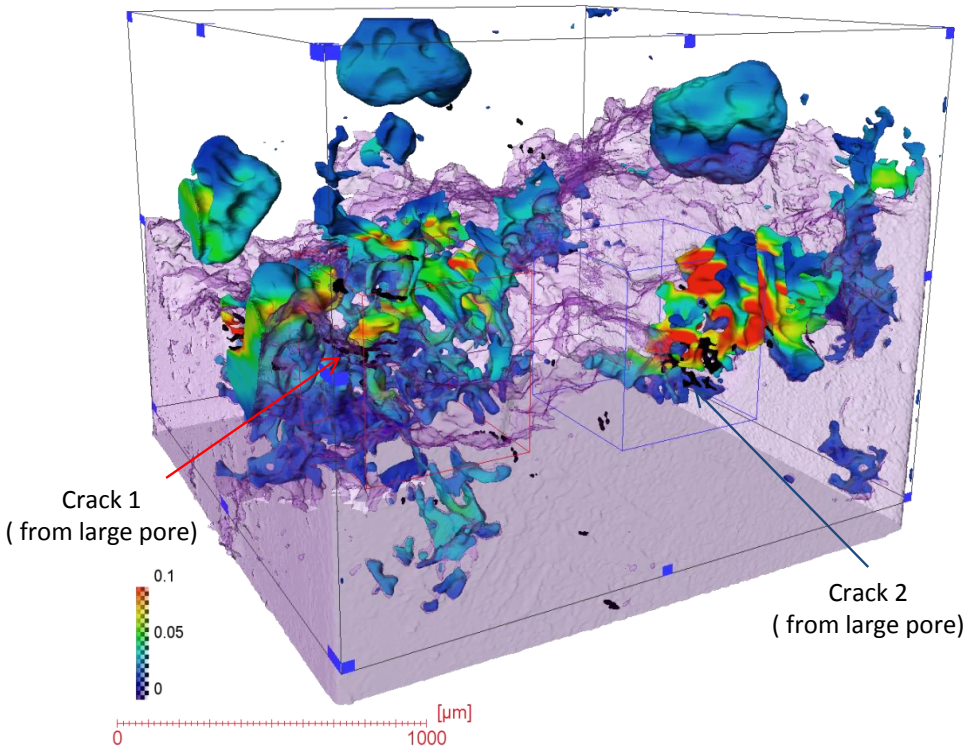

Figure 5-16: 3D rendering of pores and cracks (in black) with the fracture surface of Specimen HT1a; the ε_{zz} strain calculated by DVC at the step before final fracture (165MPa) is superimposed on the pores

5.4.1.1 Crack 1

Figure 5-17 shows the 3D evolution of the main crack 1 (see in Figure 5-16) around pore A during the tensile test. Pores are shown in translucent purple and cracks in red and the strain field calculated by DVC were superimposed on iron-intermetallics at different loading steps.

As shown in Figure 5-17(a), the iron-intermetallics are distributed in the vicinity of Pore A (in translucent purple). Indeed, although the crack is not visible at the first loading step (145MPa), a small strain value along the loading direction (less than 5%) is already visible at the crack location in the strain field of iron-intermetallic (Figure 5-17(a)) and it increases as the load is increased (see Figure 5-17(b)). This confirms that the crack initiation site is located on the iron-intermetallic which is around the tortuous pores.

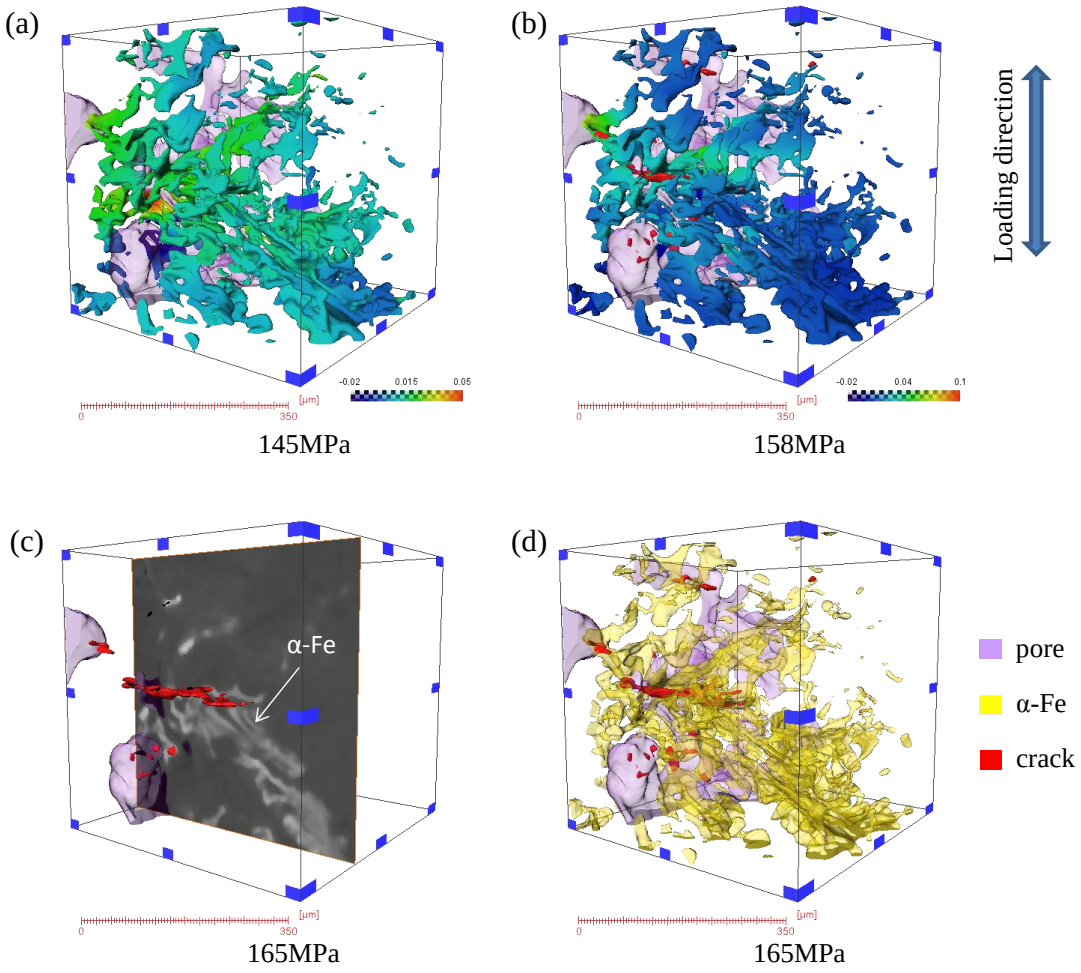

Figure 5-17: (a), (b) 3D rendering of pores (in translucent purple) and iron-intermetallics on which is superimposed the ε_{zz} strain calculated by DVC during the tensile test; 3D rendering of cracks (red) shown with (c) one slice of tomographic image and (d) 3D rendering of iron-intermetallics at the step before final fracture (165MPa)

The crack 1 was detected in the tomographic image at an applied stress of 158 MPa (see Figure 5-17(b)). Then it was observed to grow with a further increase in the applied stress. Finally, the evolution of cracks during the tensile test was analysed slice by slice by comparing the images and strain fields from the in-situ tensile test with microstructure in the high resolution tomographic images taken before the test.

One slice of high resolution tomographic image, which contains the pore and α-Fe phase, is shown with 3D rendering of cracks in Figure 5-17(c). It indicates that the crack went through the α-Fe phase. The translucent iron-intermetallic in Figure 5-17(d) helps to confirm that crack 1 has grown through the iron-intermetallic in an area that corresponds to the zone where fracture was observed at a platelet iron-intermetallic located around Pore A (see the blue dotted box in the Figure 5-15(c)) in the fracture surface observed using SEM. The result shows that the growth of crack 1 occurred along clusters of iron-intermetallic.

5.4.1.2 Crack 2

Figure 5-18 shows the evolution of crack 2 (see blue arrow in Figure 5-16), i.e. initiation and growth, in a subvolume during the tensile test. The strain fields along the loading direction were computed by DVC and the 3D rendering of pores and iron-intermetallics was superposed to these fields to allow comparison of the crack initiation with local deformation in Figure 5-18(a) and (b), respectively.

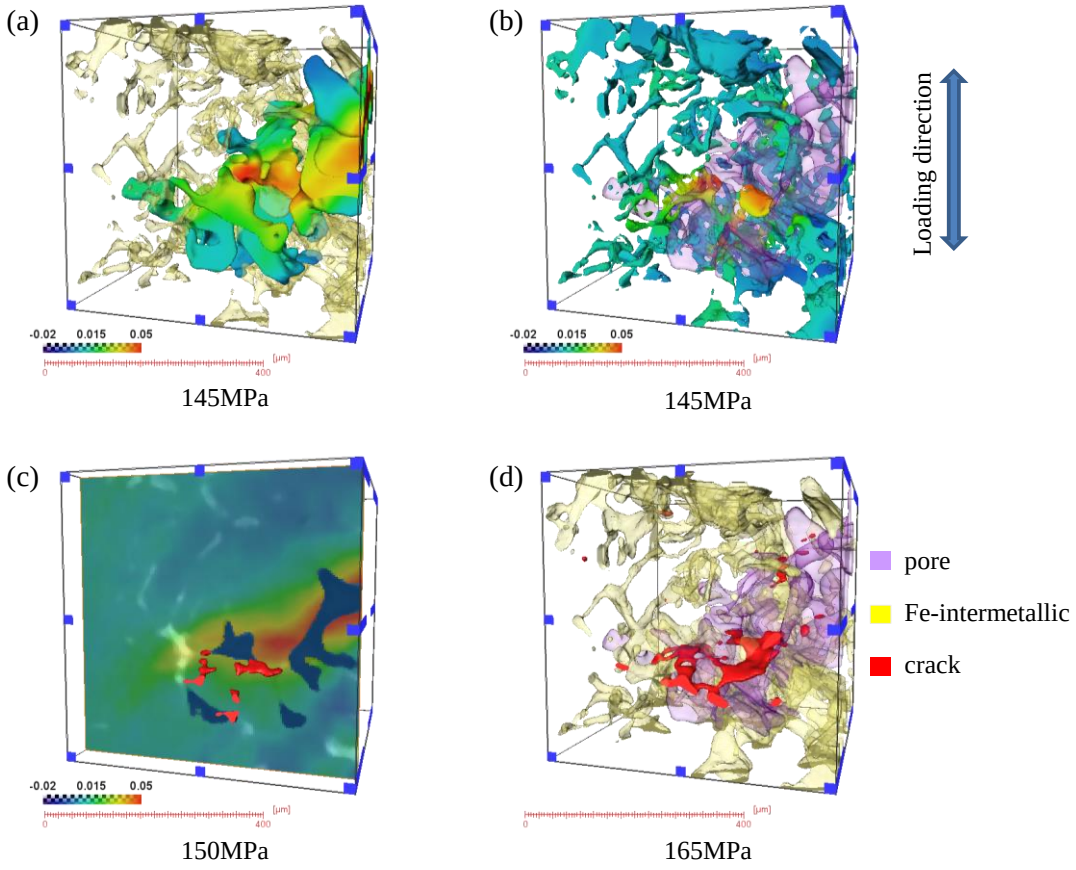

Figure 5-18: ε_{zz} strain superimposed on the (a) pores and (b) iron-intermetallics at 145MPa, and 3D rendering of cracks with (c) one slice and (d) microstructures in transparent

At an early loading step, i.e. at 145 MPa, no cracks can be detected from the tomographic images. However, as shown in Figure 5-18(a) and (b), slight strain localization has already been observed in the iron-intermetallics close to the pore; the nucleation of a crack (see Figure 5-18(c)) in this intermetallic becomes visible with the load increase (e.g 150 MPa). These relations emphasize the influence of strain localizations on cracks initiation. Thus, the crack 2 was found to initiate at iron-intermetallics where there is a stress concentration high enough due to the pore B.

Figure 5-18(d) shows that crack 2 at last loading step before failure (165 MPa), and the iron-intermetallics have been made transparent to render crack 2 visible. The analysis of tomographic image slice by slice shows that crack 2 did not just follow the iron-intermetallics, but it was found to grow along eutectic Si, iron intermetallics and copper containing phases together. This result also can

be confirmed by the observations of fracture surface by SEM-EDS, as shown in Figure 5-15(c) (the red dotted box): eutectic Si, iron intermetallics and Al_2Cu phases were all detected in zone 2.

5.4.2 Specimen HT2

The same analysis process for specimen HT1a was performed on specimen HT2. As shown in Figure 5-19, three large pores, i.e. pore A, B and C, were observed on the fracture surface; the measured strain fields along the loading direction are superimposed on the 3D rendering of the fracture surface.

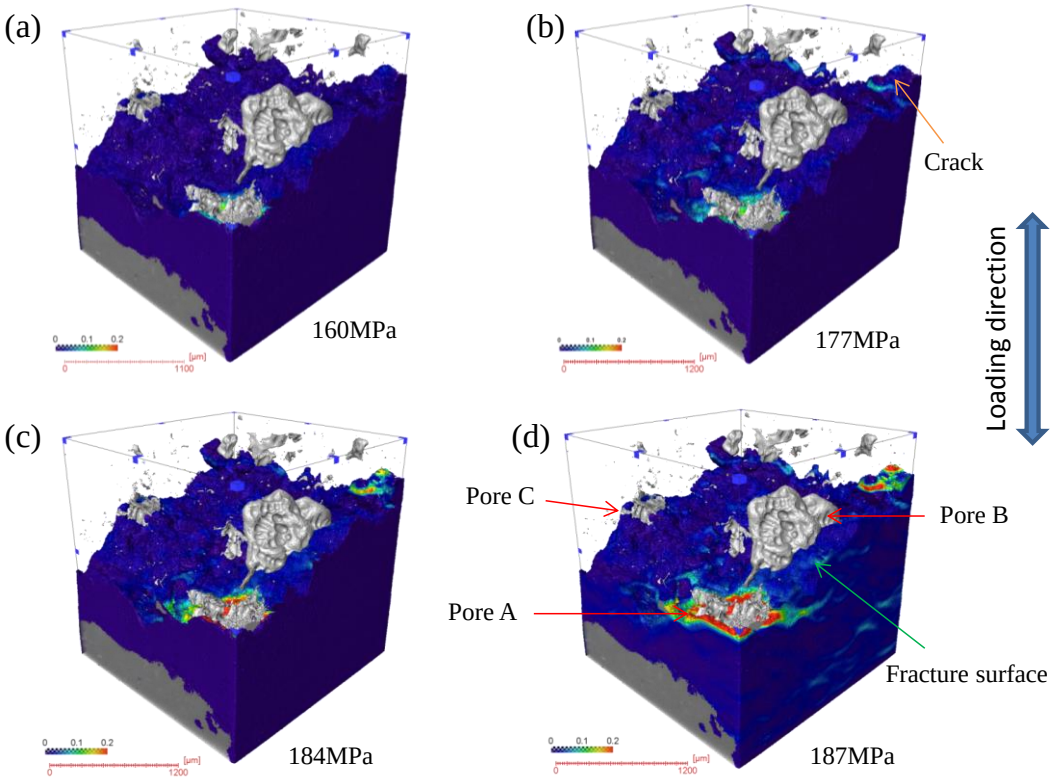

Figure 5-19: 3D rendering of pores on the fracture surface of specimen HT2, the ε_{zz} strain calculated by DVC for different loading step, (a) 160MPa, (b) 177MPa, (c) 184MPa and (c) 187MPa, are superimposed on the fracture surface

In Figure 5-19, Pores A, B and C are the three largest pores and they occupy 83% of all the pores volume in the ROI of specimen B while other pores are smaller than 511 µm; their main parameters are given in Table 5-6.

Table 5-6: Parameters of the pores on the fracture surface of specimen HT2

Pore	Feret diameter (µm)	Volume (mm^3)	Sphericity (F)	Type	Region
A	842	0.0177	0.078	Surface pore	Crack initiation and growth zone
B	1176	0.0976	0.422	Subsurface pore	
C	523	0.0037	0.164	Surface pore	Final failure zone

The tomography images analysis allows observing small cracks around surface shrinkage Pore A at an applied stress of 160 MPa (Figure 5-19(a)), while only a small crack was observed around the subsurface Pore B before the last loading step, although it is the largest pore. Therefore the morphology and location are two important factors for cracks initiation as large surface shrinkage pore is more dangerous than large subsurface round pore.

Although only a small crack nucleated around Pore B, and no crack was observed around Pore C before the final fracture, they are likely to have an influence on fracture damage by increasing the stress concentration around Pore A, which is located in the same plane perpendicular to the loading direction, hence facilitating the final fracture. Another main crack (see yellow arrow in Figure 5-19(b)) was observed to initiate close to the corner of the specimen at an applied stress of 177 MPa, and then it was observed to grow with a further increase in the applied stress. As shown in Figure 5-19, a good correlation was observed between the crack path and local deformation. Two high strain locations, which correspond to the visible cracks, were observed in the area around Pore A and in the corner of specimen. However, it should be noted that the large deformations in Figure 5-19(c) and (d) around cracks are caused by crack opening instead of by real deformation.

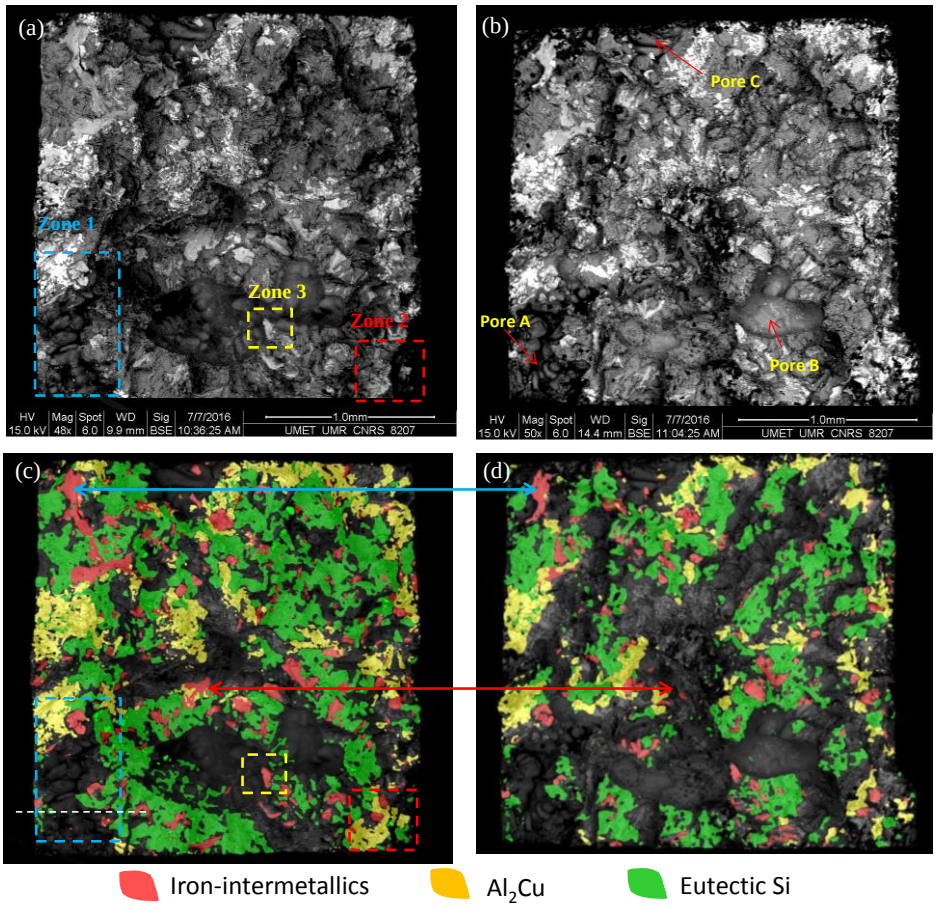

Figure 5-20: (a), (b) BSE images of the fracture surface of specimen HT2 and (c), (d) corresponding X-ray mapping images showing the distribution of hard inclusions (eutectic Si, iron-intermetallics, Al_2Cu phases); zone 1, 2 and 3 are representative of the three main cracks initiation and growth zone

As shown in Figure 5-20, SEM-EDS analysis was performed on the fracture surface of specimen HT2. The areas where the cracks were observed to initiate and grow during the in-situ tensile test were marked by dotted box in Figure 5-20(a) and (c). They also correspond to the three main cracks detected from the slice by slice analysis of the tomographic images of specimen HT2 at different loading steps.

Quantitative analyses show that the three pores (i.e. pore A, B and C), which are marked with red arrows in Figure 5-20(b), occupy about 14% of the cross-sectional area of the fracture surfaces of specimen B. Meanwhile the hard inclusions, i.e. iron-intermetallics, Al_2Cu phase and Si particles, also occupy a large area proportion of the fracture surface. A high content (i.e. 12%) of Al_2Cu phases was detected as compared to the 3D examination result (i.e. 1.3%). Almost 9.3% iron-intermetallics and 28% eutectic Si were examined in one part of fracture surface (Figure 5-20(c)) while the 2/3D examination results in the specimen HT2 give only 4.0% of iron-intermetallics and 7.1% of eutectic Si. It indicates that the cracks growth and final fracture are prone to occur along eutectic Si, iron-intermetallics and Al_2Cu phases.

The decohesion and fracture of hard inclusions include eutectic Si, iron-intermetallics and Al_2Cu phases, which are observed in the fracture surface, as shown in Figure 5-20(c) and (d). Decohesion (see the red arrows in Figure 5-20(c) and (d)) and fracture (see the blue arrows in Figure 5-20(c) and (d)) of iron-intermetallics are found in cracks propagations regions, and the observations revealed that more fracture than decohesion is found in all fracture surfaces.

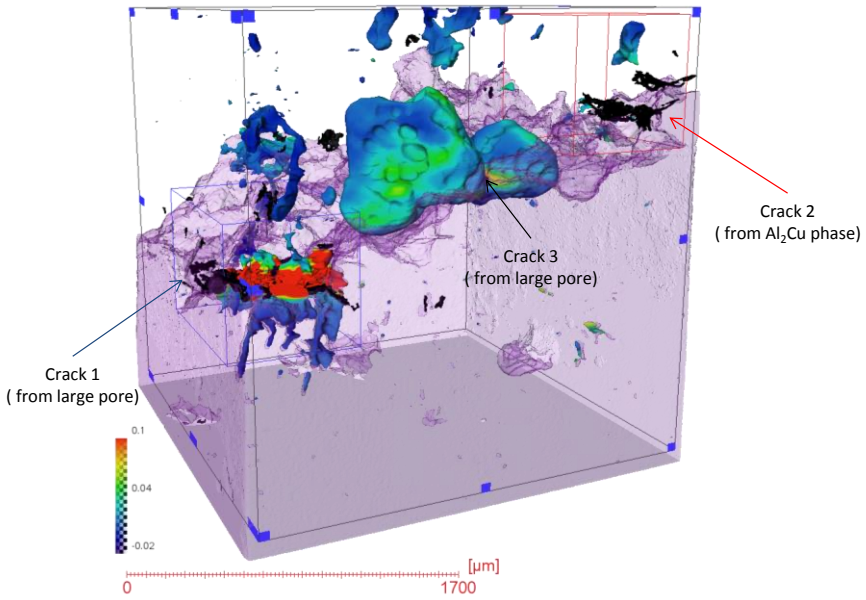

Figure 5-21: 3D rendering of pores and cracks (in black) with the fracture surface of Specimen HT2, the ε_{zz} strain calculated by DVC at the step before final fracture (187MPa) is superimposed on the pores

The 3D rendering of cracks at the last loading step before fracture is shown with the pores and broken specimen in Figure 5-21. Two large cracks in black (i.e. crack 1 and 2) were visible around the pore A and near the corner of specimen, respectively. The strain field calculated by DVC at an applied stress of 187 MPa (last step before final fracture) is superimposed on the pores. A good correlation can be observed between strain localization in the measured fields and the crack 1 location, which is vertical to the loading direction. Meanwhile, another small crack 3 was initiated from the corner of large subsurface Pore B. Three small subvolumes, in which the three main cracks were observed, were extracted for the following analysis to illustrate the mechanisms of crack initiation and propagation.

5.4.2.1 Crack 1

Figure 5-22 shows the evolution of crack 1 during the in-situ tensile test. Figure 5-22(a) shows that a slight strain localization was firstly observed around Pore A at the early step (i.e. 145 MPa), although no crack is visible at this loading step. With the load increase, the strain localizations become more obvious both at Pore A and the nearby Al_2Cu particles, and crack 1 was first observed around Pore A. As shown in Figure 5-22(b), the relation between strain localization at pore and crack are well observed. Then strain localizations were observed to grow with crack growth.

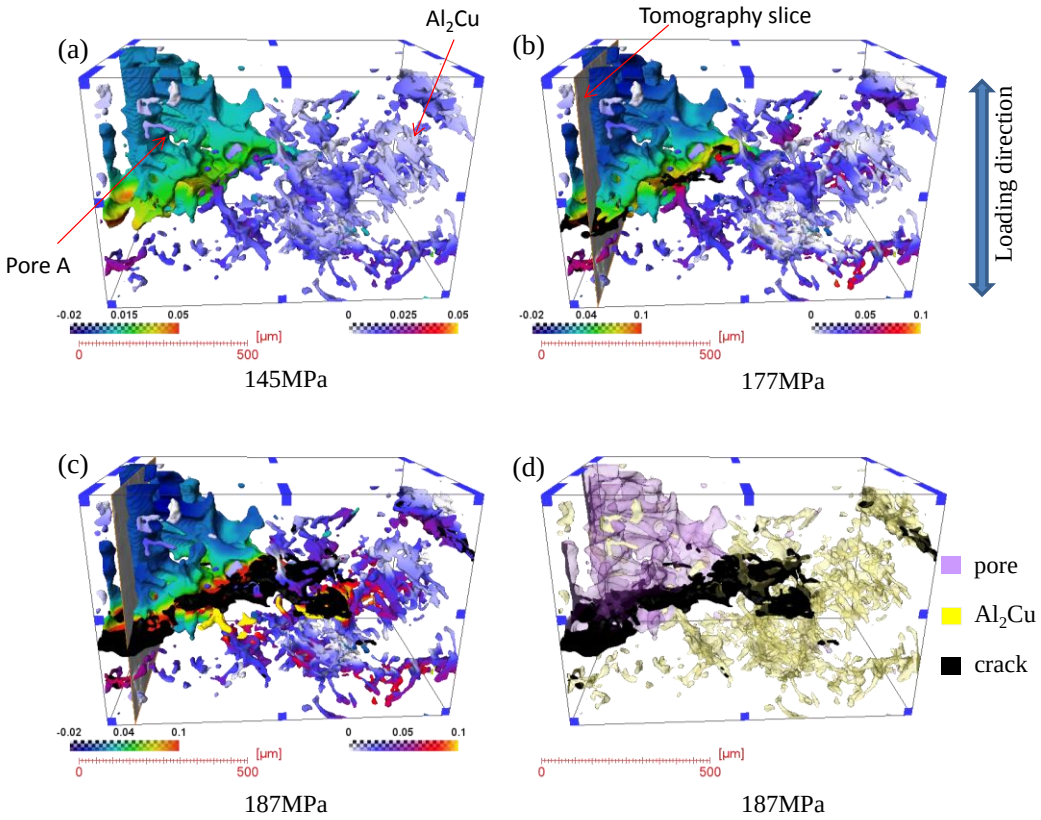

Figure 5-22: 3D rendering of the pore A and nearby Al_2Cu phases on which are superimposed the ε_{zz} strain calculated by DVC at the different maximum applied stresses, (a) 145 MPa, (b) 177 MPa; 3D crack (in black) at the step before final fracture (187MPa) through the Al_2Cu phase, (c) with strain field, (d) in transparent

Figure 5-22(c) shows the 3D rendering of crack 1 at the last loading step before failure, i.e. at 187MPa, and the corresponding high strain localizations at Pore A and Al_2Cu particles are well observed.

Because eutectic Si phase cannot be revealed using Lab-CT, the tomography slice that contains the crack shown in Figure 5-22(b) and (c) was compared to the fracture surface examined with EDS. At the slice location, which corresponds to the dotted white line in Figure 5-20(c) (in zone 1), eutectic Si was detected in the fracture surface.

The crack 1 initiated around Pore A and went through the Al_2Cu phase as shown in Figure 5-22(d) (Pore A and Al_2Cu particles are shown in transparency). Thus, from these observations, we can consider that crack 1 fractured a Si particle and advanced into iron-intermetallic and Al_2Cu particle.

5.4.2.2 Crack 2

The evolution of crack 2 in specimen HT2 at different loading steps is presented in Figure 5-23. The crack is extracted from the residual errors of DVC and rendered in black colour. The strain field was superimposed on the 3D rendering of Al_2Cu phases in the selected volume and corresponds to different loading steps before failure.

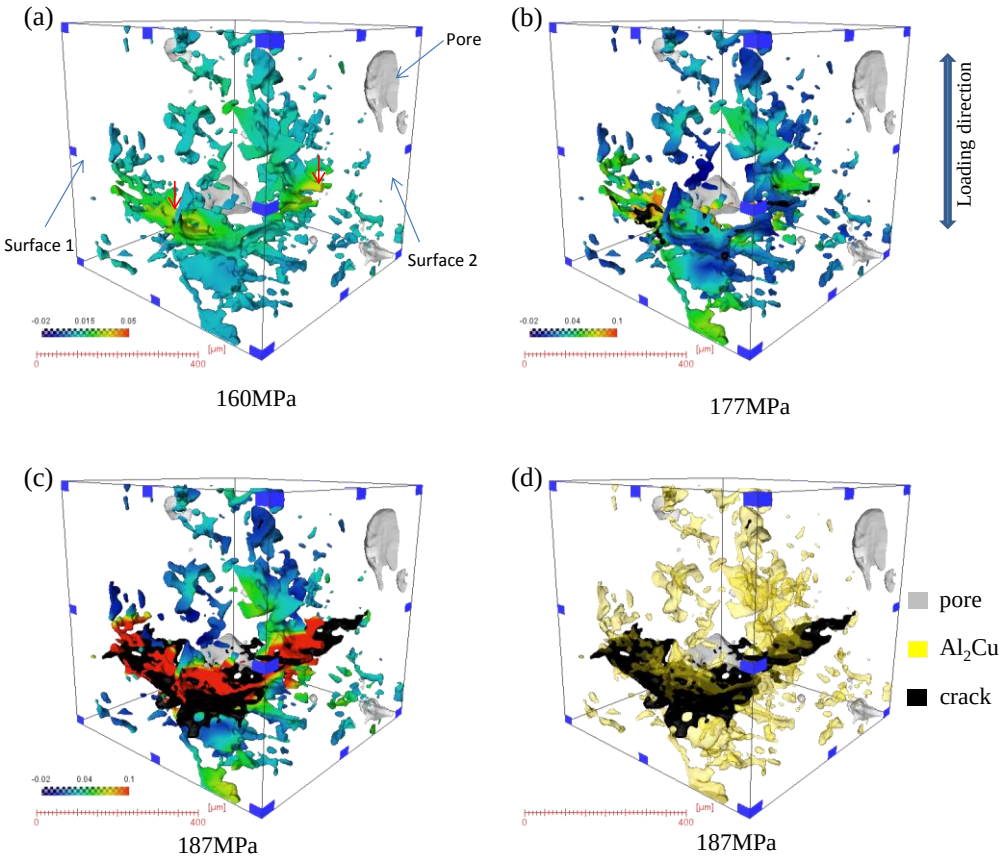

Figure 5-23: 3D cracks (in black) and 3D rendering of the Al_2Cu phases on which are superimposed the ε_{zz} strain calculated by DVC at the different maximum applied stresses: (a) 160 MPa, (b) 177 MPa, (c) 184 MPa and (d) 187 MPa

The strain localizations with a small strain value appeared in the Al_2Cu phases at an applied stress of 160 MPa (see the red arrow in Figure 5-23(a)). Indeed, no obvious cracks can be detected from the tomographic images at this loading step. Then crack initiation was clearly identified at an applied stress of 177 MPa, where cracks became visible, and a good correlation can be observed between strain localization and the crack location at Al_2Cu phase (Figure 5-23(b)). This result confirms that the strain localization calculated by DVC can predict the crack initiation site at an early loading step. Once the crack has initiated, the growth becomes visible with the load increase. Figure 5-23(c) shows strain fields on the Al_2Cu phases at an applied stress of 187 MPa, where growth of the crack is observed. Figure 5-23(d) shows that crack 2 seems to go mainly through the Al_2Cu phase close to the corner of specimen. This result is in accordance with the SEM-EDS observations, fracture of large Al_2Cu phase can be observed in the zone 2 of fracture surface (see Figure 5-20(c)) as expected.

5.4.2.3 Crack 3

Figure 5-24(a) and (b) show the strain field calculated by DVC at an applied stress of 150 MPa along the loading direction; the 3D rendering of pore B and of the iron-intermetallic nearby were superposed to this field to allow comparison between the evolution of crack and local deformation. Strain localization is well observed in the α-phase, which is located on the corner of the pore B, although no obvious crack can be detected at this loading step.

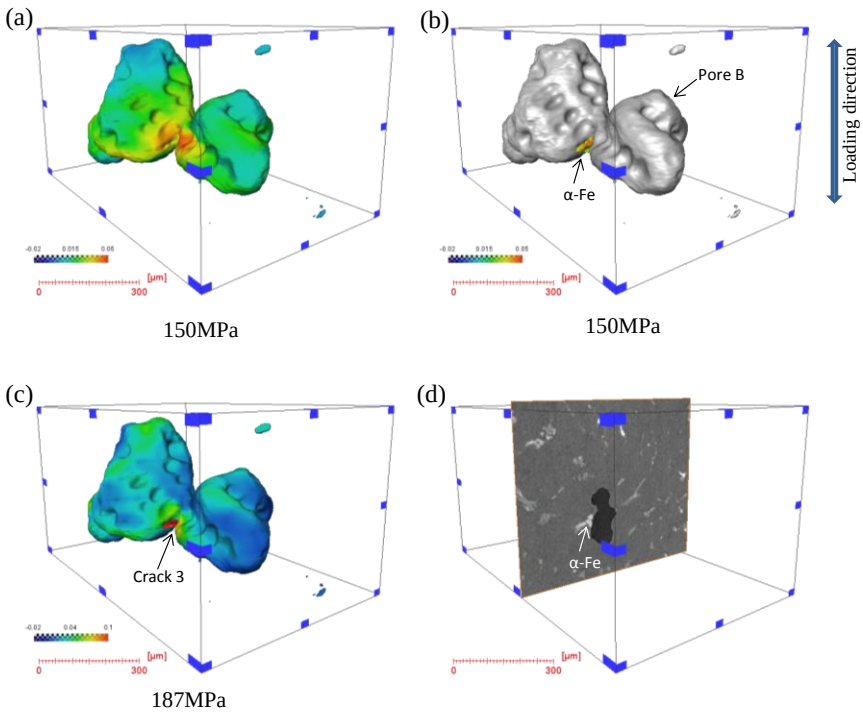

Figure 5-24: 3D rendering of (a) pore B close to (b) an iron-intermetallic on which was superimposed the ε_{zz} strain calculated by DVC at an applied stress of 150MPa. (c) 3D rendering of crack 3 (in red) with the pore B on which is superimposed the strain field before the final fracture. (d) One tomographic slice shows the location of iron-intermetallic

Strain localization was also observed to increase at increasing load and with the crack initiation at the applied stress of 160 MPa. However, once the crack is visible in the α-phase, it grows very slowly. As it can be observed in Figure 5-24(c) in which the crack 3 is represented in red and the strain field was superimposed to the pore at the last step before the final fracture, a good correlation is observed between the crack location and the strain localization.

Figure 5-24(d) shows the tomographic image slice where where crack 3 initiated in the α-phase. The fracture of this α-phase also can be identified from the SEM-EDS analysis of the fracture surface (see the yellow dotted box in Figure 5-20(b)).

5.4.3 Specimen HT1b

In-situ tensile test observation was also performed on specimen HT1b which was subjected to same heat treatment as specimen HT1a but contains fewer pores, i.e. 1.09% vs. 2.04%.

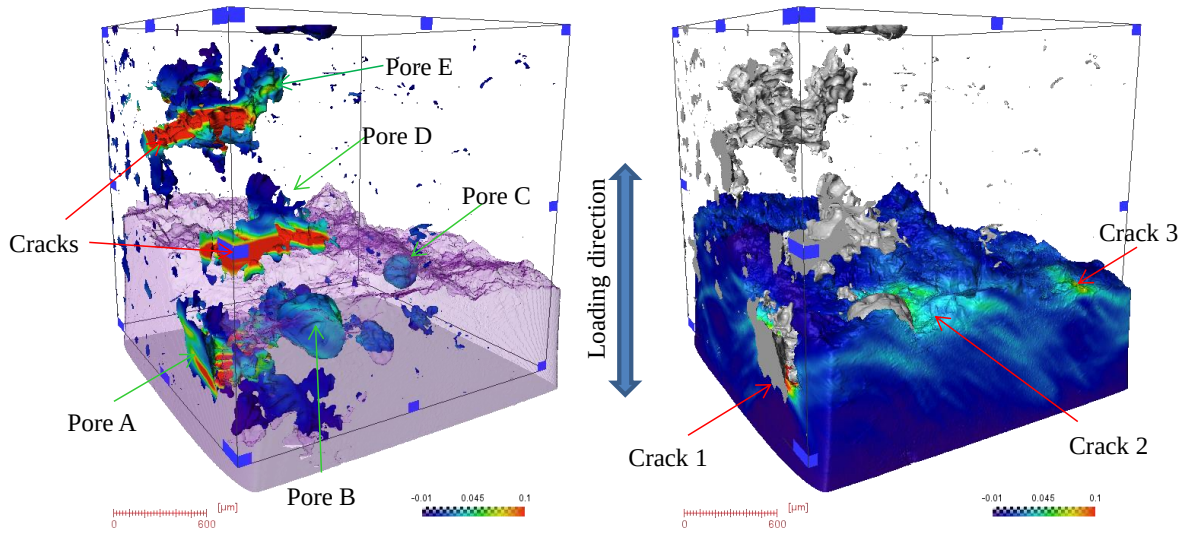

Figure 5-25: 3D rendering of pores and fracture surface of specimen HT1b: the ε_{zz} strain calculated by DVC for last loading step before failure (186MPa) is superimposed on the (a) pores and (b) fracture surface

As shown in Figure 5-25, the ε_{zz} strain, which was measured from DVC at last loading step before failure (186 MPa), was superimposed on the pores (Figure 5-25(a)) and one part of fracture surface (Figure 5-25(b)) of specimen HT1b. The evolution of cracks was analysed slice by slice in the tomographic images. A good correlation can be observed between strain localization in the measured fields and the cracks location.

Three main cracks (i.e. crack 1, 2 and 3) were observed during the tensile test. After initiation, they grew with increasing load, and then these three cracks connected and contributed to the final fracture.

Two secondary cracks were also observed close to the large surface pores D and E, which are located away from the final fracture surface.

As shown in Table 5-7, the pores A, D and E, as the three largest surface shirinkage pores, all act as cracks nucleation site. Hard inclusions such as iron-intermetallics and Al_2Cu phase were observed in the area around Pore A, D and E where cracks nucleated during the tensile loading. This result is consistent with previous observations of specimen HT1a and HT2, large surface shrinkage pores provide high stress concentration and cracks initiate around hard inclusions. No crack was observed around subsurface/internal round pore B and C before the final fracture of specimen HT1b. It proves that the morphology and location are important factors for cracks initiation.

Table 5-7: Parameters of the pores in the analysis volume of specimen HT1b

Pore	Feret diameter (µm)	Volume (mm^3)	Sphericity	Type	Region	Location
A	309	0.0039	0.069	Surface pore	Crack initiation and growth zone	Located on fracture surface
B	256	0.0048	0.728	Subsurface pore	Final failure zone	
C	183	0.0019	0.814	Internal pore		
D	418	0.0023	0.144	Surface pore	Crack initiation and growth zone	Away from fracture surface
E	712	0.0087	0.084	Surface pore		

From the slice by slice analysis of tomographic images, crack 2 and crack 3, which are located close to the surface of specimen (Figure 5-25(b)), are not initiated from iron-intermetallics and Al_2Cu phases. However, we cannot precise if these locations are due to the Si phase as Si could not be observed by Lab-CT. However, it may be confirmed by the SEM-EDS analysis as shown in Figure 5-26.

Zone 1, 2 and 3, which are marked with purple, yellow and red dotted box in Figure 5-26(b), represent the initiation and growth zone for cracks 1, 2 and 3, respectively. In zone1, eutectic Si, iron-intermetallics and copper containing phases are all observed close to pore A. In addition, the eutectic Si phase can be identified in the zone 2 and 3. Thus, we can suppose that the initiation of crack 2 and 3 occur at the eutectic Si phase, and then the nucleated cracks grow mainly along the hard inclusions. This observation is consistent with the study of (Wang 2015): crack was found to initiate from eutectic Si in the corner of two flat surfaces, and propagate along eutectic Si, iron-intermetallics and copper containing phases.

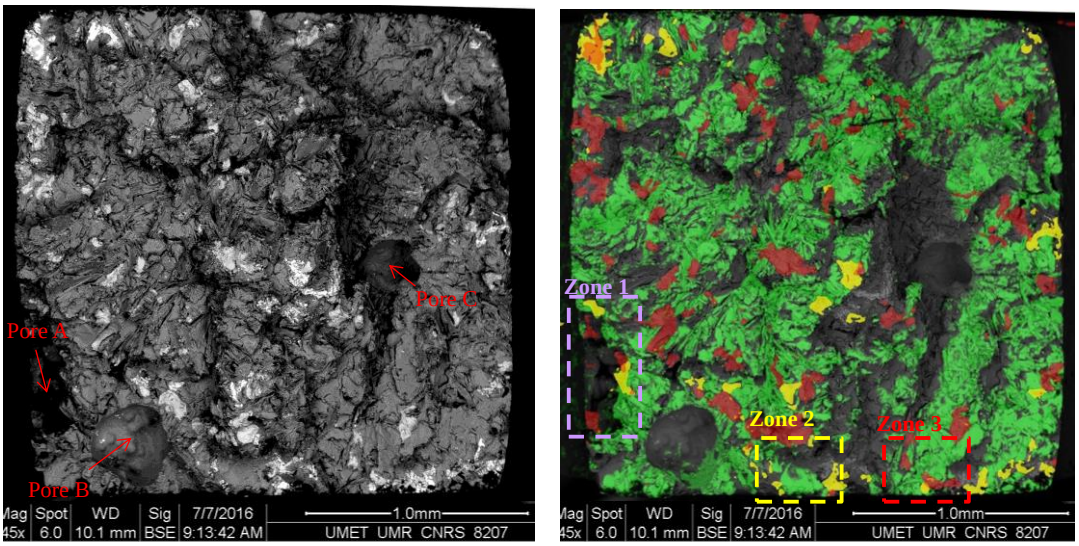

Figure 5-26: (a) BSE images of the fracture surface of specimen HT1b and (b) corresponding X-ray mapping images showing the distribution of hard inclusions (eutectic Si, iron-intermetallics, Al_2Cu phases); zone 1, 2 and 3 are representative of the three main cracks initiation and growth zone

5.5 Quantitative analysis

As shown in the previous results, strain localizations were observed in zones where cracks initiations were observed, and the localization is noticeable before the crack observation, thus the strain evolution at cracked particles until failure can be quantitatively assessed by DVC.

In this work, particles analyses with DVC were made in order to determine the strain behavior of Al_2Cu phase and iron-intermetallic in sample HT2. Determined local values from the analysis of strain fields obtained with YaDICs depend on the selected point locations (9 to 10 points were selected on each phase). The analysis of local strain values can clearly confirm the response of Al_2Cu phase and iron-intermetallic regarding the strain field evolution during the tensile loading.

Figure 5-27 illustrates the comparison between the DVC element size and the size of selected particles. The Von Mises' equivalent strain field measured at the last load step before final fracture is superimposed on the tomographic image. The selected points, which are inside the subset, can represent the Al_2Cu phase well.

The evolution of Von Mises' equivalent strain value in the selected particles (Al_2Cu-1 to Al_2Cu-9 and Fe-intermetallic-1 to Fe-intermetallic-10) as function of load step is shown in Figure 5-28 and Figure 5-29. The particles once broken are not shown in the Figure. It can be seen that the strain values in these particles increase with the load increase. The average local strain levels that lead to the cracking of particles are about 4.6±1.2% (standard deviation) for the Al_2Cu phase and 3.9±1.0% for the iron-intermetallics.

Chapter 5

The results indicate that in-situ tensile tests under Lab-CT analyzed with DVC techniques can successfully be used to quantify the 3D spatial and temporal strain patterns for the studied alloys. DVC is able to monitor the deformation at the microstructure level during the tensile test.

The quantitative DVC analysis highlights the possibility to understand the roles of the various hard inclusions (i.e. Al_2Cu phase and iron-intermetallic) on the damage mechanisms of LFC A319 through the local measurement of strain.

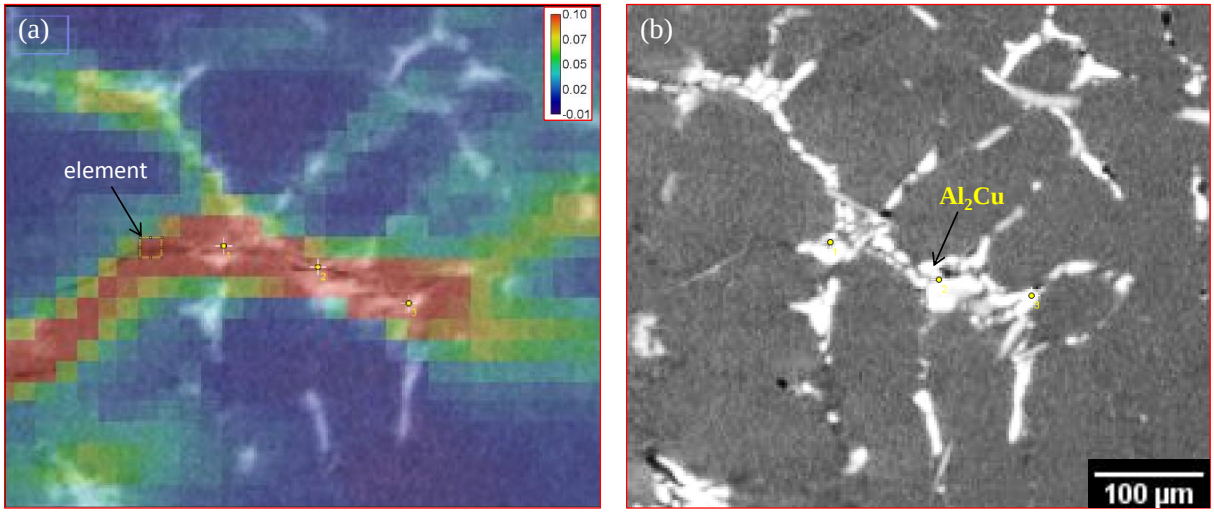

Figure 5-27: Comparison of DVC element size in the ε_{zz} strain field with the size of the selected particles

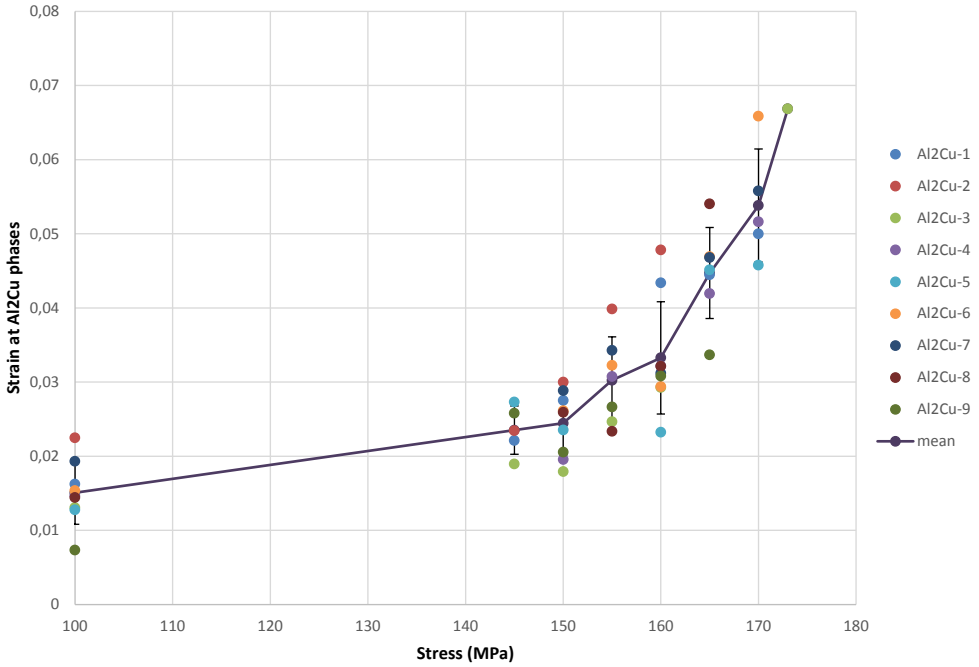

Figure 5-28: Evolution of the Von Mises' equivalent strain value in the Al_2Cu particles before the fracture during the tensile test

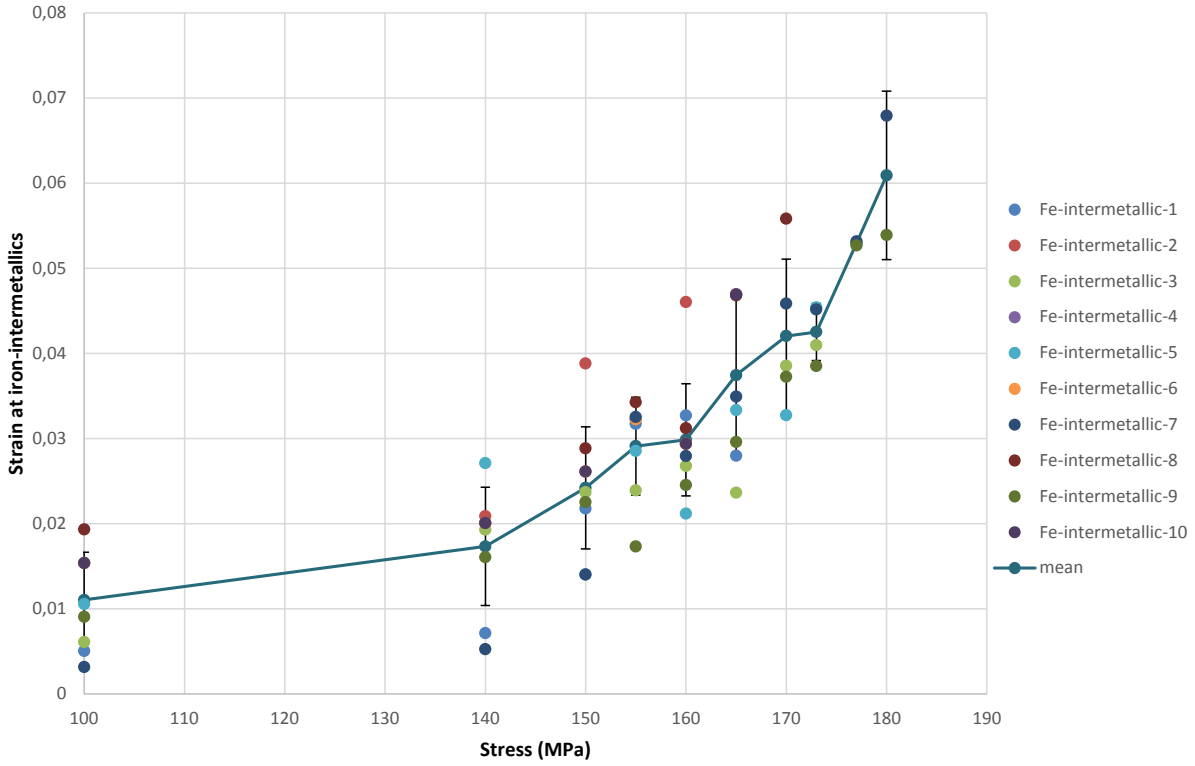

Figure 5-29: Evolution of the Von Mises' equivalent strain value in the iron-intermetallic particles before the fracture during the tensile test

5.6 Discussion

5.6.1 The effect of heat treatment on the microstructure

Microstructural characteristics such as the size, shape and distribution of the pores and Al_2Cu phase, as well as the morphologies and amounts of eutectic silicon particles and iron-intermetallic phases were analyzed in the studied alloys for different heat treatment conditions. The results presented above show that the heat treatment can affect the microstructural characteristics of hard inclusions in LFC A319 alloy.

5.6.1.1 Al_2Cu

Heat treatment affects the microstructure by causing the fragmentation and dissolution of the Al_2Cu phase during solution treatment (Li, Samuel et al. 2003). The average volume fraction of Al_2Cu in the studied alloys decreased from 1.4% in the as-cast condition to 0.66% after the 50 h solution treatment at 495°C. Meanwhile, we observe from Figure 5-6~Figure 5-10 that the Al_2Cu phase undergoes morphological and size changes during solution heat treatment.

During the first 2h30 of solution heat treatment at 495°C, the Al_2Cu phase undergoes the fragmentation of the larger Al_2Cu particles by pinching off the thinner arms (see Figure 5-6(c) and (d)) and by the dissolution of average size Al_2Cu particles (see Figure 5-6(e) and (f))) with radial diffusion of Cu atoms into the surrounding aluminum matrix.

In the following 50 h of solution heat treatment, the volume fraction of Al_2Cu phase decreases further. The main process of fragmentation and dissolution of the Al_2Cu particles involves the disintegration of the structure at the thinnest sections of the Al_2Cu particles and the dissolution of the smallest Al_2Cu particles in the aluminum matrix in the same time period.

However, comparison of Figure 5-8(d) and (f) shows that the fragmentation of the large Al_2Cu particles seems more difficult than the dissolution of Al_2Cu particles with smaller radii. After 2h30 of solution heat treatment, almost all the smaller particles have indeed already disappeared as can be observed from the comparison of size distributions of Al_2Cu phase in samples HT1a/b and sample HT2 in Figure 5-10.

These observations are in good agreement with the conclusions drawn by (Li 2003) and (Crowell and Shivkumar 1995). (Li 2003) reported that the blocky Al_2Cu phase particles are difficult to dissolve during solid solution heat treatment, unlike the fine Al_2Cu phase particles that can dissolve within 2 h of solid solution heat treatment. (Crowell and Shivkumar 1995) found that the blocky Cu phase in B319 alloys may be partially dissolved with increasing solution heat treatment time at the recommended solution temperature of 495°C.

5.6.1.2 Fe-intermetallics

No noticeable changes were detected in specimens HT1a and HT1b as regards the Fe-intermetallic phase before and after the 2h30 heat treatment at 495°C. The slight decrease of volume fraction of Fe-intermetallics in specimen HT2 after 50 h at 495°C might be due to the dissolution of β-Al5FeSi phase during solution heat treatment.

As mentioned at chapter 3, the Fe-intermetallic is expected to precipitate at 568°C during the solidification of A319 alloy (cooling rate ~0.8°C/s). In the present work, the maximum solution temperature was selected to be 495 ± 5°C, to avoid incipient melting of the copper phase. On account of this, the decomposition of iron-intermetallics phase may not take place.

Figure 5-30 displays reconstructed 2D tomographic slices of the same region of the sample HT2 at as cast condition and after 50 h of solution treatment at 495°C. The dissolution of Al_2Cu (yellow arrow) was observed clearly. In contrast to the α- phase (see red arrow) which remains unchanged during heat treatment, the needle-like β-phase (see red dotted circle) seems to undergo partial dissolution during solution treatment of 50 h at 495°C.

These observations confirm the findings of (Moustafa, Samuel et al. 2003). According to them, the dissolution of the β-phase occurs after solution treatment for 24 h at 500°C while no noticeable changes occur for α-phase after solution treatment.

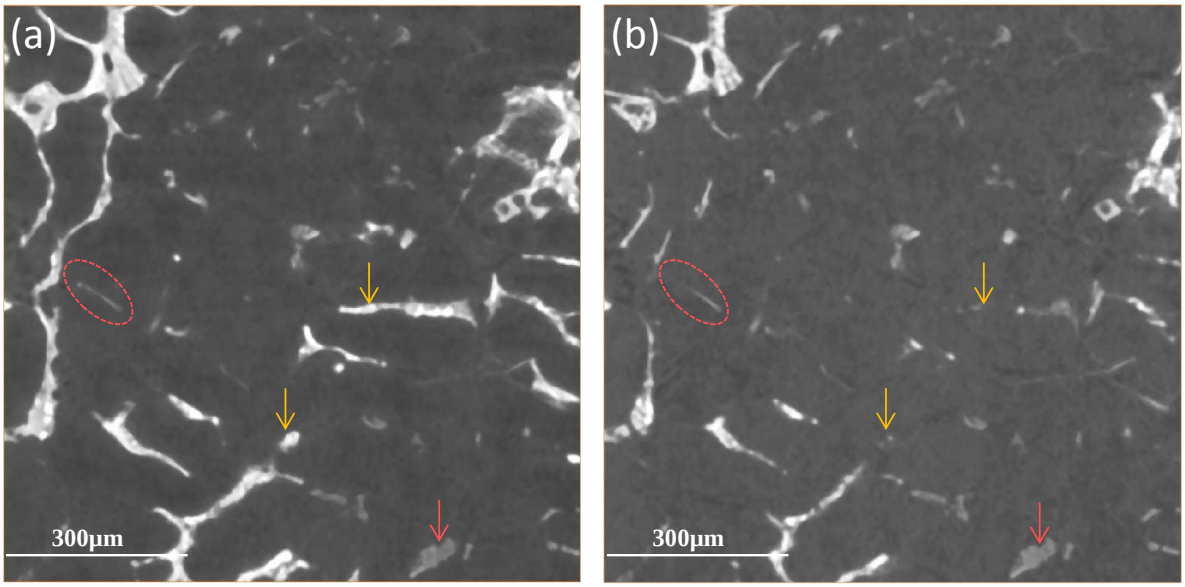

Figure 5-30: Tomographic images showing the effect of heat treatment at 495°C on the microstructures of specimen HT2: (a) 0 h, (b) 50 h

5.6.1.3 Pores

Quantitative analysis was performed on the porosity for the specimens in as cast and different heat treatment conditions. The results indicate that heat treatment at 495°C does not affect the physical dimensions of porosity. This result is in accordance with the findings of (Boileau and Allison 2003).

At a high temperature solution treatment, i.e. 532°C, (Toda, Nishimura et al. 2010) reported that micro pores can form heterogeneously in eutectic regions, and that the micro pores show significant growth immediately after exposure to a temperature higher than ternary and binary eutectic temperatures.

5.6.1.4 Si particles

The eutectic silicon morphology, viz., particles size and shape, plays an important role in determining the mechanical properties in A1-Si alloy castings (Tash, Samuel et al. 2007). The effect of heat treatment on the morphology of eutectic silicon has been widely reported (Mohamed and Samuel 2012) (Moustafa, Samuel et al. 2003).

The silicon particles are coarse, acicular needles in the as-cast LFC A319 alloys (Figure 5-4(a)). After a solution heat treatment as shown in Figure 5-4(b) and Figure 5-4(c), the silicon particles are modified. This morphological evolution may be interpreted as follows: the fragmentation and spheroidization of the eutectic Si particles in the studied LFC A319 alloy occurs when the alloy is

subjected to solution heat treatment and increases as the solution treatment time increases from 2h30 to 50 h at 495°C, as reflected in the continual increase in the Si particle sphericity.

The analysis of eutectic Si distributions after different heat treatment conditions reveals that modification of the silicon particles can also be achieved by solution heat treatment, where the silicon particles are initially broken down into smaller fragments that are then gradually spheroidized.

5.6.2 Damage mechanisms (3D tensile damage mechanisms)

This study revealed that the crack path in LFC A319 alloy under monotonic tensile loading is sensitive to microstructure. A summary of the crack growth characteristics of the three studied samples is presented in Table 5-8.

Table 5-8: Basic information on tensile tests

Specimen	HT1a	HT1b	HT2
Heat treatment conditions	495°C, 2h30 + 200°C, 150h		495°C, 50h + 200°C, 200h
Max. stress (MPa)	162.1	186.6	187.5
Initiation	Pore	Pore + Si	Pore + Al2Cu
Propagation	Hard inclusions (Si, iron intermetallics, Al_2Cu phases)		

In addition, as predicted by FEM simulation, all the main cracks and the final fracture occured in the selected ROI. Undoubtedly, the large pores play the most important role in the failure of specimens. However, we can also assume that the hard inclusions, which are located in the vicinity of the large pores, have an important influence on the damage mechanisms of the specimens.

As shown in the results of microstructure characterization presented before, the hard inclusions are distributed randomly in the alloys. Although the total volume fraction of Al_2Cu phase decreased when the heat treatment time increases, the local volume fraction in the heat treated specimen can reach higher value than the average volume fraction in the as cast specimen. Comparison of the volume fraction of Al_2Cu phase between the large volume (ROI of tensile test) and one small sub-section, which includes the main cracks and final fracture of the specimen, is summarized in Table 5-9.

For specimen HT1a, the volume fraction of Al_2Cu (0.88%) in the sub-volume is near the one (0.83%) in the large volume (ROI of tensile test) which was analyzed in previous part. In contrast, the specimen B, which was subjected to longer solution treatment and contains less Al_2Cu phase than specimen A, shows the highest volume fraction of Al_2Cu (1.4%) in the selected sub-section.

Thus, the results presented here cannot be representative for the effect of heat treatment on the damage mechanisms of LFC A319 alloy. Despite all this, we can get some information about the damage mechanisms of the studied alloy.

Table 5-9: Quantitative analysis of Al_2Cu phase in the studied specimens

Specimen	Heat treatment conditions	Al_2Cu phase		
		Vol. fraction% (ROI)[1]	Vol. fraction % (sub-section)[2]	Surf. fraction % (fracture surface)[3]
HT1a	495°C, 2h30 + 200°C,150h	0.83	0.88	5.7
HT1b		0.87	0.41	2.5
HT2	495°C, 50h + 200°C,200h	0.66	1.40	11.6

Note: 1.Volume of ROI=10.58mm^3 2.Volume of sub-section=1.2 mm^3 3. Fracture surface=4mm²

5.6.2.1 Crack initiation

The experimental study of 3D in-situ tensile test with DVC analysis revealed a very important effect of pores on strain localization and crack initiation.

In the present work, most of the cracks initiated around large pores in all tensile test specimens, and it was found that the size, the location and the shape of pores can affect the cracks initiations during the tensile test.

In specimen HT1a, Pores A, B and C are all surface shrinkage pores. The cracks initiated from the surface Pore A (volume: 0.101 mm^3) and Pore B (volume: 0.017 mm^3) rather than from the smaller surface Pore C (volume: 0.005 mm^3), which proves that **the size of pores** is an important factor on cracks initiations.

The size of the pore can affect the crack initiation as reported by many researchers (Wang, Limodin et al. 2016) (Mu, Nadot et al. 2014) (Wang, Apelian et al. 2001). (Wang, Apelian et al. 2001) suggested that there exists a critical pore size in the range of 25 to 50 μm for fatigue crack initiation in Sr modified cast A356 alloy. In the present results, all the pores which initiate cracks are in the range of 309 to 1913 μm, they are apt to induce stress concentration during tensile loading.

It should also be noted that the alloys used in previous studies were castings other than lost foam casting which introduces some large defects.

In addition, the cracks in LFC A319 alloy were found to initiate preferentially close to large shrinkage pores. For example, cracks initiated from Pores A (sphericity: 0.039) and B (sphericity: 0.139) in specimen HT1a, and from Pore A (sphericity: 0.078) in specimen HT2, and from Pores A (sphericity: 0.069), D (sphericity: 0.144) and E (sphericity: 0.084) in specimen HT1b. They were all shrinkage pores with sphericity below 0.015. These pores act as preferred crack nucleation sites because of the high stress concentration at the sharp radius of curvature (Chan, Jones et al. 2003). This observation is consistent with the observations by (Wang, Limodin et al. 2016) that cracks initiation is dominant at large pores. Shrinkage pores with sharp radii of curvature can be considered as morphologically crack-

like (Chan, Jones et al. 2003). These crack-like pores appeared to have a high stress concentration factor and often showed cracks initiation.

Large gas pores (Pore D in specimen HT1a, volume: 0.034 mm^3, sphericity: 0.64; Pore B in specimen HT1b, volume: 0.048 mm^3, sphericity: 0.72) were also observed in the studied specimens, but they did not initiate any cracks before the final fracture of specimen. This may be explained by the fact that the large rounded pores had a lower stress concentration factor compared to the crack-like shrinkage pores and were thus less likely to initiate cracks.

Besides, one can also note that: in specimen HT2, the small crack 3 was located on corner of the Pore B (volume: 0.098 mm^3, sphericity: 0.42), this might be because the corner of the pore B has a sharp radii of curvature hence a higher stress concentration. The strain localization calculated by DVC was also observed in here; the complex **morphology of the pores** has thus a significant influence on the local stress concentrations, and therefore, on the crack initiation process at pores.

The **location of pores** is also an important factor on cracks initiations. As it can be observed in Figure 5-11(b), in specimen HT2, some shrinkage pores are located inside the specimen. However, no cracks can be detected at these pores; this implies that the location of pore also can affect cracks initiations during tensile test. (Wang 2015) reported that the preferred site for crack initiation always occurred at pores located at or near the surface or the specimen. We can propose that the relatively high stress concentration at pores, particularly surface pores, is responsible for strain localization leading to crack initiation.

In addition, the experimental evidence indicates that tensile failures of the studied LFC A319 alloy often initiate at hard inclusions (i.e. eutectic Si, Al_2Cu phase and iron-intermetallic) that are located around large pores or near surface of specimen rather than at Al matrix.

- In specimen HT1a, cracks 1 and 2 are both initiated at α-Fe phase close to the two largest pores.
- In specimen HT2, cracks 1 and 3 were observed to initiate at eutectic Si and α-Fe phase around the largest Pore A, respectively. Meanwhile, Al_2Cu in the corner of two surfaces, where stress concentration is easy to generate, acted as another crack nucleation site (crack 2) in this region without large pores.
- In specimen HT1b, crack 2 and crack 3 are both initiated from eutectic Si particles close to the surface of specimen.

In general, the presence of large pores or/and specimen geometry will result in stress concentration in the surrounding matrix and hard inclusions during tensile test. However, hard inclusions have a higher elastic modulus and are more fragile than Al matrix (Chen, Richter et al. 2010). Besides, as characterized previously, hard inclusions have local sharp morphologies compared to the Al matrix, thus, a larger stress concentration is easier to generate at hard inclusions than in Al matrix and crack

initiation occurs very rapidly by rupture of this particle. (Dezecot, Buffiere et al. 2016) explain that hard inclusions are prone to cracking during mechanical loading because of the strain incompatibility between the aluminum matrix, which has an elasto-viscoplastic behavior, and the hard inclusions (particularly Si particles).

In details, the acicular eutectic Si particles, which are brittle and fragile, serve as a bridge for crack propagation. Although the studied alloy was slightly modified with Sr and solution treated for 2h30 or 50 h at 495°C, Si particles were still large and interconnected into a network, which may show high stress concentration factors (Chan, Jones et al. 2003). In the literature (Bacaicoa, Dwivedi et al. 2016) (Ma, Samuel et al. 2014), cracks initiations were found through the fragmentation of Si particles, iron intermetallics (especially for platelets-like β-phase), as well as Al_2Cu particles in Al-Si-Cu alloy.

In addition, as discussed before, the hard inclusions, which are distributed in the vicinity of the large pores, have an important influence on the damage mechanisms of the specimens.

From the results of observations, one can also note that:

- Although specimen HT2 was subjected to a longer heat treatment than specimens HT1a and HT1b, a high volume fraction of Al_2Cu (1.4%) was found in the sub-section that contains the large pores. Crack was found to initiate from Al_2Cu phase in the corner of flat surfaces where stress concentration is prone to occur.
- In specimen HT1b, the lowest volume fraction of Al_2Cu (0.41%) was detected in the areas that contain the fracture surface and the two main cracks (i.e. crack 2 and 3) were observed to initiate from the eutectic Si rather than from Al_2Cu phase.

This implies that the volume fraction of hard inclusions in the neigbourhood of the large pores is also an important factor on cracks initiation sites.

5.6.2.2 Crack growth and final fracture

After these cracks initiated at hard inclusions in the areas with high enough stress concentration, they appeared to continue growing along the hard inclusions.

As discussed before, the analysis of 3D cracks evolution revealed that cracks growth was prone to occur along the hard inclusions including eutectic Si phase, iron intermetallics and Al_2Cu phases. This can be ascribed to strain localizations at these hard inclusions with the increasing applied stress. The strain localizations were well observed in areas where cracks growths were observed in following loading step.

One slice of tomographic image, which is about 850 μm below the flat surface, is shown with 3D rendering of cracks and fracture surface in Figure 5-31(a). This slice is located in a region that is away from the tip of the main cracks at the last loading step before failure. The strain field (Figure 5-31(b))

in the same slice at the last loading step is shown in translucent with the tomographic image slice in behind.

The relations between strain localizations at hard inclusions and final failure are observed. However, it is impossible to know if there are microcracks at these strain localizations areas due to the limited resolution of tomographic images (voxel size=3µm). The final failure (red line marked in Figure 5-31(b)) went through the areas where strain localizations are marked by white dotted circles during the fast failure stage. This indicates that hard inclusions play an important role for strain distribution affecting crack propagation and final fracture.

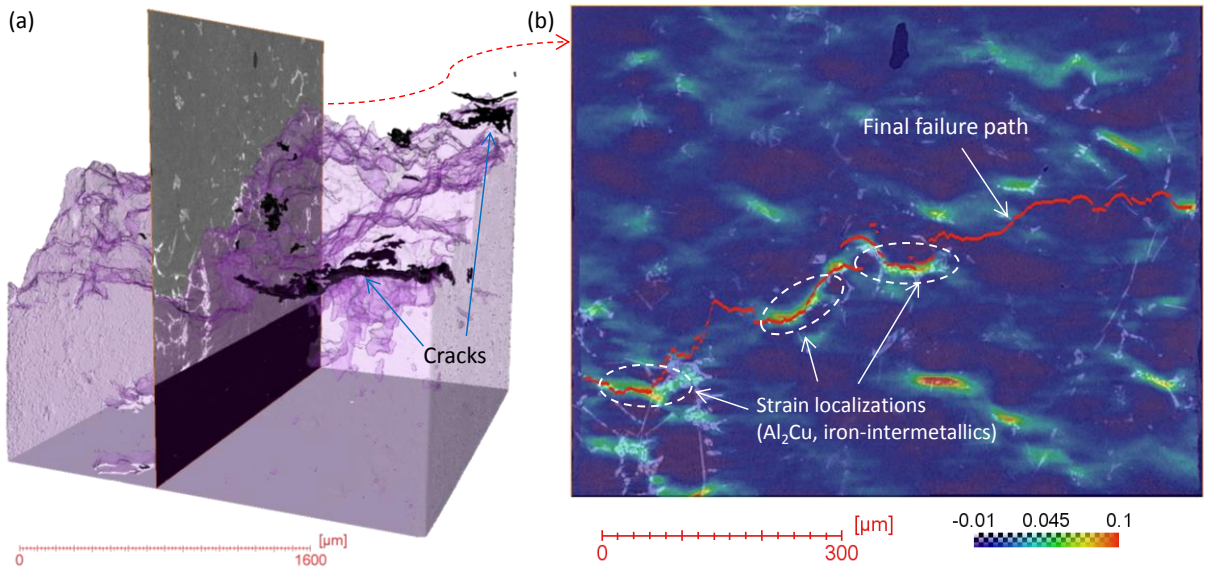

Figure 5-31: (a) One slice (about 850 µm below the flat surface) shown with a 3D rendering of cracks (at last loading step before failure) and fracture surface of Specimen HT2, (b) strain field of this slice in the last loading step before failure

In addition, post-mortem observations clearly revealed the role of hard inclusions (i.e. eutectic Si, Al_2Cu phase and iron-intermetallic) in the crack growth and final fracture process in the studied LFC A319 alloy.

Looking at the SEM-EDS observations in Figure 5-15, Figure 5-20 and Figure 5-26, whether one considers cracks initiation, cracks propagation or final fast fracture, they are all more likely to occur along hard inclusions.

Table 5-10: Ratios of phase's fraction on fracture surface and on sub-section/flat surface

Specimen	Heat treatment conditions	Ratios ($\frac{surface\ fraction\ on\ fracture\ surface}{surface\ fraction\ on\ sub-section/flat\ surface}$)		
		Al_2Cu	Iron-intermetallics	Eutectic Si
HT1a	495°C, 2h30 +200°C,150h	6.3	2.0	3.6
HT1b		5.9	1.9	4.0
HT2	495°C, 50h +200°C,200h	8.6	2.2	3.9

Note: for Al_2Cu and iron-intermetallic phase, the ratio is surface fraction on fracture surface over the volume fraction on the sub-section close to the final fracture reported in Table 5-9; for eutectic Si, the ratio is surface fraction on fracture surface over that on the flat surface.

Comparison of phases surface fraction between fracture surfaces and sub-volume or flat surfaces (Table 5-10) shows that the amount of eutectic Si particles, iron intermetallic phases and Al_2Cu phases is higher in the fracture surfaces than elsewhere in the specimen. It implies that cracks and final fracture are more prone to occur at hard inclusions than in Al dendrites.

The similar ratios of eutectic Si's fraction on fracture surface and on flat surface between HT1a, HT1b and HT2 show that the modification of eutectic Si with solution heat treatment does not decrease its importance in the fracture surface.

Besides, comparisons of phases distribution on each fracture surface of the same specimen reveals that more fracture than decohesion of hard inclusions is found in all fracture surfaces.

(Lee, Major et al. 1995) showed that fracture of Si particles is the dominant mechanism in an unmodified Al-Si-Mg alloy with large (~3-9 μm) Si particles. In contrast, decohesion of Si particles from the Al-matrix always occurs in the smaller Si particles. In the present work, the average size of Si particles is larger than 10 μm in all the test specimens. This can be considered one of the reasons why more fracture than decohesion of Si particles is detected in the fracture surface.

In addition, the force being applied in tensile test also can affect the damage mechanism of hard inclusions. (Gall, Yang et al. 1999) deduced that debonding of Si particles dominates the fatigue crack growth process at a maximum stress intensity factor, K_{max}, of less than 6 MPa√m, but fracture of Si particles dominates at K_{max} > 6 MPa√m. In our study, the specimens were subjected to high stress during the tensile test so that the Si particles are rather fractured than debonded.

The present work also shows that more fracture than decohesion is found in iron intermetallics and Al_2Cu phases. (Ma, Samuel et al. 2014) reported that in Al-Si alloy castings, cracks appear within the β-Al_5FeSi platelets rather than at the β/Al interface. This is due to the brittle nature of the β-phase, whereby the platelets are easily split into two halves. (Ma, Samuel et al. 2014) have also reported that cracks propagate also through the fracture of undissolved Al_2Cu. This is consistent with observations in this study.

In the final fast fracture stage, hard inclusions in the unbroken ligament are under a much higher stress level. Thus, as shown in Figure 5-32, a large number of micro-cracks (red arrows) initiate at hard inclusions including eutectic Si particles, iron intermetallics and Al_2Cu phases; we can also see that the fracture of hard inclusions is the dominant mechanism observed in this area.

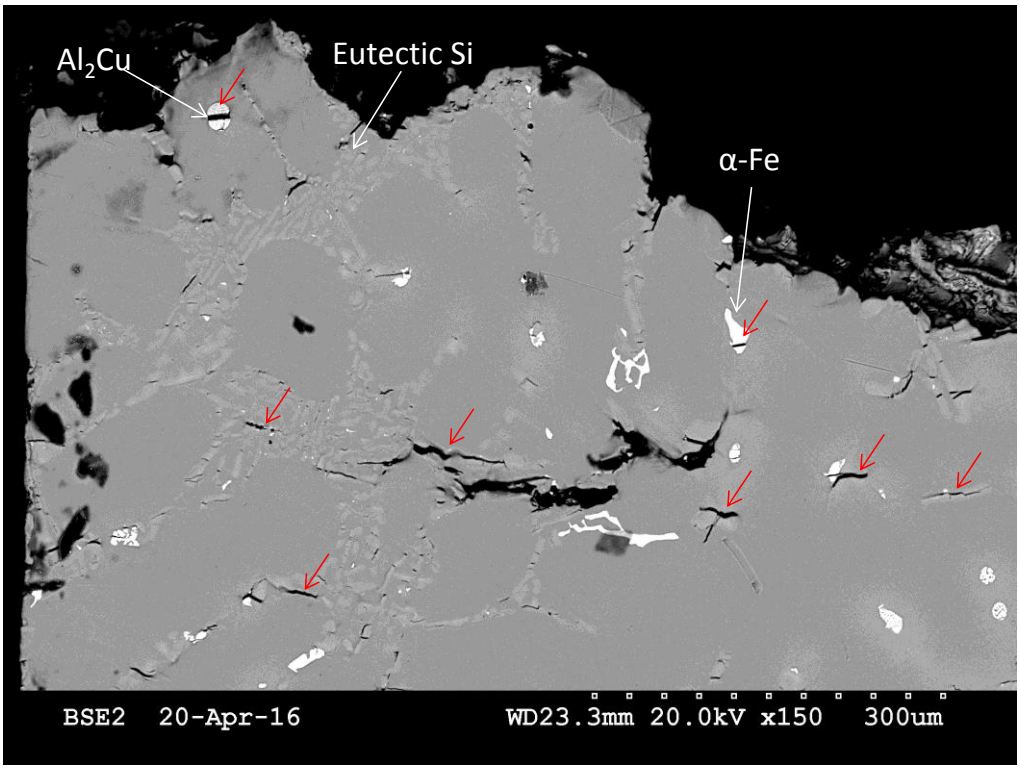

Figure 5-32: BSE image showing the micro-cracks in the failure zone of specimen HT1a

5.6.3 Strain measurements and crack formation

Strain measurements by DVC coupled with the observation of 3D crack evolution indicated that the crack path corresponds to the strain localization observed. The correlation between strain localization and tensile crack initiation and growth is well observed.

A quantitative assessment of the local material response prior to crack initiation was performed on the studied specimens. With an accurate assessment of strain localization prior to crack formation, the locations of potential tensile cracks and their severity can be predicted.

5.7 Summary

In this chapter, three samples were extracted from the as cast LFC A319 cylinder head and investigated. These specimens were subjected to different heat treatments conditions. These different processes lead to three different microstructures for the three studied specimens. In addition, the nucleation and growth of cracks in these three alloys has been observed using Lab-CT during in-situ tensile test. Then, the damage mechanisms of the alloys were discussed.

5.7.1 Experimental protocol

Tensile test with 3D in-situ observation were performed using X-ray tomography on the LFC A319 alloys with different heat treatment conditions. A preliminary 3D characterization of pores using Lab-CT was carried out; then the FE simulation based on these tomographic images was efficiently used to simulate the strain distribution during the tensile test and thus select ROI.

A full metallographic 2D and 3D characterization of the microstructure through optical microscopy and laboratory X-ray tomography was performed on the studied samples in order to study the effect of various heat treatments on the microstructure of LFC Al–Si–Cu alloys.

3D in-situ tensile test allows cracks initiation and propagation being revealed directly in 3D while the DVC measurements enable real time deformation measurements. The results in this work point out to where tensile cracks form, and when (local strain value in phases) initiation takes place in the studied LFC A319 alloy. The localization of strain at the microstructural level prior to crack formation determines the location of micro-cracks which form later during the tensile loading.

Finally, postmortem analyses were performed using SEM and EDS on flat surfaces and fracture surfaces; they helped identifying final failure, micro-cracks, crack initiation zone and thus allow the damage mechanisms being understand thoroughly.

5.7.2 Influence of heat treatment

The effect of solution heat treatment on the microstructure of LFC A319 alloy was studied. The temperature of solution heat treatment was 495°C and the solution time ranged from 0 to 50 h (0, 2h30 and 50 h). The comparison with the microstructure in as-cast and different heat treatment conditions has led to the following conclusions:

1. The main processes that take place during solution treatment are: the dissolution of Cu in the Al matrix and the spheroidization and coarsening of the eutectic Si.
2. The solution heat treatment results in dissolution of the Al_2Cu phase that evolves in the following processes: dissolving the small Al_2Cu particles; the loss of interconnectivity by pinching off arms of the larger Al_2Cu particles, further dissolving of the disconnected particles.
3. The morphology of the eutectic Si particles changes with solution treatment time; it undergoes the following transformations: fragmentation, spheroidization, and coarsening during the solution treatment.
4. A few needle-like β-Fe phases undergo partial dissolution after 50 h of solution treatment at 495°C. However, there were also no noticeable changes for α-phase during solution treatment at 495°C.
5. The solution treatment at 495°C has no significant effect on porosity level of LFC A319 alloy.

5.7.3 Damage mechanisms

For the studied LFC A319 alloy, the tensile damage mechanisms can be summarized as:

1. Cracks initiate at hard inclusions in the areas with sufficient stress concentrations, which are mainly provided by large pores. The different size, location and shape of pores result in different stress concentrations thus they affect the cracks initiations during the tensile test. For example, large shrinkage pores located at or near the surface of the specimen more easily introduce stress concentrations than small rounded gas pores within the interior, thus they lead to the crack initiation sites.
2. The large pores can decrease the effective bearing area in the plane perpendicular to the loading direction, and introduce large stress concentration during the tensile test. Consequently, cracks can initiate at hard inclusions near the pores. Besides, with the load increase, cracks can also initiate at hard inclusions (i.e. Al_2Cu and eutectic Si) located in the same plane as pores, away from the pores but close to the surface of specimen.
3. The high stress concentration, which is induced by large pores or/and by specimen geometry, in the surrounding matrix and hard inclusions, leads to earlier local yielding before the applied stress reaches the yield stress of the alloy, hard inclusions can act as crack initiation sites due to their higher elastic modulus and because they are more fragile than Al matrix. Besides, hard inclusions, especially for iron intermetallics and unmodified acicular eutectic Si particles, have locally sharp morphologies, which are prone to generate stress concentration.
4. The quantitative analysis revealed that the iron-intermetallics show a lower average strain level for the cracking of particle than Al_2Cu phase.
5. Once cracks initiated, they prefer to grow through the cracked hard inclusions, i.e. eutectic Si, iron intermetallics and Al_2Cu phase. The fast final fracture is more prone to occur at Si phase, iron intermetallics and Al_2Cu phases than in Al dendrites. In a tensile test, more fracture of hard inclusions is observed than decohesion in all the fracture surfaces whether in cracks initiation region, cracks propagation region and final fast fracture region.

6 Chapter 6 Elaboration for control the defects distributions in lost wax casting Al-Si-Cu alloy

Contents

6.1 Introduction

The inter-valve zone in fire deck is the most critical area in cylinder head. Therefore, it is important to study the damage mechanisms of samples with a microstructure that is representative of that in this area. The in-situ observation can reveal the micromechanics during the test well. Thus, the primary aim is to have specimen representative of as cast parts that have a skin free of pores; however, it is difficult to achieve this with cut specimens. Although some previous studied specimens are cut from industrially manufactured cylinder heads obtained by LFC, due to the complex shape of the inter-valve zone in fire deck, effective region for machine specimen is limited in each cylinder heads. Besides,

most of the machined specimens cannot be used for the in-situ test. When large defects are located near the shoulder of the specimens, specimens should be discarded because in this case the fracture will not happen in the middle of the gauge length or Region Of Interest (ROI) where in-situ observation is performed during the tensile/fatigue test.

Thus, the aim of this chapter is to realize normalized specimens with an equivalent microstructure as in fire deck area of cylinder heads while controlling the defects in the center of specimen. These normalized specimens could then allow studying the relationship between the microstructure and mechanical property of Lost Foam Casting Al-Si-Cu alloy by in-situ observations.

The difficulty met, is that as the both ends of specimen are bigger than the center of the sample, they will solidify last in the case of non-controlled cooling, generating all the defects in these parts. The solution studied in this thesis is to realize a casting system which can simulate a casting process such as LFC process, and control the cooling rate to have the last solidification in the central part of the sample in order to concentrate the defects in this part.

Therefore, the liquid alloy will be poured in a tubular furnace in vertical position with a temperature control in the different parts of the furnace. Another parameter has to be taken in consideration in order to replicate the LFC process as closely as possible: the Dendrite Arm Spacing (DAS), a good witness of the dendrite size in the alloy.

Thus, the elaboration of the specimens has to respect these three conditions:

1. A SDAS of 76 μm (± 5 μm)
2. Defects (pores) concentrated in the central part
3. A good surface finishing

In order to achieve this, a furnace with a temperature control system was developed firstly; as shown in Figure 6-1, three independent resistances were used along the vertical direction of furnace. The resistance 1 is on the top of the furnace, the resistance 2 in the middle and the resistance 3 on the bottom of the furnace. The “specimen” is centered on the resistance 2. Three K-type thermocouples are positioned at the top, middle and bottom of the specimen, separately, and they are used for the temperature measurement of the casting part. A prototype has been developed during a previous internship (H. Merienne 2013) and I finished this part of work with the help of another doctoral student N. Dahdah (PhD thesis (2013-2016) at LML).

Chapter 6

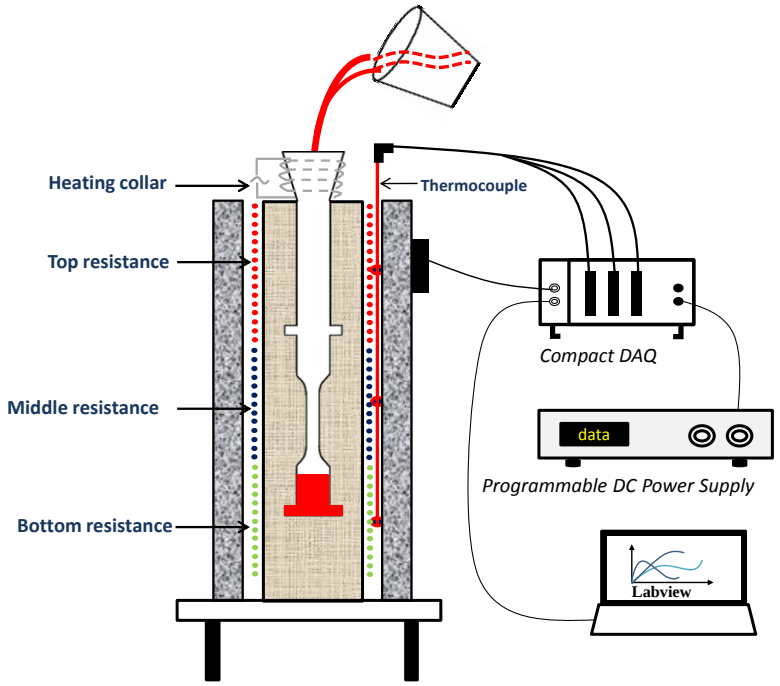

Figure 6-1: Schematic diagram of the casting system

An additional temperature control system was created to control the temperature distribution of the specimen during the solidification. Meanwhile, in order to find a cooling process of the three parts of furnace for controlling the defects in the center of specimen during solidification, some simulations were made by the Centre Technique des Industries de la Fonderie (CTIF) using QuickCast software. The Figure 6-2 shows the simulated different temperatures to input at the locations of the three resistances. The middle part of the furnace is solidified slower than both ends.

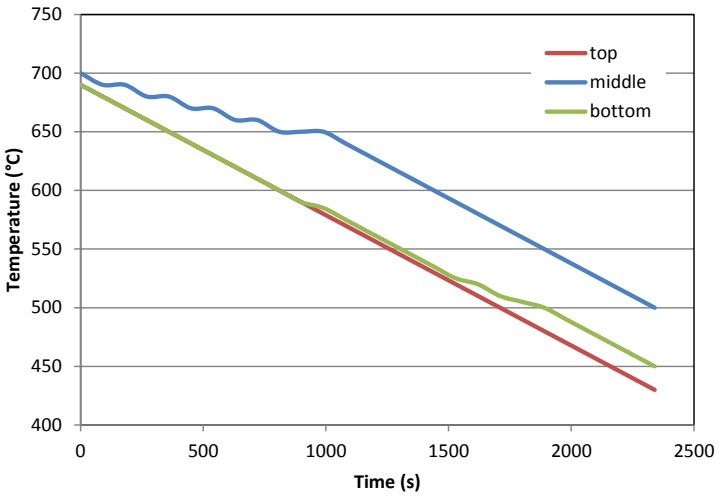

Figure 6-2: Simulation of the cooling curves for the top, bottom and middle resistances that should allow obtaining defects in the middle of the specimen

As shown in Figure 6-3, the result of simulation shows that the temperature gradient could cause casting defects (in purple) in the center of specimen.

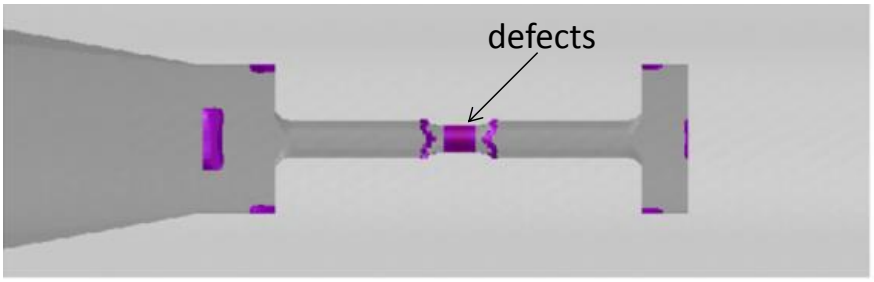

Figure 6-3: Location of defects in VisualCast using the temperature gradient shown in Figure 6-2

In the present work, the casting experiments will be performed using the home-made solidification device. Molten metal is poured into a mold that has been created by means of a wax/resin model. The solidification process of different parts of specimen will be controlled and should follow the simulated cooling curves, which are expected to introduce defects in the center of specimen.

After the casting, the sample will be characterized with Lab-CT (LML, ISIS4D) in fast scan mode with an 80 kV acceleration voltage to ensure a 10% transmission of the X-ray beam through the sample. The scan was made at a medium resolution with a voxel size of 6 µm and an acquisition time per image of 500 ms; this coarse resolution images allow revealing the large pores in the bulk of the specimens gauge length rapidly. Generally speaking, this work focuses on the combination of casting simulation, casting experiments and characterization of the produced cast parts in order to obtain a specimen with controlled defects.

6.2 Implementation of a furnace with temperature control system

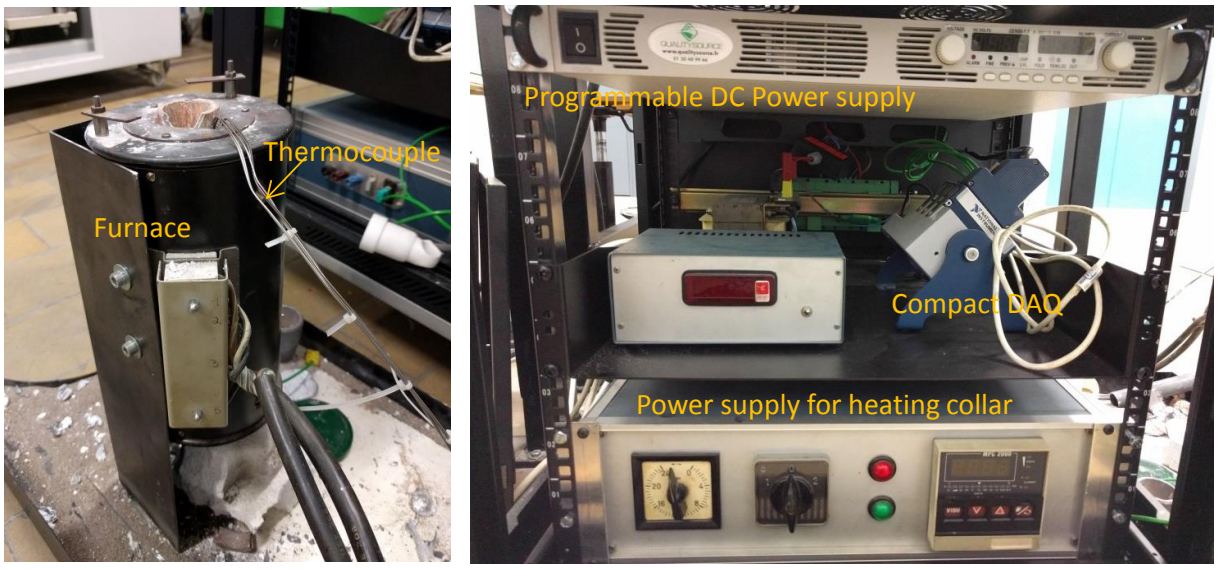

Figure 6-4: Experimental setup

As mentioned before, in this work, a furnace with temperature control system was developed to create a temperature gradient for the cast part during solidification. The whole experimental setup is shown in Figure 6-4.

Three K-type thermocouples were inserted close to resistance wire of the vertical tube furnace. Temperatures were recorded by a PC-based NI (National Instrument) data acquisition system. The system consists of compact DAQ, programmable DC Power supply and LabVIEW software. The DAQ was connected to a computer through LabVIEW.

Besides, based on LabVIEW, a temperature control system was designed to monitor the temperature of the furnace using Schmitt trigger algorithm. Then, real-time measurement and control of temperature can be attained.

An example of temperature controlled with Schmitt trigger controller by LabVIEW is shown in Figure 6-5. This system enables process monitoring of the temperature at the different parts of specimen during casting. From this program, the actual value of the temperature can be compared with the input temperature in real time. Figure 6-5(b) shows that the temperature control error is less than 1°C.

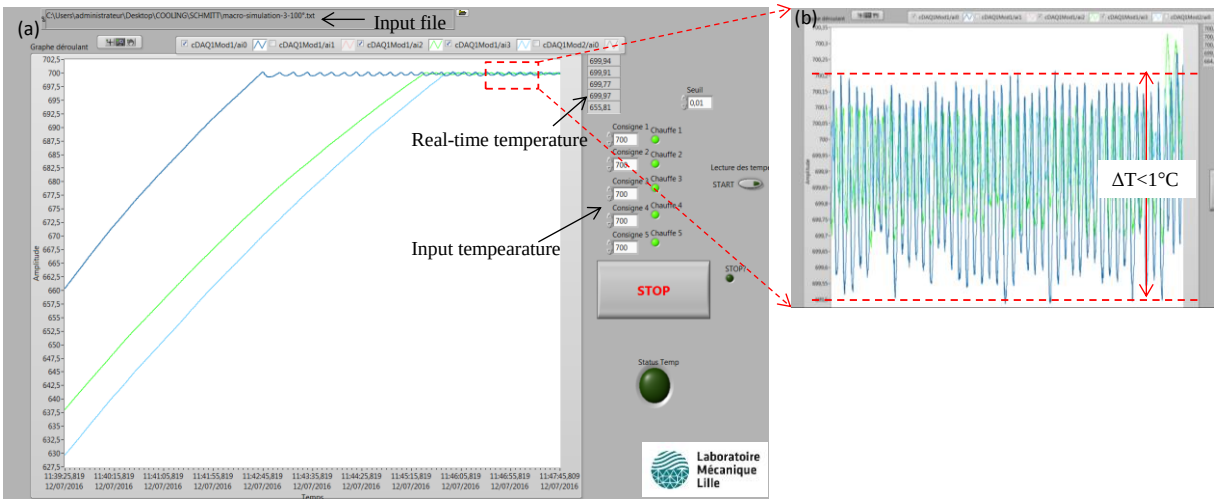

Figure 6-5: LabVIEW display for the temperature control

6.3 Fabrication of plaster molds

In this part, two methods for making the pattern are presented and discussed, and then the plaster mold will be created by means of a wax/resin model.

6.3.1 Realization of the Specimen in Wax

The first step is to design the 3D geometry of specimen using CATIA (Figure 6-6(a)). The dimensions of the specimen are represented in the Figure 6-6(b).

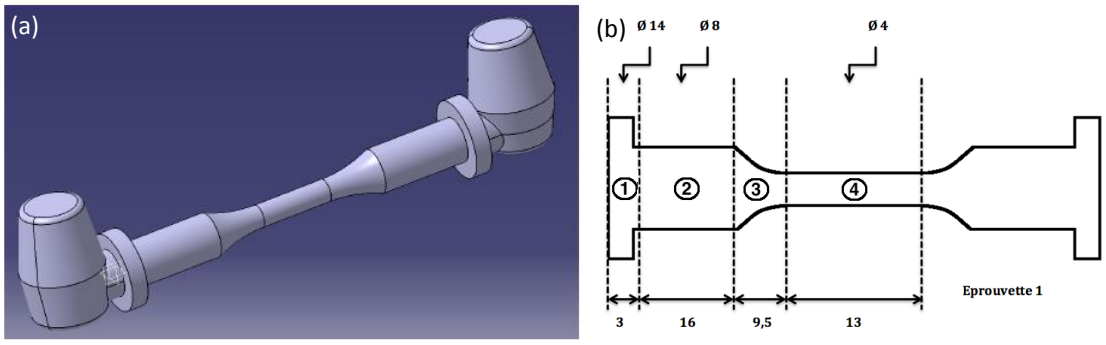

Figure 6-6: (a) Catia design and (b) dimensions of the wax model

The second step is to make the wax sample from a silicon mold. As shown in the Figure 6-7, the rapid prototyping process 3D printing is employed to make the original wax patterns (Figure 6-7(a)) to prepare silicone molds (Figure 6-7(b) and (c)). Then, silicone molding is used for duplicating wax patterns (Figure 6-7(d)).

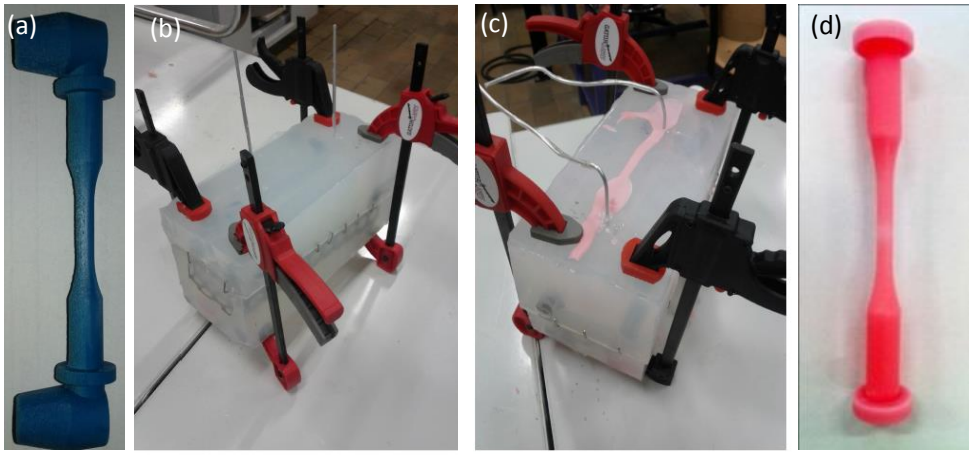

Figure 6-7: (a) Sample from 3D printing, (b) silicone mold and (c) Wax model

However, there are some disadvantages for this method of wax model manufacturing:

1) It is difficult to control the pressure for pouring melted wax into the silicone mold, thus incomplete filling often occurs;
2) There will be burr in the wax model due to the gap between the two parts of silicone mold at the parting line. This causes a rough surface finish of casting specimen. Besides, perfect alignment of the two parts of the mold is difficult to achieve. Therefore a good cylindricity of the specimen is difficult to achieve all the more so as the wax is very soft and deform easily during unmolding;
3) It needs another wax cylinder at one extremity of the wax model to support the wax model (Figure 6-7(c)) on the right position (in the center of resistance 2) during the casting. However, it is difficult to connect these two wax parts straight and hard.

6.3.2 Realization of the Specimen in Resin

- **The first step is 3D sample obtained by the Catia design.**

Figure 6-8 shows a CAD model of the specimen model produced by Catia software and the dimensions of the specimen. As shown in Figure 6-8(a), part A is representative of the specimen, and part B allows positioning the center of specimen on the resistance 2 in the furnace. The two parts will be produced together to avoid the problem of connecting them mentioned before.

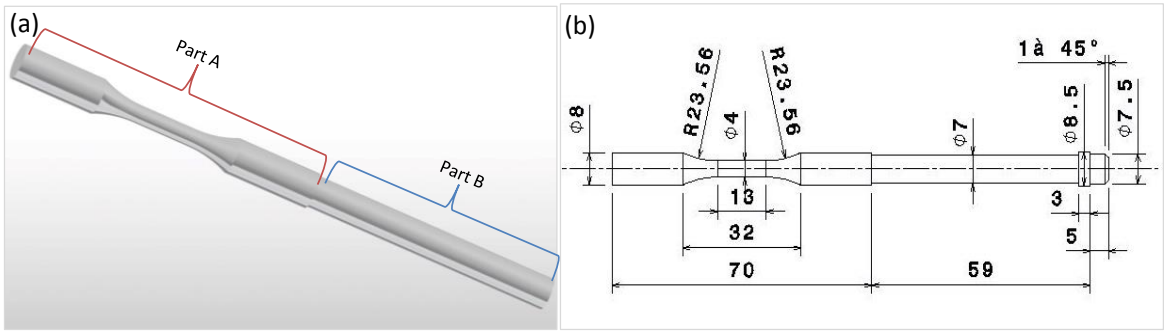

Figure 6-8: (a) Catia design and (b) dimensions of the resin model

- **The second step is to make the resin model by 3D printing**

The CAD model was then converted to a STL file. As shown in Figure 6-9, Stalactite 102 HD 3D printer was used to prepare the resin models. For this 3D printer, the resolution of features is determined by laser beam, in this study, the resin can reach feature details of 50 µm. After 3D printing, the molds were dried by UV beams. A picture of the prepared molds is shown in Figure 6-9.

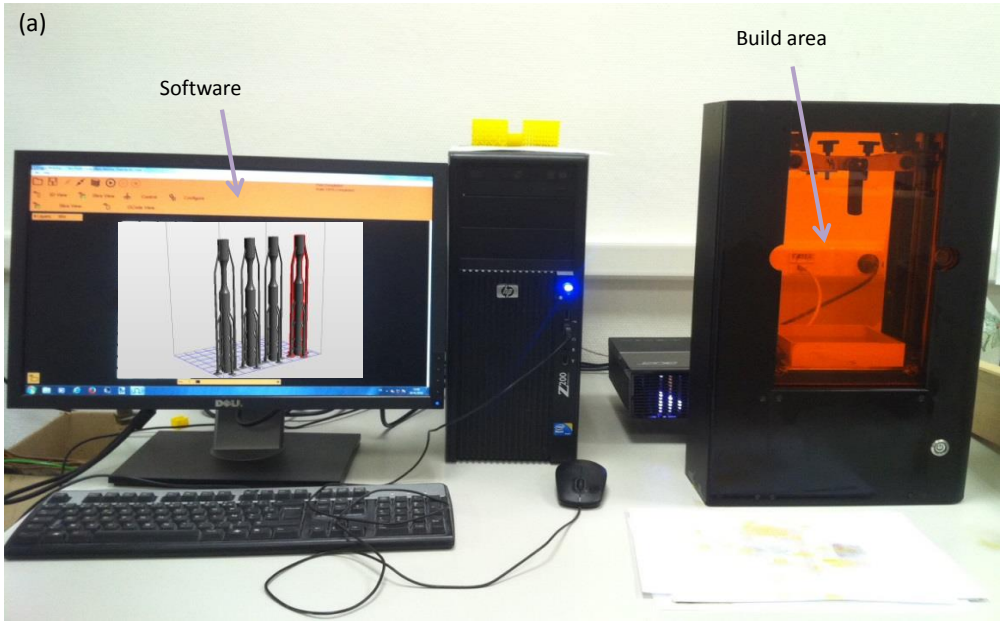

Figure 6-9: Stalactite 102 HD 3D printer

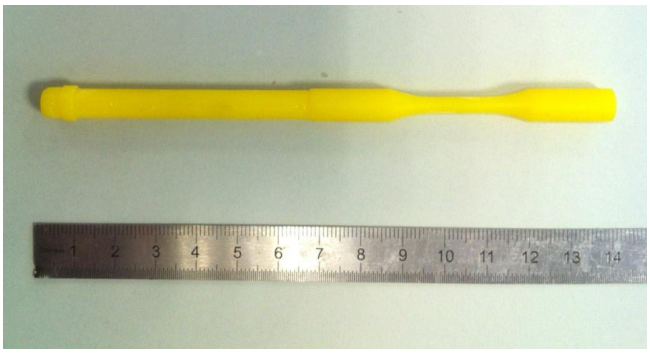

Figure 6-10: A photograph of the printed resin model

6.3.3 Realization of plaster mold

Realization of plaster mold was conducted in the following steps:

1. The plaster is mixed and degassed under vacuum. This processing step will reduce the number of bubbles in the mixed plaster dramatically.
2. The resin mold will be fixed inside a metallic crucible (as shown in Figure 6-11) which can be put into the furnace during casting.
3. The plaster is then poured over the metallic crucible with the resin mold.
4. The plaster is degassed in the metallic mold under vibration again so that the plaster fills any small features of the resin mold. Then the plaster is let to set stand for one hour.
5. The crucible with the plaster inside is then put in the furnace for a thermal cycle of 30 hours presented in Figure 6-11. This thermal cycle was adapted from the one used for wax models. During this stage, melting of the resin model should leave a precise mold cavity. Due to limited time, only two tests have been performed using this thermal cycle that still needs optimization.

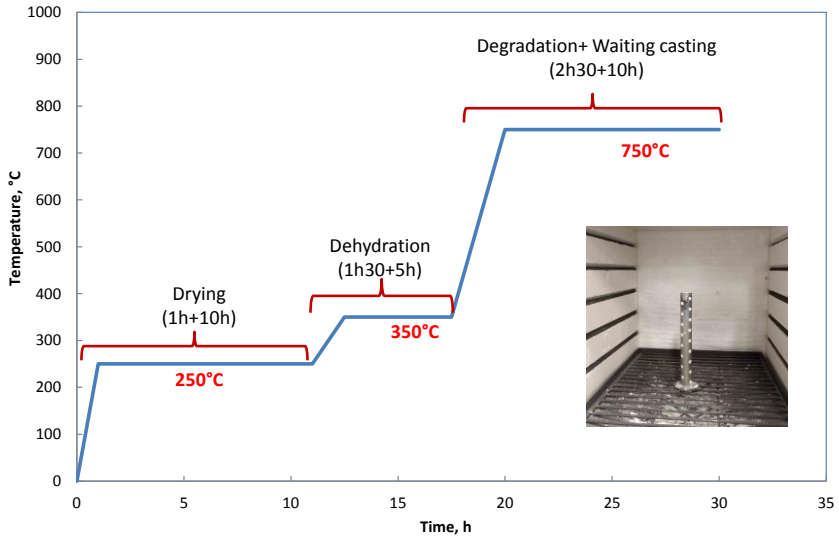

Figure 6-11: Thermal cycle of mold in the furnace

It should be noted that the mold should be kept at 750°C in the furnace before pouring, which avoids destruction of the state of the mold surface.

6.4 Casting process (Experiment procedure)

This section briefly describes the operating procedure for conducting the casting trials.

6.4.1 Melt preparation

Figure 6-12 shows how the alloy melting is performed during the process. Ingots of aluminium A319 alloy provided by PSA were sectioned into small pieces and melted in a crucible using a resistance furnace as shown in Figure 6-12 . The melt temperature was carefully monitored for repeatability at a temperature of 750°C.

Hydrogen is easily removed from liquid aluminum by gas purging with argon. In this work, a silicon tube with a sintered disc (see Figure 6-12) was used to obtain small argon bubbles in order to increase the removal efficiency.

The parameters for degassing were found after several tests. In the present work, the degassing flow was fixed at 1L/min argon. The aluminum alloy was firstly melted in a crucible at 750°C, and different durations of degassing were tested on the melted metal. For each test, then the crucible was rapidly put into the vacuum chamber after degassing. When the solidification of sample is finished, the sample is takent out and cut from the center of the sample. The visible pores can reveal the effectiveness of degassing.

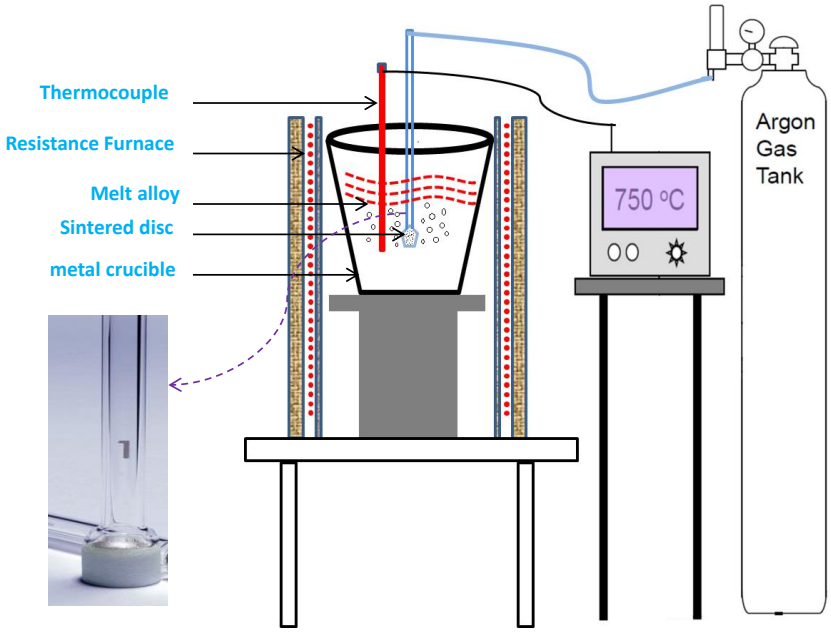

Figure 6-12: Schematic diagram of the alloy melting

Figure 6-13(a) shows the porosity level in the specimen without degassing; Figure 6-13(b) and (c) show the porosity levels after 20 min and 35 min of degassing under 1L/min argon. As can be seen, with 20 min of argon processing, the hydrogen level in the melt was so low that only few pores could be seen on the polished surface cut from the center of the specimen. These results show that the degassing with argon during 20min under 1L/min argon can achieve the aim of removal of most of hydrogen in the alloy. Thus, the melt was well degassed with argon for 20 minutes under 1L/min argon at 750°C before pouring. The oxide layer at the top of the liquid metal was removed to ensure consistent quality metal entered the mold.

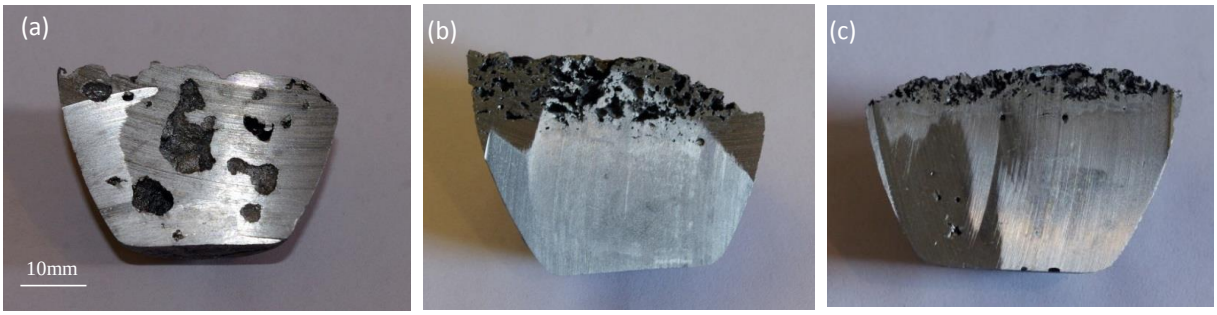

Figure 6-13: Porosity in the specimens at various degassing times with 1L/min argon (a) 0min; (b) 20min; (c) 35min

In addition, as illustrated in Figure 6-14, a ball float flowmeter was used to measure the flow rate of argon gas. The flowmeter consists of a glass tube with scale and a ball which floats on the stream of moving gas. As presented in Figure 6-14(a), calibration curves show the response of the flow-meter under various conditions. The flow rate depends on both the size and density of the ball. In this work, a tantalum ball float was used, and in order to control the flow at 1L/min, the floating ball should rise to 15 mm height.

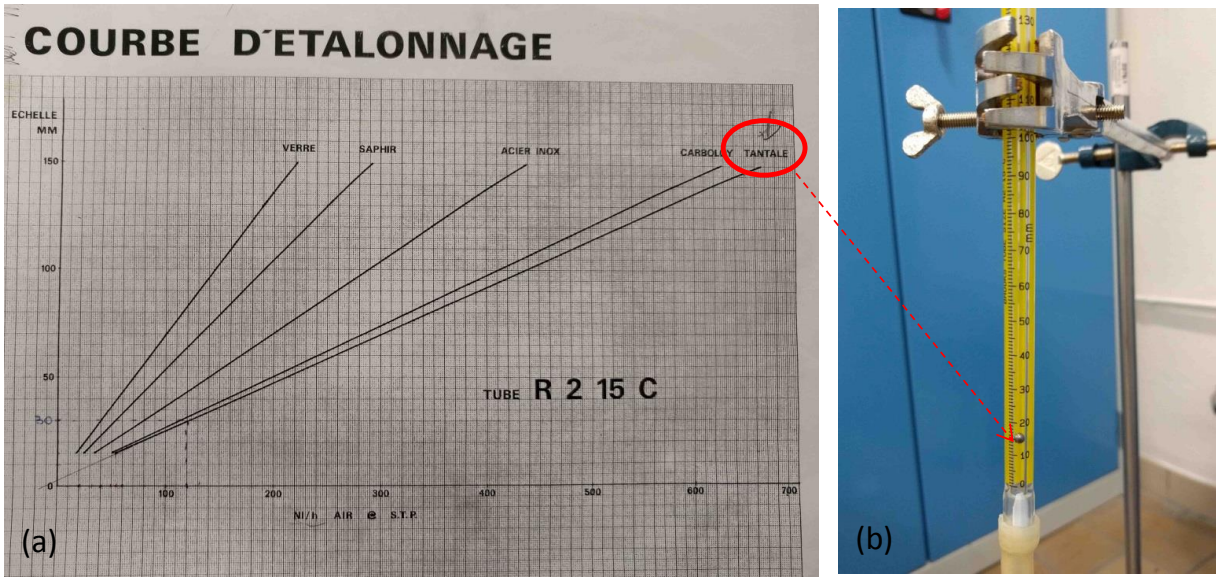

Figure 6-14: Ball float flowmeter

6.4.2 Mold and heating collar preheating

The furnace and heating collar were preheated before pouring the liquid metal.

Firstly, as described in previous sections, the three positions (top, middle and bottom) of the specimen in the furnace were preheated to 700°C using the LabVIEW program mentioned before for temperature control.

Besides, in order to avoid that bubbles inside the solidifying sample cannot go out due to the liquid metal solidified earlier in the open top riser which is exposed to air during the solidification, a heating collar was used, and preheated to 600°C due to its limited capacity. This temperature is enough to keep the metal inside the riser liquid.

6.4.3 Pouring

After the degassing, the oxide layer at the top of the liquid metal was removed to ensure that consistent quality metal entered the mold. Then the molten metal at a temperature of 750°C was carefully taken out of the furnace and poured into the plaster mold.

6.4.4 Casting with controlled temperature

As shown in Figure 6-1. The liquid metal will be solidified with a controlled temperature.

The basis for controlling cooling process may be summarized as follows:

1) After pouring, wait until the temperature reading of the three thermocouples has stabilized at 700°C again (<30s).
2) Input the cooling data file to LabVIEW program.
3) Click the “Start” button in the LabVIEW platform and acquire temperature data for monitoring the cooling curve.
4) Stop heating the “heating collar” after the temperature of specimen is below 500°C.
5) Stop the platform when the temperature of resistance 2 is below 400°C.
6) Take out the metal mold, then take off the plaster coating and reveal the cast part using a high pressure water gun.

6.5 Casting results and discussion

In this section, some trial scenarios are presented and discussed.

6.5.1 The role of heating collar

The effect of heating collar is shown in Figure 6-15. Compared to the casting part produced with the heating collar, the specimen produced without the heating collar shows large surface defects in the top and middle positions (red dotted circle in Figure 6-15(a)).

This can be explained by the fact that the top of the casting part (marked with yellow dotted box in Figure 6-15(a)) was solidified prior to the other part of the specimen due to its exposition to air, therefore, the bubbles, which are trapped in the melted metal, cannot go out during the solidification.

This indicates that the heating collar plays an important role during the casting in the furnace. It can provide an additional heat and increase the fluidity of metal during casting, thus reducing the gas which is trapped in the casting during solidification.

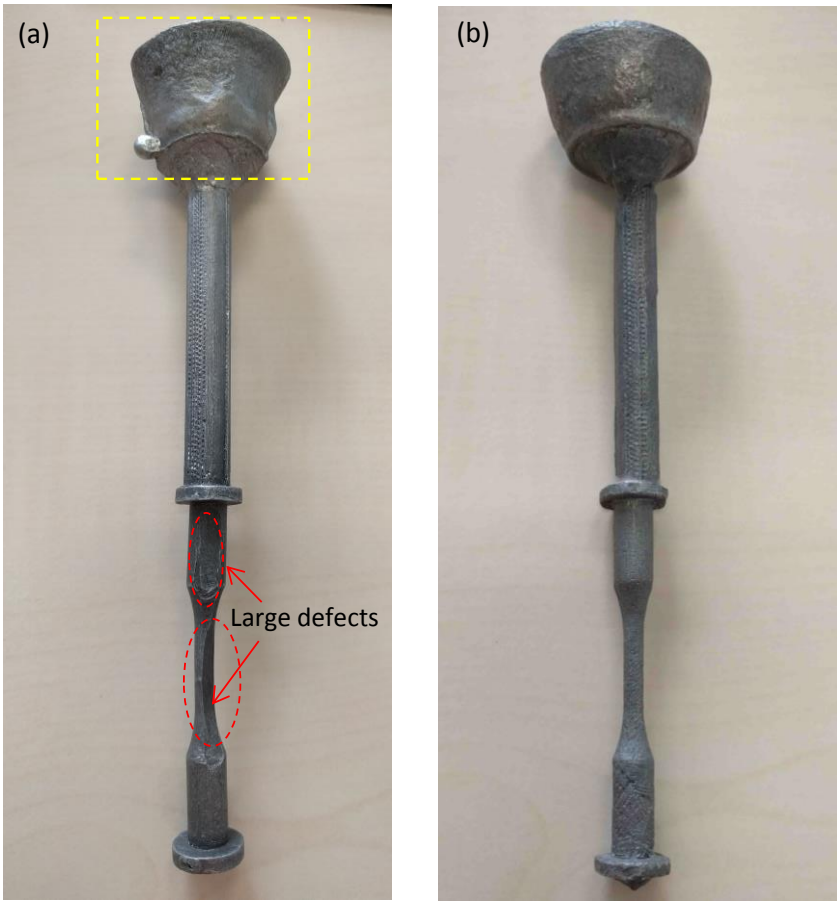

Figure 6-15: The cast parts (a) without and (b) with heating collar

6.5.2 Scenario A: Natural cooling

Firstly, a casting without temperature control was performed in the furnace as the reference case. In this test, the casting is poured at 750 °C, the furnace is stopped and the temperature is recorded.

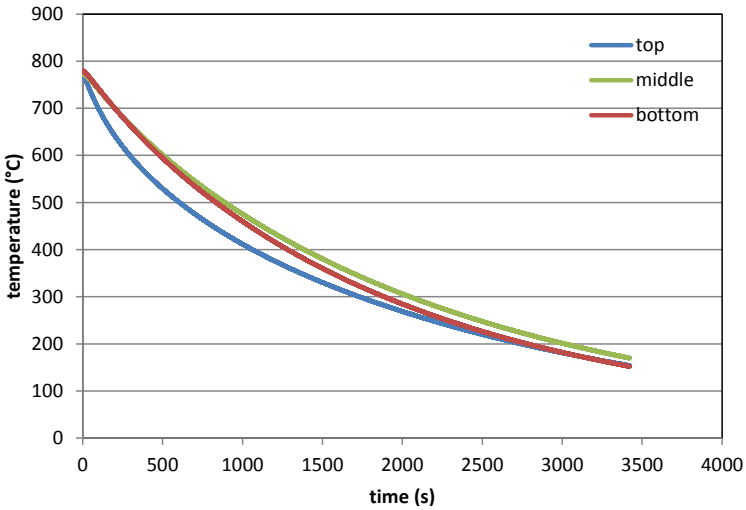

Figure 6-16: Cooling curve of the three part of sample A

As shown in Figure 6-16, the three curves represent the temperature measured at different positions of the castings during cooling. The cooling time measured until the casting reaches the temperature of 300°C when the alloy has completely solidified is around 30min. The average cooling rate is about 0.19°C/s. As expected, the cooling rate in the casting at the beginning of the cooling process is higher than at the end of the cooling process, due to a more inhomogeneous temperature distribution.

Figure 6-17(a) shows the produced casting part. The corresponding 3D rendering of the pores in the specimen A and tomography image (Figure 6-17(b) and (c)) allow observing the porosity distribution, and as expected the pores are in the whole sample not only in the central zone.

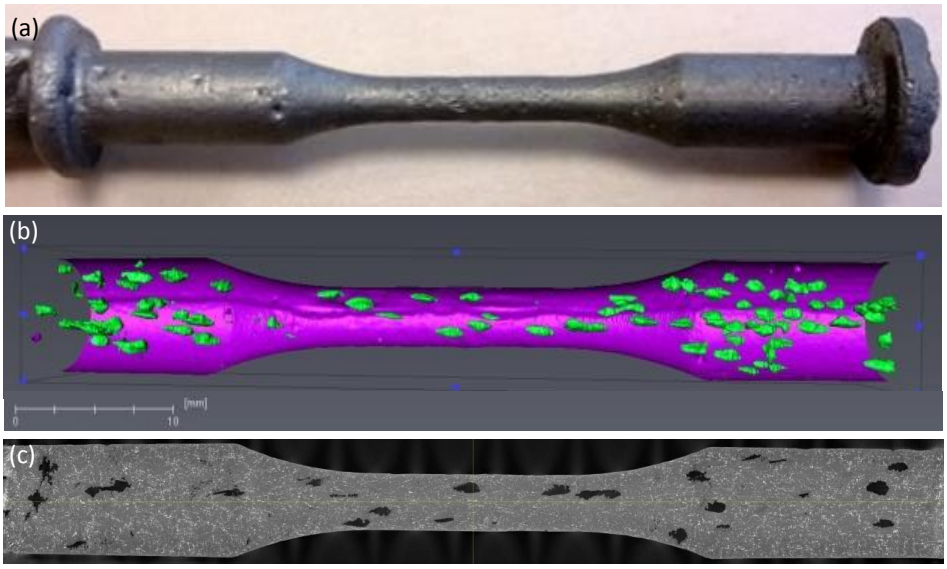

Figure 6-17: (a) Casting sample A, (b) 3D rendering of pores in sample A and (b) tomographic image slice showing the pore distribution

6.5.3 Scenario B: Gradient temperature cooling 1 (ΔT=60°C)

A casting with temperature control of the cooling rate was performed in the furnace.

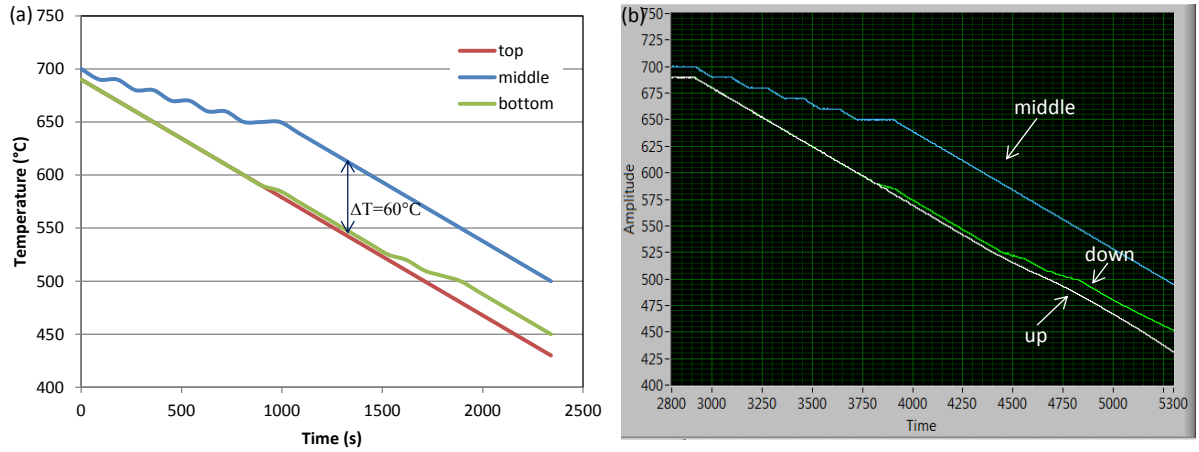

Figure 6-18: Comparison of (a) simulated and (b) measured temperature-time profile for sample B

Comparing the experimental results concerning the cooling curves in three positions and simulated cooling curves by QuickCast Software (as shown in Figure 6-2) during solidification process, the efficiency of the temperature control system is proved. Figure 6-18 illustrates that the experimental cooling curves match well with simulated ones. It can be seen that the temperature in the centre is near 60°C higher than at both ends of specimen.

After casting, X-ray computed tomography (CT) and metallographic investigation were carried out to identify microstructures of sample B. Unfortunately, the 3D characterization of the sample B did not match the porosity distribution expected from simulation.

There is one possible reason: The thermocouples, which are located at the resistance wires, are not attached to the specimen, so that the temperatures which we recorded are not the same as the temperature of the specimen, and the real temperature distribution along the specimen is not like the simulation.

The metallographic sample B was taken from the position which is marked out with a red square in Figure 6-19(a). The optical microscope images of sample B are shown in Figure 6-20. The common features of alloy can be recognized: Al dendrites, surrounded by Al–Si eutectic structures with Al_2Cu phase and iron-intermetallics in the interdendritic region.

In addition, the quantitative measurement of SDAS was performed, and the measured value of SDAS was 73µm ± 6µm, which is closed to the SDAS value (76µm ±5µm) of LFC cylinder head. This result indicates that the cooling rate (5.1°C/min) used for the center of the sample in this study is suitable to get an alloy with a microstructure similar with that of LFC alloy.

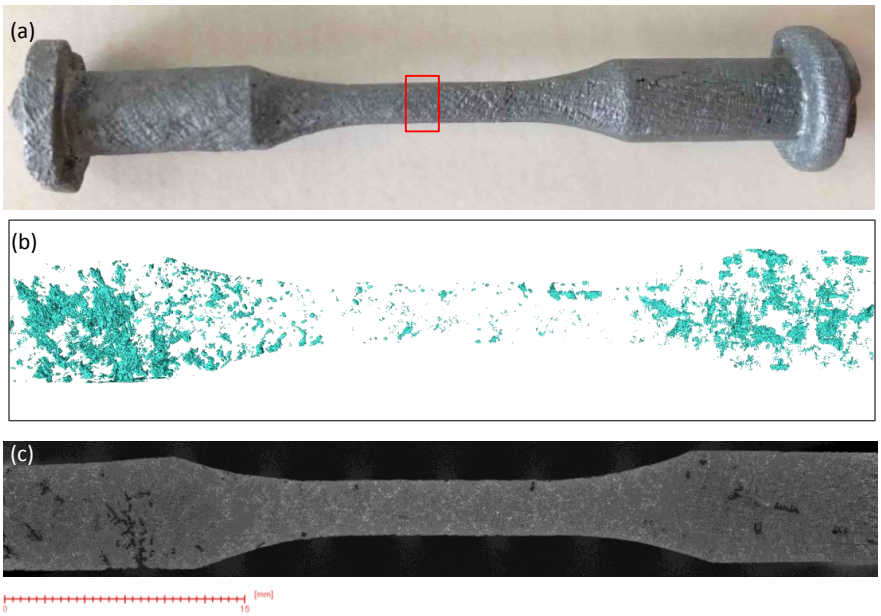

Figure 6-19: (a) Casting sample B, (b) 3D rendering of pores in sample B and (b) tomographic image slice showing the pores distribution

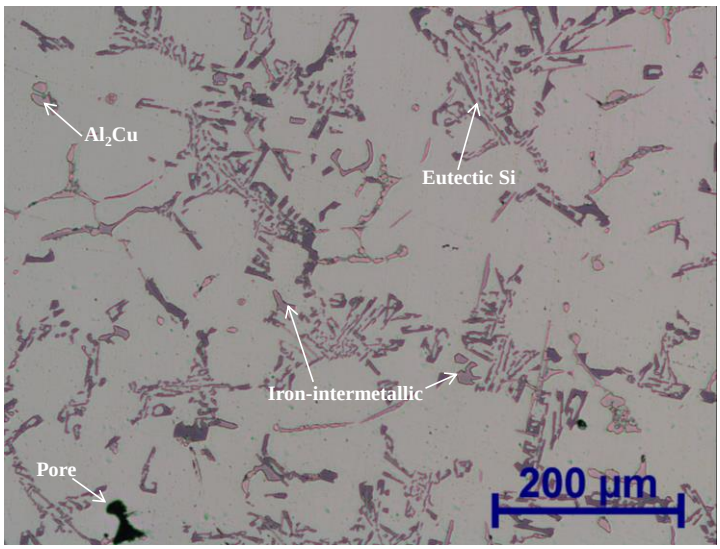

Figure 6-20: Optical microscope image of the center of sample B

6.5.4 Scenario C: Gradient temperature cooling 2 (ΔT=100°C)

After the specimen B, we increase the temperature differential between the center and both ends of the specimen from 60°C in specimen B to 100°C in specimen C as shown in Figure 6-21(a). However, the experimental cooling curves at both ends of specimen seem not to follow the simulation well. The higher temperature in the middle of specimen may reduce the cooling rate of the other part of specimen, even without any additional temperature compensation (i.e. natural cooling).

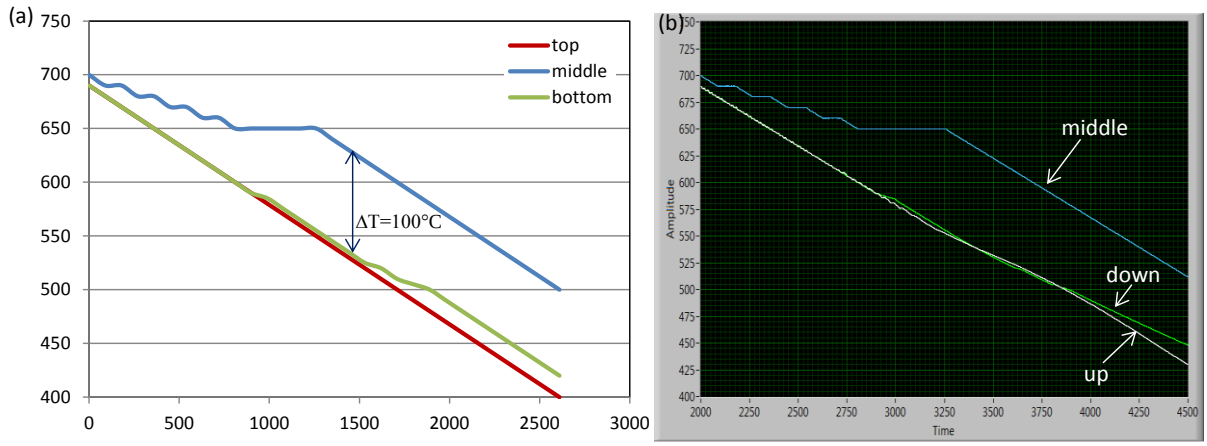

Figure 6-21: Comparison of (a) simulated and (b) measured temperature-time profile for sample C

In addition, the surface state of this specimen is not very smooth as expected by the use of resin model. Although thermal test shows that the resin model could melt and leave a precise mold cavity after the thermal cycle which is shown in Figure 6-11, this cycle still needs optimization and validation to result in a good surface finish of the casting.

The porosity distribution of the produced specimen B (Figure 6-22(a)) was analyzed by X-ray computed tomography with Avizo software. As shown in Figure 6-22(b) and (c), the center of the specimen contains fewer pores than both ends, the reasons may be the same as specimen B. Thus the real temperature distribution along the specimen during the solidification should be measured in the next step.

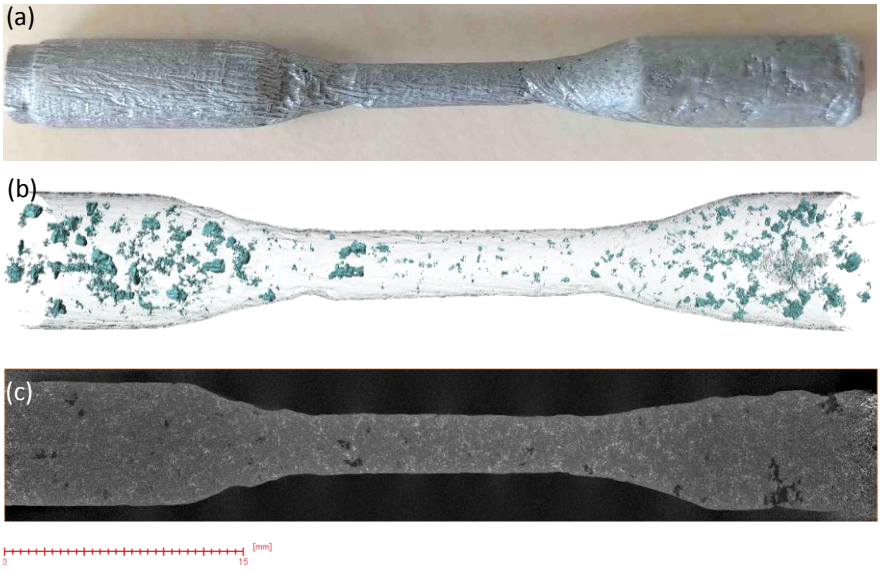

Figure 6-22: (a) Casting sample C, (b) 3D rendering of pores in sample C and (b) tomographic image slice showing the pores distribution

6.6 Summary

In this work, experimental trials were carried out by casting normalized specimens into a plaster mold. The casting was allowed to solidify under different cooling conditions. Three thermocouples were located between the resistance wire and casting to record the cooling curve of the solidification.

The following works were made:

1. The feasibility of plaster casting starting from 3D-printed model was proven.
2. An advanced temperature control system was carried out to provide precise control of furnace temperatures during solidification, ant it satisfies the requirement that the steady-state error is less than 1°C.
3. The temperature gradient was achieved by the advanced control system during solidification, and a normalized specimen with an equivalent microstructure as in fire deck area of cylinder heads was realized.
4. X-ray computed tomography (CT) was performed to be able to show the porosity distribution of castings produced under each condition.

6.7 Future development

Due to the present results, the following improvements could be done in the future:

1. In order to measure the real temperature within the cast part, it is better to install three thermocouples that go through the plaster mold and are attached to the specimen. This will allow making sure if the center of specimen is the last solidification area and compare the temperature difference between the center and both ends.
2. A vibrating table could be applied to reduce the number of bubbles in specimens during the casting, it can cause complete filling of thin walls of the mold cavity and improve the quality of the casting part.
3. An effective cooling system should be designed to provide a higher temperature differential during the solidification, thus resulting in a more rapid heat transfer and higher cooling rate of the specimen.
4. More casting experiments should be carried out in order to validate the simulation result on the cast parts.

Conclusions and future work

General conclusions

Al-Si alloy is widely used in automotive industry; A319 alloy is one of the preferred choices in cylinder heads. In order to better understand the influence of the microstructure on mechanical properties and damage mechanisms in A319 alloy. Some experiments have been carried out in this work.

Firstly, a full metallographic 2D and 3D characterization of the microstructure through optical- and Scanning Electron Microscopy (SEM) and laboratory X-ray tomography was performed in order to study the effect of different alloying elements (Sr, Fe and Mn) contents, casting processes (DC and LFC) and two solution heat treatments on the microstructure of Al–Si–Cu alloys (A319 alloy). The effect on mechanical properties was also investigated through a study of the tensile properties and damage mechanisms. Besides, thermal analysis experiments were also performed and the results have highlighted the evolution of microstructure in Al-Si-Cu alloy with different alloying elements (Sr, Fe and Mn) addition.

Then, two developed experimental protocols that allow following cracks initiation and propagation both on surface and in volume were used to identify the relation between casting microstructure, damage mechanisms and measured strain fields.

2D in-situ tensile tests with DIC were performed on two DC A319 alloys with different Fe content using Questar microscope. Damage mechanisms were revealed by the field measurements and fractographic observations.

3D in-situ tensile tests with DVC were performed on three LFC A319 alloys with two different heat treatment using Lab-CT. Strain measurements and damage mechanisms of the alloys were discussed.

In addition, in order to obtain cast specimens with controlled defects for in-situ tensile test, a melting/solidification device with a temperature control system was developed. It can create a temperature gradient during solidification and the cooling rate is controlled to obtain the same SDAS as in LFC cylinder heads.

Microstructure

In this thesis, optical Microscopy (OM) and Scanning Electron Microscope (SEM) with Energy Dispersive X-ray Spectroscopy (EDS) were used for 2D microstructure characterization. Laboratory (lab-CT) X-ray tomography was used for 3D microstructure characterization. 3D measurements provide more information of microstructures than 2D measurements, and the results indicate that they

are more reliable and more representative. Based on the measurement results obtained, the following conclusions can be made:

- **Sr addition**

Increase of strontium content slightly depresses the growth temperature of eutectic Si phase, a finer and more fibrous eutectic Si structure can be obtained with an increased Sr content. However, the modification effect of Sr is not significant at high cooling rate (such as in DC alloy), and the Sr addition can also introduce more pores in the DC alloy.

- **Fe and Mn content**

1. Increasing the Fe/Mn level shifts the precipitation sequence of the α+β phase toward a higher temperature. At higher Fe/Mn level, the majority of α+β phase precipitates prior to the eutectic Si. However, at low Fe/Mn level, the majority of α+β phase is expected to form at a lower temperature which is close to the eutectic Si precipitation.
2. The size, morphology and surface fraction of iron-intermetallics are influenced by the Fe and Mn content, i.e. the size and amount of Fe-intermetallics (α-$Al_{15}(Fe,Mn)_3Si_2$ and β-Al_5FeSi phase) increase with an increase in the Fe-Mn level.
3. Mn additions result in an increased amount of the α-Fe phase and the ratio of α and β phase increases with the increase of Mn/Fe in the alloys.
4. The higher Fe content can introduce more and smaller Al_2Cu particles. However, the amount of Al_2Cu phases also depends on the Cu content, which is not exactly the same in the four alloys.
5. A slight decrease of pores volume fraction is observed with the Fe and Mn content increase in some extent for the DC Al-Si-Cu alloys.

- **Casting process**

The different cooling rates that result from the different casting processes (i.e. DC and LFC) play an important role on all microstructural features in size and morphology.

1. The cooling rate has a dominant impact on SDAS: increasing the cooling rate decreases significantly the SDAS.
2. The cooling rate is also of great importance to the modification of eutectic Si: finer eutectic Si particles can be achieved at high cooling rate for the same Sr content.
3. The amount, size and morphology of intermetallic compounds are affected by the cooling rate. Compared to the DC alloy, the LFC AlSi7Cu3 alloy with lower cooling rate shows more casting defects, i.e. larger pores and microshrinkage cavities, and a coarser microstructure, i.e. larger SDAS, plate-like eutectic Si particles, needle-like iron-intermetallics.

Besides, the thermal analyses show that the temperature for the nucleation of aluminium dendrites depends on the amount of Si and Cu as expected. It was also found that the chemical composition of the alloys has also some effect on the SDAS, which slightly decreases with the incremental addition of Sr, Fe and Mn.

- **Heat treatment**

The effect of solution heat treatment on the microstructure of LFC A319 alloy was studied. The temperature of solution heat treatment was 495°C in order to put Al_2Cu in solid solution without generating incipient melting. The solution time was 0, 2h30 and 50 h. The main processes that take place during solution treatment are: the dissolution of Cu in the Al matrix and the spheroidisation and coarsening of the eutectic Si.

1. The solution heat treatment results in dissolution of the Al_2Cu phase that evolves in the following processes: dissolving the small Al_2Cu particles; the loss of interconnectivity by pinching off arms of the larger Al_2Cu particles, further dissolving of the disconnected particles.
2. The morphology of the eutectic Si particles changes with solution treatment time; it undergoes the following transformations: fragmentation, spheroidisation, and coarsening during the solution treatment.
3. A few needle-like β-Fe phases undergo partial dissolution after 50 h of solution treatment at 495°C. However, there were no noticeable changes for α-phase during solution treatment at 495°C.
4. The solution treatment at 495°C has no significant effect on porosity level of LFC A319 alloy.

Mechanical Properties

Mechanical properties of Al-Si-Cu alloy are strongly affected by the microstructures. In this thesis, mechanical characterizations were performed to relate microstructural features resulting from different metallurgical parameters to mechanical properties. The major conclusions of this work can be listed as follows:

1. Although a finer and more fibrous eutectic Si structure was obtained with an increase from 47 ppm to 130 ppm of Sr content, no change of the tensile properties was noticed.
2. Iron has a detrimental effect on the UTS and above all on ductility in terms of the amount of β-Al_5FeSi phase. However, Fe addition increases YS in the studied alloys, i.e. the presence of iron can harden the alloy to some extent.
3. Mechanical properties of AlSi7Cu3 alloy are highly influenced by casting process via the microstructure. The LFC AlSi7Cu3 alloy shows more casting defects (larger pores and microshrinkage cavities), a coarser microstructure (larger SDAS, plate-like eutectic Si particles, needle-like iron-intermetallics) than DC AlSi7Cu3 alloy. DC alloys showed higher UTS, YS, and elongation than LFC alloy.

Conclusions and future work

Experimental protocol

In this study, two experimental protocols to evaluate the damage mechanisms of Al-Si-Cu alloy in 2D/3D were developed and verified.

- **2D in-situ tensile test with DIC**

In order to study the surface damage micromechanisms at a fine microstructure scale, an etching procedure was successfully developed and applied to generate speckle patterns suitable for DIC analysis without using a speckle pattern that will mask the microstructure. Tensile tests on flat specimens were performed and a Questar long distance microscope was used for the in situ observation during tensile tests. The field measurements allowed identifying and tracking the development and localization of deformation.

- **3D in-situ tensile test with DVC**

Tensile test with 3D in-situ observation were performed using X-ray tomography on the LFC A319 alloys. A preliminary 3D characterization of pores using Lab-CT was carried out; then the FE simulation based on these tomographic images was efficiently used to simulate the strain distribution during the tensile test and thus select ROI. 3D in-situ tensile test allows cracks initiation and propagation being revealed directly in 3D while the DVC measurements enable 3D deformation measurements. It can also point out where tensile cracks form and at which local strain value initiation takes place in the different phases during tensile loading.

- **Postmortem analyses**

Postmortem analyses, which were performed using SEM and EDS on flat surfaces and fracture surfaces of studied specimen, help identifying final failure, micro-cracks and thus allow the damage mechanisms being understood thoroughly.

Damage mechanisms of Al-Si-Cu alloy

The tensile damage mechanisms of studied DC A319 alloys, i.e. with different Fe content, and LFC A319 alloys, i.e. with different heat treatment conditions, were revealed using the experimental protocol developed in this thesis:

- **DC A319 alloy**

Low Fe alloy: Crack initiation occurs through the fracture of Si particles, and Al_2Cu particles in the high stress concentration region in the low-Fe alloy (0.1 wt.%Fe). Cracks growth is prone to occur along the eutectic Si and Al_2Cu phases. Fractography analysis highlighted the role of hard inclusions on crack propagation, and revealed that crack propagation under monotonic load occurs through the eutectic Si, Al_2Cu phases and primary phases, exhibiting some fracture of the Al_2Cu phases and eutectic Si particles.

High Fe alloy: Cracks initiate at hard inclusions in areas with sufficient stress concentrations in the high-Fe alloy (0.8 wt.%Fe). Cracks appear more likely to occur through the fracture of iron-intermetallics. Thereafter, crack growth occurs through the cleavage of iron-intermetallics. Cracks also propagate through the fracture of Al_2Cu, as well as through brittle Si particles.

- **LFC A319 alloy**

Cracks initiation: Cracks initiate at hard inclusions in the areas with sufficient stress concentrations, which are mainly provided by large pores. The different size, location and shape of pores result in different stress concentrations thus they affect the cracks initiations during the tensile test. In addition, a high stress concentration can be also induced by specimen geometry.

Crack propagation: Once cracks initiated, they prefer to grow through the cracked hard inclusions, i.e. eutectic Si, iron intermetallics and Al_2Cu phase. The fast final fracture is more prone to occur at Si phase, iron intermetallics and Al_2Cu phases than in Al dendrites.

In a tensile test, more fracture of hard inclusions is observed than decohesion in all the fracture surfaces whether in cracks initiation region, cracks propagation region and final fast fracture region.

The quantitative analysis revealed that the iron-intermetallics show a lower average strain level for the cracking of particle than Al_2Cu phase.

Gradient solidification casting

An advanced temperature control system was developed for a melting/solidification device that generates a temperature gradient along the height of the specimen during solidification. It can provide precise control of furnace temperatures during solidification ($\Delta T<1°C$).

3D-printed resin model was used to realize a normalized specimen with an equivalent microstructure as in fire deck area of cylinder heads. Several castings with controlled cooling rate were created and compared with the simulation results.

Future work

From the results of this thesis, possibilities for future work are evoked on the following topics as well as the links with ongoing studies:

1. Microstructural characterization for LFC alloys with different Sr, Fe and Mn contents can be performed so as to have a general overview of the effects of alloying elements on cast alloys microstructural features at a low cooling rate.
2. Cooling rate can also affect the solidification parameters and microstructure of Al-Si alloy. The cooling rate for the thermal analysis used in the present work (0.13°C/s) is slower than for LFC (0.15-0.8°C/s), thus maybe it would be better to perform thermal analysis at the cooling rates of LFC and DC in the future work.

3. It will be exciting to cast the Al-Si alloy with different alloying elements through in-situ solidification experiments. In-situ 3D observation of Al-Si alloy solidification structure using synchrotron X-ray microtomography could provide new insights into the eutectic Si, intermetallic compounds and porosity evolution. In addition, the damage mechanisms of A319 alloys with different heat treatment could also be studied using in-situ tensile test with SR-CT, because eutectic Si phase which plays an important role on crack initiation and propagation cannot be detected by Lab-CT, however, it can be revealed by SR-CT due to phase contrast.
4. Hard inclusions, which are located in the vicinity of the large pores, have an important influence on the damage mechanisms of the specimens. Thus, the volume fraction of different hard inclusions should be considered in the selected specimen when we want to study the damage mechanisms of A319 alloy with different heat treatment.
5. A FE model representing pores, Al matrix and various hard inclusions could help to verify strain localizations at hard inclusions and to reveal the influence of different hard inclusions on strain localizations by comparison with the experimental results.
6. More casting experiments should be carried out in order to realize the specimen with controlled defects. Then the damage mechanism of the normalized specimen with different hard inclusions inherited from different Sr, Fe and Mn content could be studied by in-situ fatigue test.

References

Al Kahtani, S., H. Doty and F. Samuel (2014). "Combined effect of melt thermal treatment and solution heat treatment on eutectic Si particles in cast Al-Si alloys." International Journal of Cast Metals Research **27**(1): 38-48.

Alkahtani, S. A., E. M. Elgallad, M. M. Tash, A. M. Samuel and F. H. Samuel (2016). "Effect of Rare Earth Metals on the Microstructure of Al-Si Based Alloys." Materials **9**(1): 45.

Argo, D. and J. Gruzleski (1988). "Porosity in modified aluminum alloy castings." AFS Transactions **96**: 65-74.

Armanjo, J. (2015). "The influence of microstructural deformations and defects on mechanical properties in cast aluminium components by using Digital Image Correlation Techniques (DICT)."

Bacaicoa, I., P. K. Dwivedi, M. Luetje, F. Zeismann, A. Brueckner-Foit, A. Geisert and M. Fehlbier (2016). "Effect of non-equilibrium heat treatments on microstructure and tensile properties of an Al-Si-Cu alloy." Materials Science and Engineering: A **673**: 562-571.

Backerud, L., G. Chai and J. Tamminen (1990). "Solidification Characteristics of Aluminum Alloys. Vol. 2. Foundry Alloys." American Foundrymen's Society, Inc., 1990: 266.

Bay, B. K., T. S. Smith, D. P. Fyhrie and M. Saad (1999). "Digital volume correlation: three-dimensional strain mapping using X-ray tomography." Experimental mechanics **39**(3): 217-226.

Boileau, J. M. and J. E. Allison (2003). "The effect of solidification time and heat treatment on the fatigue properties of a cast 319 aluminum alloy." Metallurgical and materials transactions A **34**(9): 1807-1820.

Boromei, I., L. Ceschini, A. Morri, G. Nicoletto and E. Riva (2010). "Influence of the solidification microstructure and porosity on the fatigue strength of Al-Si-Mg casting alloys." Metallurgical Science and Technology **28**: 18-24.

Boulos, V., V. Fristot, D. Houzet, L. Salvo and P. Lhuissier (2012). Investigating performance variations of an optimized GPU-ported granulometry algorithm. Design and Architectures for Signal and Image Processing (DASIP), 2012 Conference on, IEEE.

Buffière, J. Y., S. Savelli, P. H. Jouneau, E. Maire and R. Fougères (2001). "Experimental study of porosity and its relation to fatigue mechanisms of model Al–Si7–Mg0.3 cast Al alloys." Materials Science and Engineering: A **316**(1–2): 115-126.

Campbell, J. and M. Tiryakioğlu (2010). "Review of effect of P and Sr on modification and porosity development in Al–Si alloys." Materials Science and Technology **26**(3): 262-268.

Canales, A., J. Talamantes-Silva, D. Gloria, S. Valtierra and R. Colás (2010). "Thermal analysis during solidification of cast Al–Si alloys." Thermochimica Acta **510**(1): 82-87.

Ceschini, L., I. Boromei, A. Morri, S. Seifeddine and I. L. Svensson (2009). "Microstructure, tensile and fatigue properties of the Al–10% Si–2% Cu alloy with different Fe and Mn content cast under controlled conditions." Journal of Materials Processing Technology **209**(15): 5669-5679.

Ceschini, L., A. Morri, A. Morri, A. Gamberini and S. Messieri (2009). "Correlation between ultimate tensile strength and solidification microstructure for the sand cast A357 aluminium alloy." Materials & Design **30**(10): 4525-4531.

Chan, K. S., P. Jones and Q. Wang (2003). "Fatigue crack growth and fracture paths in sand cast B319 and A356 aluminum alloys." Materials Science and Engineering: A **341**(1): 18-34.

References

Chen, C.-L. (2006). Characterisation of intermetallic phases in multicomponent Al-Si alloys for piston applications, Loughborough University.

Chen, C. L., A. Richter and R. C. Thomson (2010). "Investigation of mechanical properties of intermetallic phases in multi-component Al–Si alloys using hot-stage nanoindentation." Intermetallics **18**(4): 499-508.

Chen, X., H. Geng and Y. Li (2006). "Study on the eutectic modification level of Al–7Si Alloy by computer aided recognition of thermal analysis cooling curves." Materials Science and Engineering: A **419**(1): 283-289.

Chirita, G. (2011). "Mechanical and fatigue properties of functionally graded aluminium silicon alloys."

Cobden, R. and A. Banbury (1994). "Aluminium: physical properties, characteristics and alloys." Talat lecture **1501**: 19-26.

Crowell, N. and S. Shivkumar (1995). "Solution Treatment Effects in Cast Al-Si-Cu Alloys (95-107)." Transactions of the American Foundrymen's Society **103**: 721-726.

Dahdah, N., N. Limodin, A. El Bartali, J. Witz, R. Seghir, E. Charkaluk and J. Buffiere (2016). "Damage Investigation in A319 Aluminium Alloy by X‐ray Tomography and Digital Volume Correlation during In Situ High‐Temperature Fatigue Tests." Strain **52**(4): 324-335.

Dahle, A., K. Nogita, S. McDonald, C. Dinnis and L. Lu (2005). "Eutectic modification and microstructure development in Al–Si Alloys." Materials Science and Engineering: A **413**: 243-248.

Dash, M. and M. Makhlouf (2001). "Effect of key alloying elements on the feeding characteristics of aluminum–silicon casting alloys." Journal of Light Metals **1**(4): 251-265.

Dezecot, S. and M. Brochu (2015). "Microstructural characterization and high cycle fatigue behavior of investment cast A357 aluminum alloy." International Journal of Fatigue **77**: 154-159.

Dezecot, S., J.-Y. Buffiere, A. Koster, V. Maurel and F. Szmytka (2015). Characterization of damage in a cast aluminum alloy during cyclic loading test at high temperature by x-ray tomography. COM 2015: The conference of metallurgists.

Dezecot, S., J.-Y. Buffiere, A. Koster, V. Maurel, F. Szmytka, E. Charkaluk, N. Dahdah, A. El Bartali, N. Limodin and J.-F. Witz (2016). "In situ 3D characterization of high temperature fatigue damage mechanisms in a cast aluminum alloy using synchrotron X-ray tomography." Scripta Materialia **113**: 254-258.

Dinnis, C., A. Dahle, J. Taylor and M. Otte (2004). "The influence of strontium on porosity formation in Al-Si alloys." Metallurgical and materials transactions A **35**(11): 3531-3541.

Dinnis, C., J. Taylor and A. Dahle (2004). Porosity formation and eutectic growth in Al-Si-Cu-Mg alloys containing iron and manganese. Materials Forum-Aluminium Alloys Their Physical and Mechanical Properties, The Institute of Materials Engineering Australasia Ltd.

Dinnis, C. M., J. A. Taylor and A. K. Dahle (2005). "As-cast morphology of iron-intermetallics in Al–Si foundry alloys." Scripta Materialia **53**(8): 955-958.

Dinnis, C. M., J. A. Taylor and A. K. Dahle (2006). "Iron-related porosity in Al–Si–(Cu) foundry alloys." Materials Science and Engineering: A **425**(1): 286-296.

Djurdjevic, M., H. Jiang and J. Sokolowski (2001). "On-line prediction of aluminum–silicon eutectic modification level using thermal analysis." Materials characterization **46**(1): 31-38.

Djurdjevic, M., T. Stockwell and J. Sokolowski (1999). "The effect of strontium on the microstructure of the aluminium-silicon and aluminium-copper eutectics in the 319 aluminium alloy." International Journal of Cast Metals Research **12**(2): 67-73.

Dobrzanski, L., R. Maniara and J. Sokolowski (2007). "The effect of cooling rate on microstructure and mechanical properties of AC AlSi9Cu alloy." Archives of Materials Science **106**: 106.

References

Dobrzański, L. A., R. Maniara, J. Sokołowski and W. Kasprzak (2007). "Effect of cooling rate on the solidification behavior of AC AlSi7Cu2 alloy." Journal of Materials Processing Technology **191**(1–3): 317-320.

Đurđević, M. B. and S. Manasijević (2014). "Impact of major alloying elements on the solodification parameters of cast hypoeutectic AlSi6Cu (1-4 wt.%) and AlSi8Cu (1-4 wt.%) alloys." Metallurgical and Materials Engineering **20**(4): 235-246.

El Sebaie, O., A. Samuel, F. Samuel and H. Doty (2008). "The effects of mischmetal, cooling rate and heat treatment on the eutectic Si particle characteristics of A319. 1, A356. 2 and A413. 1 Al–Si casting alloys." Materials Science and Engineering: A **480**(1): 342-355.

Emadi, D., J. Gruzleski and J. Toguri (1993). "The effect of Na and Sr modification on surface tension and volumetric shrinkage of A356 alloy and their influence on porosity formation." Metallurgical Transactions B **24**(6): 1055-1063.

Emadi, D. and J. E. Gruzleski (1995). "Combating Al-Si porosity: the strontium/hydrogen myth." Modern casting **85**(3): 46-47.

Fabrizi, A., S. Ferraro and G. Timelli (2013). "The influence of Sr, Mg and Cu addition on the microstructural properties of a secondary AlSi9Cu3 (Fe) die casting alloy." Materials characterization **85**: 13-25.

Fan, J., D. L. McDowell, M. F. Horstemeyer and K. Gall (2003). "Cyclic plasticity at pores and inclusions in cast Al–Si alloys." Engineering Fracture Mechanics **70**(10): 1281-1302.

Farahany, S., A. Ourdjini, M. Idris and S. Shabestari (2013). "Computer-aided cooling curve thermal analysis of near eutectic Al–Si–Cu–Fe alloy." Journal of thermal analysis and calorimetry **114**(2): 705-717.

Gall, K., N. Yang, M. Horstemeyer, D. L. McDowell and J. Fan (1999). "The debonding and fracture of Si particles during the fatigue of a cast Al-Si alloy." Metallurgical and Materials Transactions A **30**(12): 3079-3088.

Goldstein, J., D. E. Newbury, P. Echlin, D. C. Joy, A. D. Romig Jr, C. E. Lyman, C. Fiori and E. Lifshin (2012). Scanning electron microscopy and X-ray microanalysis: a text for biologists, materials scientists, and geologists, Springer Science & Business Media.

Gruzleski, J. E. and B. M. Closset (1990). The treatment of liquid aluminum-silicon alloys, Amer Foundry Society.

Hafiz, M. F. and T. Kobayashi (1994). "Mechanical properties of modified and nonmodified eutectic Al-Si alloys." Keikinzoku **44**(1): 28-34.

Han, Y., A. Samuel, H. Doty, S. Valtierra and F. Samuel (2014). "Optimizing the tensile properties of Al–Si–Cu–Mg 319-type alloys: role of solution heat treatment." Materials & Design **58**: 426-438.

Hansen, M., K. Anderko and H. Salzberg (1958). "Constitution of binary alloys." Journal of the Electrochemical Society **105**(12): 260C-261C.

Hashmi, S. (2014). Comprehensive materials processing, Newnes.

Hegde, S. and K. N. Prabhu (2008). "Modification of eutectic silicon in Al–Si alloys." Journal of materials science **43**(9): 3009-3027.

Hess, P. and E. Blackmun (1975). "Strontium as a modifying agent for hypoeutectic aluminum-silicon alloys." Paper from" Transactions of the Americal Foundrymen's Society. **83**.

Hielscher, U., H. Sternau and H. Koch (2002). Aluminum-silicon alloy, Google Patents.

Horstemeyer, M. F. (2012). Integrated Computational Materials Engineering (ICME) for metals: using multiscale modeling to invigorate engineering design with science, John Wiley & Sons.

Ibrahim, M. F., E. M. Elgallad, S. Valtierra, H. W. Doty and F. H. Samuel (2016). "Metallurgical Parameters Controlling the Eutectic Silicon Charateristics in Be-Treated Al-Si-Mg Alloys." Materials **9**(2): 78.

References

ISO, E. (2009). "6892-1: 2009." Metallic materials–tensile testing–Part **1**: 6892-6891.
Jafari, H., M. H. Idris and A. Shayganpour (2013). "Evaluation of significant manufacturing parameters in lost foam casting of thin-wall Al–Si–Cu alloy using full factorial design of experiment." Transactions of Nonferrous Metals Society of China **23**(10): 2843-2851.
Ji, S., W. Yang, F. Gao, D. Watson and Z. Fan (2013). "Effect of iron on the microstructure and mechanical property of Al–Mg–Si–Mn and Al–Mg–Si diecast alloys." Materials Science and Engineering: A **564**: 130-139.
Kaufman, J. G. and E. L. Rooy (2004). Aluminum alloy castings: properties, processes, and applications, ASM International.
Khan, S. and R. Elliott (1996). "Quench modification of aluminium-silicon eutectic alloys." Journal of materials science **31**(14): 3731-3737.
Kirkwood, D. (1985). "A simple model for dendrite arm coarsening during solidification." Materials Science and Engineering **73**: L1-L4.
Labisz, K., M. Krupiński and L. Dobrzański (2009). "Phases morphology and distribution of the Al-Si-Cu alloy." Journal of Achievements in Materials and Manufacturing Engineering **37**(2): 309-316.
Lasagni, F. and H. P. Degischer (2010). "Enhanced Young's Modulus of Al-Si Alloys and Reinforced Matrices by Co-continuous Structures." Journal of composite materials **44**(6): 739-755.
Lee, F., J. Major and F. Samuel (1995). "Effect of silicon particles on the fatigue crack growth characteristics of Al-12 Wt Pct Si-0.35 Wt Pct Mg-(0 to 0.02) Wt Pct Sr casting alloys." Metallurgical and Materials Transactions A **26**(6): 1553-1570.
Li, Y. J., S. Brusethaug and A. Olsen (2006). "Influence of Cu on the mechanical properties and precipitation behavior of AlSi7Mg0.5 alloy during aging treatment." Scripta Materialia **54**(1): 99-103.
Li, Z. (2003). "Parameters Controlling the Precipitation and Dissolution of CuAI2 Phase in 319 Alloys and Their Influence on the Alloy Performance." MEng thesis, Université du QuebecaChicoutimi, Chicoutimi, Que., Canada.
Li, Z., A. Samuel, F. Samuel, C. Ravindran, H. Doty and S. Valtierra (2004). "Parameters controlling the performance of AA319-type alloys: Part II. Impact properties and fractography." Materials Science and Engineering: A **367**(1): 111-122.
Li, Z., A. Samuel, F. Samuel, C. Ravindran and S. Valtierra (2003). "Effect of alloying elements on the segregation and dissolution of CuAl2 phase in Al-Si-Cu 319 alloys." Journal of materials science **38**(6): 1203-1218.
Li, Z., A. Samuel, F. Samuel, C. Ravindran, S. Valtierra and H. Doty (2004). "Parameters controlling the performance of AA319-type alloys: Part I. Tensile properties." Materials Science and Engineering: A **367**(1): 96-110.
Limodin, N., J. Buffière, J. Réthoré, F. Hild, S. Roux and W. Ludwig (2013). Three-dimensional study of fatigue crack propagation using synchrotron X-ray microtomography. ICF12, Ottawa 2009.
Limodin, N., A. El Bartali, L. Wang, J. Lachambre, J.-Y. Buffiere and E. Charkaluk (2014). "Application of X-ray microtomography to study the influence of the casting microstructure upon the tensile behaviour of an Al–Si alloy." Nuclear Instruments and Methods in Physics Research Section B: Beam Interactions with Materials and Atoms **324**: 57-62.
Limodin, N., J. Réthoré, J.-Y. Buffière, A. Gravouil, F. Hild and S. Roux (2009). "Crack closure and stress intensity factor measurements in nodular graphite cast iron using three-dimensional correlation of laboratory X-ray microtomography images." Acta materialia **57**(14): 4090-4101.
LIU, L. (2003). "liu_ALLIAGES DE FONDERIE AL-SI-MG ET AL-SI-CU_PhD-2003.pdf."

References

Liu, L. (2004). Paramètres métallurgiques contrôlant l'évolution microstructurale dans les alliages de fonderie Al-Si-Mg et Al-Si-Cu, Université du Québec à Chicoutimi Chicoutimi.

Liu, L., A. Mohamed, A. Samuel, F. Samuel, H. Doty and S. Valtierra (2009). "Precipitation of β-Al5FeSi phase platelets in Al-Si based casting alloys." Metallurgical and Materials Transactions A **40**(10): 2457-2469.

Liu, L., A. Samuel, F. Samuel, H. Doty and S. Valtierra (2003). "Influence of oxides on porosity formation in Sr-treated Al-Si casting alloys." Journal of materials science **38**(6): 1255-1267.

Lu, L. and A. Dahle (2005). "Iron-rich intermetallic phases and their role in casting defect formation in hypoeutectic Al− Si alloys." Metallurgical and Materials Transactions A **36**(13): 819-835.

Lu, S.-Z. and A. Hellawell (1987). "The mechanism of silicon modification in aluminum-silicon alloys: impurity induced twinning." Metallurgical Transactions A **18**(10): 1721-1733.

Ma, Z., A. Samuel, H. Doty, S. Valtierra and F. Samuel (2014). "Effect of Fe content on the fracture behaviour of Al–Si–Cu cast alloys." Materials & Design **57**: 366-373.

Ma, Z., A. M. Samuel, F. H. Samuel, H. W. Doty and S. Valtierra (2008). "A study of tensile properties in Al–Si–Cu and Al–Si–Mg alloys: Effect of β-iron intermetallics and porosity." Materials Science and Engineering: A **490**(1–2): 36-51.

Makhlouf, M. and H. Guthy (2001). "The aluminum–silicon eutectic reaction: mechanisms and crystallography." Journal of light metals **1**(4): 199-218.

Mayer, H., M. Papakyriacou, B. Zettl and S. Stanzl-Tschegg (2003). "Influence of porosity on the fatigue limit of die cast magnesium and aluminium alloys." International journal of fatigue **25**(3): 245-256.

Mohamed, A. and F. Samuel (2012). "A review on the heat treatment of Al-Si-Cu/Mg casting alloys." Heat Treatment: Conventional and Novel Applications; InTech: Rijeka, Croatia.

Moustafa, M. (2009). "Effect of iron content on the formation of β-Al 5 FeSi and porosity in Al–Si eutectic alloys." Journal of Materials processing technology **209**(1): 605-610.

Moustafa, M., F. Samuel and H. Doty (2003). "Effect of solution heat treatment and additives on the microstructure of Al-Si (A413. 1) automotive alloys." Journal of Materials Science **38**(22): 4507-4522.

Moustafa, M. A. (2009). "Effect of iron content on the formation of β-Al5FeSi and porosity in Al–Si eutectic alloys." Journal of Materials Processing Technology **209**(1): 605-610.

Mu, P., Y. Nadot, C. Nadot-Martin, A. Chabod, I. Serrano-Munoz and C. Verdu (2014). "Influence of casting defects on the fatigue behavior of cast aluminum AS7G06-T6." International Journal of Fatigue **63**: 97-109.

Mugica, G. W., D. O. Tovio, J. C. Cuyas and A. C. González (2004). "Effect of porosity on the tensile properties of low ductility aluminum alloys." Materials Research **7**(2): 221-229.

Narayanan, L. A., F. Samuel and J. Gruzleski (1994). "Crystallization behavior of iron-containing intermetallic compounds in 319 aluminum alloy." Metallurgical and Materials Transactions A **25**(8): 1761-1773.

Narayanan, L. A., F. Samuel and J. Gruzleski (1995). "Dissolution of iron intermetallics in Al-Si alloys through nonequilibrium heat treatment." Metallurgical and Materials Transactions A **26**(8): 2161-2174.

Niane, N. T. and J.-P. Michalet (2011). VALIDATION OF FOUNDRY PROCESS FOR ALUMINUM PARTS WITH FLOW3D® SOFTWARE. Proceedings of the 2011 International Symposium on Liquid Metal Processing and Casting.

Niane, N. T. and J.-P. Michalet (2011). "VALIDATION OF FOUNDRY PROCESS FOR ALUMINUM PARTS WITH FLOW3D® SOFTWARE."

Nylese, T. and R. Anderhalt (2014). "Advanced Materials Characterization with Full-Spectrum Phase Mapping." Microscopy Today **22**(02): 18-23.

References

Okayasu, M., Y. Ohkura, S. Takeuchi, S. Takasu, H. Ohfuji and T. Shiraishi (2012). "A study of the mechanical properties of an Al–Si–Cu alloy (ADC12) produced by various casting processes." Materials Science and Engineering: A **543**: 185-192.

Onifade, I. (2013). "Internal structure characterization of asphalt concrete using x-ray computed tomography."

Pan, B., Z. Lu and H. Xie (2010). "Mean intensity gradient: an effective global parameter for quality assessment of the speckle patterns used in digital image correlation." Optics and Lasers in Engineering **48**(4): 469-477.

Pan, E., Y. Cherng, C. Lin and H. Chiou (1994). "Roles of Sr and Sb on Silicon Modification of A356 Aluminum Alloys (94-70)." Transactions of the American Foundrymen's Society **102**: 609-630.

Paray, F. and J. Gruzleski (1994). "Microstructure-mechanical property relationships in a 356 alloy. Part I: Microstructure." Cast Metals **7**: 29-29.

Pavlović-Krstić, J., R. Bähr, G. Krstić and S. Putić (2009). "The effect of mould temperature and cooling conditions on the size of secondary dendrite arm spacing in Al-7Si-3Cu alloy." Metalurgija **15**(2): 106-113.

Peterson, R. E. and R. Plunkett (1975). "Stress concentration factors." Journal of Applied Mechanics **42**: 248.

Petzow, G. (1999). Metallographic etching: techniques for metallography, ceramography, plastography, ASM international.

Pilkey, W. D. and D. F. Pilkey (2008). Peterson's stress concentration factors, John Wiley & Sons.

Plumtree, A. and S. Schafer (2013). Initiation and short crack behaviour in aluminium alloy castings. EGF1.

Popescu, G., I. Gheorghe, F. Dănilă and P. Moldovan (1996). Vacuum Degassing of Aluminium Alloys. Materials science forum, Trans Tech Publ.

Prasad, B. and T. Dan (1991). "Influence of solutionizing temperature and duration on the microstructure and properties of a hypereutectic aluminium-silicon alloy-graphite composite." Journal of materials science letters **10**(23): 1412-1414.

Puga, H., J. Barbosa, E. Seabra, S. Ribeiro and M. Prokic "New Trends in Aluminium Degassing–A Comparative Study."

Puncreobutr, C., P. Lee, K. Kareh, T. Connolley, J. Fife and A. Phillion (2014). "Influence of Fe-rich intermetallics on solidification defects in Al–Si–Cu alloys." Acta Materialia **68**: 42-51.

Puncreobutr, C., P. D. Lee, R. W. Hamilton and A. B. Phillion (2012). "Quantitative 3D Characterization of Solidification Structure and Defect Evolution in Al Alloys." JOM **64**(1): 89-95.

Roy, M., Y. Nadot, D. Maijer and G. Benoit (2012). "Multiaxial fatigue behaviour of A356 - T6." Fatigue & Fracture of Engineering Materials & Structures **35**(12): 1148-1159.

Roy, N., A. Samuel and F. Samuel (1996). "Porosity formation in AI-9 Wt pct Si-3 Wt pct Cu alloy systems: Metallographic observations." Metallurgical and Materials transactions A **27**(2): 415-429.

Rui, C., Y.-f. SHI, Q.-y. XU and B.-c. LIU (2014). "Effect of cooling rate on solidification parameters and microstructure of Al-7Si-0.3 Mg-0.15 Fe alloy." Transactions of Nonferrous Metals Society of China **24**(6): 1645-1652.

Ruxanda, R. and D. M. Stefanescu (2002). "Graphite shape characterisation in cast iron-from visual estimation to fractal dimension." International Journal of Cast Metals Research **14**(4): 207-216.

Salvo, L., P. Cloetens, E. Maire, S. Zabler, J. Blandin, J.-Y. Buffière, W. Ludwig, E. Boller, D. Bellet and C. Josserond (2003). "X-ray micro-tomography an attractive characterisation

References

technique in materials science." Nuclear instruments and methods in physics research section B: Beam interactions with materials and atoms **200**: 273-286.
Salvo, L., M. Suéry, A. Marmottant, N. Limodin and D. Bernard (2010). "3D imaging in material science: Application of X-ray tomography." Comptes Rendus Physique **11**(9): 641-649.
Samuel, A. and F. Samuel (1992). "Various aspects involved in the production of low-hydrogen aluminium castings." Journal of Materials Science **27**(24): 6533-6563.
Samuel, A. and F. Samuel (1995). "A metallographic study of porosity and fracture behavior in relation to the tensile properties in 319.2 end chill castings." Metallurgical and Materials Transactions A **26**(9): 2359-2372.
Samuel, F. (1998). "Incipient melting of Al5Mg8Si6Cu2 and Al2Cu intermetallics in unmodified and strontium-modified Al–Si–Cu–Mg (319) alloys during solution heat treatment." Journal of materials science **33**(9): 2283-2297.
Samuel, F., A. Samuel and H. Doty (1996). "Factors Controlling the Type and Morphology of Cu-Containing Phases in 319 Al Alloy (96-30)." Transactions of the American Foundrymen's Society **104**: 893-902.
Sanna, F., A. Fabrizi, S. Ferraro, G. Timelli, P. Ferro and F. Bonollo (2013). "Multiscale characterisation of AlSi9Cu3 (Fe) die casting alloys after Cu, Mg, Zn and Sr addition." La Metallurgia Italiana(4).
Savelli, S., J. Y. Buffière and R. Fougeres (2000). Pore characterization in a model cast aluminum alloy and its quantitative relation to fatigue life studied by synchrotron X-ray microtomography. Materials science forum, Trans Tech Publ.
Seghir, R., J. F. Witz and S. Coudert. (2014). "YaDICs - Digital Image Correlation 2/3D software." from http://www.yadics.univ-lille1.fr.
Seifeddine, S. (2007). "The influence of iron and Mg content on the microstructure and tensile properties of cast Al–Si–Mg alloys." Vilmer Project-5.2 Casting.
Seifeddine, S., S. Johansson and I. L. Svensson (2008). "The influence of cooling rate and manganese content on the β-Al5FeSi phase formation and mechanical properties of Al–Si-based alloys." Materials Science and Engineering: A **490**(1–2): 385-390.
Seifeddine, S. and E. Sj (2013). "On the role of copper and cooling rates on the microstructure, defect formations and mechanical properties of Al-Si-Mg alloys."
Seifeddine, S. and I. L. Svensson (2013). "The influence of Fe and Mn content and cooling rate on the microstructure and mechanical properties of A380-die casting alloys." Metallurgical Science and Tecnology **27**(1).
Serrano-Munoz, I., J. Y. Buffiere, C. Verdu, Y. Gaillard, P. Mu and Y. Nadot (2016). "Influence of surface and internal casting defects on the fatigue behaviour of A357-T6 cast aluminium alloy." International Journal of Fatigue **82, Part 3**: 361-370.
Serrano Munoz, I. (2014). Influence of casting defects on the fatigue behaviour of an A357-T6 aerospace alloy, Lyon, INSA.
Shabani, M. and A. Mazahery (2011). "Prediction of mechanical properties of cast A356 alloy as a function of microstructure and cooling rate." Arch Metall Mater **56**(3): 671-675.
Shabestari, S. and S. Ghodrat (2007). "Assessment of modification and formation of intermetallic compounds in aluminum alloy using thermal analysis." Materials Science and Engineering: A **467**(1): 150-158.
Shabestari, S. and M. Malekan (2005). "Thermal analysis study of the effect of the cooling rate on the microstructure and solidification parameters of 319 aluminum alloy." Canadian Metallurgical Quarterly **44**(3): 305-312.
Shabestari, S. G. and H. Moemeni (2004). "Effect of copper and solidification conditions on the microstructure and mechanical properties of Al–Si–Mg alloys." Journal of Materials Processing Technology **153–154**: 193-198.

References

Shivkumar, S., S. Ricci, C. Keller and D. Apelian (1990). "Effect of solution treatment parameters on tensile properties of cast aluminum alloys." Journal of Heat Treating **8**(1): 63-70.

Sinha, A. and Z. Farhat (2015). "Effect of surface porosity on tribological properties of sintered pure Al and Al 6061." Materials Sciences and Applications **6**(06): 549.

Sofyan, B. T., D. J. Kharistal, L. Trijati, K. Purba and R. E. Susanto (2010). "Grain refinement of AA333 aluminium cast alloy by Al–Ti granulated flux." Materials & Design **31**: S36-S43.

Standard, A. (2010). "E155." Standard Reference Radiographs for Inspection of Aluminum and Magnesium Castings.

Sui, Y., Q. Wang, G. Wang and T. Liu (2015). "Effects of Sr content on the microstructure and mechanical properties of cast Al–12Si–4Cu–2Ni–0.8 Mg alloys." Journal of Alloys and Compounds **622**: 572-579.

Sutton, M., C. Mingqi, W. Peters, Y. Chao and S. McNeill (1986). "Application of an optimized digital correlation method to planar deformation analysis." Image and Vision Computing **4**(3): 143-150.

Sutton, M. A., J. J. Orteu and H. Schreier (2009). Image correlation for shape, motion and deformation measurements: basic concepts, theory and applications, Springer Science & Business Media.

Tabibian, S. (2011). Contributions to Thermomechanical Fatigue Criteria for Lost Foam Casting Aluminum Alloys: Thèse de Doctorat, S. Tabibian.

Tabibian, S., E. Charkaluk, A. Constantinescu, G. Guillemot and F. Szmytka (2015). "Influence of process-induced microstructure on hardness of two Al–Si alloys." Materials Science and Engineering: A **646**: 190-200.

Tabibian, S., E. Charkaluk, A. Constantinescu, A. Oudin and F. Szmytka (2010). "Behavior, damage and fatigue life assessment of lost foam casting aluminum alloys under thermo-mechanical fatigue conditions." Procedia Engineering **2**(1): 1145-1154.

Tash, M., F. Samuel, F. Mucciardi and H. Doty (2007). "Effect of metallurgical parameters on the hardness and microstructural characterization of as-cast and heat-treated 356 and 319 aluminum alloys." Materials Science and Engineering: A **443**(1): 185-201.

Taylor, J., G. Schaffer and D. StJohn (1999). "The role of iron in the formation of porosity in Al-Si-Cu-based casting alloys: Part I. Initial experimental observations." Metallurgical and Materials transactions A **30**(6): 1643-1650.

Taylor, J. A. (2004). The effect of iron in Al-Si casting alloys. 35th Australian foundry institute national conference, Adelaide, South Australia.

Thévenaz, P. and M. Unser (2007). "User‐friendly semiautomated assembly of accurate image mosaics in microscopy." Microscopy research and technique **70**(2): 135-146.

Thomas, J.-J., L. Verger, A. Bignonnet and E. Charkaluk (2004). "Thermomechanical design in the automotive industry." Fatigue & Fracture of Engineering Materials & Structures **27**(10): 887-895.

Tillová, E., M. Chalupová and E. Ďuriníková (2012). "EFFECT OF CHEMICAL COMPOSITION OF SECONDARY Al-Si CAST ALLOY ON INTERMETALLIC PHASES."

Toda, H., T. Nishimura, K. Uesugi, Y. Suzuki and M. Kobayashi (2010). "Influence of high-temperature solution treatments on mechanical properties of an Al–Si–Cu aluminum alloy." Acta Materialia **58**(6): 2014-2025.

Valtierra, S. and J. Lacaze (2005). "Effect of strontium and cooling rate upon eutectic temperatures of A319 aluminum alloy." Scripta Materialia **52**(6): 439-443.

Wang, L. (2015). Influence of the casting microstructure on damage mechanisms in Al-Si alloys by using 2D and 3D in-situ analysis, Ecole Centrale de Lille.

References

Wang, L., D. Apelian and M. Makhlouf (1997). Tensile properties of aluminum die-casting alloys. Proceedings of the 19th International Die Casting Congress, Minneapolis, NADCA, Rosemont, IL.

Wang, L., N. Limodin, A. El Bartali, J.-F. Witz, R. Seghir, J.-Y. Buffiere and E. Charkaluk (2016). "Influence of pores on crack initiation in monotonic tensile and cyclic loadings in lost foam casting A319 alloy by using 3D in-situ analysis." Materials Science and Engineering: A.

Wang, Q. G., D. Apelian and D. A. Lados (2001). "Fatigue behavior of A356-T6 aluminum cast alloys. Part I. Effect of casting defects." Journal of Light Metals **1**(1): 73-84.

Wang, R. and W. Lu (2012). "Direct electrolytic Al–Si alloys (DEASA)—an undercooled alloy self-modified structure and mechanical properties." by V. Linkov (Intech, Rijeka, 2012): 107-140.

Warmuzek, M. (2004). Aluminum-silicon Casting Alloys: An Atlas of Microfractographs, ASM International.

Wicke, M., M. Luetje, I. Bacaicoa and A. Brueckner-Foit (2016). "Characterization of Casting Pores in Fe-rich Al-Si-Cu Alloys by Microtomography and Finite Element Analysis." Procedia Structural Integrity **2**: 2643-2649.

Xu, H., Q. Han and T. T. Meek (2008). "Effects of ultrasonic vibration on degassing of aluminum alloys." Materials Science and Engineering: A **473**(1–2): 96-104.

Yi, J. Z., Y. X. Gao, P. D. Lee and T. C. Lindley (2004). "Effect of Fe-content on fatigue crack initiation and propagation in a cast aluminum–silicon alloy (A356–T6)." Materials Science and Engineering: A **386**(1–2): 396-407.

Zamani, M. and S. Seifeddine (2016). "Determination of Optimum Sr Level for Eutectic Si Modification in Al–Si Cast Alloys Using Thermal analysis and Tensile Properties." International Journal of Metalcasting: 1-9.

Zappa, E., P. Mazzoleni and A. Matinmanesh (2014). "Uncertainty assessment of digital image correlation method in dynamic applications." Optics and Lasers in Engineering **56**: 140-151.

Zeng, L., J. Sakamoto, A. Fujii and H. Noguchi (2014). "Role of eutectic silicon particles in fatigue crack initiation and propagation and fatigue strength characteristics of cast aluminum alloy A356." Engineering Fracture Mechanics **115**: 1-12.

Zhang, B., W. Chen and D. R. Poirier (2000). "Effect of solidification cooling rate on the fatigue life of A356. 2-T6 cast aluminium alloy." Fatigue and Fracture of Engineering Materials and Structures **23**(5): 417-424.

Zhang, B., M. Garro and C. Tagliano (2013). "Dendrite arm spacing in aluminium alloy cylinder heads produced by gravity semi-permanent mold." Metallurgical Science and Tecnology **21**(1).